

Dissertation zur Erlangung des Doktorgrades der Fakultät für Chemie  
und Pharmazie der Ludwig-Maximilians-Universität München

**Mesoporous silica nanostructures:  
A versatile platform in Drug-Delivery and  
Material Science**

Timo Lebold

aus

Miltenberg am Main

2010



## **Erklärung**

Diese Dissertation wurde im Sinne von § 13 Abs. 3 bzw. 4 der Promotionsordnung vom 29. Januar 1998 von Herrn Prof. Dr. Christoph Bräuchle betreut.

## **Ehrenwörtliche Versicherung**

Diese Dissertation wurde selbständig, ohne unerlaubte Hilfe erarbeitet.

München, den 07. Juni 2010

.....  
Dipl.-Chem. Timo Lebold

Dissertation eingereicht am:	15.06.2010
1. Gutachter:	Prof. Dr. Christoph Bräuchle
2. Gutachter:	Prof. Dr. Thomas Bein
Mündliche Prüfung am:	20.07.2010



# Contents

<b>1</b>	<b>Introduction .....</b>	<b>1</b>
<b>2</b>	<b>Mesoporous Materials.....</b>	<b>7</b>
2.1	Thin mesoporous silica films .....	8
2.2	Oriented mesoporous silica through Micromoulding in Capillaries (MIMIC) .....	10
2.3	Mesoporous SBA-15 silica particles .....	12
<b>3</b>	<b>Fluorescence Microscopy and Diffusion Analysis .....</b>	<b>15</b>
3.1	Fluorescence: the phenomenon and basic principles.....	16
3.2	Fluorescence spectroscopy and microscopy.....	20
3.2.1	Single molecule microscopy techniques.....	22
3.2.1.1	Laser Scanning Confocal Microscopy (LSCM) .....	22
3.2.1.2	Wide-field Fluorescence Microscopy .....	24
3.2.1.3	Optical resolution and positioning accuracy: Single Particle Tracking (SPT) .....	26
3.2.1.4	Diffusion Theory .....	29
3.2.2	Fluorescence recovery after photobleaching (FRAP) .....	34
3.2.2.1	The basic principles of FRAP .....	35
3.2.2.2	Data evaluation.....	36
3.2.2.3	Data modelling.....	38

<b>4</b>	<b>Mesoporous silica materials for drug-delivery applications .....</b>	<b>43</b>
4.1	Introduction to Drug-Delivery .....	44
4.2	Tuning single molecule dynamics in functionalized mesoporous silica.....	47
4.2.1	Introduction to the sample systems: preparation and characterization ...	47
4.2.2	Single molecule trajectories .....	54
4.2.3	Diffusion dynamics in mesoporous films.....	56
4.2.4	Correlation of the diffusion coefficients to the pore-to-pore distance.....	62
4.2.5	Controlling the homogeneity in the distribution of the functional groups. ....	63
4.2.6	General view on the diffusion of a individual molecule inside the pores of functionalized mesoporous silica .....	66
4.2.7	Conclusion .....	69
4.3	Nano-structured silica materials for drug-delivery of the anti-cancer drug Doxorubicin.....	70
4.3.1	Introduction to the sample systems: preparation and characterization ...	71
4.3.2	Drug dynamics in the mesoporous delivery structure .....	73
4.3.3	Characterization of the drug release kinetics.....	81
4.3.4	Live-cell measurements for testing the applicability of the delivery system.....	85
4.3.5	Conclusion .....	87
4.4	Silica films and particles with nanometer-sized channels for siRNA and DNA delivery.....	88
4.4.1	Introduction to the sample systems: preparation and characterization ...	89
4.4.2	Thin mesoporous silica films for the delivery of siRNA .....	94
4.4.3	Observing oligonucleotide diffusion inside mesoporous silica delivery particles on a single molecule level .....	98
4.4.4	Loading SBA-15 mesoporous silica particles with siRNA.....	102
4.4.5	Determining oligonucleotide mobility inside the delivery structure with FRAP .....	107
4.4.6	Conclusion .....	116

<b>5</b>	<b>Fabricating mesoporous silica with large domains.....</b>	<b>119</b>
5.1	Controlling domain size in P123 templated films through adjusting the relative humidity .....	120
5.1.1	Introduction to the sample systems: preparation and characterization .	120
5.1.2	Relative humidity dependent domain formation observed through single molecule diffusion .....	122
5.1.3	Conclusion .....	128
5.2	Active patterning of channel alignment in mesoporous silica through Micromoulding in Capillaries .....	129
5.2.1	Introduction to the sample systems: preparation and characterization .	130
5.2.1.1	The PDMS stamps .....	131
5.2.1.2	The mesoporous silica created through pattern transfer .....	134
5.2.2	Characterizing channel alignment in actively patterned mesoporous silica with the help of single molecule microscopy .....	138
5.2.2.1	Pattern transfer from UV-stamp I.....	139
5.2.2.2	Pattern transfer from UV-stamp II.....	140
5.2.3	Conclusion .....	144
<b>6</b>	<b>Summary and Outlook.....</b>	<b>147</b>
6.1	Drug-delivery using mesoporous silica hosts.....	147
6.2	Creating large domains in mesoporous silica .....	149
<b>7</b>	<b>List of Abbreviations.....</b>	<b>151</b>
<b>8</b>	<b>List of Publications and Contributions to Conferences .....</b>	<b>155</b>
8.1	Publications .....	155
8.2	Contributions to Conferences .....	156
<b>9</b>	<b>Bibliography .....</b>	<b>159</b>
	<b>Acknowledgements.....</b>	<b>171</b>
	<b>Curriculum Vitae .....</b>	<b>173</b>



# 1 Introduction

Small objects can create a big impact in life. This is basically the credo of the emerging field of nanotechnology! The physicist Richard Feynman can be considered as the father of this new scientific discipline since already in 1959 he gave a talk at an American Physical Society meeting at Caltech University called: "There's Plenty of Room at the Bottom". In his talk he outlined the high potential of the ability to manipulate matter on an atomic scale. However, the term "nanotechnology" was first introduced only in 1974 by Norio Taniguchi. Nowadays, it generally refers to the understanding and control of matter at nanometer ( $10^{-9}$  m) dimensions. This nano-universe shows many unique and interesting phenomena that offer intriguing material properties and thereby pave the way for novel applications spanning nearly all scientific disciplines, such as material science,<sup>1, 2</sup> chemistry,<sup>3-5</sup> physics,<sup>6-10</sup> biology,<sup>11</sup> medicine ("nano-medicine")<sup>12-15</sup> and the food industry.<sup>16, 17</sup> The work presented in this thesis would not exist without substantial nanotechnological know-how.

In this work, mesoporous silica materials are investigated.<sup>18-21</sup> The materials possess a network of nanometer-sized channels. They can thus act as host systems for the incorporation of a wide amount of differently sized guest molecules. However, in contrast to zeolites, applications for mesoporous silica materials are rare so far even though the materials show a high potential since they are very versatile structures: their pore topologies, sizes and surfaces can be fabricated according to the respective requirements. The entire work presented in this thesis is devoted to highlighting ways towards potential applications for these promising materials. The materials can act as host structures for the incorporation of a wide amount of differently sized

guests. For any possible application it is thus of paramount importance to understand in great detail the intricate interplay between the host matrix and the guest molecules.

However, applications of nanotechnology, such as the above mentioned host-guest-systems, remain a vision unless there are efficient techniques to characterize nanostructures and to indeed manipulate matter on the atomic scale. Consequently, nanotechnology boomed with the invention of the Scanning Tunneling Microscope (STM)<sup>22, 23</sup> in 1982 and the Atomic Force Microscope (AFM)<sup>24</sup> in 1986 both by G. Binnig, H. Rohrer and co-workers. Accordingly, the invention of the STM was acknowledged in 1986 with the Nobel Prize in Physics to Binnig and Rohrer and to E. Ruska for fundamental works on electron optics. Nowadays, these techniques have become standard methods for the investigation and manipulation of nanometer-sized matter. Yet, they allow conclusions mainly about the surface of the investigated samples. In the case of mesoporous silica host-guest structures, the important processes that need to be observed do occur deep inside the materials. This problem can be overcome by optical microscopy techniques for observing single molecules, pioneered by Moerner and Orrit<sup>25-28</sup> in 1989 and 1990, only shortly after the developments of Binnig and Rohrer. In this thesis, individual molecules are used extensively as beacons that explore the porous network of the host structure and through their fluorescence report about the nature of this novel class of materials. This thesis also makes use of ensemble fluorescence microscopy techniques, however single molecule approaches prevail in most cases since the amount of detailed information that can be gathered is unprecedented. Ensemble techniques generally suffer from an inevitable averaging associated with the ensemble populations. In contrast, single molecule microscopy can reveal subpopulations and mechanistic details of the subtle host-guest interactions. These techniques play a major role for gaining the insights discussed in this work and they were accompanied by additional standard characterization techniques, such as X-ray diffractometry, nuclear magnetic resonance spectrometry or infrared spectrometry.

The work presented in this thesis emerges from a close collaboration with the research group of T. Bein (LMU Munich, Department of Chemistry, Munich, Germany), that synthesized most of the mesoporous silica materials investigated in this thesis. Furthermore, they provided their materials scientific expertise about porous silica and characterized the investigated structures. The collaborating colleagues in the group of T. Bein and their contributions are named in detail in the respective chapters. The terylene diimide dye derivatives utilized throughout this thesis

were kindly provided by the research group of K. Müllen (Max-Planck-Institute for Polymer Research, Mainz, Germany).

The first part of this thesis focuses on applications of mesoporous silica in the emerging field of drug-delivery. “Drug-delivery” denotes the strategy of administering a drug wisely such that it reaches its target size under minimization of the negative side-effects experienced by the patient. Further, smart drug-delivery strategies should guarantee a maximum therapeutic effect with only the lowest possible dose of a pharmaceutical. To realize that, different carrier structures have been developed so far, ranging from organic polymers<sup>29</sup>, via liposomes<sup>30</sup> to nanoparticle constructs.<sup>31</sup> A wide number of different drug carriers is already applied clinically. However, especially cell-targeting and a controlled release of the drug at the target-site still represent a great challenge. The high versatility of mesoporous silica thus raises the question whether this novel class of nanomaterials can be utilized for drug-delivery purposes. Chapter 4 of this thesis shows three studies that exemplarily discuss different aspects of this question. First, the tunability of molecular dynamics inside mesoporous silica through the covalent attachment of organic functional groups is discussed comprehensively (Chapter 4.2). The ability to fine-tune the host-guest interaction inside the delivery system is an essential prerequisite for creating a depot effect, which means for releasing the drug with a defined rate over a prolonged period of time. The study shows how such a fine-tuning of the guest dynamics inside the carrier can be realized.

Efficient drug-delivery strategies can contribute to the improvement of therapies in many fields of medicine. One important field is certainly cancer therapy. Thus, Chapter 4.3 introduces a study dealing with mesoporous silica for drug-delivery of a the widely used anti-cancer drug Doxorubicin hydrochloride. Especially chemotherapy could profit substantially from a smart delivery strategy since the cytostatic drugs are usually accompanied by a number of sever side-effects.<sup>32,33</sup> Doxorubicin, for example, shows a high cardiac and renal toxicity. The experiments depicted in this work demonstrate how the drug dynamics can be tuned. They further prove the efficient drug release off the delivery system and the applicability of the drug-delivery strategy is demonstrated: the drug retains its cytotoxicity and can efficiently kill tumor cells after being released from the delivery vehicle.

Another important field in modern medicine showing a tremendous evolution within the last decades is certainly gene technology for the treatment of gene defects and hereditary diseases. In 2006 the Nobel Prize in Physiology or Medicine was awarded to A. Fire and C. Mello for their discovery of the mechanism of RNA interference (RNAi) and gene silencing.<sup>34, 35</sup> Gene technology and silencing utilize short interfering RNA (siRNA) or DNA sequences in order to manipulate the genome for achieving a medical effect. For example with the help of RNAi damaged genes can be selectively switched off in order to prevent them from exerting their malicious effects. Yet, there is an eager quest ongoing for retrieving efficient delivery vehicles to transport the fragile DNA or RNA sequences to their destination. A third study in Chapter 4.4 thus investigates the diffusion of oligonucleotides in mesoporous silica films and particles. It will be shown that the biomolecules can be successfully incorporated into the carrier particles, in case a favourable drug-host interaction is provided by coating the channels with appropriate organic groups. Furthermore, the study proves the stability of the biomolecules inside the delivery system, which is of course essential such that they keep their therapeutic effects. Some of the experiments presented in this chapter were measured using the “Fluorescence Recovery after Photobleaching” (FRAP) technique. Modelling of the FRAP data was done by collaborators in the group of H. Leonhardt (LMU Munich, Department of Biology, Munich Germany). The collaborating colleagues and their contributions are listed in detail in the respective chapters.

The second part of this thesis is dedicated to maximizing the application potential of mesoporous silica structures. There are two parameters that so far could not be controlled sufficiently: the domain size and the absolute orientation of the channels in the material. However, these parameters play an important role. For industrially applications of the materials a reliable and reproducible domain growth must be realized under distinct conditions. Furthermore, applications such as electrophoresis, catalysis or lab-on-a-chip techniques could profit from the possibility to control the orientations of channels on the substrate and thus create a tailor-made pattern of mesoporous silica channels.

The first study presented in Chapter 5.1 assesses the role of the relative humidity as a parameter to control the domains size in Pluronic P123 templated thin films. It is shown that tuning the humidity during the mesoporous silica self-assembly results in drastically different domain sizes: ranging from short domains to micrometer-sized domains.

The second study in Chapter 5.2 goes one step further, towards realizing an active patterning of mesoporous silica. The Micromoulding in Capillaries Technique is used to transfer a pattern from a stamp to mesoporous silica thereby controlling the channel orientation. This active patterning technique allows the fabrication of tailor-made materials with channels oriented over macroscopic scales (mm). This pushes the application potential of mesoporous silica to an unprecedented level.

**The thesis is structured in the following way:**

After this introductory chapter, Chapter 2 introduces the diverse morphologies of mesoporous silica utilized throughout this work. Thin mesoporous silica films are introduced, followed by an explanation of the Micromoulding in Capillaries technique to fabricate actively patterned silica structures. This chapter closes with the introduction of mesoporous hexagonal ordered mesoporous silica particles.

Chapter 3 is dedicated to explaining the basic principles of Fluorescence and introducing the Fluorescence Microscopy apparatus and techniques utilized throughout this thesis. First, the applied Single Molecule Microscopy techniques are explained and the theoretical background of Single Particle Tracking and Diffusion Analysis is outlined since this is necessary to extract dynamical data of recorded microscopy movies. Additionally, the Fluorescence Recovery after Photobleaching technique is presented since this ensemble method will be utilized later for determining oligonucleotide dynamics.

Chapter 4 displays the first part of the results of this thesis. It deals with the application of mesoporous silica in drug-delivery. The chapter is further subdivided into four parts. After an introduction to drug-delivery, the tunability of molecular dynamics inside porous silica carrier structures is demonstrated through covalent linking of organic functional groups. After that study, mesoporous silica particles are introduced as host for oligonucleotide delivery in gene technology. Finally, the potential of mesoporous silica in cancer therapy is shown as an efficient delivery structure for the cytostatic Doxorubicin hydrochloride.

Chapter 5 presents the second part of the results in this work. This chapter focuses on understanding and controlling the domain growth and channel orientation inside mesoporous silica. The first study investigates the humidity dependent domain growth in thin P123

templated silica films. This chapter closes with a study that demonstrates how mesoporous silica can be actively pattern through Micromoulding in Capillaries.

The results of the thesis are summarized in Chapter 6 also providing an outlook to future perspectives in the field.

The work closes with a List of Abbreviations (Chapter 7), a List of Publications and Contributions to Conferences (Chapter 8) and the Bibliography (Chapter 9).

After the official part of the thesis the Acknowledgements can be found as well as a Curriculum Vitae of the author of this work.

## 2 Mesoporous Materials

The porous materials that were investigated in this work are introduced in this chapter. According to the International Union of Pure and Applied Chemistry (IUPAC) porous materials can be classified with respect to the diameter  $d$  of their pores into three categories (Table 2.1):<sup>36</sup>

**Table 2.1: IUPAC Classification for porous solids**

<b>Pore Diameter <math>d</math></b>	< 2.0 nm	2.0 – 50 nm	> 50 nm
<b>Classification</b>	Micropores	Mesopores	Macropores

All porous materials investigated in this work have mesopores and show pore diameters of ~ 2 – 15 nm. The structural framework of the materials consists of silica (SiO<sub>4</sub>) units and the porosity is created by a liquid-crystal templating process with the help of a surfactant as structure directing agent. Mesoporous silica structures are thus a novel class of hybrid nanomaterials.

Initially, the materials date back to 1992, when scientists of the Mobil company discovered this new class of silica/aluminosilicate mesoporous materials, the so-called M41S materials.<sup>18, 19</sup> In 1998 the portfolio of accessible materials got enriched by the so-called Santa Barbara Amorphous (SBA) type materials.<sup>20, 21</sup> M41S and SBA type materials are a very versatile class of nanomaterials and ended the long-standing pore-size constraint of zeolites by offering pore sizes ranging from 2 – 30 nm. Besides their pore diameter, surface properties and topologies can be fine-tuned over a large range. This makes them an ideal platform for various

applications, since their specifications can be tailor-made according to the individual requirements. Consequently, within the recent years a growing number of applications for mesoporous silica materials has been suggested, such as molecular sieves<sup>37</sup>, catalysis<sup>38</sup>, chromatography<sup>39</sup>, stabilization of conducting nanoscale wires<sup>40-42</sup> and novel drug-delivery systems.<sup>43-47</sup> In general, these applications imply the incorporation of guest molecules inside the porous silica host matrix with its large network of interconnected channels consisting of differently sized domains of parallel aligned pores: they are thus called host-guest systems. Applications in nanotechnology and the emerging field of nano-medicine (drug-delivery) are within the focus of this work.

In this chapter the diverse mesoporous silica structures used for the studies in this work are presented. First, thin mesoporous silica films are described, followed by an explanation of the Micromoulding in Capillaries (MIMIC) technique to create large oriented silica structures. An introduction to silica particles with nanometer-sized channels closes this chapter.

## 2.1 Thin mesoporous silica films

One further advantage of mesoporous silica materials is the fact that they can be synthesized in various forms, such as powders or thin films of a thickness of about 50 nm to several micrometers. Thin films are an interesting object to study since they can act as coatings on diverse substrates for applications either in catalysis or in drug-delivery. Further, thin films can be prepared with large domains of parallelly aligned pores. Large domains with good connectivity are a desired feature for many applications. Finally, the thin films can be coated on a transparent substrate, *e.g.* glass, such that the samples can be easily studied with optical techniques. Thin mesoporous silica films play an important role for some of the projects described in this work.

There are basically two methods for the synthesis of thin films: dip-coating (Figure 2.1 a) and spin-coating (Figure 2.1 b). Both methods start from a precursor solution containing silica building blocks, such as tetraethyl orthosilicate (TEOS) and surfactant molecules as templates in an acidic ethanol/water solution. In the dip-coating method (Figure 2.1 a) a cover slip gets

immersed into the precursor solution and slowly retracted. This leads to the formation of a thin film of solution onto the substrate, from which the solvent can slowly evaporate. During spin-coating (Figure 2.1 b) solvent evaporation is caused by rotation of the cover-slip on which the precursor solution was placed. The evaporation of the solvent during dip- and spin-coating leads to a process called *Evaporation Induced Self-Assembly* (EISA) which results in the formation of a condensed mesoporous silica structure. There are two synthesis mechanisms that can explain EISA: a two-step mechanism and a cooperative one-step mechanism.<sup>48, 49</sup> In the precursor solution, before EISA occurs, the surfactant concentration is below the *critical micelle concentration* (CMC). This means that no surfactant micelles are present. Now, solvent evaporation leads to crossing that CMC. In a two-step mechanism this leads to the formation of a liquid-crystal phase around which the silica can condense subsequently. In contrast, the one-step mechanism postulates a cooperative self-organization of the silica precursor and the surfactant below the CMC. In this case, the inorganic silica induces the formation of an ordered hexagonal array of surfactant molecules. Recent results favour the one-step mechanism.<sup>50-54</sup> Depending on the silica to surfactant ratio different pore topologies (hexagonal, cubic, lamellar) are accessible.<sup>55-57</sup> In this work only hexagonal mesoporous structures were investigated (for a schematic view of such a pore topology see Figure 2.1 c).

Guest molecules such as different dyes or drugs can be added directly to the precursor solution and get incorporated into the pores during the EISA process. This works well for various different molecules as long as the molecular size does not exceed the pore-size of the synthesized silica material. Furthermore, if the guest molecules are too polar, they will not be embedded inside the apolar part of the surfactant micelles, which prevents their incorporation into the channels. Due to the acidic conditions in the precursor solution this method is not suited for the incorporation of biomolecules. In order to make the porous network accessible for such molecules the template can be removed by calcination or solvent extraction and the silica structures can be loaded after the synthesis (post-synthetic loading).

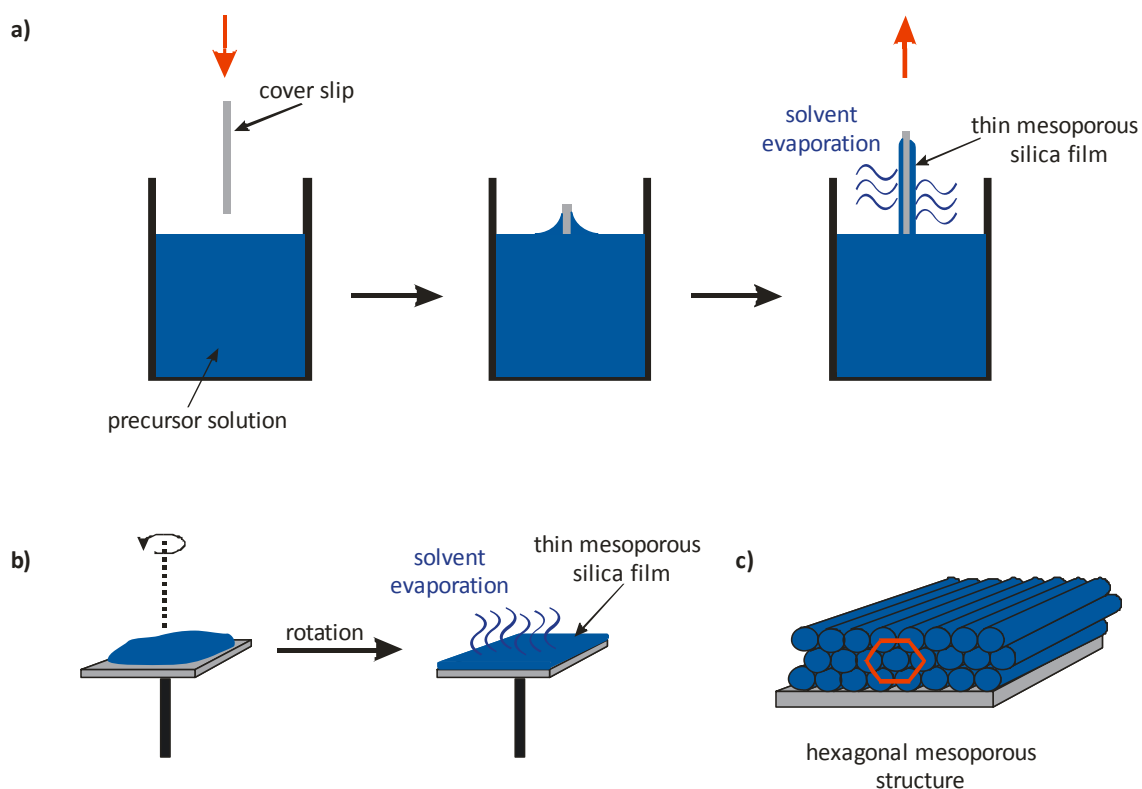


**Figure 2.1: Synthesis methods for thin hexagonal mesoporous silica films.** (a) Dip-coating. The cover-slip is immersed into the precursor solution. Through slow retraction of the cover-slip from the precursor solution a thin film forms on both sides of the substrate. Solvent evaporation induces the formation of a hexagonal mesoporous structure. (b) Spin-coating. A droplet of the precursor solution is placed onto a cover-slip. Rotating the cover slip at about 3000 rotations per minute leads to solvent evaporation and the formation of a thin mesoporous film. (c) Schematic view of a hexagonal mesoporous structure.

## 2.2 Oriented mesoporous silica through Micromoulding in Capillaries (MIMIC)

In the previously discussed thin films, domains of parallel aligned channels can be observed with domain sizes up to several micrometers. However, the different domains are randomly distributed. For maximizing the application potential of mesoporous silica the ability to design tailor-made structures is essential. To realize this, the channel alignment needs to be controlled over a large scale. This can be realized through a growth of mesoporous silica that is guided by an external pattern. For example, Cauda *et al.* have demonstrated that anodic alumina membranes (AAMs) can be used to gain control over the channel alignment and they

used the fabricated silica to incorporate an antibiotic drug.<sup>58</sup> Towards the end of the 1990s several studies demonstrated that a guided growth of orientated mesoporous silica can also be achieved by a technique called *Micromoulding in Capillaries* (MIMIC).<sup>59, 60</sup> Since MIMIC will be utilized in Chapter 5.2 of this work, it is explained in the following section in detail.

In Figure 2.2 two different strategies to fabricate ordered hexagonal mesoporous silica *via* MIMIC are shown. In both cases a poly(dimethylsiloxane) (PDMS) stamp is used as a pattern offering confinements that can be filled with precursor solution. In this work only stamps with linear confinements have been used. The PDMS stamp can simply be pressed onto a droplet of the precursor solution deposited on the substrate (Figure 2.2 a). The solution fills the confinements and since the stamp is permeable for the solvents the EISA process can take place slowly. The slow evaporation of the solvent is crucial for the fabrication of a highly ordered structural organization, since the micelles and the silica have time to rearrange. After condensation of the structure the stamp can be removed and the hexagonal mesoporous silica showing oriented channels is accessible. Hence, the stamp can act as a structure directing pattern. An alternative way of fabricating such structure ordering is depicted in Figure 2.2 b, where the PDMS stamp is placed onto the substrate first, and afterwards droplets of the precursor solution are added close to the entrances of the stamp pattern. The solution gets effectively sucked into the confinements since capillary forces promote this process. Again, EISA can take place and after stamp removal the ordered mesoporous silica can be obtained.

The general idea behind MIMIC is not limited to mesoporous silica. Already before the application on silica MIMIC was used in 1995 for generating polymer microstructures.<sup>61</sup> Further, MIMIC is a low-cost approach since the PDMS stamps are easy to create and can be fabricated with basically any possible pattern. Highly ordered silica structures fabricated with MIMIC are of high interest for applications in optoelectronic devices, such as mesostructured waveguides for mirrorless lasing.<sup>62, 63</sup> In these studies mesostructured silica was fabricated in the form of a linear fibre by using the MIMIC technique and a PDMS stamp. In order to create a laser the mesoporous silica was doped with Rhodamine 6G as a laser dye and pumped by a Nd:YAG laser. Additionally, the mesostructured fibre was mounted on a lower refractive index support in order to prevent light transmission out of the fibre and thus provide waveguide characteristics. Other applications of porous silica fabricated through MIMIC include photochromic materials and optical or chemical sensors.<sup>64</sup> Optical sensors for example are

based on the incorporation of a dye anchored to the mesoporous silica walls. The emission, transmission or lifetime of the dye can be monitored and if a dye is chosen that reacts very pH sensitive in its emission spectrum, such as certain covalently linked fluorescein derivatives, a pH sensor is created.

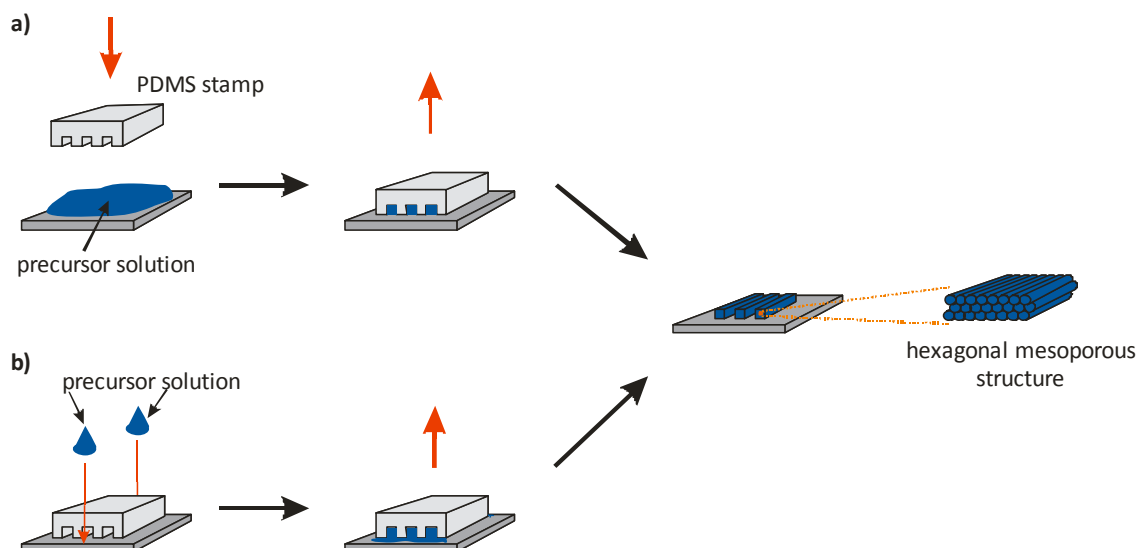


**Figure 2.2: Different Micromoulding in Capillaries techniques for the fabrication of ordered mesoporous silica.** (a) A stamp of poly(dimethylsiloxane) (PDMS) is pressed onto a droplet of the precursor solution deposited on a glass cover slip. The precursor solution fills the cavities of the stamp and through EISA a hexagonal mesoporous silica structure forms. After condensation of the structure the stamp can be removed. (b) The PDMS stamp is placed on the substrate. Droplets of the precursor solution are deposited close to the entrances to the pattern of the PDMS stamp and get sucked in due to capillary forces. Again, EISA takes place and the structure condensates. Afterwards, the stamp can be removed, making the mesoporous structure accessible.

## 2.3 Mesoporous SBA-15 silica particles

For many applications such as drug-delivery and molecular sieving spherically shaped particles are required. Consequently, some of the experiments described in this work deal with mesoporous silica in the form of particles. For these studies a SBA-15 material was chosen. The suffix “-15” indicates that the particles were synthesized using the tri-block copolymer poly(ethylene oxide)<sub>20</sub>-poly(propylene oxide)<sub>70</sub>-poly(ethylene oxide)<sub>20</sub> (short: PE<sub>20</sub>PO<sub>70</sub>PE<sub>20</sub>) as a surfactant. The surfactant is commercially available as Pluronic P123. These SBA-15 particles

have been introduced by Katiyar *et al.* especially for the incorporation of biomolecules.<sup>65</sup> They possess a large pore surface area ( $> 700 \text{ m}^2/\text{g}$  estimated by the theory of Brunauer, Emmett and Teller (BET theory)<sup>66</sup>) as well as a large pore diameter (9 – 12 nm) and a high pore wall thickness (2 – 4nm). Their wall thickness is an important parameter for providing a high degree of hydrothermal stability and thus a sufficiently long lifetime in biological environments.<sup>20</sup> In contrast M41S materials possess thinner walls and are hence less stable. Consequently, SBA-15 particles are an ideal host for the drug-delivery studies in this work.

The materials are prepared again from a precursor solution. The spherical morphology is accessible through stirring and ageing sequences at increased temperature. In order to further maximize their potential for the incorporation of biomolecules, a swelling agent (*e.g.* 1,3,5-trimethylbenzene (TMB)) can be added to the precursor solution, which leads to an increase in the pore diameter and volume of the resulting mesoporous particles.<sup>65</sup> The existence of swelling agents for the materials is a highly advantageous feature since the size of certain biomolecules, such as enzymes, often still exceeds the limits of mesoporous materials. Furthermore, using a positively charged co-surfactant, such as cetyltrimethyl ammonium bromide (CTAB), proved useful. In the absence of such a co-surfactant, the particle size and shape gets rather undefined. In contrast, adding CTAB offers a precise control over the particle morphology, which is of course an essential prerequisite for any further applications. This phenomenon was attributed to an advantageous electrostatic interaction of the co-surfactant with the silica species.<sup>67</sup>



# 3 Fluorescence Microscopy and Diffusion Analysis

We have now learnt the basic principles about mesoporous silica structures and different ways of fabricating tailor-made mesoporous materials. This entire work is devoted to exploring the complicated host structures and making them accessible to applications. Consequently, in this chapter, techniques are introduced that “shed light” onto these mesoporous channel networks. The fluorophore is used as a molecular probe that illuminates the interior of the mesoporous structures. In order to understand and evaluate the collected fluorescence data, we first need to learn the basics about fluorescence, the microscopy of fluorescent molecules and the analysis of diffusion processes.

This chapter is subdivided into two sections. First, the general phenomenon of fluorescence is introduced. The second section introduces the techniques used to record and monitor fluorescence: fluorescence microscopy under single molecule and ensemble concentrations. It is divided again in two subsections. Many of the studies depicted in this thesis utilize *Single Molecule Microscopy* (SMM) techniques. Hence, first different techniques for the microscopy of individual molecules are introduced and the sophisticated methods of data evaluation with the help of Single Particle Tracking (SPT) and Diffusion Theory are explained. After that, the *Fluorescence Recovery after Photobleaching* (FRAP) technique is introduced, since FRAP is utilized in this work to reveal oligonucleotide dynamics inside mesoporous SBA-15 particles under ensemble concentrations. The chapter closes by explaining models used for evaluating the recorded FRAP data.

### 3.1 Fluorescence: the phenomenon and basic principles

The emission of light from any substance is called luminescence.<sup>68</sup> Formally, luminescence can be divided into two categories, fluorescence and phosphorescence. In order to understand the differences between these phenomena and to illustrate the processes associated with the absorption and emission of light, a schematic diagram, the so-called Jablonski diagram, is very useful. Figure 3.1 displays a typical Jablonski diagram.

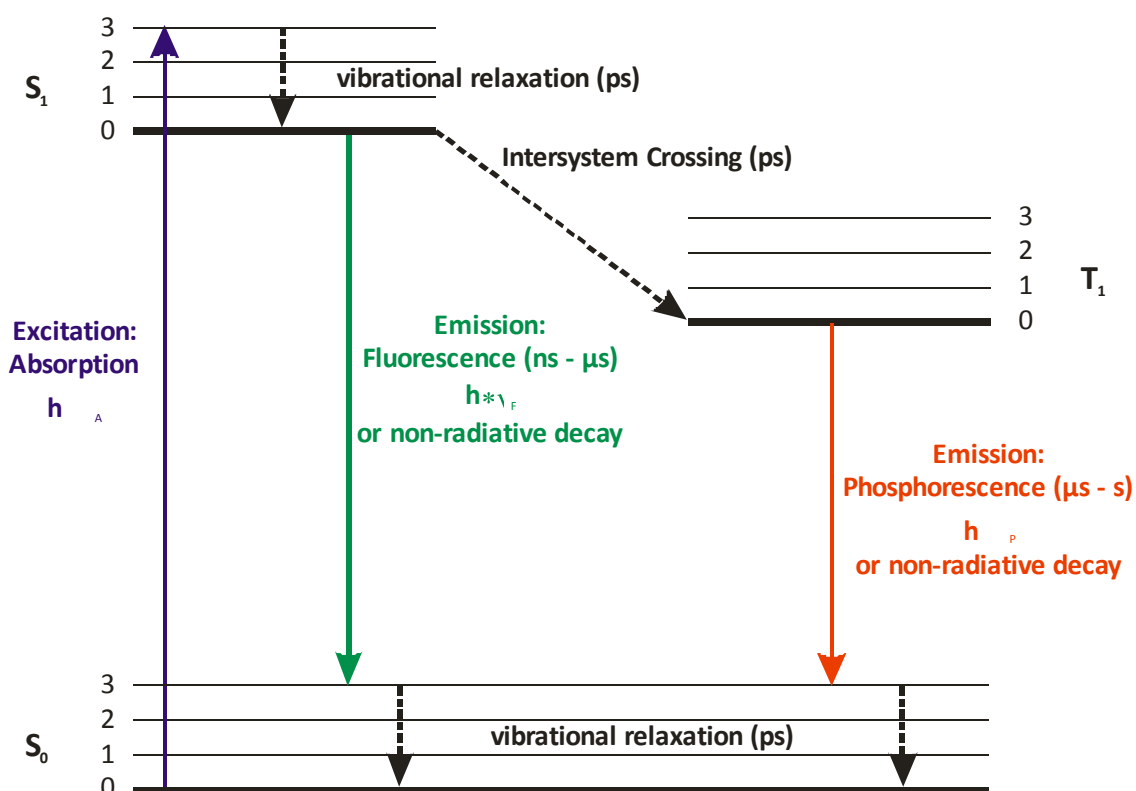


**Figure 3.1: Typical Jablonski Diagram.** Schematic representation of the electronic (—) and vibrational (0, 1, 2, 3) energy levels.  $S_0$  is the ground singlet state,  $S_1$  the first excited singlet state,  $T_1$  the lowest triplet state. For each electronic state additional vibrational levels are displayed. Absorption (—), Fluorescence (—), Phosphorescence (—) and vibrational relaxation processes (---) are indicated.

The ground singlet state  $S_0$ , the first excited singlet state  $S_1$  and the lowest triplet state  $T_1$  are depicted. Each of the electronic states is accompanied by a number of vibrational energy levels, indicated by 0, 1, 2, 3. Absorption of a photon  $h \cdot \nu_A$  usually occurs from the energy minimum, the lowest vibrational level 0 of the ground state  $S_0$ . Since absorption takes only

$\sim 10^{-15}$  s (1 fs) the nuclei cannot respond to the displacement of the electronic charge by adjusting their position and thus  $S_1$  gets populated in an excited vibrational level (Franck-Condon principle). After exciting the molecule, usually rapid vibrational relaxation takes place within femtoseconds to picoseconds ( $1 \text{ ps} = 10^{-12}$  s) and the molecule relaxes non-radiatively from the excited vibrational level of  $S_1$  to the corresponding ground vibrational level. From there the molecule can emit a photon  $h * \nu_F$ , longer in wavelength (and lower in energy) compared to the absorbed photon and relax within nanoseconds to microseconds usually to a vibrational excited level of  $S_0$ . This process is called fluorescence. The molecule can then return non-radiatively to the lowest vibrational level of the ground state. The characteristic difference between the excitation and the emission wavelength is known as Stokes shift. It is a critical parameter that makes the observation of fluorescence highly powerful for optical microscopy since the weak fluorescence signal can easily be separated from the incident excitation laser light.

Additionally, molecules in  $S_1$  can also relax through *Intersystem Crossing* (ISC) to the lowest triplet state  $T_1$ . Since ISC involves spin-conversion of an electron the transition from  $T_1$  to  $S_0$  is forbidden and consequently the emission occurs several orders of magnitude slower ( $\mu\text{s} - \text{s}$ ). This process is called phosphorescence. The phosphorescence emission energies are usually lower compared to fluorescence. Phosphorescence normally also leads to a vibrationally excited level of  $S_0$ , where through vibrational relaxation the molecule returns to the lowest vibrational level of  $S_0$ .

In order to characterize the absorption and emission properties of a fluorophore, usually absorption and emission spectra are recorded.

Figure 3.2 shows the absorption (black) and fluorescence emission (red) spectra of the dye ATTO647N (in the form of the free acid) in aqueous solution as well as its molecular structure. The dye is commercially available from Atto-tec GmbH (Siegen, Germany) and is used for labelling purposes. In this work oligonucleotides (short DNA and RNA double strands) are labelled with this dye. The structure of the spectra maps the energy landscape of the molecule depicted schematically in for example a Jablonski diagram. For most fluorophores the fluorescence emission spectrum mirrors the absorption spectrum. This again is a result of the Franck-Condon principle. Since the electronic excitation does not change the nuclear coordinates significantly, also the relative separation of the vibrational energy levels of the

### 3.1 Fluorescence: the phenomenon and basic principles

ground and excited electronic states is comparable, resulting in a very similar vibrational structure in both spectra. As previously discussed in the Jablonski diagram, emission shows always a lower energy (or longer wavelength) compared to absorption. The corresponding shift that can be observed between the absorption and emission spectrum is called Stokes-Shift. It mainly originates from the rapid non-radiative relaxation mechanisms present due to the molecular electronic structure and the interactions of the molecule with its surrounding environment (*e.g.* solvent, host matrix). The emission spectrum is dependent on the electronic structure of the molecule, but typically independent of the excitation wavelength.

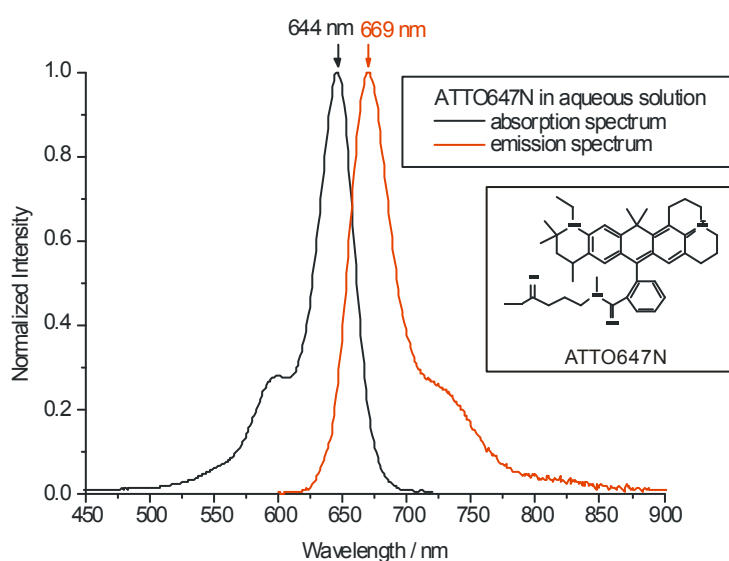


**Figure 3.2: Spectra and molecular structure of the dye Atto647N.** Absorption (black) and fluorescence emission (red) spectra of the commercially available dye Atto647N.<sup>69</sup> The structure of the dye (in the form of the free acid) is shown in an inset.

In the last part of this section the terms quantum yield, absorption cross-section, fluorescence lifetime as well as photoblinking, -bleaching and fluorescence quenching, key principles related to the phenomenon of fluorescence are introduced.

Especially for single molecule studies it is absolutely essential to use fluorophores with excellent photo-physical properties. One key parameter that characterizes these properties is the fluorescence quantum yield  $\Phi$ , the ratio of the number of emitted photons to the number of absorbed photons. If all absorbed photons are reemitted,  $\Phi$  will be unity. However, as previously mentioned, there are always non-radiative relaxation pathways present, such as

intersystem crossing, that minimize the number of emitted photons and thereby also the quantum yield. An equivalent definition of  $\Phi$  can be given through the rates of radiative decay  $k_{rad}$  and non-radiative decay  $k_{non-rad}$ :

$$\Phi = \frac{\# \text{ emitted photons}}{\# \text{ absorbed photons}} = \frac{k_{rad}}{(k_{rad} + k_{non-rad})} \quad (3.1)$$

Modern powerful fluorophores such as terrylene diimide derivatives show high quantum yields above 60% up to more than 90% even in solution.<sup>70-72</sup> The quantum yield critically depends on the utilized solvent since the solvent interferes with the non-radiative deactivation pathways. Consequently in rigid solid matrices  $\Phi$  is usually higher than in solution.<sup>73</sup>

Besides the quantum yield, a powerful fluorophore needs to possess a high absorption cross section  $\sigma$ . Physically, this parameter can be interpreted as the area with which the molecules can collect photons. A high quantum yield is not sufficient, if the molecule cannot efficiently “harvest” the photons offered by the laser beam.

Three other phenomena need to be discussed since they are frequently observed during single molecule experiments: photoblinking, fluorescence quenching and photobleaching of the fluorescent molecule (see Figure zzz). Photoblinking denotes a reversible transition of the molecule to a non-radiative state. It can result from the population of triplet states or other interactions with the surrounding matrix.<sup>74, 75</sup> If the molecule’s environment, *e.g.* the solvent, the host matrix or other added substances (so-called quenchers), causes a temporary decrease in the fluorescence intensity of the fluorophore, this process is called fluorescence quenching. After removing the quencher, the fluorophore regains its previous fluorescence intensity. In contrast, photobleaching is per definition an irreversible deactivation of the fluorophore. Often this occurs due to photo-oxidation or other reactive degradation processes of the molecule.

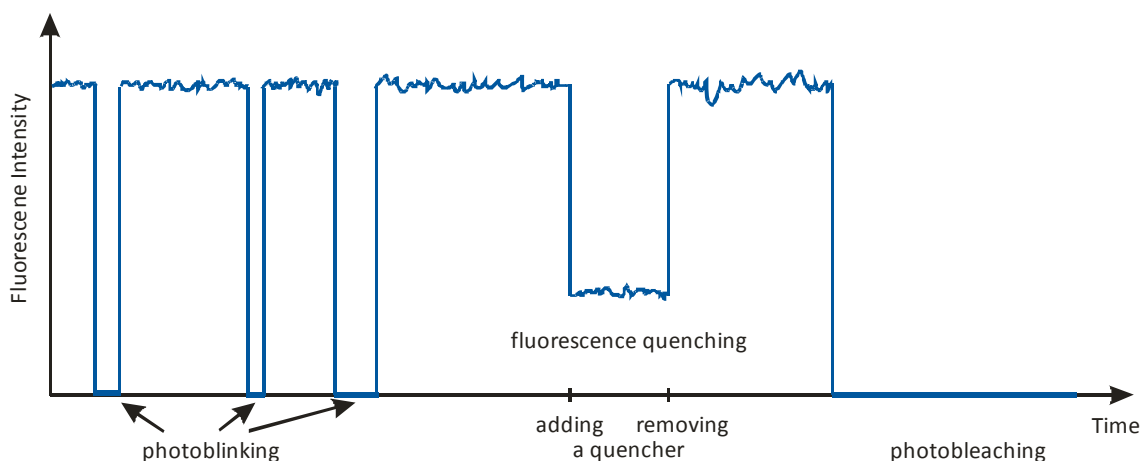


**Figure 3.3: Photoblinking, -bleaching and fluorescence quenching.** During monitoring the fluorescence intensity of an individual fluorophore, photoblinking and -bleaching can be observed. In case of photoblinking the molecule reversibly changes to a non-radiative state, e.g. by population of triplet states. An irreversible deactivation of the fluorophore is called photobleaching. Additionally, fluorescence quenching, a temporary decrease in the fluorescence intensity, can be observed due to interactions with the environment (solvents, host matrix, ...) or due to adding other substances, so-called quenchers, that interact with the fluorophore by offering non-radiative relaxation pathways.

## 3.2 Fluorescence spectroscopy and microscopy

In the previous chapter we have learnt the basic principles of fluorescence. The fluorescence light emitted by a fluorophore contains a high amount of information about the molecule itself and its environment (see Jablonski Diagram, Figure 3.1). The most direct way to access this information is analyzing the fluorescence signal with a spectroscope. A spectroscope collects the incident fluorescence and separates the individual wavelengths with the help of a prism or a diffraction grating. The individual signals can then be detected for example on a charge-coupled device (CCD) camera. If the fluorescence is analyzed by such a detector the device is usually referred to as a spectrometer. With a spectrometer fluorescence spectra such as in Figure 3.2 can be acquired.

In this thesis some fluorescence spectra are displayed however the majority of experiments were conducted utilizing another important device: the optical microscope. The optical microscope is an instrument with the help of which objects too small for the human eye can be

magnified and visualized. Here, the optical microscope is used to observe the fluorescence of molecules and to monitor their motion. Throughout this work, this was mostly done with samples in which the fluorescent molecules were diluted to such a high extent ( $\sim 10^{-10} - 10^{-11}$  mol/L) that individual molecules can be observed separately. This technique is called Single Molecule Microscopy (SMM). The apparatus used to observe the fluorescence of single molecules are described in detail in Chapter 3.2.1.

With SMM subpopulations of differently behaving molecules can easily be distinguished due to the low concentration of the molecules. A microscopy technique based on observing and fluorescence entity under ensemble concentrations would not reveal these subpopulations since the recorded signal yields an averaged value for the entire observed sample. This averaging problem is inevitable for ensemble methods. Single molecule microscopy is utilized in this work for the investigation of fluorescent (bio-) molecules inside mesoporous silica structures (see Chapter 2). The individual molecules are used as probes, which explore the porous host structure. SMM is well-suited for these experiments since it offers very detailed insights into the sample structure. For example, structural heterogeneities of the materials can be clearly resolved with SMM. Additionally, SMM is a non-invasive technique that does not alter or damage the samples. The mesoporous materials do not get affected negatively due to the extremely low concentrations of fluorescent molecules.

Moreover, the Single Molecule Microscopy yields data that can be used for an accurate positioning (tracking) of the recorded fluorescence signals. With these so-called *Single Particle Tracking* (SPT) methods a map of the molecular movements, a so-called trajectory, can be obtained. The trajectories often reveal mechanistic details of the investigated structures. The methods for Single Particle Tracking and Diffusion analysis are explained in detail in Chapter 3.2.1.3 and 3.2.1.4.

Consequently, SMM has become a powerful tool<sup>76-78</sup> for studies in several scientific disciplines ranging from biology<sup>79-85</sup> to material science.<sup>86-89</sup> SMM has also been used extensively for the investigation of porous host-guest systems. This revealed many hidden details that are inaccessible to other techniques.<sup>90-95</sup> Consequently, SMM plays a crucial role for the investigation of mesoporous silica structures described in this work.

One study depicted in this thesis deals with the investigation of oligonucleotide dynamics inside mesoporous silica particles. Due to the nature of these samples the fluorescence signal of the dye labeled oligonucleotides was very low. Consequently, these samples were

investigated under ensemble concentrations with a technique called *Fluorescence Recovery after Photobleaching* (FRAP). The technique and the corresponding models for data evaluation are described in Chapter 3.2.2.

### 3.2.1 Single molecule microscopy techniques

In this subsection two basic techniques for the observation of single molecule fluorescence: Laser Scanning Confocal Microscopy and Wide-field Microscopy are introduced. After that, the Single Particle Tracking (SPT) methods are explained that are essential for extracting molecular trajectories, *i.e.* detailed maps of the individual motional behaviour of the single molecules. Finally, the diffusion theory relevant for this work is outlined.

#### 3.2.1.1 Laser Scanning Confocal Microscopy (LSCM)

In this section a detailed explanation of Laser Scanning Confocal Microscopy for the observation of individual molecules is presented.

Detecting the weak fluorescence of single molecules through optical methods is very challenging since for example only a tiny fraction of the photons emitted by the laser are actually absorbed by the molecule. The cross-section  $\sigma$  of a single molecule (see Chapter 3.1) is in the order of  $\text{nm}^2$  and thus small compared to the illuminated region. Additionally, within the sample there may be other fluorescent molecules stemming for example from impurities. This is not a problem for a measurement at ensemble concentration. However, after diluting the fluorophore of interest to single molecule concentrations ( $\sim 10^{-10}$  -  $10^{-11}$  mol/L), fluorescence due to impurities can make single molecule observations impossible. One way to overcome these limitations is to minimize the size of the excitation volume. A first important step towards a microscopy of single molecules was done in 1986 when Amos and White, two researchers at Cambridge University, developed the first working prototype of a confocal microscope. Through the small excitation volume a lot of noise could be removed and further

improvements on the optical setup, namely a pinhole installed in front of the detector, very efficiently excluded photons coming from outside the detection volume. This aperture reduces the background substantially and paves the way for single molecule detection sensitivity. In modern confocal microscopes a typical size of the confocal volume is  $\sim 300$  nm in the focal plane and  $\sim 900$  nm along the optical axis.

Figure 3.4 depicts the scheme of a Laser Scanning Confocal Microscope. The sample is excited by a laser. Typical laser wavelengths for single molecule studies are 633 nm (He-Ne laser) or 532 nm (frequency doubled diode pumped Nd:YAG solid state (dpss) laser). Through an objective the laser is focused onto the sample thereby exciting the single molecules to fluoresce. In order to be able to detect a maximum amount of photons from the weakly fluorescing single molecule, an oil-immersion objective with a so-called high Numerical Aperture (NA) has to be used. The NA determines the range of angles under which an objective can collect (or emit) light. The higher the NA, the more light can be collected. The emitted fluorescence light is collected again through that very same objective (epi-fluorescence setup) and separated from the blue-shifted excitation light (see Stokes-Shift, Section 3.1). The fluorescence light then passes the detection pinhole and can further be filtered before it is detected by a so-called avalanche photo-diode (APD). Since the APD is a point detector, the focused laser has to be scanned over the entire region of interest in the sample in order to record fluorescence images with such a setup. This can be done in the lateral plane (2D) or even for many consecutive 2D slices by moving the objective or the sample such that a 3D-object can be reconstructed.

Additionally, a prism-spectrometer is attached to the setup with a beamsplitter. This allows the spectra of single molecules to be observed simultaneously to measuring the fluorescence signal. The spectra of single molecules are not static but do often show highly dynamic behavior. They react for example to differences in the local environment of the molecule or change due to molecular aggregation. Hence, through its spectrum the molecule offers a high amount of information about its immediate surroundings and its interactions with the solvent for example. Hence, much additional information can be gained by monitoring spectral fluctuations.

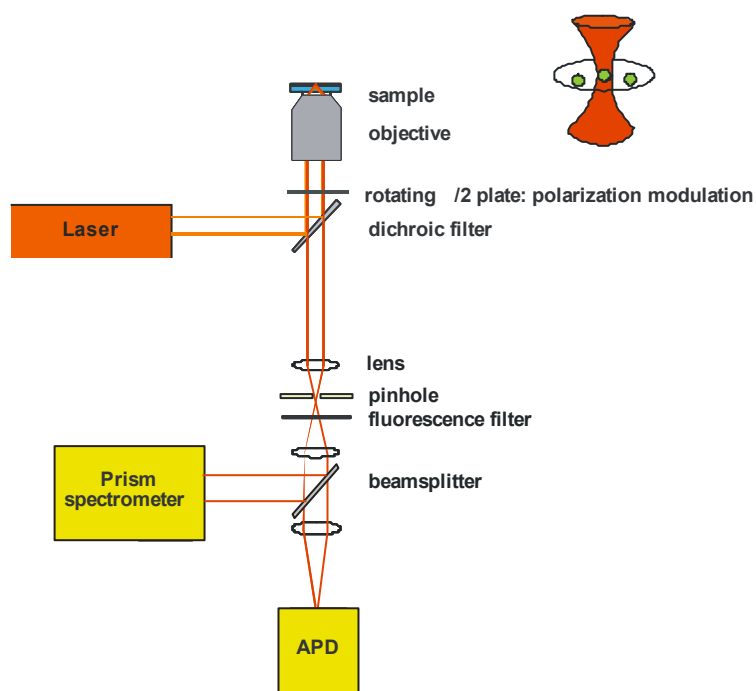


**Figure 3.4: Typical Laser Scanning Confocal Microscopy setup with additional optics to record single molecule spectra and to observe molecular orientation.** The sample is illuminated by a laser through a high numerical aperture objective and the fluorescence is collected through that same objective (epi-fluorescence setup). Through a dichroic filter and further fluorescence filters the red-shifted fluorescence light can be separated from the excitation light. The fluorescence can be detected with an avalanche photo-diode (APD). Additionally, a prism-spectrometer allows measuring single molecule spectra.

In this work, confocal laser scanning microscopy is used on a single molecule level to unravel the complex interplay of drugs with mesoporous silica delivery structures. However, the CSLM technique also suffers from some drawbacks with respect to the microscopy of individual molecules inside mesoporous host structures. Due to the time-consuming scanning process, the technique is limited when fast molecular dynamics needs to be monitored. This can be overcome by a technique called Wide-field Fluorescence Microscopy.

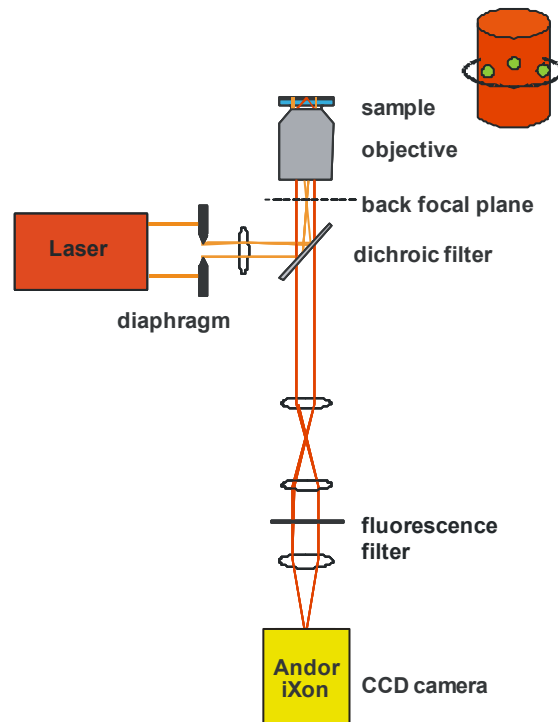
### 3.2.1.2 Wide-field Fluorescence Microscopy

Figure 3.5 shows a typical setup used for Wide-field Fluorescence Microscopy. With this technique a large area on the sample is illuminated homogeneously. This can be realized by a diaphragm placed into the laser beam and cutting out a certain region of interest that is

reduced in size by lenses and focused onto the back-focal plane of the high NA oil-immersion objective. Due to focusing onto that back-focal plane, the laser light leaves the objective unfocused illuminating homogeneously a certain area on the sample. All fluorescent molecules inside this region get excited and thus a high number of single molecules can be monitored at the same time. The molecular fluorescence is then collected in epi-fluorescence mode and through passing a dichroic mirror and a fluorescence filter it gets efficiently separated from the exciting laser wavelength. The signal is focused onto a back-illuminated cooled charge-coupled device (CCD) camera. A highly sensitive camera is an essential prerequisite since the single molecule fluorescence is very weak. Especially when the molecules move fast, the intensity per camera pixel is low. In this work an Andor iXon model DV897 was used. Besides the ability to simultaneously monitor several molecules, the camera has another important advantage. Individual images can be recorded with a very low integration time per image down to 10 ms. Consequently, movies can be recorded with a high frame rate per image, thereby allowing to monitor fast molecular dynamics. This overcomes a central disadvantage of the Scanning Confocal Microscope introduced above. The maximum observation time for the single molecules is then only limited by the photostability of the individual fluorophore. The ability to record long movies also guarantees sufficient data for further statistical evaluation. This is a crucial point for single molecule studies. Since each individual molecule behaves differently, good statistics are a key requisite for drawing well-founded conclusions.

A drawback of the wide-field technique is the high background due to out-of-focus fluorescence that gets collected by the high NA objective. The typical resolution in the axial direction is only about 1  $\mu\text{m}$ . However, for the investigation of thin mesoporous films, this is of no consequence, since the film thickness lies typically between 100 – 200 nm and thus there are no fluorescent molecules present in out-of-focus planes.

In summary, fast dynamics can be recorded with a high frame rate in a short timescale, yielding a high amount of data. This makes Wide-field Fluorescence Microscopy a valuable tool for single molecule studies of fluorescent guest molecules incorporated inside mesoporous silica host structures.



**Figure 3.5: Wide-field Fluorescence Microscopy Setup.** The laser light is first cut by a diaphragm to a rectangular shaped region. This image of the diaphragm is then focussed by a lens to the back focal plane of the high NA oil-immersion objective and from there this focused image of the diaphragm is drawn onto the sample where it homogeneously illuminates a certain area. All fluorophores inside this illuminated area are excited and their fluorescence can be monitored simultaneously. The fluorescence light is collected in an epi-fluorescence setup through the same objective and is separated from the excitation light through a dichroic filter and a fluorescence filter. The image can then be recorded typically on charge-coupled device (CCD) camera.

### 3.2.1.3 Optical resolution and positioning accuracy: Single Particle Tracking (SPT)

In order to understand Single Particle Tracking (SPT), we first have to distinguish between the term “resolution” and the term “positioning accuracy”.

The former denotes the optical limit of the microscope. The resolution limit is defined as the smallest distance between two objects that still allows them to be distinguished. The image of any object that is significantly smaller than the wavelength of the utilized laser light (a so-called point source) does not appear as a point, but as a so-called Airy disc (see Figure 3.6). This Airy disc is created since the laser light gets diffracted by the small object. Consequently

the Airy disc is a diffraction pattern characterized by several orders of maxima and minima (Figure 3.6 a). According to the Rayleigh criterion, in optical microscopy also referred to as the Abbe resolution limit, two point sources can only just be resolved if their distance equals the radius of the Airy disc  $r_{Airy}$ , which is defined as the distance from the center of the Airy disc to its first minimum and is given by:

$$r_{Airy} = 0.61 \frac{\lambda}{NA} \quad (3.2)$$

in the lateral plane (perpendicular to the optical axis).  $\lambda$  is the wavelength of the laser light and  $NA$  denotes the numerical aperture of the objective. A schematic view of two Airy discs separated by  $r_{Airy}$  is given in Figure 3.6 b. As mentioned above, the point sources can only just be resolved individually. If they are closer (Figure 3.6 c), they cannot be distinguished as two individual objects. This resolution limit is typically 1/2 of the wavelength of the utilized laser light, which gives a resolution of about 300 nm for a red He-Ne laser

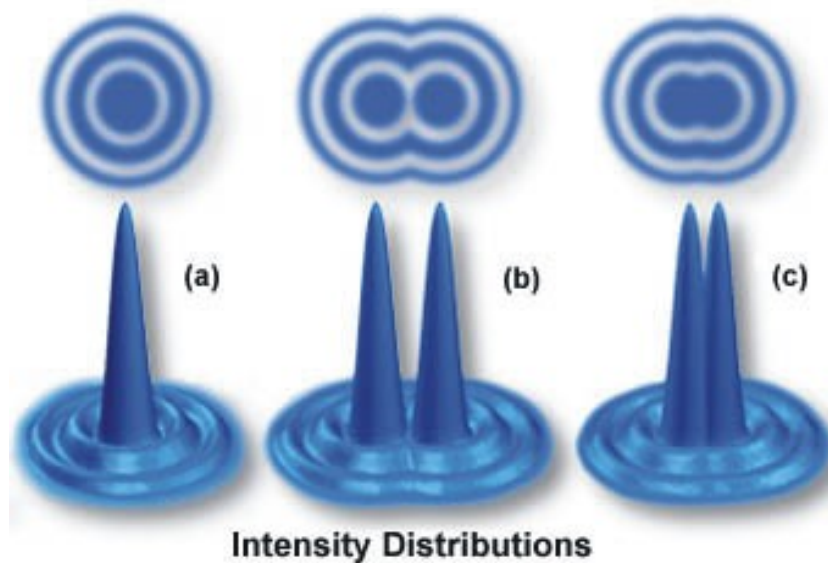


**Figure 3.6: The airy disc and the Rayleigh criterion for spatial resolution.** a) An Airy disc created by one point source is shown (upper panel) as well as its corresponding intensity distribution (lower panel). The Airy disc shows a sequence of intensity maxima and minima due to higher orders of diffraction. b) Two point sources separated by a distance  $r_{Airy}$ . This is the minimal distance necessary to resolve two adjacent point sources, since in  $r_{Airy}$  the maximum of one Airy disc overlaps with the first minimum of the second Airy disc. c) If the two Airy discs are closer than  $r_{Airy}$  the point sources cannot be resolved individually. Image adapted from Nikon-MicroscopyU.<sup>96</sup>

However, the position of such a point source can be determined with a much higher accuracy of a few nanometers by fitting the recorded fluorescence signal to a two-dimensional Gaussian function:

$$I_0 = A_0 \exp\left(\frac{-(x - x_0)^2}{2\sigma^2}\right) * \exp\left(\frac{-(y - y_0)^2}{2\sigma^2}\right) \quad (3.3)$$

where  $I_0$  is the recorded fluorescence intensity,  $A_0$  the amplitude of the signal and  $\sigma$  the full width at half-maximum of the Gaussian curve.  $x_0$  and  $y_0$  denote the coordinates of the position of the individual molecule. This process of positioning the individual molecule by fitting an appropriate function to the single molecule fluorescence signal is called Single Particle Tracking. Fitting Eq. 3.3 to a single molecule fluorescence signal thus yields the molecular coordinates. Repeating that procedure for example for all individual frames of a movie recorded on a Wide-field Microscope showing diffusing molecules yields a so-called trajectory. The trajectory is a detailed map of the motion of the individual molecule.

This positioning accuracy and thus the quality of the information in a trajectory is only limited by the signal-to-noise ratio.<sup>97,98</sup> There are obviously two options to increase the signal-to-noise ratio. On the one hand, we need to find ways to increase the signal. This is the reason, why in single molecule microscopy a “bright” fluorophore is needed with a high quantum yield and a high absorption cross-section. Furthermore, it should show blinking only rarely. On the other hand, we need to find ways to reduce the noise. There are two categories of noise: the shot noise and the background noise. The shot noise represents the situation, when the finite number of recorded photons is low enough that statistical fluctuations in the number of detected photons occur. This again can get minimized by using a dye with good photo-physical properties. In contrast, the background noise describes the out-of-focus fluorescence that gets recorded. This background noise is typically much higher for Wide-field Microscopy than for Confocal Microscopy due to the confocal pinhole in the latter case. In Wide-field Microscopy this background can be reduced through using thin samples with a thickness far below the axial resolution of the microscope, as mentioned above.

A single particle trajectory is the starting point in a thorough evaluation of the diffusion data. In a second step, the data acquired through SPT can be fitted to an appropriate diffusion model in order to quantify the dynamical information contained in the measured movies.

### 3.2.1.4 Diffusion Theory

In order to make mesoporous silica structures accessible for applications as host systems, understanding, and in a further step controlling, the dynamics of guest molecules embedded inside these structures is an essential prerequisite. We need to characterize in detail, the motional behavior of the molecules incorporated in the materials. In order to understand the modeling of the SPT data, diffusion theory needs to be introduced first.

Mathematically, the theory of diffusion can be divided into macroscopic and microscopic diffusion theory. The macroscopic diffusion theory is well described by Fick's laws of diffusion. In this model, diffusion is considered as a net transport of particles from a region with higher concentration to a region with lower concentration. The mobility of the particles is a result of their thermal motion (Brownian motion). These laws will not be discussed here, since we investigate diffusion on a microscopic level by observing the mobility of individual molecules. In our case no net transport occurs. The movies acquired on the microscope setups described above only show diffusion due to thermal (Brownian) motion.

In order to characterize diffusion microscopically, the *mean square displacement* (MSD)  $\langle r^2(t) \rangle$  is a very useful parameter. It describes the mean square of the displacements of the particles between individual steps (recorded frames) of the movement with time  $t$ . The longer the time for the particle to diffuse the higher the MSD will be. For an undisturbed free Brownian diffusion of the particle Einstein developed a model in 1905.<sup>99</sup> This model has a high relevance in many fields of science, for example in biology.<sup>100</sup> The MSD obeys

$$\langle r^2(t) \rangle = 2nDt \quad (3.4)$$

where  $n$  denotes the spatial dimension. Thus,  $n = 1$  characterizes a diffusion in one dimension, whereas  $n = 2$  refers to a two-dimensional motion and  $n = 3$  characterizes a diffusion process taking place in all three dimensions. For the microscopic investigations in this work usually a two-dimensional projection of a three-dimensional motion is recorded since the motion along the optical axis was not resolved. Thus, the MSD is given by

$$\langle r^2(t) \rangle = 4Dt \quad (3.5)$$

However, in real samples, the diffusional behaviour often deviates from the ideal Brownian diffusion. There are three categories of non-ideal diffusion: diffusion with flow, anomalous diffusion and corralled diffusion. The MSDs for the different categories are compared in Figure 3.7.

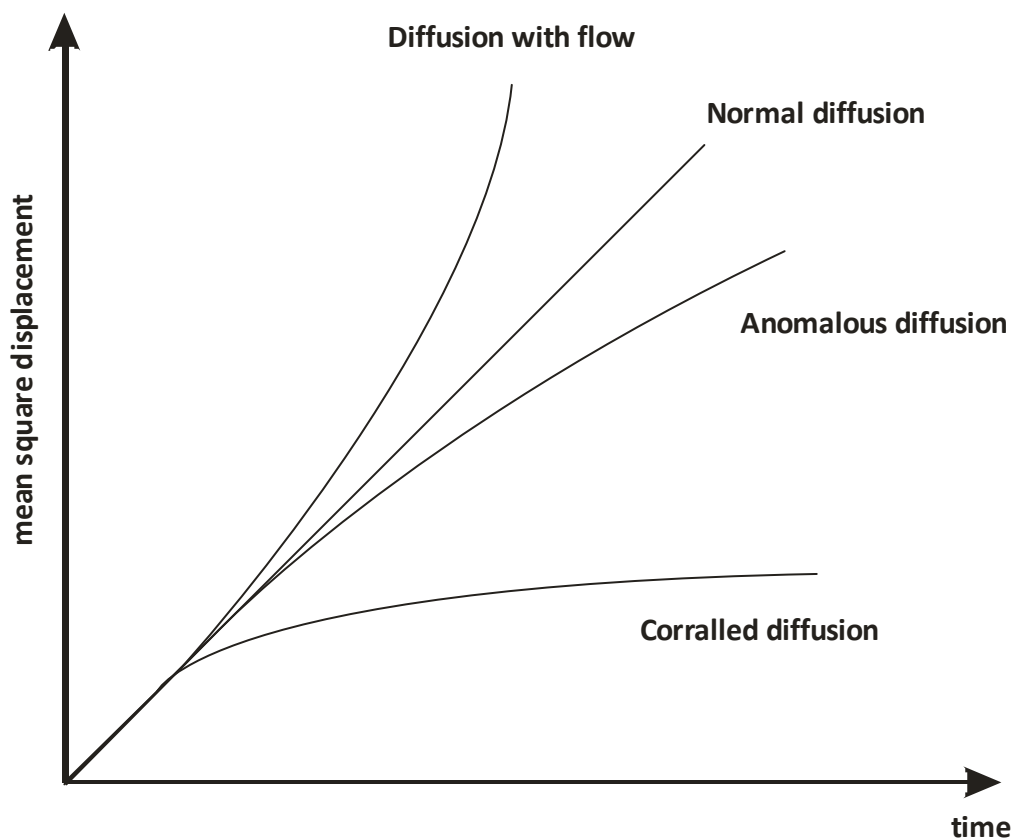


**Figure 3.7: Mean square displacement (MSD) curves for four different modes of diffusion.** The MSD as a function of time for diffusion with flow, normal diffusion, anomalous diffusion and corralled diffusion.

According to Eq. 3.5 the MSD in the case of normal diffusion is a straight line. The functions for the other modes of diffusion are given by:

Diffusion with flow:

$$\langle r^2(t) \rangle = 2nDt + (Vt)^2 \quad (3.6)$$

where  $V$  is the velocity of the flow. Diffusion with flow for example occurs when a leaf of a tree falls into a river and floats on the water surface. The flow in this example is provided by the water that runs with a certain velocity along the course of the river. Additionally, there is a diffusive contribution by the motion of the leaf itself on the water surface.

Anomalous diffusion:

$$\langle r^2(t) \rangle = 2nDt^\alpha \quad (3.7)$$

where the MSD obeys a power law with the coefficient  $\alpha$  ( $0 < \alpha < 1$ ). Anomalous diffusion can be observed for example for macromolecules in highly crowded areas, *e.g.* inside the cytoplasm of a cell. The presence of a high number of obstacles prevents the macromolecules from diffusing normally.

Corralled diffusion:

$$\langle r^2(t) \rangle = \langle r_c^2 \rangle \left[ 1 - A_1 \exp\left(\frac{-4A_2}{\langle r_c^2 \rangle} Dt\right) \right] \quad (3.8)$$

where  $\langle r_c^2 \rangle$  is the mean squared confinement radius.  $A_1$  and  $A_2$  are constants defining the corral geometry. Corralled diffusion can be observed when particles move inside confined geometries. Fitting the MSD curve to Eq. 3.8 allows to extract the mean radius of the confinement, a structural information about the investigated material.

However, much more detailed information can be extracted from the SPT data. The step lengths  $r_i$  that result from the distances between two consecutive points in a trajectory offer insights into the structure of the mesoporous silica host. Within this work, diffusion coefficients extracted from the distribution of step lengths will be used to discuss heterogeneities in the structure of the silica materials. The distribution of functional groups attached to the walls of the silica pores is tested for heterogeneities with this method. The theoretical background for the analysis is described below in brief. A detailed derivation of the below given equations can be found in the thesis of J. Kirstein.<sup>101</sup>

First, the step lengths are extracted from the trajectory. This can be done for various time lags  $t_{lag} = m\tau$ , where  $\tau$  corresponds to the integration time for a frame in the recorded movie. For

$m = 1$ , for example, the distances between data points 1 and 2 or 2 and 3, etc. are taken. For  $m = 2$  the distances between data points 1 and 3 or 2 and 4, etc. are calculated, and so on. From this, the probability distribution  $p(r^2, t)$  of the squared displacements  $r^2$ , at time  $t$  can be obtained. For normal diffusion in two dimensions with one diffusive component it is given by<sup>102, 103</sup>

$$p(r^2, t) = \frac{1}{\langle r^2(t) \rangle + \delta^2} \exp\left(-\frac{r^2}{\langle r^2(t) \rangle + \delta^2}\right) \quad (3.9)$$

where  $\delta$  corresponds to the positioning accuracy. Diffusion in one or three dimensions is not relevant for this work and will not be considered here. Eq. 3.9 expresses that the probability of finding a molecule is highest at the origin and gets reduced exponentially with increasing distance from the origin. Furthermore, the probability of finding a molecule at certain distance from the origin increases with time.

Knowing the probability distribution  $p(r^2, t)$ , the cumulative probability distribution  $P(R^2, t)$  for a given squared step length  $R^2$  can be calculated.

$$P(R^2, t) = 1 - \exp\left(-\frac{R^2}{\langle r^2(t) \rangle + \delta^2}\right) \quad (3.10)$$

$P(R^2, t)$  describes the probability that the mean square displacement of the guest molecule in the mesoporous host for does not exceed a value  $R$  in time  $t$ . This means that the molecule can be found within a circle of radius  $R$  at time  $t$ . Figure 3.8 shows an exemplary cumulative probability distribution for normal diffusion in two dimensions with one diffusing component.

Often, the analyzed data are displayed as an inverse of the cumulative probability distribution  $C(R^2, t)$ , which is given by

$$C(R^2, t) = |1 - P(R^2, t)| \quad (3.11)$$

Figure 3.9 shows the inverse of the cumulative probability distribution plotted in Figure 3.8.

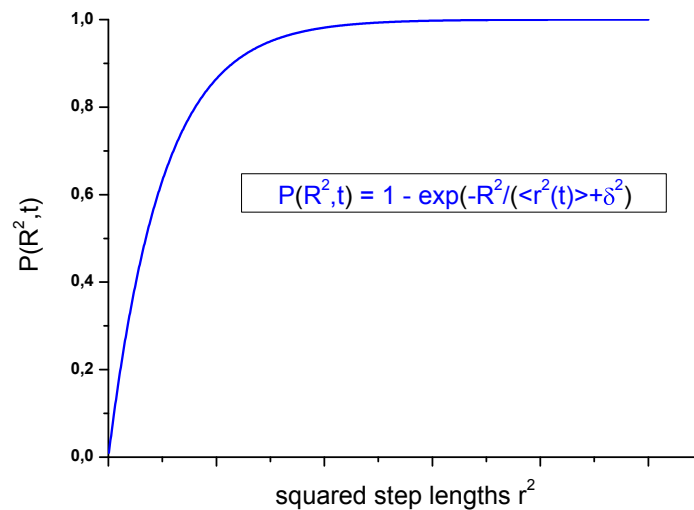


**Figure 3.8:** Cumulative probability distribution function  $P(R^2, t)$  for normal diffusion in two dimensions with only one diffusive component for a certain time lag  $m\tau$ . For diffusion in two dimensions  $P(R^2, t)$  follows an exponential distribution.

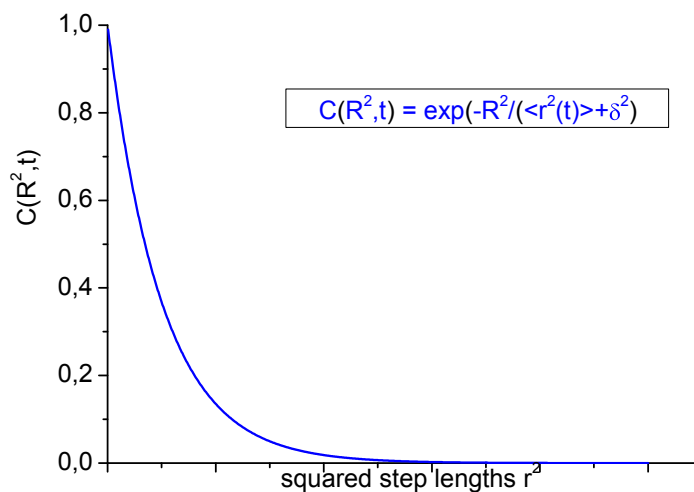


**Figure 3.9:** Inverse of the cumulative probability distribution function  $C(R^2, t)$  for normal diffusion in two dimensions with only one diffusive component for a certain time lag  $m\tau$ . For diffusion in two dimensions  $C(R^2, t)$  follows an exponential decay.

A convenient way to display the data is plotting  $C(R^2, t)$  versus the squared displacements. With a logarithmic scaling of the y-axis (semi-logarithmic plot) a straight line results if only one diffusion coefficient  $D$  is sufficient to describe the molecular motion inside the pore (see Figure 3.10 a). In case the curve is bent, several diffusion coefficients have to be taken into

account (Figure 3.10 b). The resulting experimental distribution can thus be fitted to a mono-, bi- or higher exponential function:

$$C(R^2, t) = c_1 \cdot \exp\left(-\frac{R^2}{\langle r_1^2(t) \rangle + \delta^2}\right) + c_2 \cdot \exp\left(-\frac{R^2}{\langle r_2^2(t) \rangle + \delta^2}\right) + \dots + c_n \cdot \exp\left(-\frac{R^2}{\langle r_n^2(t) \rangle + \delta^2}\right) \quad (3.12)$$

where  $\sum c_i = 1$ . The mean square displacements  $\langle r_n^2 \rangle$  can then be obtained by fitting the experimental data to Eq.3.12, thus giving diffusion coefficients according to Eq.3.5. This step length analysis thus offers insights into heterogeneities of the diffusional motion of the recorded single molecules inside the mesoporous host.

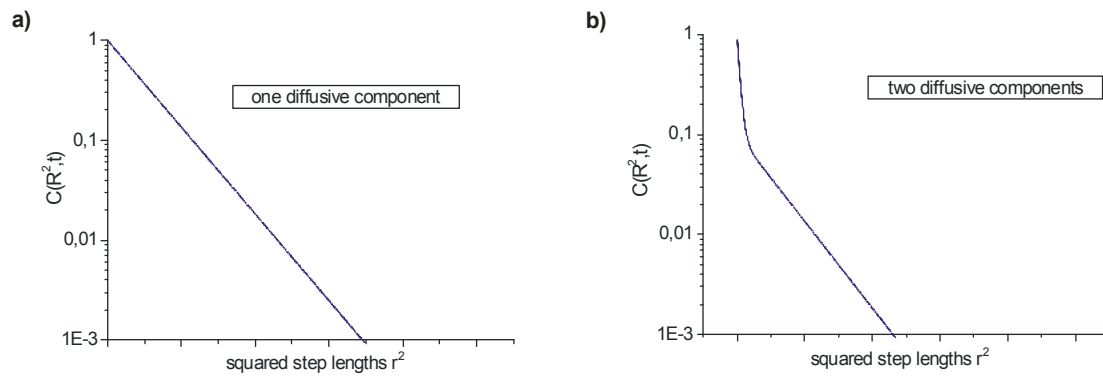


**Figure 3.10: Semi-logarithmic plot of the inverse of the cumulative distribution function for a certain time lag  $m\tau$ .** a) Only one component of diffusion. b) Two components of diffusion.

### 3.2.2 Fluorescence recovery after photobleaching (FRAP)

Within this subsection the FRAP technique is introduced. First, the basic principles of the method are explained. Later, the data analysis and modelling are described.

### 3.2.2.1 The basic principles of FRAP

The *Fluorescence Recovery after Photobleaching* (FRAP) technique was developed in 1976.<sup>104, 105</sup> Since then it has become a standard tool especially for determining dynamics of all kinds of fluorophores or fluorescently labelled molecules inside living cells. FRAP was utilized for example to investigate the dynamics of proteins and lipids within membranes and to address the mobility of solutes inside the cytoplasm and the nucleus.<sup>106-111</sup> Furthermore, this method has been applied to study diffusion in confined biological spaces, such as tumor tissues.<sup>112, 113</sup> The FRAP technique has been reviewed extensively by Meyvis *et al.* also highlighting many applications.<sup>114</sup> In this thesis, FRAP is used for the investigation of siRNA and DNA mobility inside mesoporous silica particles.

The key idea of FRAP consists of determining the dynamics of fluorescent molecules by bleaching all the molecules moving inside the focal volume through an intense laser beam and subsequently monitoring the fluorescence recovery with the help of a greatly attenuated beam (Figure 3.11 a). Before bleaching ( $t < 0$ ) the fluorescence in the solution is homogeneously distributed. At  $t = 0$  the laser is placed at a certain position, lasing with full power such that the fluorophores get efficiently bleached. The time required for bleaching should be short compared to the characteristic diffusion time of the investigated species. With increasing time the fluorescence recovers in the bleached region until it is fully recovered ( $t = \infty$ ). Recovery occurs due to molecules diffusing from unbleached regions of the sample back into the focal volume and bleached molecules diffusing out. From monitoring the increase in fluorescence intensity in the focal volume after bleaching  $t < 0$ , a so-called recovery curve can be obtained (Figure 3.11 b). Assuming a certain diffusion model, a diffusion coefficient  $D$  for the fluorescent molecules can be derived. A FRAP measurement can be conducted on a conventional Laser Scanning Confocal Microscope (see Chapter 3.2.1.1).

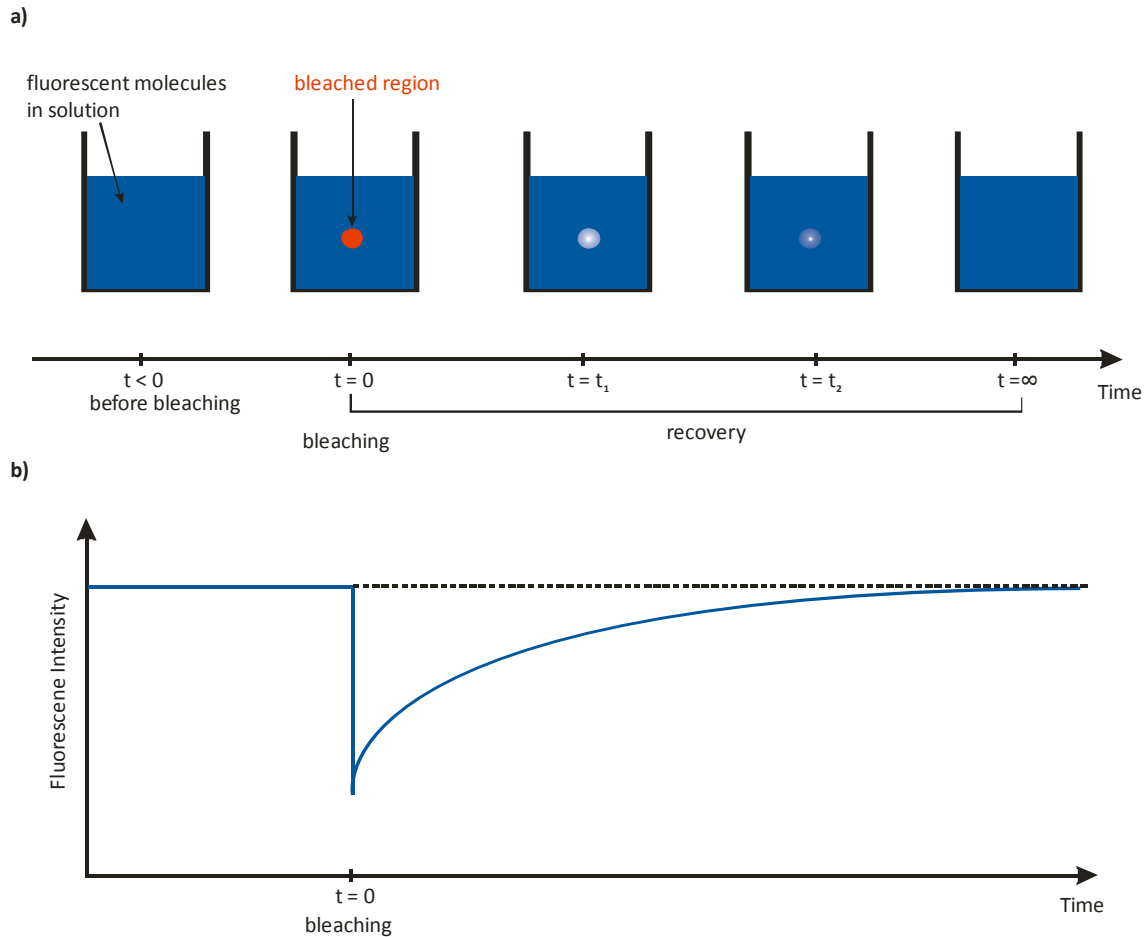


**Figure 3.11: Fluorescence Recovery after Photobleaching (FRAP) experiment.** (a) Schematic view of the experimental sequence. Before bleaching ( $t < 0$ ) the fluorescence in the solution is homogeneously distributed. At  $t = 0$  the laser is placed at a certain position, lasing with maximum power in order to bleach the fluorophores efficiently. With increasing time the fluorescence recovers in the bleached region until full recovery ( $t = \infty$ ). (b) Recovery curve of the fluorescence intensity.

### 3.2.2.2 Data evaluation

In this section, it will be explained how the fluorescence intensities that are necessary to obtain the recovery curve (see Figure 3.11 b) are extracted from the FRAP experiment depicted in Figure 3.11 a.

Data evaluation for the FRAP experiments discussed in this work was done by K. Schneider in the group of H. Leonhardt (LMU Munich, Department of Biology, Munich Germany). The analysis of the recorded sequences of fluorescence images that display the bleaching and

subsequent fluorescence recovery (see Figure 3.11 a)) was performed using automated processing with ImageJ<sup>115</sup> including a set of self-developed macros. The imported image series were first Gauss-filtered (2 pixel radius) and converted to 8-bit since this facilitates image analysis. Datasets that showed lateral movement of particles were corrected by image registration using the *StackReg* plug-in of ImageJ since a sample drift on the microscope leads to biased results for the diffusion coefficients. Next, mean fluorescence intensities were extracted from all individual images of the recorded sequence. Three regions of interest (ROIs) were evaluated: the bleached region ( $B$ ), the total particle area ( $T$ ) as a reference and a background ROI outside the particle. Whereas the total particle area and a reference area outside the particle can be defined easily from the images, the bleached region was analyzed in the following way: a cross-section was done through the spherical bleached regions, yielding a roughly Gaussian shaped fluorescence intensity profile. Then, the full width at half maximum (FWHM,  $\omega$ ) was determined from that bleached profile. This parameter is important for the modeling of the data discussed in the next Chapter 3.2.2.3.

Furthermore, this parameter  $\omega$  was used as the diameter of the circular bleached region  $B$ . The fluorescence intensity value for region  $B$  is then the mean value of all individual pixel signals in region  $B$ . From the raw fluorescence intensity data of  $T$  and  $B$  the fluorescence background was subtracted. The resulting postbleach values were multiplied by  $T_{postbleach}/T_{prebleach}$  to correct for the superimposed gain or loss of total fluorescence during postbleach acquisition, potentially caused by import, bleaching-by-acquisition and flux of residual fluorescence from above and below the recorded optical plane. To correct for particle-to-particle differences in bleaching depth, a value  $\varphi$  was subtracted from all mean fluorescence values such that the starting mean fluorescence intensity for all curves was set to the same value. From this value  $\varphi$  a value  $\phi$  results that is necessary for the modeling discussed in Chapter 3.2.2.3. This is important in order to be able to compare different recovery curves. The corrected values for  $T$  and  $B$  were normalized to the respective means of the last 5 prebleach values, which represent 100% recovery.

To summarize, the fluorescence intensity value extracted from region  $B$ , was background corrected, corrected by data from an unbleached reference area in the sample and normalized to the same starting fluorescence intensity value and normalized to the prebleach values. If this is done for each recorded image of the frame sequence, the individual fluorescence intensity values of the recovery curves are obtained.

### 3.2.2.3 Data modelling

In order to extract diffusion coefficients from the recovery curve and thereby quantifying the molecular mobility a certain diffusion model has to be assumed. The model used in this work has been introduced by Axelrod *et al.*<sup>104</sup> further elaborated by Soumpasis<sup>116</sup> and McNally.<sup>117</sup> Data modeling for the FRAP experiments presented in this work were done by K. Schneider and A. Dobay in the group of H. Leonhardt (LMU Munich, Department of Biology, Munich Germany). In the following paragraph the model will be described in brief.

We consider the photobleaching event as a simple irreversible first-order reaction with the rate  $\alpha I(r)$ , where  $\alpha$  is the rate constant and  $I(r)$  the bleaching intensity at a certain position  $r$ . The concentration of unbleached fluorophore  $C(r, t)$  at a position  $r$  at time  $t$  is given by

$$\frac{dC(r, t)}{dt} = -\alpha I(r)C(r, t) \quad (3.13)$$

due to the bleaching at this position.

So far, no diffusion is assumed. After bleaching with an intense light pulse for a time interval  $T$ , which needs to be short compared to the characteristic diffusion times, the concentration profile of the fluorophore at the beginning of the recovery phase ( $t = 0$ ) is given by

$$C(r, 0) = C_0 \exp[-\alpha T I(r)] \quad (3.14)$$

with the initial homogeneous fluorophore concentration  $C_0$ . Eq. 3.14 is the solution to the differential Eq. 3.13. For simplicity, the “amount” of bleaching induced in time  $T$  is expressed by a parameter  $K$

$$K \equiv \alpha T I(0) \quad (3.15)$$

Assuming a Gaussian laser intensity profile,  $I(r)$  can be written as

$$I(r) = \left(\frac{2P_0}{\pi\omega^2}\right) \exp\left(\frac{-2r^2}{\omega_G^2}\right) \quad (3.16)$$

with  $\omega_G$  the half-width at  $e^{-2}$  height and  $P_0$  the total laser power.

However, when a distinct small region of interest is bleached, the approximation of the laser intensity in the form of a circular disc profile describes the real situation better. For such a profile  $I(r)$  is given by

$$I(r) = \begin{cases} \frac{P_0}{\pi\omega} & r \leq \omega \\ 0 & r > \omega \end{cases} \quad (3.17)$$

where  $\omega$  is the radius of the disc.

Whereas Eq. 3.16 and Eq. 3.17 determine the geometry of the laser profile, Eq. 3.14 determines the bleaching behavior of the fluorophores with a certain bleaching rate  $\alpha I(r)$ .

Figure 3.12 illustrates the bleaching behavior of fluorophores bleached by a Gaussian laser profile for different values of the bleaching parameter  $K$  (see Eq. 3.15).

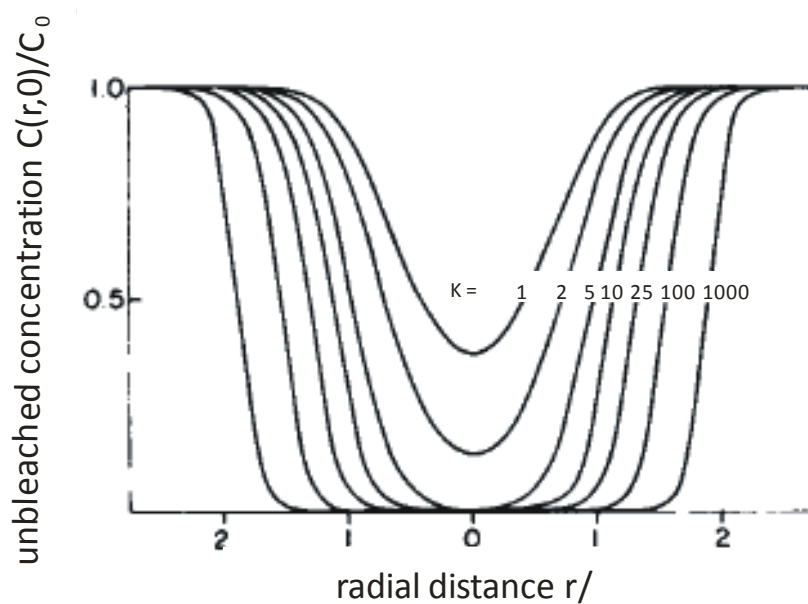


**Figure 3.12: Normalized initial post-bleach fluorophore concentration  $C(r,0)/C_0$ .** The fluorophore concentration was calculated assuming a Gaussian beam according to Eq. 3.16 for different values of the bleaching parameter  $K$  (see Eq. 3.15). Figure adapted from Axelrod *et al.*<sup>104</sup>

The differential equation for a lateral transport of a single species of fluorophores through diffusion with a diffusion coefficient  $D$  is

$$\frac{\partial C(r, t)}{\partial t} = D\nabla^2 C(r, t) \quad (3.18)$$

This description omits any active transport or flow. The fluorescence observed at time  $t \geq 0$  is given by

$$F_K(t) = \left(\frac{q}{A}\right) \int I(r) C_K(r, t) d^2r \quad (3.19)$$

Where  $C_K(r, t)$  is the solution of Eq. 3.18 for the  $K$ -dependent initial condition given in Eq. 3.14. The parameter  $q$  is the product of all quantum yields and  $A$  is the attenuation factor of the beam used for the observation of fluorescence recovery. Fluorescence recovery curves can be displayed conveniently in the following notation, called fractional form  $f_K(t)$

$$f_K(t) \equiv \frac{[F_K(t) - F_K(0)]}{[F_K(\infty) - F_K(0)]} \quad (3.20)$$

According to Soumpasis *et al.*<sup>116</sup> for uniform circular beams this fractional recovery curve can be modified to a simple closed form

$$f(t) = \exp\left(\frac{-2\tau_D}{t}\right) \left[ I_0\left(\frac{2\tau_D}{t}\right) + I_1\left(\frac{2\tau_D}{t}\right) \right] \quad (3.21)$$

where  $I_0$  and  $I_1$  are modified Bessel functions and

$$\tau_D = \omega^2/4D \quad (3.22)$$

for diffusion in two dimensions. In this form the fractional recovery curve is independent of the bleaching parameter  $K$ . This recovery model prescribes the data assuming one population and hence one diffusion coefficient  $D$ . McNally *et al.*<sup>117</sup> adapted this fractional recovery curve, taking into account fractional bleaching, *i.e.* only part of the molecules are bleached, which is closer to the real situation.

$$f(t) = 1 - \phi + \phi \exp\left(\frac{-2\tau_D}{t}\right) \left[ I_0\left(\frac{2\tau_D}{t}\right) + I_1\left(\frac{2\tau_D}{t}\right) \right] \quad (3.23)$$

where  $\phi$  is the bleached fraction. This model can then be fitted to the data set, the fluorescence recovery curve  $f(t)$ . The model of Eq. 3.23 requires the parameters  $\phi$  and the  $\omega$  (see Eq. 3.22) that result from the evaluation of the experimental data (see Chapter 3.2.2.2).



# 4 Mesoporous silica materials for drug-delivery applications

Mesoporous silica structures with nanometer-sized channels have been introduced as a group of versatile host materials in Chapter 2. They can thus form an interesting platform for diverse applications. The studies within this chapter shall now highlight possible routes towards applications in the evolving field of nanomedicine.

First, an introduction to the status quo in drug-delivery is given, outlining as well the current challenges and limitations. The second section demonstrates how a fine-tuning of the dynamics of the guest molecules embedded inside the delivery vehicle can be realized. This is a central prerequisite for efficient drug-delivery, namely for generating a depot-effect, *i.e.* a controlled release profile of the drug over a prolonged period of time. In Chapter 4.3 and 4.4 two studies accentuate very different ways of applying mesoporous silica in drug-delivery. The studies depicted here span a broad scope, ranging from cancer treatment to gene therapy and silencing. The experiments thus demonstrate that mesoporous silica nanomaterials can provide solutions for current challenges in nanomedicine.

## 4.1 Introduction to Drug-Delivery

The term “drug-delivery” designates a method of administering a drug wisely such that a maximum therapeutic effect can be achieved. A drug-delivery system is a carrier structure or matrix, with the help of which the drug gets transported to its target site. An ideal drug-delivery system should satisfy the following essential requirements in order to guarantee an efficient therapy.

- (i) The drug delivery system should offer a high loading capacity such that a high amount of drug can be stored in the carrier system.
- (ii) An ideal drug delivery system should further provide means to fine-tune the drug dynamics in the carrier in order to generate a depot effect.
- (iii) It is essential that the drug carrier protects the sometimes fragile drugs from decomposition (*e.g.* short interfering RNA (siRNA) or enzymes), for example due to contact with body fluids. The drug delivery system should promote drug stability.
- (iv) The drug delivery system should further protect the body from severe side-effects of the drug (*e.g.* in cancer treatment: chemotherapy).
- (v) An ideal drug delivery system should show cell-targeting ability, *i.e.* the ability to navigate the small carrier structure throughout the human organism exactly to the target-site, where the cause of the illness is located (for example the site where the tumor sits). This shall prevent drug accumulation in other regions of the body and would reduce the necessary amount of administered drug.
- (vi) The drug carrier system should tightly seal the drug, for example through using cap systems in order to prevent the drug from being released prior to reaching the target-site.
- (vii) However, after reaching that target-site the caps should open reliably in order to release the drug efficiently and completely. Hence, the cap system must be able to react upon a certain trigger at the target-site (*e.g.* a pH change).
- (viii) Finally, the drug delivery system itself should be non-toxic and biodegradable.

This is obviously a very challenging list of requirements, however a variety of different drug-delivery strategies have been developed so far. Currently available nanocarriers for drugs consist for example of synthetic organic polymers,<sup>29, 118, 119</sup> micelles and liquid crystals,<sup>120</sup>

liposomes,<sup>30</sup> polymeric nanocapsules<sup>121, 122</sup> and diverse nanoparticle constructs.<sup>31, 123</sup> Yet, a drug-delivery system that completely satisfies all above criteria is not available yet. For example, liposomal carrier systems do not offer a depot effect. Upon liposome opening the drug gets released instantaneously. Furthermore, cell-targeting remains a great challenge for many classes of drug-delivery systems. Consequently, the search for smart drug-delivery strategies must go on and therapeutic alternatives are desperately needed in many fields of medicine, since the patients still suffer from severe side-effects. The studies in this chapter should demonstrate that mesoporous silica can become a novel option in drug delivery. Mesoporous silica shows many promising characteristics that could satisfy the above listed requirements (the numbering refers to the corresponding criteria listed above).

- (i) Mesoporous silica offer due to their tunable porous network a high pore volume and surface area, such that a high amount of differently sized guests can be incorporated.
- (ii) The question of the tunability of drug dynamics and thus the creation of a depot effect is thoroughly discussed in the study presented in the next section of this work.
- (iii) The ability to covalently attach functional groups offers a wide choice of surface modifications compatible with the used drug.
- (iv) If the drug is incorporated in a porous network that can be capped (see 6), the body will be protected from the drug.
- (v) Cell-targeting is probably the most challenging criterion. However, mesoporous silica can be modified through click-chemistry in a variety of ways such that specific receptors could be attached on the delivery system's surface.
- (vi) There are various strategies for capping the pores of mesoporous silica already available, *e.g.* a protease responsive cap system introduced by Schlossbauer *et al.*,<sup>124</sup> pH-sensitive gates reported by Cauda *et al.*,<sup>125</sup> DNA based caps,<sup>126</sup> CdS nanocrystals,<sup>43</sup> or magnetic caps<sup>45</sup> (this also refers to vii).
- (viii) The question of porous silica toxicity is discussed ambivalently. There are studies by Lin<sup>127</sup> and Park *et al.*<sup>128</sup> showing non-toxic porous silica constructs. Biodegradation studies by Cauda *et al.* showed for example that partial degradation of mesoporous silica nanoparticles takes place already 2 – 24 h after immersion of the particles in a simulated body fluid.<sup>129</sup> Good biocompatibility was also found by Kumar *et al.*<sup>130</sup> for organically modified silica nanoparticles. In contrast, there is a study by Di Pasqua *et al.*<sup>131</sup> reporting about cytotoxicity of mesoporous silica materials. Additionally,

cytotoxic effects of silica nanoparticles on human bronchial epithelial cells<sup>132</sup> and endothelial cells<sup>133</sup> were reported recently. A comprehensive study of the influence of mesoporous silica nanoparticle size, pore ordering and pore integrity on hemolytic activity was reported by Lin *et al.* in 2010.<sup>134</sup> The general conclusion so far seems to be that the morphology of the porous silica (fibers, particles, etc.) plays a crucial role as well as the size, the surface topology (edges, kinks) and the surface functionalization. However a general assessment of the toxicity is hard to make *a priori*, instead detailed testing has to be done for each individual construct.

Consequently, mesoporous silica has the potential to form a new class of promising drug-delivery systems. This was also shown by Cauda *et al.* in 2008 in a study investigating the diffusion of a large antibiotic in confined mesoporous silica.<sup>58</sup>

Figure 4.1 summarizes the criteria discussed above and schematically depicts a mesoporous drug-delivery particle (not drawn to scale).

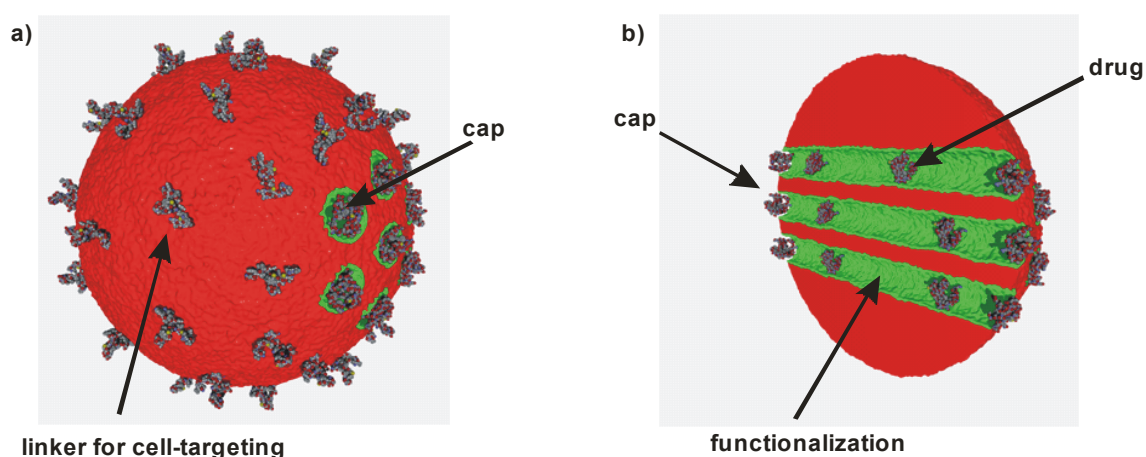


**Figure 4.1: Schematic view on an ideal mesoporous silica drug-delivery particle.**<sup>135</sup> a) The mesoporous particle possesses covalently attached biolinkers for cell-targeting purposes on its external surface. Caps are attached to the exits of the functionalized pores (green). b) Insight into the porous network. The channels are coated with a functionalization (green) for generating a depot effect through tuning drug dynamics. The caps at the pore exits are shown as well as drug molecules inside the pores.

The following studies in this chapter now highlight further possible ways towards drug-delivery with porous silica. They address very different challenges in nanomedicine and thus prove exemplarily the high potential of silica drug carriers.

## 4.2 Tuning single molecule dynamics in functionalized mesoporous silica

A key requisite for efficient drug-delivery is the above mentioned ability to fine-tune the drug dynamics in order to generate a depot effect. To realize this, organic functionalizations that can be covalently attached to the walls inside the mesoporous silica network are introduced in this section. They can be used for precisely controlling the dynamics of the guest molecules incorporated in the porous host.

Using single-molecule fluorescence microscopy, introduced in the previous chapter, the diffusion behaviour of single DIP-TDI dye molecules (N,N'-Di(2,6-diisopropylphenyl)terrylene-3,4:11,12-tetracarboxydiimide, a terrylene diimide derivative, see Figure 4.12)<sup>71</sup> in functionalized mesoporous silica films is studied. The dye was chosen due to its excellent photo-physics and acts as a model guest molecule for a drug that can be incorporated into the host structure. The study clearly shows that through variation of the chemical nature and density of the functional groups, the diffusion dynamics of the dye molecules, in the presence of the surfactant template, can be controlled precisely. The mean diffusion coefficient of the dye molecules increases or decreases depending on the functional groups attached to the silica wall. This allows fine-tuning of the diffusion dynamics of the dye by approximately one order of magnitude. The observed changes in the mean diffusion coefficients can be explained by shielding of hydroxyl groups on the silica surface in combination with changes in the rigidity of the micellar surfactant packing in the film, as well as direct interactions between the functional groups and the dye molecules.

### 4.2.1 Introduction to the sample systems: preparation and characterization

Three principal methods have been developed for an organic functionalization of mesoporous materials. The first is the so-called post-synthesis grafting method.<sup>136, 137</sup> For this approach, the synthesized silica material is modified with alkoxy- or chloro-organosilanes after the initial

synthesis.<sup>138, 139</sup> An alternative approach is based on direct post-synthetic substitution of silica with organometallic compounds.<sup>140-143</sup> Finally, organic modification of mesoporous silica can be achieved by copolymerization of an organosilane with a silica precursor in the presence of the surfactant template.<sup>144, 145</sup> This process is called co-condensation.<sup>146, 147</sup> In the study presented here, the co-condensation method was used as it enables homogeneous incorporation of functional groups into the walls of the mesoporous films. The study shows that the organic functionalizations have a profound influence on the dynamics of individual guest molecules inside the porous network.

The functionalized mesoporous silica films were synthesized according to the EISA method explained in Chapter 2.1. The sample synthesis described in this subsection was done by L. Mühlstein and M. Riederer in the group of Prof. T. Bein (Ludwig-Maximilians-University Munich, Germany). Samples were prepared by spin-coating precursor solutions onto cleaned glass cover slips. For the preparation of precursor solutions for unfunctionalized films, tetraethyl orthosilicate (TEOS, 10 mmol, 2.08 g) in ethanol (3.83 g) was prehydrolyzed at 60 °C for 1 h with acidic catalysis (3 g of 0.2 M hydrochloric acid and 1.8 g of water). The surfactant Brij 56 (566 mg, Polyethylene glycol hexadecyl ether,  $C_{16}H_{33}(OCH_2CH_2)_nOH$ ,  $n \sim 10$ ) in ethanol (7.81 g), used as structure directing agent, was added. N,N'-Di(2,6-diisopropylphenyl)terrylene-3,4:11,12-tetracarboxydiimide (DIP-TDI),<sup>71</sup> a very photo-stable dye with a high fluorescence quantum yield, was added to the solution at an ultralow concentration ( $10^{-10} - 10^{-11} \text{ molL}^{-1}$ ). The dye has kindly been provided by Prof. K. Müllen (Max-Planck-Institute for Polymer Research, Mainz, Germany). The structure of the dye can be found in Figure 4.12. Next, 80  $\mu\text{l}$  of this precursor solution were spin coated at 3000 rpm for 1 min onto a cover slip to give a structured thin silica film (100 – 200 nm) on the glass surface. For the synthesis of the functionalized silica films, a certain molar fraction (2.5, 5, 10, 20, or 30 mol %) of the silica source (TEOS) was replaced with a functionalized silica source (see Table 4.1). A functionalization density of 10 mol % indicates that a functional group is covalently attached to about every tenth silicon atom. All other reaction conditions were kept constant compared to unfunctionalized films.

**Table 4.1: Silica sources used to incorporate the respective functionalizations.**

Functionalization	Silica source
methyl	$\text{CH}_3\text{Si}(\text{OC}_2\text{H}_5)_3$
ethyl	$\text{C}_2\text{H}_5\text{Si}(\text{OCH}_3)_3$
propyl	$\text{C}_3\text{H}_7\text{Si}(\text{OCH}_3)_3$
cyanopropyl	$\text{CNC}_3\text{H}_6\text{Si}(\text{OC}_2\text{H}_5)_3$
phenyl	$\text{C}_6\text{H}_5\text{Si}(\text{OC}_2\text{H}_5)_3$
trifluoropropyl	$\text{F}_3\text{C}_3\text{H}_4\text{Si}(\text{OCH}_3)_3$

The functionalized mesoporous thin films were characterized by L. Mühlstein, M. Riederer and T. Reuther in the group of Prof. T. Bein (Ludwig-Maximilians-University Munich, Germany) and by H. Amenitsch (Austrian Academy of Sciences, Graz, Austria) using a range of methods to determine the pore structure and to test for successful functionalization.

One dimensional (1D) X-ray diffractograms (XRDs) (Figure 4.2) were recorded using a Scintag XDS 2000 powder diffractometer in  $\theta/\theta$  Bragg-Brentano scattering geometry. The XRDs indicate that the mesoporous films exhibit 2D hexagonal order, *i.e.* the amorphous silica surrounding the Brij micelles forms hexagonally packed cylindrical pores parallel to the substrate.<sup>93</sup> The pore-to-pore distance decreases with increasing length of the functional group (Figure 4.2 a) and with increasing functional group density (Figure 4.2 b-d).

In addition, Grazing-Incidence Small-Angle X-ray Scattering (GISAXS) patterns of selected samples were recorded (Figure 4.2 e-g). The experiments were performed at beamline BL 5.2 L of the electron storage ring ELETTRA (Triest, Italy). The wavelength of the incident beam was 0.155 nm (8 keV), and the sample-detector distance 640 mm. The data were recorded in reflection geometry close to the total-reflection angle to achieve maximum intensity. The data confirm that the mesoporous films exhibit 2D hexagonal order. The elliptical shape of the hexagonal pattern is due to shrinkage perpendicular to the glass surface owing to drying effects resulting in elliptically shaped pores.<sup>148</sup> The pore-to-pore distances (*a*-values) and

percentage of the shrinkage are shown in Table 4.2. As only the (10) reflection can be seen in 1D X-ray diffractograms, the values calculated for the pore-to-pore distance from those experiments must be compared to the  $a(10)$ -value obtained from the GISAXS patterns. The values obtained from 1D XRD experiments are in good agreement with those calculated from the GISAXS patterns (Table 4.2).

Besides that, Raman and solid-state  $^{13}\text{C}$  nuclear magnetic resonance (ssNMR) spectroscopy experiments were conducted to further characterize the samples. As the volume of the thin films is very small, a model system providing a larger sample volume has been utilized for these experiments to access a wider spectrum of analytical techniques and to achieve an optimal signal-to-noise ratio for the analysis of the functionalized mesoporous silica. As a model system functionalized mesoporous silica was synthesized inside the cavities of anodic alumina membranes (AAM, ano-disc). Raman spectra of the functionalized mesoporous silica were recorded on a Horiba Jobin Yvon HR800 UV Raman microscope by using an He-Ne laser emitting at 633 nm. Using this method, it is possible to identify cyanopropyl- and phenyl-functionalization (Figure 4.3), thereby confirming incorporation of these functional groups. It is not possible to prove successful alkyl-functionalization because the C-H vibrations of the functional groups overlap with those of the Brij-template.

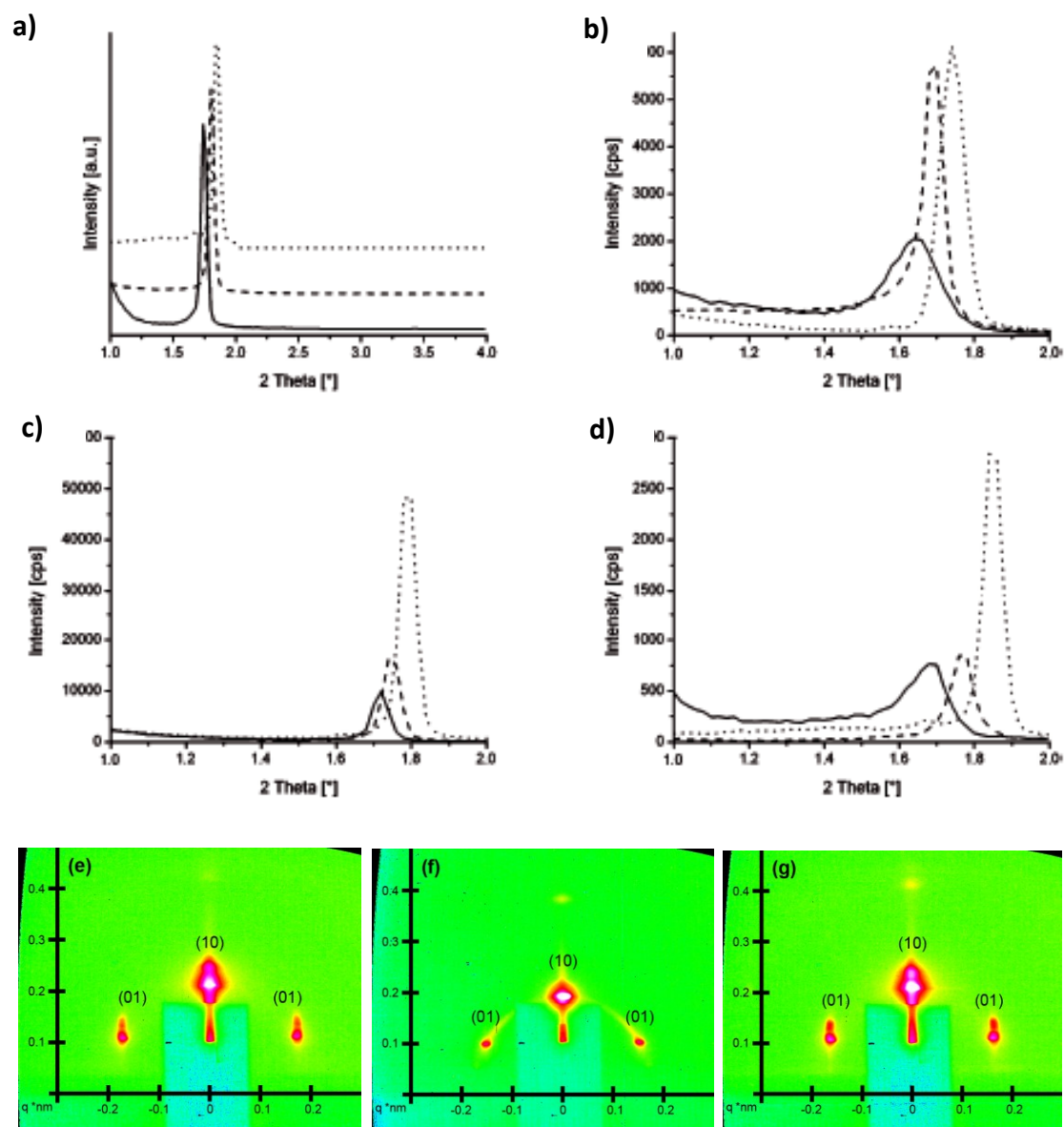


**Figure 4.2: Structural analysis.** a-d) 1D X-ray diffractograms of functionalized silica films with varying lengths of alkyl chains (a; methyl- (—), ethyl- (---), propyl- (•••)); functionalization density 10 mol %, normalized to the reflection with maximum intensity), with varying amounts of cyanopropyl-functionalization (b; 5.0 (—), 10 (---) and 20 mol % (•••)), with varying amounts of phenyl-functionalization (c; 5.0 (—), 10 (---) and 20 mol % (•••)) and with varying amounts of propyl-functionalization (d; 2.5 (—), 5.0 (---) and 10 mol % (•••)). e-g) GISAXS patterns of 10 mol % propyl-functionalized (e), 20 mol % cyanopropyl-functionalized (f) and 20 mol % phenyl-functionalized (g) silica films. The double peaks in (e) and (g) arise at very low incident angles when the distorted-wave Born approximation becomes important for highly reflective surfaces.<sup>149, 150</sup> At very low angles the incoming beam can be reflected from the substrate and then scattered by the top film. This then leads to the observed shift of Bragg-like peaks to higher angles. The lower the incoming angle the larger the distance between the two reflections.

**Table 4.2: 1D X-ray and GISAXS characterization.** The  $a$ -values obtained from 1D X-ray diffraction data as well as  $a$ -values and lateral shrinkage calculated from GISAXS patterns.

Sample	$a(10)$ [nm]	$a(10)$ [nm]	$a(10)$ [nm]	Shrinkage [%]
	from 1D-XRD	from GISAXS	from GISAXS	from GISAXS
10 mol % methyl	5.9	---	---	---
10 mol % ethyl	5.6	---	---	---
10 mol % propyl	5.5	5.4	5.7	20
5.0 mol % cyanopropyl	6.2	---	---	---
10 mol % cyanopropyl	6.0	---	---	---
20 mol % cyanopropyl	5.9	5.9	6.2	14
5.0 mol % phenyl	5.9	---	---	---
10 mol % phenyl	5.8	---	---	---
20 mol % phenyl	5.5	5.4	5.8	22

Successful phenyl- and alkyl-functionalization can be detected in the solid-state  $^{13}\text{C}$ -NMR spectra of the functionalized mesoporous silica synthesized in anodic alumina membranes. The measurements were performed on a Bruker DSX Advance 500 FT in cross-polarization mode (contact time 2 ms, spinning rate 6.0 kHz, pulse delay 2.8  $\mu\text{s}$ , recycle delay 8 s, number of scans between 640 and 16400). The relevant signals (Si-phenyl, Si- $\text{CH}_3$ , Si- $\text{CH}_2\text{-CH}_3$ , or Si- $\text{CH}_2\text{-CH}_2\text{-CH}_3$ ) are indicated in Figure 4.4 by arrows. The adjacent number in Figure 4.4 b refers to the number of C-atoms in the functional group.

Furthermore, it is possible to gain information about the conformation of the alkyl chains of the Brij-template from the  $^{13}\text{C}$ -NMR spectra. It has been reported that the presence of the gauche-conformation in longer  $n$ -alkyl chains results in a shift of the  $^{13}\text{C}$ -NMR signal by 3 or 4 ppm to lower values compared to the trans-conformation.<sup>151</sup> Thus the signal labelled # stems from the trans-conformation of the alkyl-chain of the template and the signal labelled \* originates from the gauche-conformation (Figure 4.4). Although it is difficult to derive absolute quantitative information from the NMR signals because the spectra were recorded in cross-

polarization mode, it is possible to compare the relative intensity of the trans- and the gauche-signals. In Figure 4.4 a, it can be seen that the intensity of the trans-signal decreases compared to that of the gauche-signal with increasing concentration of the phenyl-functional group. Similarly, with increasing length of the alkyl-functional groups, the ratio of trans- to gauche-signal decreases (Figure 4.4 b). This shows that increasing functional-group density and increasing the length of the alkyl-functional group causes a higher degree of disorder of the alkyl-chains of the template molecules.

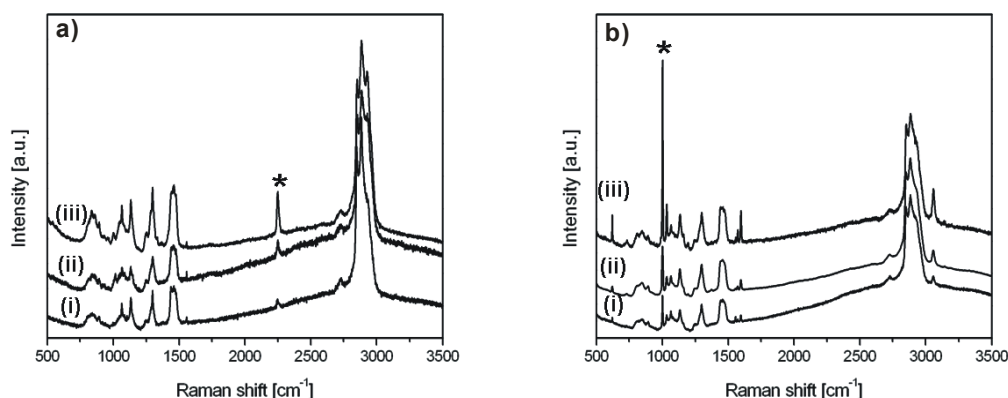


**Figure 4.3: Raman spectra.** a) Cyanopropyl-functionalized silica (functionalization density 5.0 (i), 10 (ii) and 20 mol % (iii)) and b) phenyl-functionalized silica (functionalization density 5.0 (i), 10 (ii) and 20 mol % (iii)) synthesized in anodic alumina membranes. The data were normalized to the maximum intensity of the C-H vibration of the template ( $2886\text{ cm}^{-1}$ ). The asterisks indicate the signal corresponding to (a) the C-N vibration ( $2236\text{ cm}^{-1}$ ) and (b) the aromatic C-H vibrations of the phenyl group ( $1000\text{ cm}^{-1}$ ).

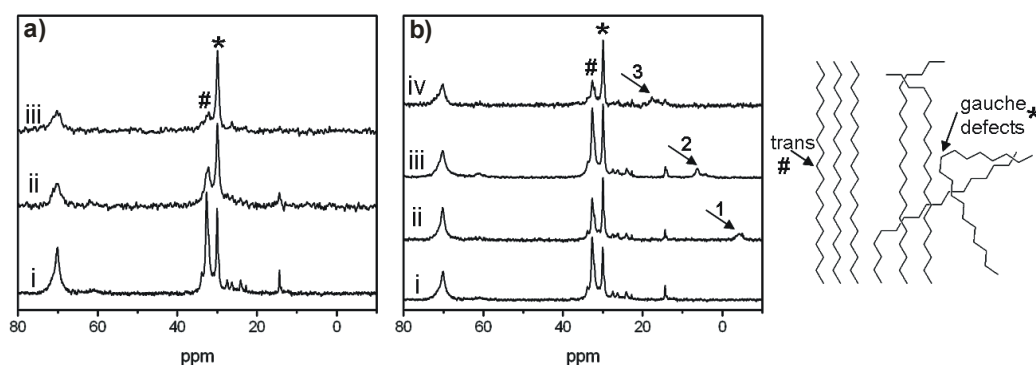


**Figure 4.4: Solid-state  $^{13}\text{C}$ -NMR spectra.** a) Phenyl-functionalized silica (unfunctionalized (i), 2.5 mol % (ii) and 20 mol % (iii) functionalization density) and b) alkyl-functionalized silica (unfunctionalized (i), methyl- (ii), ethyl- (iii), and propyl- (iv) functionalization; functionalization density 10 mol %, arrows indicate the signal/s corresponding to the functional group, the numbers above the arrow indicate the number of C-atoms in the functional group); (a-b) Mesoporous silica synthesized in anodic alumina membranes. The inset shows a graphical illustration of the gauche (\*)- and trans (#)-conformation.

## 4.2.2 Single molecule trajectories

Since the influence of organic functional groups on the diffusion of the incorporated guest molecules is in the focus of this study, information about the motional behaviour of the molecules needs to be extracted. In this context single-molecule approaches prevail over classical ensemble techniques as they offer direct insights into mechanistic details of the interaction of the guest with the host matrix.

The initial step for the further data analysis is to extract trajectories of the diffusing single molecules from recorded frame sequences (movies) of consecutive wide-field microscopy images (for details see Chapter 3.2.1.3). The fluorescence images were recorded with a wide-field setup (see Chapter 3.2.1.2) on an Eclipse TE200 (Nikon) epi-fluorescence microscope with a high numerical aperture oil-immersion objective (Nikon Plan Apo 100\*, NA = 1.40). The molecules were excited at 633 nm with a He-Ne gas laser with an intensity of  $0.20 \text{ kWcm}^{-2}$  and their fluorescence was detected with a back-illuminated electron multiplying charge-coupled device (EM-CCD) camera in frame transfer mode (Andor iXon DV897,  $512 * 512$  pixels). Incident laser light was blocked by a dichroic mirror (640 nm cutoff, AHF) and a bandpass filter (730/140 AHF).

During extracting trajectories from obtained movies, it needs to be ascertained that the molecules are indeed travelling through the pore system and not only on the film surface. This is shown by two different experiments.

On the one hand, molecules that are on the film surface can be washed off.<sup>93</sup> Each mesoporous film investigated in this study was washed, and the amount of dye molecules visible in the wide-field image was not diminished significantly. This indicates that the molecules are inside the channel system.

Secondly, molecules on the surface move in a two-dimensional random fashion, whereas molecules inside the nanoporous host move along the channels and therefore reflect the structure of the silica matrix.<sup>93</sup> The observed diffusional motion of the dye is highly structured. This proves the successful dye incorporation, because the dye maps the porous network. The single molecules act as reporters that shed light on the nature and quality of the structure in the silica matrix. As was shown previously, it is possible to directly correlate diffusion dynamics

of single molecules inside confined porous systems as detected by optical microscopy with the underlying porous structures detected by transmission electron microscopy.<sup>94</sup>

Figure 4.5 displays trajectories of single dye molecules in differently functionalized surfactant-containing films. The small black squares indicate the positioning accuracy for each point of the trajectory, which is typically around 15 nm. Molecules 1 and 2 were measured in an ethyl-functionalized film. The trajectory of molecule 1 clearly maps a curved domain of three parallel aligned pore systems as well as an area of linearly arranged channels. Non-branched trajectories can also be observed in these films (see molecule 2). Molecules 3 and 4 were recorded in propyl-functionalized films. The trajectories of molecules 3 and 4 indicate a highly structured porous network in this film. Even circularly connected pore systems could be observed (see molecule 4). The trajectories given in Figure 4.5 typically span a few micrometers. Similar well-structured trajectories were observed for all film types discussed in this study revealing the confined diffusion of the dye molecules in these porous films.

Through further analysis of the trajectories, much information about the molecular dynamics inside the functionalized silica films can be gained (for details see Chapter 3.2.1.4).

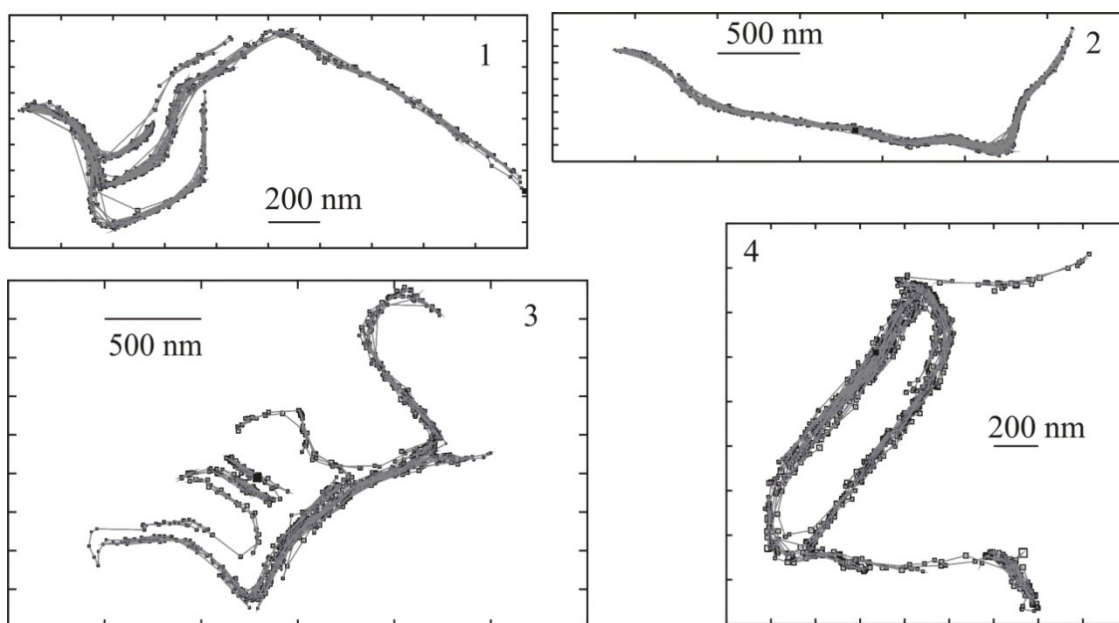


**Figure 4.5: Trajectories of single DIP-TDI (N,N'-Di(2,6-diisopropylphenyl)terrylene-3,4:11,12-tetracarboxydiimide)<sup>71</sup> dye molecules.** The trajectories were recorded in ethyl- (1 and 2) and propyl- (3 and 4) functionalized films. The functionalization density was 10 mol % and the films were measured at 80 % relative humidity. The tiny black squares indicate the positioning accuracy for each point of the trajectory, which is typically around 15 nm.

### 4.2.3 Diffusion dynamics in mesoporous films

The channels of the mesoporous silica thin films contain the template molecules and a certain amount of water, due to the sample synthesis *via* evaporation-induced self-assembly from an ethanol/water solution. It was shown previously that vapor phase water has a profound effect on the diffusion of Nile Red<sup>72</sup> as well as TDI<sup>95</sup> in silica films. Therefore, a change in the relative humidity (RH) at which the samples are measured is also expected to have significant effects on the diffusion of the guest molecules in the functionalized films.

To assess this influence, diffusion of DIP-TDI molecules in a methyl-functionalized film of 10 mol % functionalization density was studied at different relative humidities (30, 50, and 80%; Figure 4.6). The change in humidity has a profound effect on the mean diffusion coefficient of the evaluated mobile molecules, which increases from 1100 nm<sup>2</sup>/s (30%) to 3870 nm<sup>2</sup>/s (80%). Additionally, ethyl- and propyl-functionalized films were measured at 30% and 80% relative humidity with 10 mol % functionalization density. Similarly, a trend of an increasing mean diffusion coefficient with increasing humidity is observed. For comparison, the mean diffusion coefficient in an unfunctionalized film is also given in Figure 4.6. The detailed data for all films discussed above are summarized in Table 4.3.

To analyze the water content in the films at different relative humidities, measurements with a quartz-crystal microbalance (QCM) were performed with a 10 mol % propyl-functionalized film. The QCM technique is based on the fact that the frequency of an oscillating quartz crystal is proportional to the additional adsorbed mass on the crystal.<sup>152</sup> Provided the porous material can be deposited as an acoustically coupled thin film on the surface of the device, one can measure the uptake of adsorbed material on the nanogram scale as a function of partial pressure and temperature via the frequency changes of the QCM. Here, the amount of water adsorbed in the silica films was measured with a QCM experimental setup described in detail by Darga *et al.*<sup>153</sup>

Figure 4.7 clearly shows that increasing the relative humidity from 30 to 80% leads to an increase in the amount of water adsorbed in the film. This process is fully reversible and reproducible as can be seen by the three cycles (30% - 80% - 30%) shown in the graph. The change in water content from 30% to 80% relative humidity is accompanied by an increase in the mean diffusion coefficient by a factor of 2.8 (see Table 4.3). All mesoporous thin films

discussed below were measured at 30% relative humidity in order to analyze the diffusion coefficients of the dye molecules at comparable conditions.

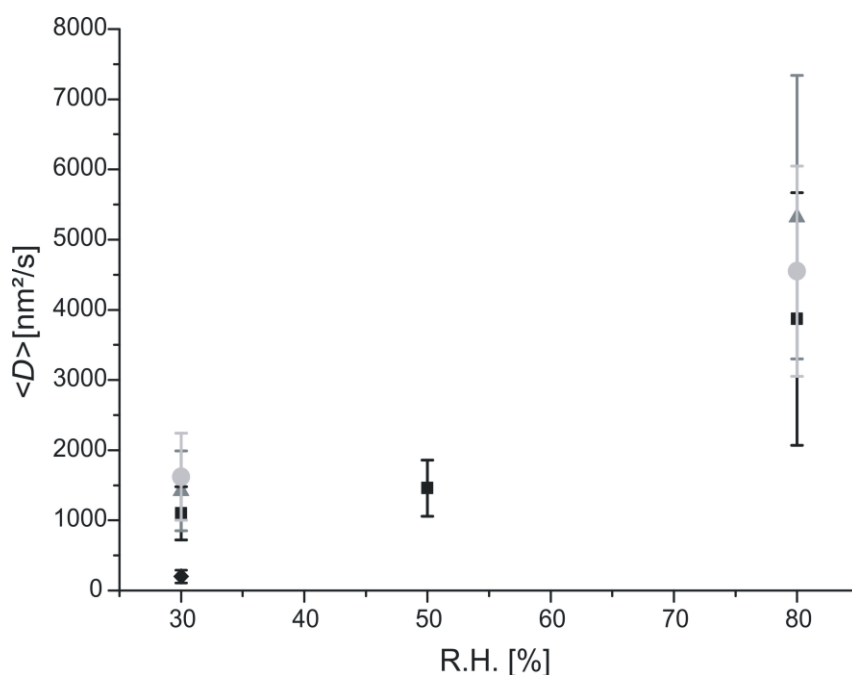


**Figure 4.6: Influence of the surrounding relative humidity (RH) on the mean diffusion coefficient of the dye molecules.** The data were obtained from methyl- (black squares), ethyl- (dark triangles) and propyl-functionalized (grey circles) films with 10 mol % functionalization density and from an unfunctionalized sample (black rhombus). The bars indicate the width of the distribution of diffusion coefficients due to the heterogeneity of the samples and not the error in the determination of the mean diffusion coefficients.

**Table 4.3: Diffusion data for measurements at different RH.** The functionalization density for the functionalized films was set to 10 mol %.

Functionalization	None	Methyl			Ethyl		Propyl	
RH [%]	30	30	50	80	30	80	30	80
# evaluated molecules	101	100	60	80	80	39	104	20
$\langle D \rangle$ [nm <sup>2</sup> s <sup>-1</sup> ]	200	1100	1460	3870	1420	5320	1620	4550
$\sigma$ [nm <sup>2</sup> s <sup>-1</sup> ]	90	380	400	1800	570	2020	620	1500

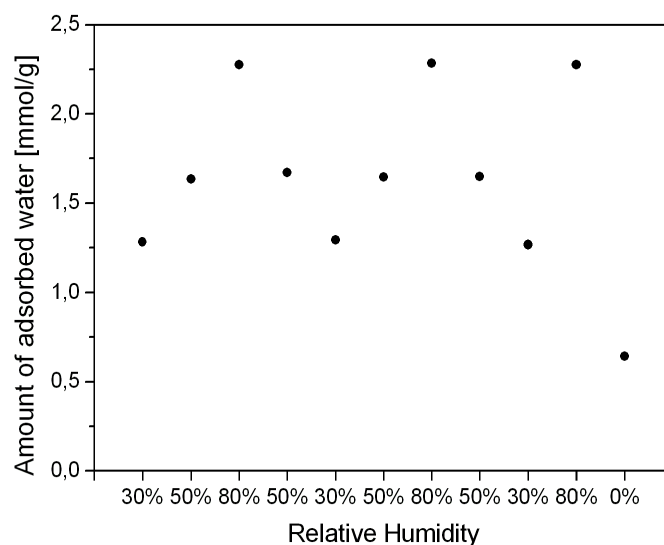


**Figure 4.7: QCM measurements.** The QCM experiments show the amount of water adsorbed in a 10 mol % propyl-functionalized silica film at different relative humidities. The sample was measured repeatedly between 30 and 80 % RH.

In the following the influence of the functionalization density on the diffusion coefficient of the DIP-TDI dye is examined.

Figure 4.8 a compares three cyanopropyl-functionalized films, with functionalization densities of 5.0, 10, and 20 mol %, respectively. In each of the films at least 80 molecules were measured and analyzed. The diffusion coefficients of all analyzed molecules were determined and then plotted as histograms. The histograms reveal the individual dynamics of the single molecules traveling through the system. They are quite broad and reflect the heterogeneity of the sample. The mean diffusion coefficient shown in Figure 4.8 d, increases substantially with higher functionalization density, namely from 410 nm<sup>2</sup>/s (5.0 mol %) to 2820 nm<sup>2</sup>/s (20 mol %). This corresponds to an increase by a factor of about 7.

In Figure 4.8 b, the diffusion coefficients of propyl-functionalized samples of 2.5, 5.0, and 10.0 mol % functionalization density are displayed as histograms. Again, the mean diffusion coefficient changes significantly with functionalization, from 380 nm<sup>2</sup>/s (2.5 mol %) to 1620 nm<sup>2</sup>/s (10 mol %). This corresponds to a 4-fold increase.

Figure 4.8 c shows histograms of diffusion coefficients for different phenyl-functionalization densities between 2.5 mol % and 30 mol %. For this functionality the film structure is retained

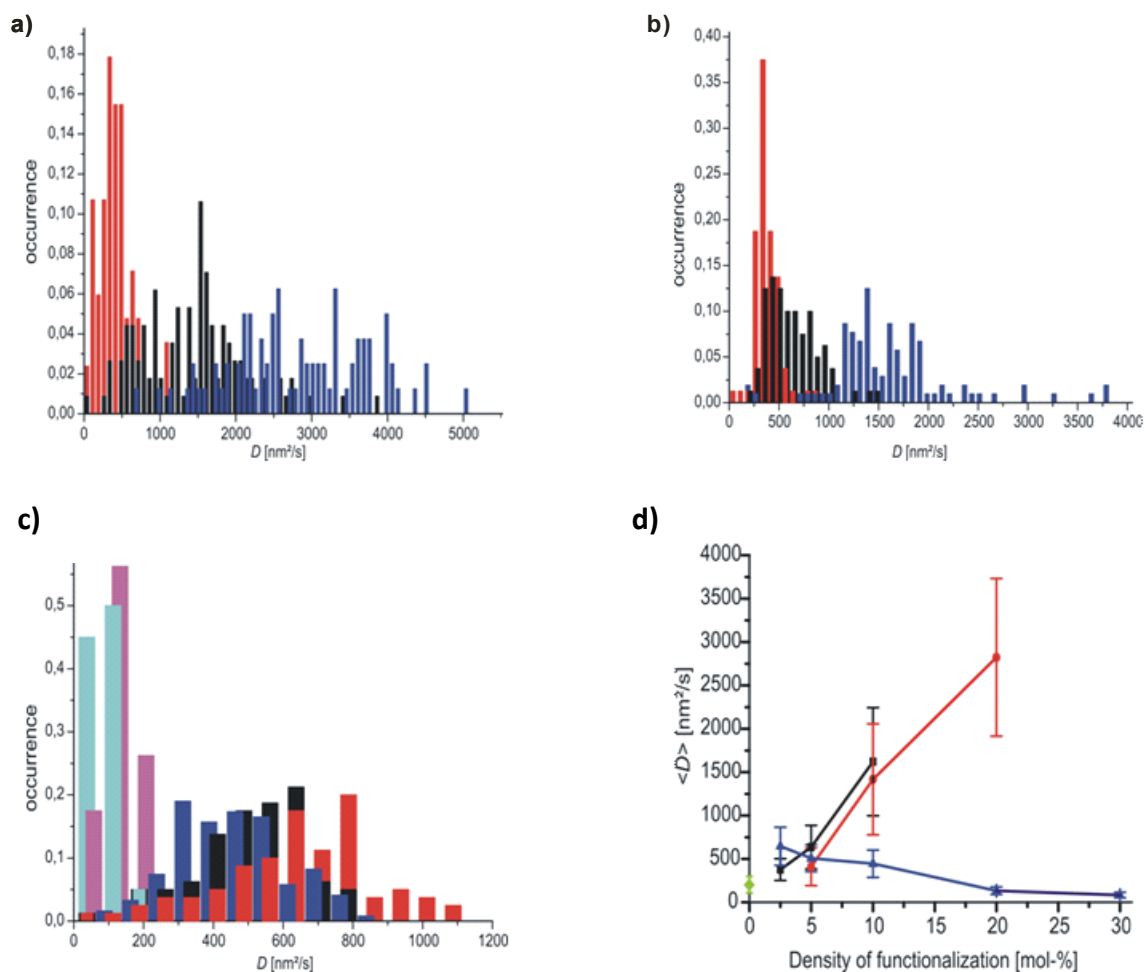
even for high densities. In contrast to the above samples functionalized with flexible chains (Figure 4.8 a and b), here the mean diffusion coefficient decreases with increasing functionalization density. The dye inside the film is slowed down by nearly one order of magnitude from a diffusion coefficient of  $650 \text{ nm}^2/\text{s}$  (2.5 mol %) to  $80 \text{ nm}^2/\text{s}$  (30 mol %).

Figure 4.8 d visualizes the different trends discussed above. Additionally, the mean diffusion coefficient for the unfunctionalized film is given with  $200 \text{ nm}^2/\text{s}$ . The bar for each data point does not indicate the error in the determination of the mean diffusion coefficient. It rather indicates the width of the distribution of the diffusion coefficients due to the heterogeneity of the samples. The distributions were calculated by fitting the experimental data to a 1D Gaussian function.

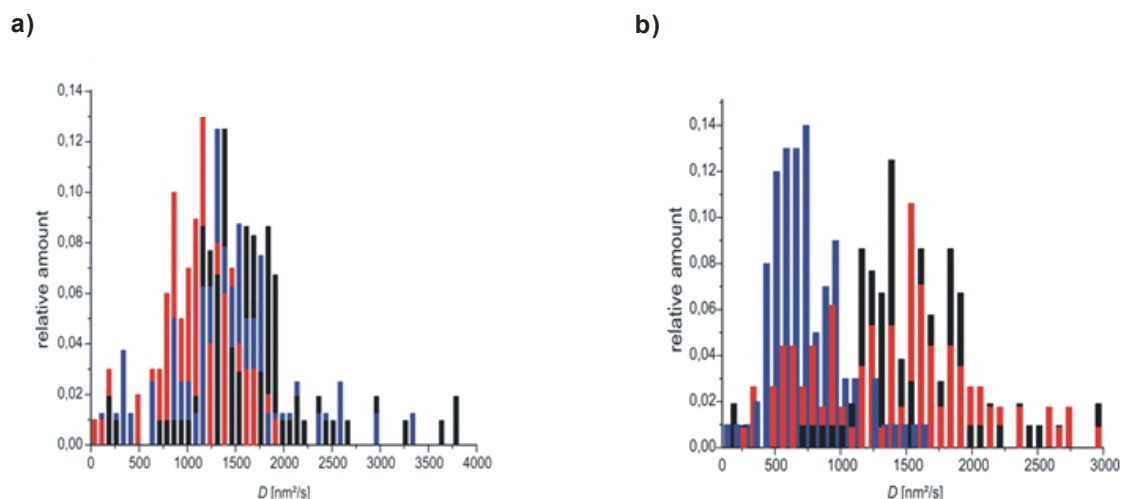
The nature of the functional groups was also changed in order to explore their influence on the guest dynamics (Figure 4.9). The template-containing films discussed in this Figure were synthesized with 10 mol % functionalization density. In Figure 4.9 a, the diffusion data for aliphatic functional groups with different alkyl-chain length (methyl, ethyl, and propyl) are shown. We note that the change in diffusion coefficients due to different alkyl-groups (Figure 4.9 a) is less significant than the change due to different functionalization densities, e.g., the propyl-densities (see Figure 4.8 a). However, an increase of diffusivity can be observed for increasing alkyl-chain lengths; the diffusion coefficient increases from  $1100 \text{ nm}^2/\text{s}$  to  $1620 \text{ nm}^2/\text{s}$  (from methyl- to propyl-functionality). Samples with longer aliphatic chains were also prepared (pentyl- and octyl-functionalizations). However, it was not possible to acquire reproducible data as the structural definition of these films was not sufficient.

Figure 4.9 b displays the influence of functional group polarity on the diffusion coefficients by comparing propyl-, cyanopropyl- and trifluoropropyl-functionalized films. The strongly polar trifluoropropyl-groups decrease the mean diffusion coefficient of the dye to about one half ( $740 \text{ nm}^2/\text{s}$ ), compared to the propyl- and cyanopropyl-functionalization ( $1620 \text{ nm}^2/\text{s}$  and  $1420 \text{ nm}^2/\text{s}$ ). Thus, increasing polarity of the functional groups leads to a decrease in dye dynamics.

The complete data obtained from these measurements are summarized in Table 4.4.



**Figure 4.8: Diffusion data for the functionalization density experiments (measured at 30 % RH).** Histogram of diffusion coefficients for a) different cyanopropyl functionalization densities, plotted in different colors (red: 5.0, black: 10 and blue: 20 mol %); b) varying propyl functionalization densities (red: 2.5, black: 5.0 and blue: 10 mol %) and c) a series of different phenyl functionalization densities (red: 2.5, black: 5.0, blue: 10, purple: 20 and light blue: 30 mol %). d) Correlation of the mean diffusion coefficients with the functionalization densities, including the data for the unfunctionalized film, given at zero density (black: propyl, red: cyanopropyl, blue: phenyl, green: unfunctionalized). The bars indicate the width of the distribution of the diffusion coefficients due to the heterogeneity of the samples and not the error in the determination of the mean diffusion coefficients.



**Figure 4.9: Influence of the alkyl chain length and the polarity of the functional groups on the diffusion dynamics of the DIP-TDI molecules.** Histogram of diffusion coefficients for a) varying alkyl chain length (red: methyl, blue: ethyl and black: propyl) and b) a variation in the polarity of the functional groups (red: cyanopropyl, blue: trifluoropropyl, black: propyl) on the diffusion dynamics of the guest molecules. The films in a) and b) were synthesized with 10 mol % functionalization density and measured at 30 % RH.

**Table 4.4: Diffusion data for measurements at a RH of 30 % and different functionalization densities.**

Functionalization	None	Methyl	Ethyl	Propyl			Trifluoropropyl
functionalization density [mol %]	---	10	10	2.5	5.0	10	10
# evaluated molecules	101	100	80	80	80	104	100
$\langle D \rangle$ [nm <sup>2</sup> s <sup>-1</sup> ]	200	1100	1420	380	640	1620	740
$\sigma$ [nm <sup>2</sup> s <sup>-1</sup> ]	90	380	570	130	250	620	280

Functionalization	Cyanopropyl			Phenyl				
	5.0	10	20	2.5	5.0	10	20	30
functionalization density [mol %]	5.0	10	20	2.5	5.0	10	20	30
# evaluated molecules	84	113	80	80	80	121	80	80
$\langle D \rangle$ [ $\text{nm}^2\text{s}^{-1}$ ]	410	1420	2820	650	510	450	130	80
$\sigma$ [ $\text{nm}^2\text{s}^{-1}$ ]	220	640	910	220	160	160	40	30

#### 4.2.4 Correlation of the diffusion coefficients to the pore-to-pore distance

Now, the question arises whether the changes in the pore-to-pore distances observed for different functionalization densities (see Figure 4.2 and Table 4.2) are correlated with the dynamics of the molecules (Table 4.4). Therefore, in Figure 4.10 the mean diffusion coefficients are compared to pore-to-pore distances obtained from 1D X-ray diffraction. In the propyl- and cyanopropyl-functionalized samples, an increase of the mean diffusion coefficient can be observed for decreasing pore-to-pore distances. In contrast, in phenyl-functionalized films a decreasing pore-to-pore distance correlates with a decrease in dye dynamics. From this we can conclude that the effect on the mobility of the dye discussed for the data in Figure 4.8 cannot be due to a simple change in the pore-to-pore distance. The underlying mechanisms that govern the dye dynamics in the presence of functional groups appear to be more complex and will be discussed later.

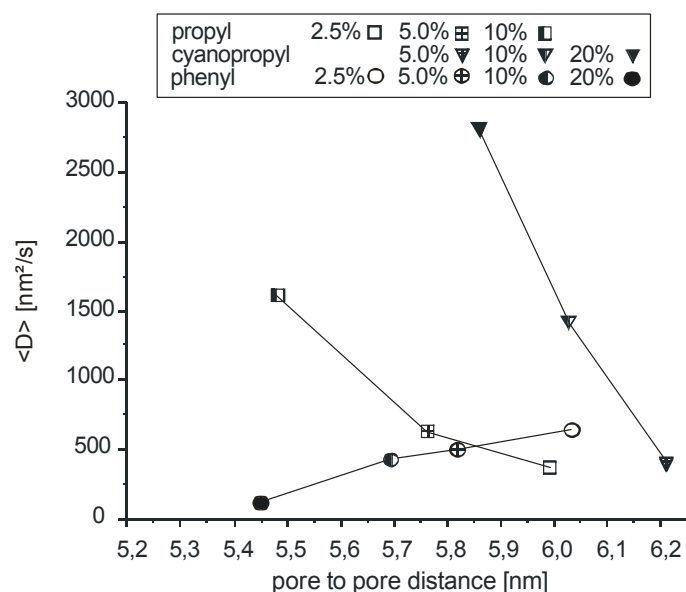


**Figure 4.10: Correlation of the diffusion coefficients for the different functionalization densities with the pore-to-pore distances from 1D X-ray diffraction measurements.** Data of propyl-functionalized films are displayed as squares, data from cyanopropyl-functionalized films as triangles and data of phenyl-functionalized samples as circles.

### 4.2.5 Controlling the homogeneity in the distribution of the functional groups.

The above results show that the diffusion dynamics of guest molecules can be strongly influenced *via* the introduction of functional groups. Now, it needs to be checked whether the functional groups are homogeneously distributed inside the porous network. Inhomogeneities in the distribution of functional groups are local variations in the functionalization density. As we know from Figure 4.8, these variations lead to very pronounced effects in the diffusion dynamics of the guest molecule. Cyanopropyl-functionalized films (20 mol % functionalization density) are ideally suited for detecting heterogeneities via the diffusional behavior of the embedded dye molecules, because the dyes respond strongly to variations in the functionalization density for these films (see Table 4.4).

While previously, the heterogeneity from molecule to molecule in the mesoporous films has been mentioned, now the focus lies on possible heterogeneities within a single molecule

trajectory. For this purpose, Figure 4.11 a displays the results of a more detailed analysis of the ranked step length distribution (see Chapter 3.2.1.4) by plotting the inverse of the cumulative probability distribution (see Eq. 3.11) of the squared step lengths for a single dye molecule. This method was used previously to characterize inhomogeneities of single molecule diffusion in unfunctionalized mesoporous silica films.<sup>93</sup> The data points display the step lengths according to their rank. The green line indicates a mono-exponential fit, the blue line a bi-exponential fit according to Eq. 3.12. Clearly the mono- and bi-exponential functions are not sufficient to fit the data adequately. The data can only be fitted by a tri-exponential fit (grey). This indicates that the diffusion of the dye molecule is extremely heterogeneous and cannot be described by only one or two diffusion coefficients. Similar data can be obtained for any other functionalization as well as for unfunctionalized films.

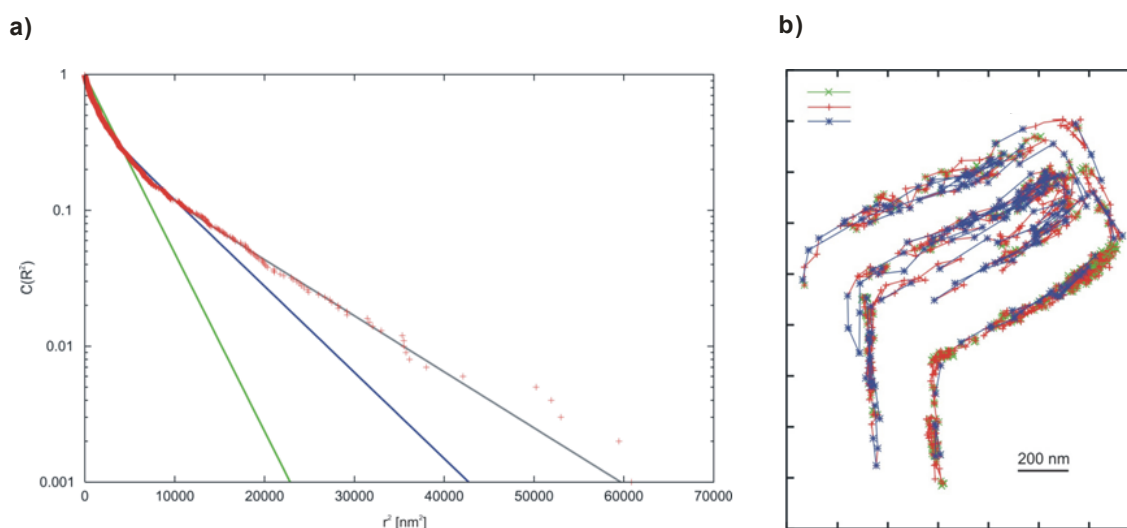


**Figure 4.11: Testing for heterogeneities in the distribution of the functional groups.** Exemplary data of one molecule diffusing in a 20 mol % cyanopropyl-functionalized film. a) The ranked step length distribution is shown by plotting the inverse of the cumulative probability distribution for  $t_{\text{lag}} = \tau$  (see Eq. 3.11). The green line shows a mono-exponential, the blue line a bi-exponential and the grey line a tri-exponential fit according to Eq. 3.12. The fitting parameters are for a mono-exponential decay:  $c_1 = 1.000$  and  $r_1^2 = 3316 \text{ nm}^2$ . The bi-exponential fit gives the following parameters:  $c_1 = 0.479$ ,  $r_1^2 = 907 \text{ nm}^2$ ,  $c_2 = 0.521$ ,  $r_2^2 = 6621 \text{ nm}^2$ . The tri-exponential fit gives the following parameters:  $c_1 = 0.149$ ,  $r_1^2 = 164 \text{ nm}^2$ ,  $c_2 = 0.557$ ,  $r_2^2 = 2006 \text{ nm}^2$ ,  $c_3 = 0.294$ ,  $r_3^2 = 10301 \text{ nm}^2$ . To fit the data (red crosses) adequately a tri-exponential fit is needed, thus illustrating the inherent heterogeneity of the film. b) The trajectory of the molecule; the step lengths are grouped into three classes and plotted in different colors (short steps (green)  $\leq 27 \text{ nm}$ ,  $27 \text{ nm} < \text{medium steps (red)} < 100 \text{ nm}$ , long steps (blue)  $\geq 100 \text{ nm}$ ).

This heterogeneous diffusion behavior of the dye can be due to general variations in the quality of the structure of the host silica material, such as the presence of defects, adsorption sites, or dead ends. On the other hand it can also result from local variations in the spatial distribution of the functional group density within different branches of the trajectory.

To further elucidate this, we display the trajectory such that the different classes of step lengths: short steps (green)  $\leq 27$  nm,  $27$  nm  $<$  medium steps (red)  $< 100$  nm, long steps (blue)  $\geq 100$  nm are displayed in different colors. Since each wide-field image in the whole frame sequence is recorded with the same integration time, longer steps are associated with a higher local diffusion coefficient. Figure 4.11 b shows this analysis for the same molecule evaluated in Figure 4.11 a. Through variation of the threshold values for the different step lengths, local accumulations of steps of a certain step size and thus local heterogeneities in the distribution of the local diffusion coefficients would become apparent. This would reveal heterogeneities in the distribution of the functional groups. However, the different step lengths are statistically distributed over the trajectory. Therefore no spatial correlation between the distinct values of  $D$  observed in Figure 4.11 a and specific areas of the molecular trajectory in Figure 4.11 b can be detected. Thus, the heterogeneities revealed by the plot in Figure 4.11 a must lie below our limits of spatial resolution.

The lower limit to which we can visualize local density fluctuations for the functional groups depends on the diffusion coefficient of the single molecule and can be roughly estimated as follows: The dye molecules in the sample evaluated in Figure 4.11 show a mean diffusion coefficient of  $2820$  nm<sup>2</sup>/s. One single wide-field frame in the whole sequence was recorded with an integration time of  $400$  ms. During this time the dye molecules explore an average distance  $\sqrt{\langle r^2 \rangle}$  (see Eq. 3.4) of about  $67$  nm.

### 4.2.6 General view on the diffusion of a individual molecule inside the pores of functionalized mesoporous silica

The experiments confirm that the surrounding relative humidity has a profound influence on the diffusion of dye molecules inside functionalized mesoporous films. For all samples studied, with increasing relative humidity faster dynamics of the dye in the host material could be observed (see Table 4.3). From QCM measurements we know that increasing the relative humidity of the environment surrounding the film leads to detectable increases in the amount of water adsorbed (see Figure 4.7). The silica pore walls are covered with hydroxyl groups: for unfunctionalized silica approximately four hydroxyl-groups per  $\text{nm}^2$  can be assumed.<sup>154</sup> They can interact with the oxygen atoms of the dye, thus forming hydrogen bonds. As was previously reported, this leads to a decrease in the dynamics of the dye due to adsorption sites.<sup>92, 95</sup> Therefore, the data suggest that the accessibility of these surface hydroxyl-groups has a significant influence on the diffusion dynamics of the dye molecule. If we assume that an average silica film has a surface area of  $800 \text{ m}^2/\text{g}$  (a typical value for these mesoporous materials),<sup>155</sup> the coverage of water molecules on the silica surface at different relative humidities can be estimated. For the 10 mol % propyl-functionalized film, the coverage of water molecules at 30% RH then results in about one water molecule per  $\text{nm}^2$ . At 80% relative humidity the coverage is about 1.7 water molecules per  $\text{nm}^2$ . With increasing RH, the adsorbed water will therefore have a greater shielding effect on the hydroxyl groups leading to faster diffusion dynamics - as observed in this study.

Our experiments further show that variations in water content alone do not explain the observed changes in diffusion dynamics of dye molecules in differently functionalized films. According to QCM measurements, the unfunctionalized film contains a much larger amount of water than the propyl-functionalized film. However, a lower mean diffusion coefficient is obtained from the measurements in an unfunctionalized film compared to propyl-functionalized films at 30% RH (see Table 4.4). As discussed above, hydrogen bonds between the oxygen atoms of the dye and surface hydroxyl-groups have an important influence on dye dynamics. The introduction of flexible alkyl groups reduces the number of hydroxyl-groups on the surface of the pores and can result in a shielding of the remaining hydroxyl groups. This reduces the accessible sites for hydrogen bonding and thereby allows the dye to diffuse faster.

The shielding effect of water is less pronounced than that of apolar alkyl chains as there is no possibility of hydrogen bonding between the functional group and the dye molecule. The shielding of hydroxyl-groups also explains the increase of the mean diffusion coefficient with increasing alkyl chain length described in Figure 4.9 a, as longer chains can be expected to have a greater shielding effect. Similarly, the effects observed for increasing propyl- and cyanopropyl-functionalization densities (Figure 4.8 a and b) can be explained. Furthermore, cyanopropyl-groups can have a similar shielding effect to the one described for propyl-groups. Consequently, faster diffusion is observed in cyanopropyl-functionalized compared to unfunctionalized films (Figure 4.8 d). Due to our synthesis conditions the solution inside the pores is acidic resulting in protonation of the cyano-groups. Hence, weak hydrogen bonds can form between the dye and the functional groups. This explains our observation that the mean diffusion coefficient in cyanopropyl-functionalized films is lower than in propyl-functionalized films (Figure 4.8 d). The effect observed for the trifluoropropyl-functionalization (Figure 4.9 b) may similarly be attributed to the polarity. However, additional effects, such as wetting, may also play a role.

The effects observed for the phenyl-functionalization can be explained by two competing effects. For low functionalization densities (2.5 mol % and 5.0 mol %) the shielding effect discussed above results in a higher mean diffusion coefficient compared to the unfunctionalized film (Figure 4.8 d). At the lowest functionalization density the bulky and rigid phenyl-groups show the best shielding effect of all functional groups studied. Consequently, at this density the largest mean diffusion coefficient was obtained in phenyl-functionalized films. Interestingly, the mean diffusion coefficient decreases with increasing functionalization density for phenyl-functionalized films (Figure 4.8 c). According to the proportions displayed in Figure 4.12, which is drawn to scale, it is reasonable to assume that the observed effects can be partially due to a direct interaction of the dye with the functional groups. The decreasing mean diffusion coefficient with increasing functionalization density can therefore be explained with attractive  $\pi$ - $\pi$  interactions between the rigid phenyl groups of the functionalization with the aromatic system of the dye or the phenyl-groups at both ends of the dye. Due to the diisopropyl-groups in the dye, those end groups are twisted out of the aromatic plane of the dye. This is sterically advantageous for interactions with the phenyl-functionality of the silica host.

An additional factor that can influence the dynamics of the dye molecule is the rigidity of the template micelles. NMR data show that the degree of disorder of the alkyl-chains of the template molecules varies depending on the functional groups or their density (Figure 3). We suggest that the micelle packing is less rigid when the alkyl-chains of the template molecules are less ordered, i.e., show a larger number of gauche defects. Therefore, the dye molecules can more easily pass through the template-containing film. With increasing length of the alkyl-functional groups, the degree of disorder increases. Accordingly, the mean diffusion coefficient of the dye molecules is larger for longer-chain alkyl-functionalizations (Figure 8a). This also explains the observation that at a low density (5.0 mol %) the mean diffusion coefficient observed in a phenyl-functionalized film is larger than in films with other functionalizations, because already at 2.5 mol % phenyl-functionalization the degree of disorder of the alkyl-chains of the template molecules is greater than in the 10 mol % alkyl-functionalized samples. Again, this can be deduced from the significantly smaller ratio of trans- to gauche-signal in the phenyl-sample. However, while the degree of disorder in the template micelles in a film with 20 mol % phenyl functionalization is greater compared to the 2.5 mol % functionalized sample, we do not observe an increase in mean diffusion coefficient. This suggests that at this high functionalization density the direct  $\pi$ - $\pi$  interactions between the functional groups and the dye have a greater influence on the dye dynamics than the order and rigidity of the micelle packing.

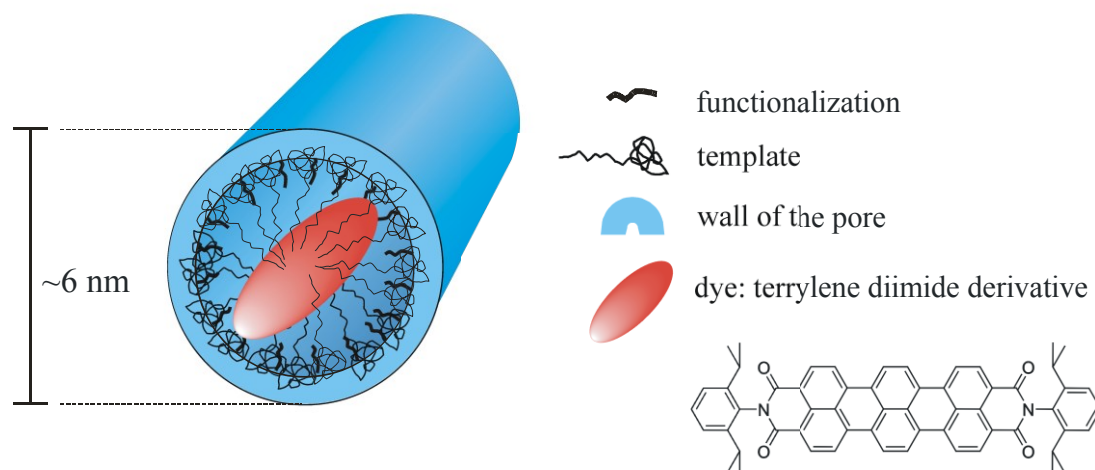


**Figure 4.12: Sketch of a DIP-TDI molecule within one mesopore.** All constituents are drawn to scale. The chemical structure of the dye is displayed on the right.

To summarize, the changes in the mean diffusion coefficient of a dye molecule moving through a functionalized mesoporous silica film can be explained by considering the shielding of silanol groups in combination with changes in the rigidity of the micelle packing in the film and direct interactions between the functional groups and the dye molecules.

### 4.2.7 Conclusion

This study has shown that the incorporation of functional groups has a profound influence on the diffusional behavior of dye molecules inside surfactant-containing mesoporous silica films. The advanced microscopy techniques employed here are uniquely suited to reveal the mechanistic details of the host-guest interactions at a single-molecule level. The molecular diffusion is heterogeneous both in space and time. Further, this comprehensive study illustrates that functional groups can be used to slow down or accelerate the diffusion of guest molecules within one order of magnitude. This now opens up the opportunity to fine-tune host-guest interactions in these systems. For drug-delivery applications utilizing mesoporous hosts this could pave the way for controlling the drug release rate. Especially, a deceleration in guest dynamics as observed for the phenyl-functionalized samples can contribute towards realizing a depot effect, which is a controlled release of the drug over a prolonged period of time.

### 4.3 Nano-structured silica materials for drug-delivery of the anti-cancer drug Doxorubicin

The last chapter dealt with tuning molecular dynamics inside templated mesoporous thin silica films in order to show that a depot effect for drugs can be realized. Now, in this study a medically relevant drug will be incorporated in such templated thin films. The interaction of the drug with the delivery structure will be investigated in great detail and the applicability of the system for drug-delivery will be assessed. This study thus represents an important step towards applying mesoporous silica in drug-delivery. An important field in medicine that could profit substantially from such advances in nanotechnology and drug-delivery is cancer therapy. The cytostatics administered in chemotherapy to treat tumors are always accompanied by a number of severe side-effects.<sup>32, 33</sup> These side-effects can be reduced by encapsulating the drug in a delivery-system, which protects the body from the toxic drug and prevents the decomposition of the drug prior to reaching the target cells. Furthermore, a specific targeting of this drug carrier onto malign cells combined with a controlled release of the drug by diffusion minimizes the amount of drug that has to be administered thereby further reducing the amount of side-effects. Clinically used nanocarriers for drugs consist for example of synthetic organic polymers<sup>29, 118, 119</sup> or liposomes<sup>30</sup>. However, especially cell-targeting and a controlled-release still represent a great challenge. In the previous chapters mesoporous silica indicated its high potential as drug-delivery device. Hence, in this study the applicability of mesoporous silica as a novel drug carrier in cancer therapy is tested. Single molecule and ensemble fluorescence microscopy were used to gain insight into the complicated drug-carrier interplay.

Surfactant-templated mesoporous silica materials<sup>18</sup> (Figure 4.13 a) are used in this study to incorporate and deliver the anti-cancer drug Doxorubicin hydrochloride (Figure 4.13 b). This is the first time ever that a clinically relevant drug has been characterized on a single molecule level. Doxorubicin and its analogues are widely used in chemotherapy, *e.g.* for the treatment of Kaposi's sarcoma,<sup>156</sup> ovarian carcinoma<sup>157</sup> or breast cancer.<sup>158</sup> However, Doxorubicin shows an especially high cardiac and renal toxicity, which limits its therapeutic applications.

Consequently, novel drug-delivery strategies for this drug are urgently needed. Various recent studies demonstrate the high efforts made in the eager quest for novel ways of delivering and administering this key drug.<sup>159, 160</sup>

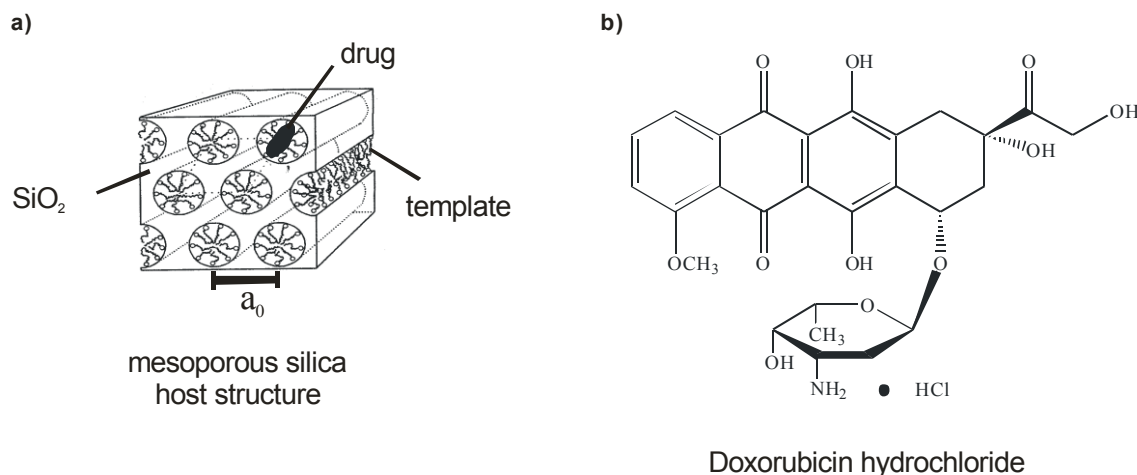


**Figure 4.13: Mesoporous silica as delivery system for the anti-cancer Drug Doxorubicin.** a) Schematic of a surfactant-templated mesoporous silica material loaded with the cytostatic Doxorubicin hydrochloride.  $a_0$  designates the pore-to-pore distance. b) Structure of the anti-cancer drug Doxorubicin hydrochloride.

### 4.3.1 Introduction to the sample systems: preparation and characterization

Doxorubicin-loaded mesoporous samples were synthesized as thin films via the evaporation-induced self-assembly (EISA) method.<sup>161, 162</sup> The morphology of a thin film was chosen not only because thin films are an easy-to-study object for optical techniques (compared to particles or filaments) but also because they could be developed towards drug-delivering thin film implants covering for example tumor tissue. Four mesoporous structures were synthesized and evaluated: i) a CTAB templated film, ii) a Pluronic P123 templated film, iii) an unfunctionalized Brij-56 templated film and iv) a Brij-56 templated mesoporous film where the silica matrix has been functionalized with covalently attached propyl groups inside the porous network. The films were assembled by spin-coating precursor solutions onto a cleaned cover

slip. The preparation of the precursor solutions started with prehydrolyzing silica building blocks (tetraethyl orthosilicate [TEOS], Aldrich) in ethanol at 60 °C for 1 h under acidic catalysis (using 3 g of 0.2 molar hydrochloric acid and 1.8 g of water). For the propyl-functionalized films 10 mol-% of the TEOS were replaced by trimethoxy(propyl)silane (Aldrich). To this prehydrolyzed solution an ethanolic template solution with the structure-directing agent was added. For P123 and Brij-56 templated structures Doxorubicin hydrochloride (Figure 4.13 b) (Sigma Aldrich) was added directly to the precursor solution. 80  $\mu$ l of this precursor solution were then spin-coated (3000 rpm, 60 s) onto a glass cover slip. For the CTAB templated structure a drug free precursor solution was spin-coated, resulting in an unloaded film. The drug was then deposited on the surface of the synthesized film, from where the porous network is accessible. This resulted in a mesoporous structured, drug-loaded thin film on a cover slip (for a detailed list of the synthesis recipes see Table 4.5).

The thin films were characterized via 1D X-ray diffractometry (XRD) on a Scintag XDS 2000 powder diffractometer in a  $\theta / \theta$  Bragg-Brentano scattering geometry. Characterization via 1D X-ray diffractometry (XRD) proved that all mesoporous thin films exhibit 2D-hexagonal order.<sup>93</sup> From the position of the diffraction peak ( $2\theta$ -value) the pore-to-pore distance  $a_0$  can be calculated (see Table 4.5 for details).  $a_0$  was determined to be i) 4.4 nm  $\pm$  0.2 nm for the CTAB templated film, ii) 10 nm  $\pm$  0.5 nm for the Pluronic P123 templated film, iii) 6.1 nm  $\pm$  0.3 nm for the unfunctionalized Brij-56 templated film and iv) 5.6 nm  $\pm$  0.3 nm for the propyl-functionalized Brij-56 templated film. In the CTAB sample  $a_0$  is significantly smaller than in the P123 sample due to the decreased size of the structure directing template. The Brij-56 samples show intermediate values. The propyl-functionalization leads to a decrease in  $a_0$  compared to the unfunctionalized film as observed previously.<sup>163</sup> A typical film thickness for the mesoporous structures investigated in this study is 150 nm. <sup>1</sup>H-NMR measurements proved the stability of Doxorubicin inside the mesoporous structures (data not shown).

**Table 4.5: Synthesis recipes and XRD characterization data.**

	<b>template</b>	P123	CTAB	Brij-56	Brij-56
	<b>functiona- lization</b>	none	none	none	propyl (10 mol-%)
	<b>2<math>\theta</math> [°]</b>	1.00 +/- 0.05	2.32 +/-0.09	1.68 +/- 0.09	1.81 +/- 0.08
	<b><math>a_0</math> [nm]</b>	10 +/- 0.5	4.4 +/- 0.2	6.1 +/- 0.3	5.6 +/- 0.3
prehydro- lized solution	<b>silica building block</b>	2.08 g (9.98 mmol) TEOS	2.08 g (9.98 mmol) TEOS	2.08 g (9.98 mmol) TEOS	1.87 g (8.97 mmol) TEOS 0.164 g (0.998 mmol) propyltri- methoxy- silane
	<b>ethanol</b>	7.90 g	7.90 g	3.83 g	3.83 g
template solution	<b>template</b>	0.750 g P123	0.638 g CTAB	0.566 g Brij-56	0.566 g P123
	<b>ethanol</b>	15.8 g	15.8 g	7.81 g	7.81 g

### 4.3.2 Drug dynamics in the mesoporous delivery structure

Single molecule fluorescence microscopy is utilized to investigate the diffusion of Doxorubicin molecules inside the four mesoporous systems. In order to observe individual molecules, Doxorubicin was added to the precursor solution in highly diluted concentrations ( $10^{-10}$  -  $10^{-11}$  mol/L). With a widefield fluorescence microscope (Nikon Eclipse TE200) movies of the molecular motion inside the different samples were recorded. Doxorubicin was excited through a high numerical aperture oil-immersion objective (Nikon Plan Apo 100\*/1.40 N.A.

oil) at 532 nm with a diode pumped solid-state laser (Cobolt Samba TM Laser, cw, 100 mW LAB) with an intensity of  $0.30 \text{ kW cm}^{-2}$  for the unfunctionalized and propyl-functionalized Brij-56 samples and  $0.76 \text{ kW cm}^{-2}$  for the P123 samples. The fluorescence was detected on a back-illuminated electron-multiplying charge-coupled device (EM-CCD) camera (Andor iXon DV897,  $512 * 512$  pixels) in frame transfer mode. Incident laser light was blocked by a dichroic mirror (dual line beamsplitter 532/633, AHF Analysentechnik) and a bandpass filter (650/250, Chroma). Details about the setup have been reported previously.<sup>93</sup> The position of the observable molecules was tracked by fitting a 2D Gaussian function<sup>164</sup> to the fluorescence signal throughout the movie, extracting molecular trajectories (see Chapter 3.2.1.3 for details).<sup>90</sup> Since the film thickness lies far below the axial resolution of the microscope, the recorded molecular movement is always a two-dimensional projection of the real three-dimensional motion. Consequently, a 2D diffusion model is the correct model for data evaluation.

With this setup, the Pluronic P123 templated samples were measured. They were washed with water prior to the measurement in order to remove molecules on the film surface and thus prevent them from obscuring the measurement and the trajectory analysis. In addition the film surface was covered with PVA such that mobile molecules can only diffuse inside the channel system and cannot leave the film and access its surface. The recorded movies show two populations: 5% mobile and 95% immobile molecules. The presence of a majority of immobile molecules is surprising.

In order to understand the origins of these mobile and immobile populations, single molecule and ensemble fluorescence spectra of Doxorubicin were recorded (see Figure 4.14) on a modified LSCM (Zeiss LSM410). A 532 nm diode pumped cw solid-state laser (Soliton, DLSOT-50, AlGaAs) was used to excite the Doxorubicin molecules inside the P123 templated film. The red-shifted fluorescence light was collected using a high NA oil-immersion objective (Zeiss Plan Apochromat 63x/1.40 oil) and separated from the excitation light with a combination of a dichroic (HQ 545LP, AHF Analysentechnik, Tübingen, Germany) and a bandpass filter (675/250, Chroma Technology Corp, Bellows Falls, Vermont, USA) Fluorescence spectra were recorded using a prism-CCD spectrometer (EEV 1300!100-EMB-chip, Princeton Instruments, Trenton, New Jersey, USA). For details of the setup see Chapter 3.2.1.1.

The setup was used to measure single molecule fluorescence spectra of Doxorubicin inside the thin films for the mobile and the immobile population (Figure 4.14 a). To measure mobile molecules the laser light was focused onto a position in the film, where no immobile molecules were present. During the measurement from time to time mobile molecules diffused through the confocal volume and could then be observed. Molecules from the two populations showed characteristic but distinct spectra. The spectrum of the immobile molecules (black line) shows a peak at 667 nm, whereas the spectrum of the diffusing population (red line) is blue-shifted with a maximum at 591 nm. Moreover, the mobile molecules are by a factor of  $\sim 2$  brighter in intensity than the diffusing molecules. These distinguishable spectra could originate from differences in the local environment for the two populations or from intrinsic differences arising directly from the Doxorubicin molecules. In order to clarify this further, single molecule spectra of Doxorubicin deposited on a glass cover slip and coated with PVA were recorded. This sample artificially creates a situation where all molecules are attached to the silica surface and are immobilized. Again, two spectral populations can be found (see Figure 4.14 b). Their maxima are 604 nm and 645 nm respectively. The spectral positions and the relative intensities of the populations vary slightly compared to the data of Figure 4.14 a. However, this is not surprising due to the different local environment. Nevertheless, the presence of again two populations indicates that the origin of the spectral difference is associated with the Doxorubicin molecules itself. If this proves true, maybe fluorescence spectra of Doxorubicin in solution can contribute to a better understanding of the underlying phenomenon. Consequently, such fluorescence spectra were recorded, starting with a saturated aqueous solution down to a highly diluted aqueous solution of single molecule concentration (Figure 4.14 c). This is the first time that fluorescence spectra of Doxorubicin in such diluted samples have been acquired. At high concentrations (from  $10^{-2}$  mol/L down to  $10^{-6}$  mol/L) the spectrum is blue-shifted with a major band at 600 nm. At a concentration of  $10^{-7}$  mol/L the spectrum gets shifted to the red with a peak at 645 nm. This change in spectrum is attributed to aggregation. The spectrum peaked at 600 nm thus corresponds to the Doxorubicin dimer and the red-shifted peak at 645 nm characterizes the Doxorubicin monomer. Based on these experimental findings, the results indicate that the blue-shifted spectra of mobile molecules, detected on glass and inside the mesoporous films can be assigned to Doxorubicin dimers. Further, the red-shifted immobile molecules are Doxorubicin monomers. This assignment also explains why on the single molecule level the immobile molecules far exceed the number of mobile aggregates. The high degree of immobility does not negatively influence the ability of

### 4.3 Nano-structured silica materials for drug-delivery of the anti-cancer drug Doxorubicin

mesoporous silica as drug-delivery structure since for clinical applications the drug will be present in ensemble concentration and thus mainly in the form of mobile aggregates. This mobility, of course, is an essential prerequisite for an efficient release from the delivery system. Nevertheless, it is noteworthy and counter-intuitive that the dimers are mobile even though they are larger in size. The dimerization process could lead to an increase of internal hydrogen-bonding with the oxygen atoms in the silica walls, reducing the attractive interactions between drug and host. The structurally related cytostatic Actinomycin D indeed aggregates to inverted dimers.<sup>165</sup>

These experiments prove the high potential of single molecule approaches for the investigation of such materials, since ensemble averaging would not have revealed these details.

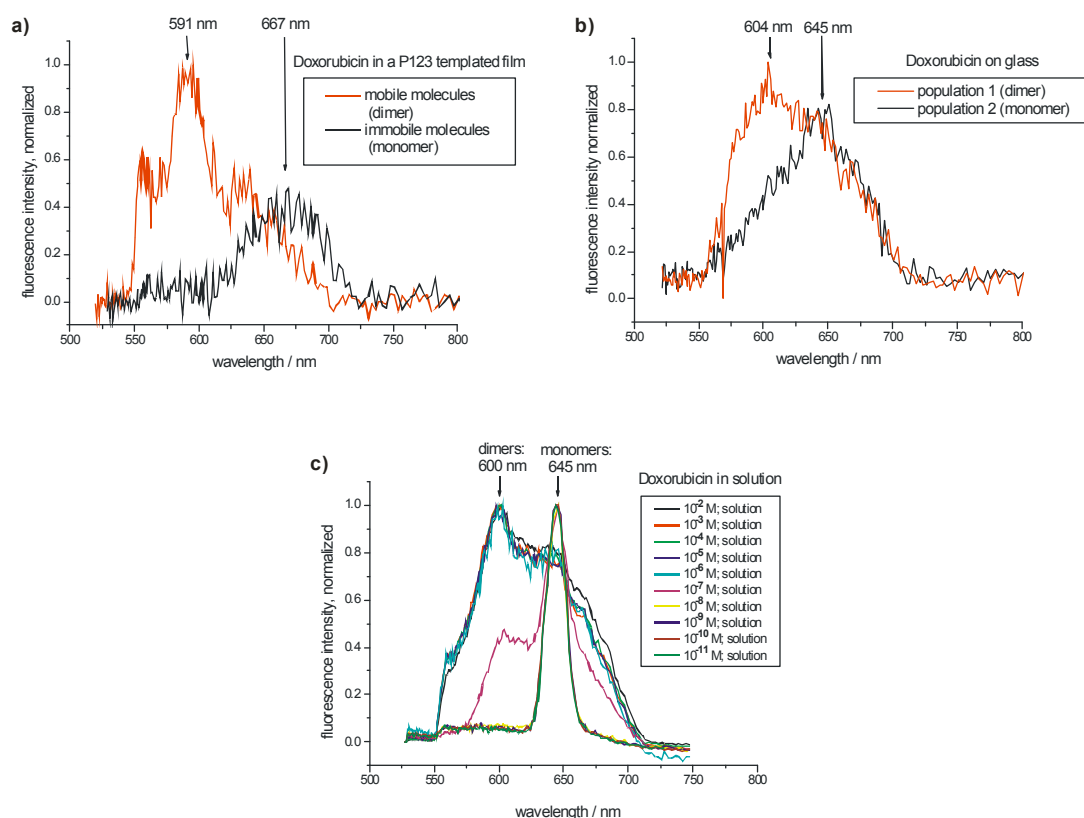


**Figure 4.14: Single molecule and ensemble fluorescence spectra of Doxorubicin.** The spectra are normalized and plotted with their relative intensities. For each population given in (a+b) the displayed spectra are averaged out of ten single molecule spectra. a) Spectra of the two populations of mobile (red) and immobile (black) molecules inside a Pluronic P123 templated film. The peaks are centered at 591 nm (mobile molecules) and 667 nm (immobile molecules) respectively. b) Average of ten single molecule spectra of Doxorubicin on glass. Two distinct populations of 604 nm (red) and 645 nm (black) can be distinguished. c) Fluorescence spectra

of Doxorubicin in aqueous solution from saturated concentration ( $10^{-2}$  mol/L) to single molecule concentration ( $10^{-11}$  mol/L). At concentrations above  $10^{-6}$  mol/L the main peak of the spectrum is situated at 600 nm. Around  $10^{-7}$  mol/L the spectrum gets red-shifted with a main peak at 645 nm.

We now understand the underlying reasons for the appearance of a mobile and immobile population. Next, the dynamics of the mobile drug shall be characterized further. Therefore, molecular trajectories are extracted from the recorded movies of Doxorubicin diffusing inside a P123 templated thin silica film. A typical trajectory is given in Figure 4.15 a. The drug molecules can diffuse throughout the porous network either along one pore or from one pore to neighbouring pores *via* defects, *i.e.* openings in the channel walls. The trajectory appears not very well structured. This is simply due to the small domain size inside these P123 templated structures and does not affect their drug-delivery applicability.

In contrast, highly structured trajectories were obtained for the mobile population in CTAB templated mesoporous thin films. Figure 4.15 b displays such a trajectory of a single Doxorubicin molecule, revealing the large linear domains inside these materials.<sup>95</sup> The domain size in the CTAB templated samples is significantly larger than in the above discussed P123 templated samples. Thus the trajectory is quite linear in contrast to the trajectory of Figure 4.15 a. In the CTAB templated samples mobile and immobile molecules were found with a ratio of about 1:9.

Surprisingly, for the unfunctionalized Brij-56 templated thin films the evaluation of the recorded movies shows that all molecules are immobile. Figure 4.15 c displays an exemplary single molecule "trajectory" of Doxorubicin inside an unfunctionalized Brij-56 templated film. The "trajectory" consists of a blue spot, displaying the immobility of the molecule. This observed immobility is attributed to strong adsorption of the Doxorubicin to the hydroxyl groups in the channel walls. Recent work has shown that those hydroxyl groups can indeed present adsorption sites.<sup>92, 95</sup> They could interact *via* hydrogen bonding with the numerous oxygen atoms in the Doxorubicin molecule (see Figure 4.13 b). In contrast, in the P123 templated samples the drug has more space to move since the pore-to-pore distance is increased by a factor of 1.6 compared to the unfunctionalized Brij-56 channel network. This apparently reduces the influence of the adsorption sites resulting in a mobile population. Interestingly, also in the CTAB templated samples with a narrow pore-to-pore distance of 4.4 nm a mobile population of Doxorubicin was found. There are several effects that can

contribute to the observed mobility in this system. The adsorption sites are shielded by the ionic template, which electrostatically saturates the channel surface and thus suppresses their capability of forming hydrogen bonds with the drug. Pluronic P123 and Brij-56 are non-ionic templates that cannot effectively shield the hydroxyl groups. The effect of ionic shielding can be important, since from other experiments with varying sodium chloride ion concentration inside the channels of mesoporous silica it is well-known that an increase in ion concentration can lead to an increase in drug diffusivity.

A mobile population can be recovered also for the Brij-56 templated samples by chemically modifying the walls with propyl functional groups. This leads to a hydrophobization of the pore inner surface through a shielding of the hydroxyl groups, resulting in weaker interactions between the drug and the host matrix. We recently found that propyl-functionalization increases the diffusivity of guest molecules inside mesoporous films compared to unfunctionalized films.<sup>163</sup> In the Brij-56 templated propyl-functionalized mesoporous film mobile and immobile molecules are observed with a ratio of  $\sim 1:9$ . A single molecule trajectory of a mobile molecule is displayed in Figure 4.15 d. The well-structured trajectory clearly maps the domains of parallelly aligned pores in channel network.<sup>93, 94</sup>

In order to quantitatively compare the dynamics of the drug in the four different nanostructures the mean square displacement (MSD) curves for the individual Doxorubicin molecules inside the different samples were evaluated (Figure 4.15 e) and a diffusion coefficient  $D$  for the individual Doxorubicin molecules as well as a mean diffusion coefficient  $\langle D \rangle$  for the entire population can be calculated assuming a 1D random walk for CTAB templated samples and a 2D random walk for Brij-56 and P123 templated samples (for details see Eq. 3.4).

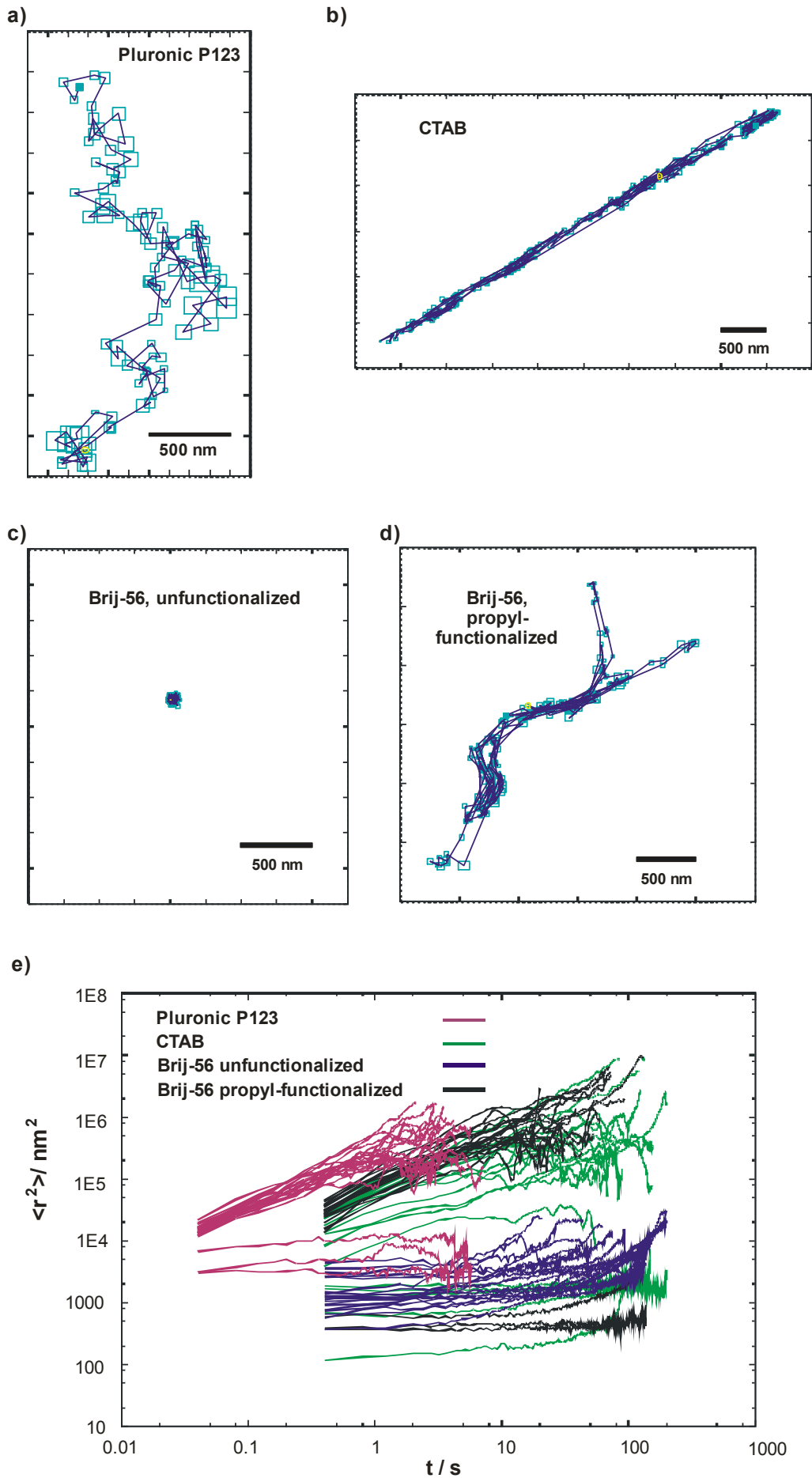


**Figure 4.15: Single molecule diffusion of Doxorubicin in nanoporous silica structures.** Exemplary trajectory of a drug molecule inside a a) Pluronic P123, b) CTAB, c) unfunctionalized Brij-56 and d) propyl-functionalized Brij-56 templated film. The small blue squares indicate the positioning accuracy for each point in the trajectory, which depends on the signal-to-noise ratio ( $\sim 60$  nm for P123,  $\sim 35$  nm for CTAB and  $\sim 40$  nm for Brij-56 templated samples). While in a), b) and d) the molecules are mobile, c) depicts an immobile molecule appearing as a spot. e) Mean square displacement (MSD) as a function of time. Each line displays a MSD curve for a single Doxorubicin molecule. For the unfunctionalized Brij-56 sample (blue) only a single population of immobile molecules can be found. The CTAB (green), propyl-functionalized Brij-56 (black) and the Pluronic P123 samples (pink) show two distinguishable populations of mobile and immobile molecules. In each of the series at least 20 molecules were evaluated. Only a selected number of MSD curves for immobile molecules has been plotted for clarity, thus the graph does not represent the real number ratio of immobile to mobile molecules.

For the CTAB templated samples (green lines in Figure 4.15 e), the two observed populations can be clearly distinguished: the immobile molecules show a constant MSD, as expected for a zero diffusion coefficient, whereas the diffusion dynamics of the mobile molecules is characterized by a MSD growing linearly with time. By averaging the single molecule diffusion coefficients, we compute the mean-diffusion coefficient for the entire mobile population as well as its standard deviation, giving  $\langle D_{CTAB} \rangle = 2.0 * 10^4 \text{ nm}^2/\text{s} \pm 2.3 * 10^3 \text{ nm}^2/\text{s}$ . The determined deviation is caused by the inherent structural heterogeneity of the samples.

The mean diffusion coefficient for the mobile population of the Pluronic P123 templated samples (pink lines in Figure 4.15 e) can be obtained as  $\langle D_{P123} \rangle = 5.4 * 10^4 \text{ nm}^2/\text{s} \pm 9.7 * 10^3 \text{ nm}^2/\text{s}$ . This increase by a factor of 2.7 compared to the CTAB samples can be explained by the increased pore-to-pore distance (from 4.4 nm to 10 nm, see Table 4.5) and differences in the interactions between the drug and the different templates.

As expected the MSDs for all molecules in the unfunctionalized Brij-56 templated films (blue lines in Figure 4.15 e) are constant since the molecules are immobile.

For the mobile population in the propyl-functionalized Brij-56 templated samples (black lines) a mean diffusion coefficient  $\langle D_{Brij-propyl} \rangle = 1.6 * 10^4 \text{ nm}^2/\text{s} \pm 1.9 * 10^3 \text{ nm}^2/\text{s}$  was determined, a  $\sim 3.4$ -fold reduction compared to the Pluronic-templated samples. This can be rationalized as the pore-to-pore distance is significantly smaller compared to P123 templated channels ( $a_0$  is reduced by a factor of  $\sim 2$ , see Table 4.5), and the introduction of propyl groups inside the pore additional to the template further reduces the volume for the molecule to move.

This is the first time that a clinically relevant cytostatic has been monitored during its motion inside a nanoporous delivery system on a single molecule level. The data of Figure 4.15 clearly demonstrate the benefits of a single molecule approach to this study, as the different populations would have been obscured by the inevitable averaging associated with ensemble methods. It could be shown that pore diameter control and pore functionalization offer possibilities to fine-tune host-guest interactions and are therefore also important techniques for controlling the dynamics of drug release. The existence of only 5-10% mobile molecules and up to 95% immobile molecules under single molecule conditions does not affect the efficiency of mesoporous silica as drug carrier, since the data of Figure 4.14 shows that during medical applications, where Doxorubicin is present in high ensemble concentrations, the drug appears in the form of mobile dimers. Consequently, the drug should be released efficiently from the delivery system. This assumption can be tested with the following experiment, where the drug release kinetics from the delivery structure is characterized.

### 4.3.3 Characterization of the drug release kinetics

Pluronic P123 templated mesoporous films were loaded with Doxorubicin (Doxorubicin concentration in the synthesis solution  $\sim 10^{-4}$  mol/L) in order to determine the drug release kinetics. The P123 templated structures were chosen for this experiment because Pluronic is well-known as biocompatible micellar nanocarrier for pharmaceuticals, such as Doxorubicin.<sup>118</sup> Figure 4.16 a schematically represents the sample setup for the release and live-cell measurements. A coverslip with the Doxorubicin loaded mesoporous structure was mounted with a magnet inside the top cover of a  $\mu$ -Dish (ibidi, ibiTreat, 35 mm, high) directly above HeLa cells and cell-medium. For the experiments HeLa cells (HeLa ACC57, DSMZ, Braunschweig, Germany) grown in Dulbecco's modified Eagle's medium (DMEM) with Ham's Nutrient Mixture F12 supplemented with 10% fetal calf serum at 37 °C in 5% CO<sub>2</sub> humidified atmosphere were utilized. Cell culture, fetal calf serum and PBS buffer were purchased from Invitrogen GmbH (Karlsruhe, Germany). Upon removing the magnet on the upper side of the cover (see Figure 4.16 a), the cover slip is immersed into the cell medium. The solution enters the pores and triggers the Doxorubicin release from the mesoporous system. The increase in fluorescence intensity of Doxorubicin in the cell-medium 50  $\mu$ m above the bottom of the  $\mu$ -

### 4.3 Nano-structured silica materials for drug-delivery of the anti-cancer drug Doxorubicin

Dish was monitored with a confocal microscope (for details see Chapter 4.3.2). During the measurement the sample was stirred to guarantee a homogeneous distribution of the Doxorubicin molecules released into solution.

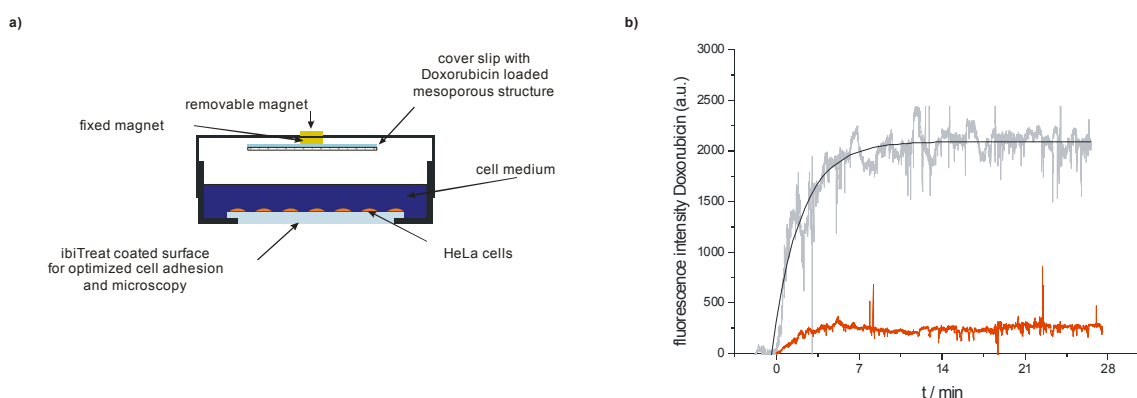


**Figure 4.16: Drug release characterization.** a) Sample setup. The sample consists of a  $\mu$ -Dish with cell medium and HeLa cells adhered to the bottom of the dish. On the upper side of the dish, a coverslip with a Doxorubicin-loaded mesoporous structure is held using magnets. Upon removing the magnet, the sample is immersed into the cell medium, which can flush the pores of the delivery system and trigger the drug release. b) Release kinetics of Doxorubicin from a Pluronic P123-templated thin film. The release was monitored via the rise of fluorescence intensity of Doxorubicin 50  $\mu\text{m}$  above the bottom of the  $\mu$ -Dish during time (grey curve). The black line shows an exponential fit to the data according to Eq. 4.24. For an unfunctionalized Brij-56 templated film, where all molecules are immobile, no significant increase in Doxorubicin fluorescence (red) can be detected.

However, this fluorescence increase can only then serve as a characteristic parameter for the release of the drug from the delivery system if the amount of Doxorubicin detaching from the film surface is negligible. Hence, the drug-loaded films were washed after synthesis in order to remove loosely bound drug from the surface. After that, a quenching experiment was used to test that the remaining molecules are incorporated in the porous network of the film. The quencher QSY 21 (Invitrogen, non-fluorescent quencher, absorption maximum: 660 nm) was used to quench Doxorubicin fluorescence. QSY 21 is non-fluorescent and only contributes a low heterogeneous background to the measurement. Movies were acquired on the wide-field microscope described in Chapter 4.3.2 with an integration time of 800 ms per image. Figure 4.17 displays images from different movies acquired through summing up all individual frames of the movie. Figure 4.17 a shows the fluorescence of Doxorubicin molecules in aqueous solution attached to a glass surface. Their fluorescence can clearly be seen. The molecules obviously tend to form large aggregates. The corresponding movie shows the molecules, as expected, fluorescent, blinking and bleaching due to the laser excitation. Figure 4.17 b shows

the same sample after adding the quencher to the solution. The majority of the drug molecules are quenched! Figure 4.17 c shows a Doxorubicin loaded P123 templated film surrounded by water. The drug molecules can clearly be detected as individual fluorescent spots. In the movie they show the typical dynamics described in Chapter 4.3.2. After adding a quencher (Figure 4.17 d) the single drug molecules can still be detected. According to the movie drug diffusion dynamics is unchanged.

To summarize, Doxorubicin on a glass surface can be quenched. In contrast, the Doxorubicin fluorescence from the loaded mesoporous films was not quenched through exposition to QSY 21. This indicates that after washing the vast majority of Doxorubicin molecules are located inside the porous network of the delivery system. Consequently the increase in fluorescence measured with a setup depicted in Figure 4.16 a is a reliable parameter for the release of Doxorubicin.

Figure 4.16 b shows the increase of Doxorubicin fluorescence intensity (grey curve) measured from the P123 templated thin silica film. Within the first few minutes after adding the drug loaded cover slip to the cell-medium no Doxorubicin fluorescence could be detected. This is regarded to be the time the cell medium needs to flush the pores and trigger the drug release. Once the release has started ( $t = 0$ ) the Doxorubicin fluorescence rapidly increases. The data were fitted to the following exponential equation:

$$y = A * \left( 1 - \exp - \left( \frac{x}{t_r} \right) \right) \quad (4.24)$$

where the amplitude  $A$  corresponds to the maximum fluorescence intensity and  $t_r$  is the characteristic release time. The good agreement between the fit and the experimental data shows that the release follows a first-order kinetics. By averaging the release times from the experiments, the mean release-time  $\langle t_r \rangle = 3.2 \text{ min} \pm 0.8 \text{ min}$  can be obtained. After about 10 min most of the drug has been released. Thus, a drug incorporated in the delivery system can efficiently be delivered to the surrounding solution. After the release the thin film was still intact according to X-ray data (data not shown). Cauda *et al.* found a similar release kinetics for the antibiotic Vancomycin from mesoporous silica.<sup>58</sup> For an unfunctionalized Brij-56 templated film, where all molecules are immobile (see Figure 4.16 b), no significant increase in Doxorubicin fluorescence and thus no drug release can be detected into the cell-medium. Therefore, we can conclude that the diffusion dynamics within the film directly affects the

### 4.3 Nano-structured silica materials for drug-delivery of the anti-cancer drug Doxorubicin

---

release kinetics from the film. It is the first time in this work that evidence could be provided for a direct relation between the diffusion dynamics in the film and release kinetics off the film. This correlation is of paramount importance, when pore functionalizations and variations in the pore sizes and topologies shall be used to create a depot-effect for the drug.

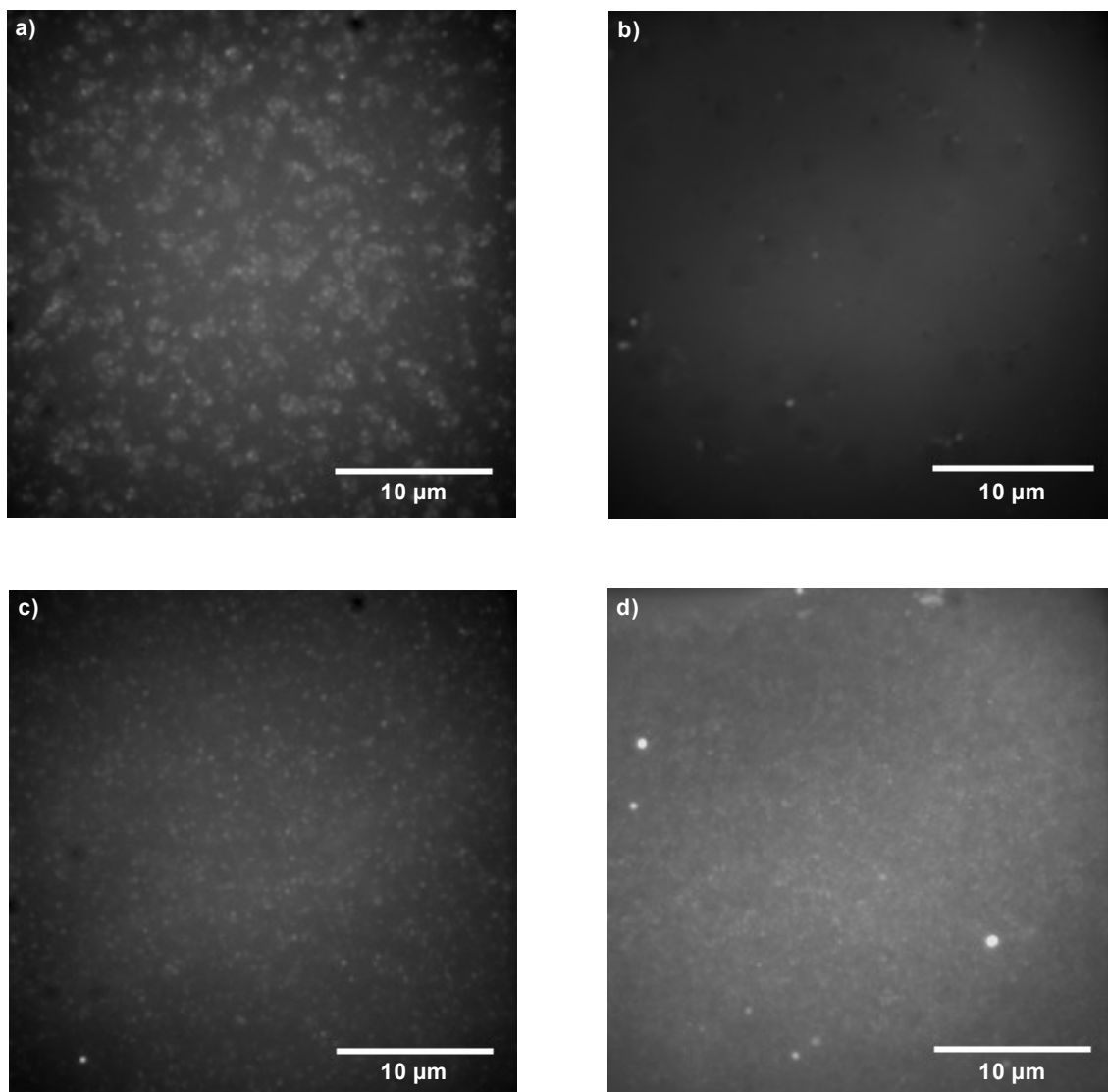


**Figure 4.17: Doxorubicin quenching experiment.** Images obtained through summing up all individual frames in movies recorded on a wide-field setup. The images show a) Doxorubicin molecules in aqueous solution attached to a glass surface, b) the sample displayed in a) after adding the quencher QSY 21. The Doxorubicin fluorescence is nearly totally quenched. c) a Doxorubicin loaded P123 templated film surrounded by water and d) the mesoporous thin film depicted in c) after adding QSY 21. The doxorubicin molecules remain fluorescent.

In this context, it should be indicated that throughout this study the exits of the mesoporous channel network were not closed with caps. Yet, for therapeutic applications capping the pores in order to prevent an early release of the drug from the delivery system prior to reaching the target-site can become necessary. To realize this, different capping strategies have been developed recently. Schlossbauer *et al.* have introduced biotin-avidin as enzyme-responsive cap system for mesoporous silica.<sup>124</sup> This cap system opens through protease-triggered hydrolysis of the avidin. Furthermore, a pH-sensitive gating system has been reported by Cauda *et al.*<sup>125</sup> Besides that a programmable DNA-based molecular valve was suggested recently for capping mesoporous silica.<sup>126</sup> Additionally, CdS nanocrystals have been used as caps on mesoporous silica *e.g.* for the controlled release of neurotransmitters.<sup>43</sup> In this case, cap opening is stimulated by reducing agents. In a further approach by Giri *et al.* magnetic nanoparticles have been employed to cap mesoporous silica nanostructures.<sup>46</sup> Thus, combining the drug-loaded mesoporous structures with one of the above discussed capping approaches can add a further functionality to these drug-delivery systems.

#### 4.3.4 Live-cell measurements for testing the applicability of the delivery system

Next, the effect of the delivered Doxorubicin onto HeLa cells is investigated in order to test the applicability of the delivery system together with living cells. Figure 4.18 shows overlays of confocal transmission images (grey) and fluorescence images of the Doxorubicin fluorescence (red). According to their shape the HeLa cells were alive before being exposed to Doxorubicin (Figure 4.18 a). The transmission image shows the adhered cells on the bottom of the  $\mu$ -Dish. No Doxorubicin fluorescence was detected at this stage of the experiment. After  $t = 60$  min Doxorubicin fluorescence could clearly be located inside the cell nucleus (Figure 4.18 b). This can be rationalized as the cytostatic properties of Doxorubicin mainly arise from direct intercalation into DNA as well as inhibition of topoisomerase II by interfering with the topoisomerase II-DNA complex.<sup>166</sup> However, the cells still appear to be alive according to the transmission image. After  $t = 24$  h the cells were highly fluorescing (Figure 4.18 c), showed a round shape and had detached from the bottom of the  $\mu$ -Dish, indicating cell death. These effects are caused by the drug itself, as demonstrated by control experiments with a

### 4.3 Nano-structured silica materials for drug-delivery of the anti-cancer drug Doxorubicin

Doxorubicin-free delivery system (Figure 4.18 d). This proves that Doxorubicin released from thin films is still cytostatic. The Doxorubicin does not degenerate through incorporation into the delivery structure and is still able to efficiently kill cancer cells. The anti-cancer drug can thus in principle be applied in combination with this mesoporous carrier for drug delivery purposes.

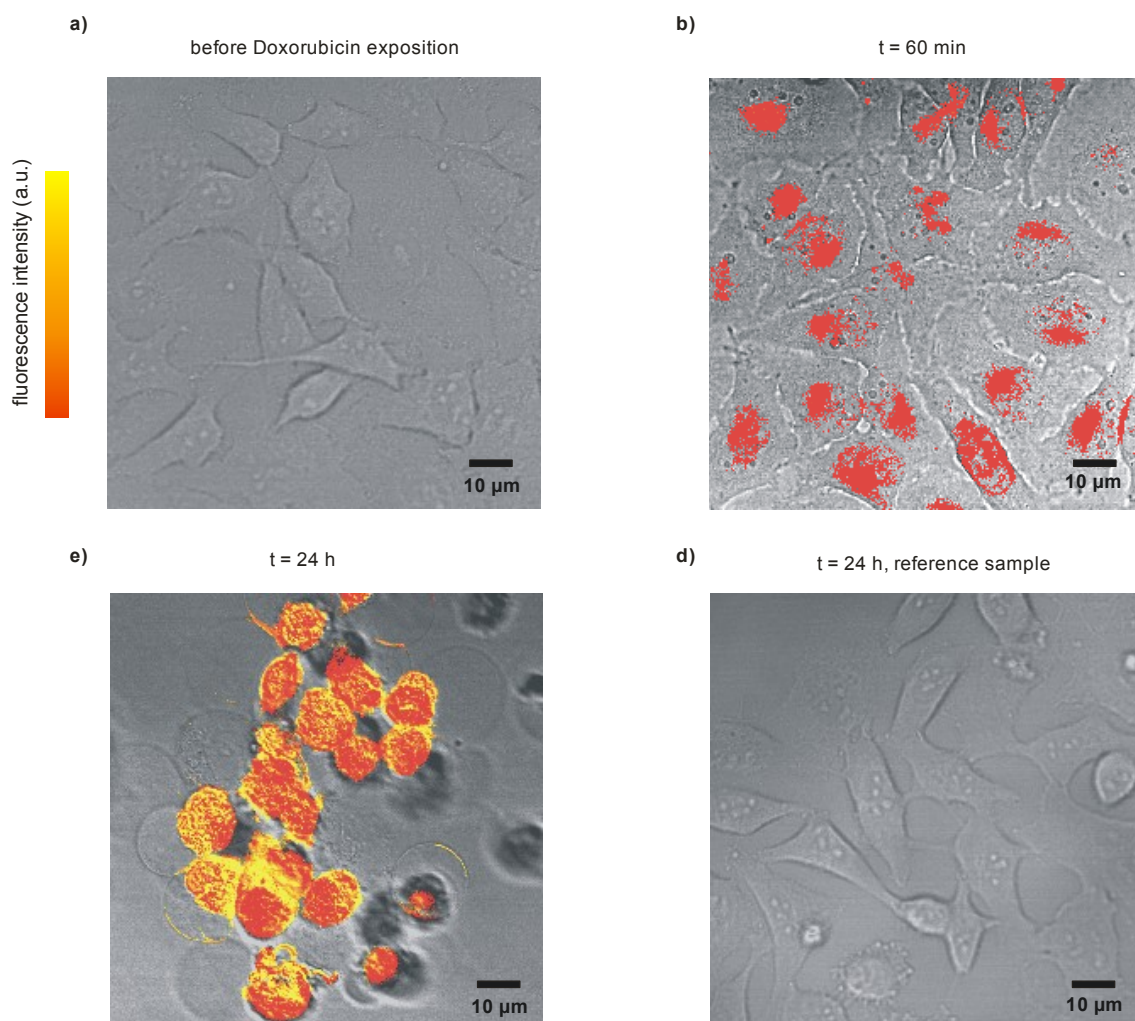


**Figure 4.18: Live-cell measurements.** Overlay of confocal transmission images (grey) and Doxorubicin fluorescence (red). Images a) before, b) 60 min and c) 24 h after adding the Doxorubicin-loaded delivery system are shown. d) Image recorded 24 h after adding an unloaded delivery system as reference.

### 4.3.5 Conclusion

In conclusion, it was demonstrated that mesoporous thin films with nanometer-sized pores can be used as drug-delivery system for the cytostatic Doxorubicin. The single molecule approach utilized in this study offers detailed mechanistic insights into the complicated host-guest interplay. It was shown how the interaction of the drug with the host-matrix can be influenced on a nanometer-scale via covalently attached organic functional groups. Such fine-tuning of the host-guest interaction is an essential prerequisite for generating a depot-effect. Furthermore, it was successfully demonstrated that the drug can be loaded and released from the nanometer-sized channels in the carrier system and can be taken up by cells. The live-cell measurements proved that the drug retains its cytotoxicity. It does not degrade inside the silica carrier structure and can efficiently kill malign cells after being released.

This study outlines several interesting concepts for future drug-delivery applications of mesoporous structures. Mesoporous silica could either be utilized in the form of drug loaded nanoparticles, for example in cancer therapy. Moreover, drug carrying thin silica films could directly be applied as implants in order to coat tumor tissue or wounds resulting from tumor resections. Hence, a wide range of applications utilizing very different drugs is within the scope for this novel class of delivery systems.

## 4.4 Silica films and particles with nanometer-sized channels for siRNA and DNA delivery

The last study presented in this chapter deals with drug-delivery strategies in gene therapy, gene silencing and RNA interference. These fields in biomedicine showed a tremendous evolution within the last decade since they offer various novel and intriguing therapeutic tools. Gene therapy, for example, refers to a therapeutic approach for treating diseases, such as hereditary diseases, through the insertion of genes and replacing deleterious mutant genes with functional genes. Related to gene therapy is the so-called gene silencing, which denotes the switching-off of genes in general. Historically, gene silencing was first observed on plants in the late 1980s, where Matzke *et al.* found that a cloned gene incorporated into the genome, a so-called transgene, cannot only stimulate but also suppress gene activity of homologous sequences.<sup>167</sup> This phenomenon was called homology-dependent gene silencing. In the 1990s, it became clear that gene-silencing can be done through histone modification (transcriptional gene-silencing)<sup>168, 169</sup> or through insertion of microRNA (miRNA) or small interfering RNA sequences (siRNA, double stranded, usually 20 – 25 base-pairs (bp) in length) as so-called post-transcriptional gene-silencing.<sup>170-173</sup> The breakthrough for understanding gene-silencing came with the experiments of Andrew Fire and Craig Mello in 1998 in the worm *Caenorhabditis elegans*.<sup>34</sup> They discovered that only short double-stranded RNA (siRNA) led to an efficient silencing of the target messenger RNA (mRNA). For this unknown mechanism they introduced the name RNA interference (RNAi).<sup>174</sup> In the subsequent years the number of publications in the field dramatically increased and through a long row of successive findings a complete understanding of the mechanism of RNAi could be achieved.<sup>175-185</sup> RNAi describes in detail how genes can be regulated in eucaryotes, including mammals. This discovery of RNA interference was awarded the Nobel Prize in Physiology or Medicine 2006. In its press release the Nobel Committee specifically acknowledged the new opportunities in health care and clinical medicine created by this discovery.<sup>35</sup>

To summarize, gene therapy and gene silencing could pave the way for the treatment of so far incurable diseases, especially concerning the high number of hereditary diseases stemming from gene defects.

However, the fragile oligonucleotides used in gene therapy and RNA interference need smart delivery strategies in order to reach their target-site within the cell. In gene therapy for example the DNA needs to be transported into the cell nucleus, whereas the siRNA used in post-transcriptional gene silencing only needs to be delivered to the cytosol. Due to the different target-sites and the biochemical challenges involved in targeting a distinct site within a cell, there is a constant need for new efficient ways of delivering oligonucleotides. Recent work, *e.g.* by Mok *et al.*,<sup>186</sup> shows that high efforts are necessary to guarantee a safe and efficient delivery of the fragile oligonucleotides. This delivery problem is currently the major hurdle to clinical applications.

This is exactly where mesoporous silica nanoparticles and films enter the stage. In the previous chapters of this work we have learnt much about the versatility of mesoporous silica. Additionally, a recent study by Hom *et al.* showed that mesoporous silica nanoparticles can be used to facilitate the delivery of siRNA in order to shutdown signalling pathways in mammalian cells.<sup>187</sup> Hence, the following study is assessing the applicability of these smart hybrid materials as novel delivery system for gene therapeutics.

#### **4.4.1 Introduction to the sample systems: preparation and characterization**

Two different host morphologies were investigated with respect to their applicability as drug-delivery systems for siRNA and DNA. Firstly, mesoporous thin silica films with template containing pores were tested since they proved very useful as drug-delivery systems in the previous chapters. Secondly, mesoporous SBA-15 silica particles with large template-free pores were investigated. This morphology was used since a particle-based approach may be even closer to a real application of mesoporous silica for the delivery of a gene therapeutic. The synthesis protocols for both sample types are given below. The sample synthesis and characterization described in this subsection was done by A. Schlossbauer in the group of Prof. T. Bein (Ludwig-Maximilians-University Munich, Germany).

The thin mesoporous silica films were prepared with the surfactant Brij-56 without any additional functionalization inside the pores exactly following the recipe for unfunctionalized

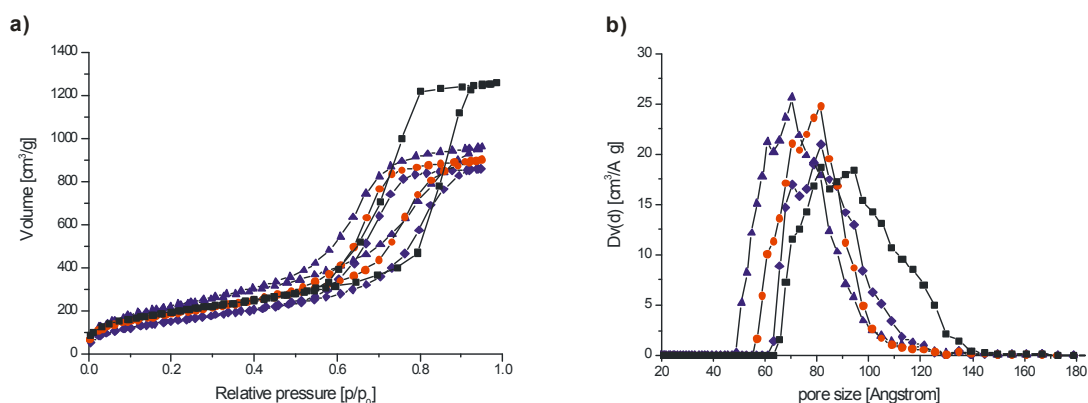
films introduced in Chapter 4.2.1. The film synthesis yields very reproducible thin hexagonal films of good quality. The 1D-Xray characterization is equivalent to the data presented in Chapter 4.2.1.

The large pore SBA-15 spherical particles were synthesized following a procedure generally introduced by Katiyar *et al.*<sup>65</sup> and later used by Schlossbauer *et al.*<sup>188</sup> for producing mesoporous silica spheres as a matrix for biofunctionalization (see Chapter 2.3 for an introduction to the SBA-15 particles). The surfactant Pluronic P123 (3.0 g, poly(ethylene oxide)<sub>20</sub>-poly(propylene oxide)<sub>70</sub>-poly(ethylene oxide)<sub>20</sub>) was used dissolved in hydrochloric acid (60 mL, 1.5 molL<sup>-1</sup>). As a co-surfactant Cetyltrimethyl ammonium bromide (CTAB, 0.6 g) was used in combination with 1,3,5-trimethylbenzene (TMB, 0.3 g) as a swelling agent to increase the pore diameter. CTAB and TMB were mixed with 25 mL of distilled water. After combining the aqueous solution with the acidic solution, ethanol (pure, 20 mL) was added under stirring. Subsequently, tetraethyl orthosilicate (TEOS, 10 mL) was added dropwise. The resulting mixture was stirred vigorously (500 rpm) at 35 °C for 45 min before being transferred into an autoclave (Parr Instrument Company, Moline, Illinois, USA) for hydrothermal treatment at 75 °C for 12 hours under static conditions. Subsequently, the mixture was aged at 125 °C for 12 h. The resulting white powder was filtered out, washed with distilled water (100 mL) and ethanol (pure, 100 mL) and dried at 60 °C for another 12 h. For the synthesis of functionalized silica particles, a certain molar fraction (up to 10 mol %) of the silica source (TEOS) was replaced with a functionalized silica source. The functionalized silica precursors were: H<sub>2</sub>NC<sub>3</sub>H<sub>6</sub>Si(OC<sub>2</sub>H<sub>5</sub>)<sub>3</sub> for aminopropyl-, C<sub>6</sub>H<sub>5</sub>Si(OC<sub>2</sub>H<sub>5</sub>)<sub>3</sub> for phenyl- and CNC<sub>3</sub>H<sub>6</sub>Si(OC<sub>2</sub>H<sub>5</sub>)<sub>3</sub> for cyanopropyl-functionalization. Four different modifications of SBA-15 materials were synthesized: (i) an unfunctionalized SBA-15, (ii) a cyanopropyl-functionalized (10 mol %) SBA-15, (iii) an aminopropyl- (8 mol %) and cyanopropyl- (2 mol %) functionalized SBA-15 and (iv) an aminopropyl- (5 mol %) and phenyl- (5 mol %) functionalized SBA-15.

Extraction of the organic template from the SBA-15 materials was performed by heating 1 g of the white powder twice under reflux at 90 °C for 30 min in 100 mL of a solution containing concentrated hydrochloric acid (10 mL) and ethanol (90 mL). The SBA-15 material was separated by filtration and washed with ethanol (100 mL) after each extraction step. The template extracted samples were obtained as white solid powders.

The SBA-15 material was characterized via Nitrogen sorption isotherms, 1D X-ray diffractometry and Scanning Electron Microscopy (SEM).

Figure 4.19 a shows the obtained isotherms of the different materials. Nitrogen sorption measurements were performed on a Quantachrome Nova 4000e instrument. The isotherms reveal the porosity of the materials. Furthermore, the pore size distributions can be extracted (Figure 4.19 b). All synthesized SBA-15 materials possess a porous network that is accessible from the outside.



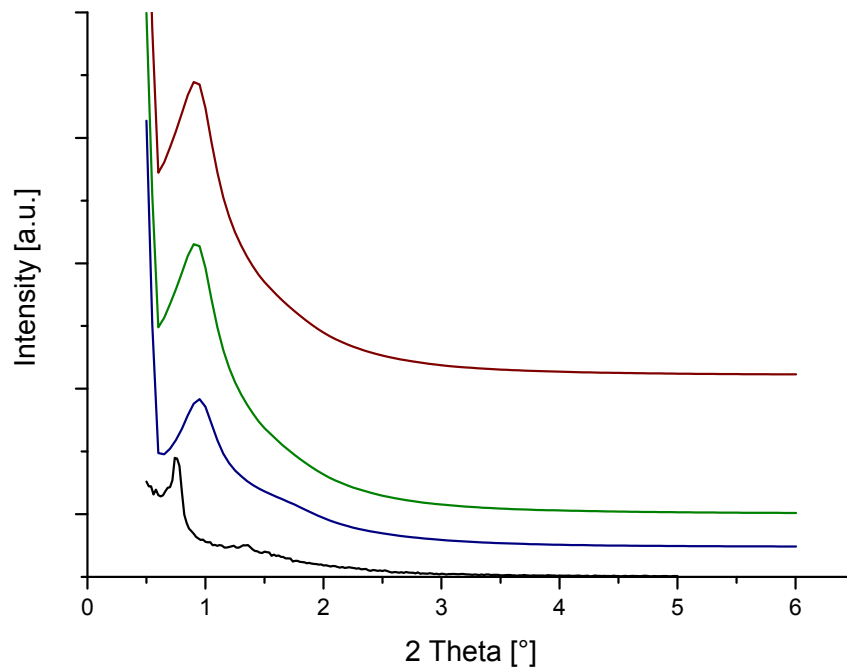
**Figure 4.19: Nitrogen sorption isotherms and pore size distribution.** The nitrogen sorption isotherms (a) and the pore size distribution (b) for the different SBA-15 materials synthesized. The colour code for both diagrams: cyanopropyl-functionalized (violet diamond), aminopropyl-/cyanopropyl-functionalized (blue triangle), aminopropyl-/phenyl-functionalized (red circle) and unfunctionalized (black rectangle) SBA-15 material.

Table 4.6 summarizes the data extracted from the nitrogen sorption characterization. It can be clearly seen that the introduction of functional groups diminishes the available pore size and volume compared to an unfunctionalized sample.

**Table 4.6: Nitrogen sorption characterization data.** The pore size, the BET surface<sup>66</sup> and the pore volume are calculated.

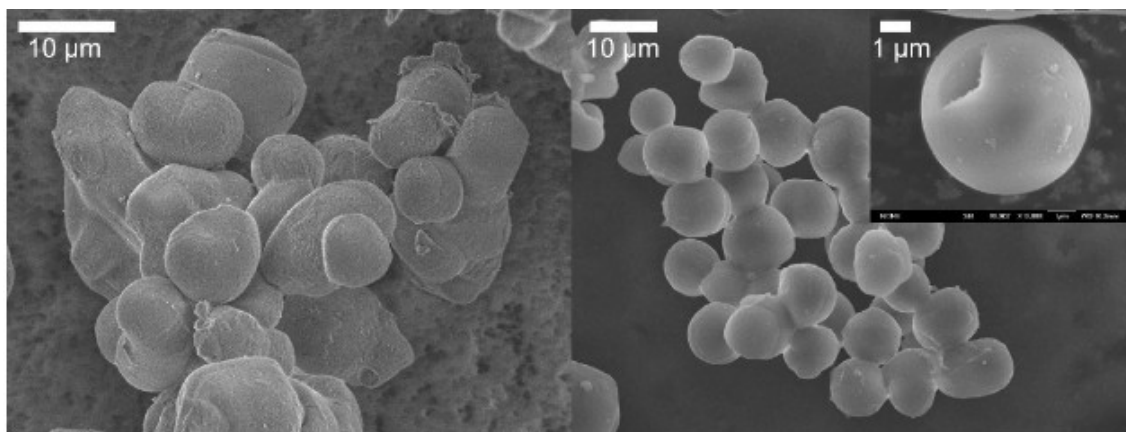
Functionalization	Pore size [nm]	BET surface [m <sup>2</sup> g <sup>-1</sup> ]	Pore volume [cm <sup>3</sup> g <sup>-1</sup> ]
unfunctionalized	8.9	700	1.80
cyanopropyl (10 mol %)	8.2	580	1.27
aminopropyl and cyanopropyl (8 + 2 mol %)	7.2	815	1.33
aminopropyl and phenyl (5 + 5 mol %)	7.8	680	1.33

Figure 4.20 presents the 1D X-ray diffractograms of the different synthesized SBA-15 materials. The structure of the SBA-15 powders was determined by using a Scintag XDS 2000 powder diffractometer in  $\theta/\theta$  Bragg-Brentano scattering geometry. The data indicate that the mesoporous particles exhibit hexagonal order. The XRD data show that the introduction of functional groups leads to an increase in the  $2\theta$ -value and thus to a reduction of the pore-to-pore distance compared to unfunctionalized SBA-15. The term “pore-to-pore distance” used here in combination with XRD data is not identical to the term “pore size” used for discussing nitrogen sorption data, since with X-ray diffractometry only the distance between the different layers (one center of a pore to the center of the adjacent pore) can be calculated and no direct conclusion about the wall thickness can be drawn. In contrast nitrogen sorption methods directly yield the pore sizes. Nevertheless, the data of Table 4.6 and Figure 4.20 display the same trend, which is a reduction of the pore dimensions upon introduction of functional groups.



**Figure 4.20: 1D XRD diffractograms.** XRD data for unfunctionalized SBA-15 (black), aminopropyl- and phenyl-functionalized (5 + 5 mol %) (blue), cyanopropyl-functionalized (10 mol %) (green) as well as aminopropyl- and cyanopropyl-functionalized (8 + 2 mol %) (brown) SBA-15 particles. All samples exhibit 2D hexagonal order. The introduction of functional groups results in a higher  $2\theta$ -value and thus a smaller pore-to-pore distance.

Figure 4.21 displays SEM micrographs of the unfunctionalized SBA-15 material. SEM micrographs were recorded on a JEOL JSM-6500F scanning electron microscope. The image clearly reveals the morphology of the synthesized particles. They are spherically shaped and micrometer-sized. Further, we can see that the particles tend to aggregate. Similar data can be obtained for the differently functionalized particles investigated here as well.



**Figure 4.21: Scanning electron micrographs of the unfunctionalized SBA-15 material.** The synthesized particles are  $\mu\text{m}$ -sized, spherically shaped and tend to aggregate.

#### 4.4.2 Thin mesoporous silica films for the delivery of siRNA

In order to test the applicability of the Brij-56 templated thin mesoporous silica films as a carrier structure for gene delivery, siRNA was incorporated into the channels of the host material. The following siRNA sequence (20 bp) was added to the precursor solution for the thin film synthesis: 5' GGA CUC CAG UGG UAA UCU C TT ATTO647N 3'; 3' ATTO532 TT CCU GAG GUC ACC AUU AGA UG 5' (IBA GmbH, Göttingen, Germany). For the experiments the siRNA was added in single molecule concentration ( $\sim 10^{-10} - 10^{-11} \text{ molL}^{-1}$ ) since the previous chapters demonstrated that a single molecule approach can yield detailed mechanistic insights and reveal information that is not accessible by ensemble methods. The investigated Brij-56 templated films were not functionalized.

First, it needs to be ascertained whether the 20 bp siRNA tolerates the thin film synthesis conditions and remains intact after incorporation into mesoporous template containing silica. This is tested in the following way. The siRNA double-strand is labelled with a green (ATTO532) and a red (ATTO647N) fluorescent dye at the opposite sides (3' and 3' end) of the opposite strands. Figure 4.22 a displays a schematic of the siRNA double-strand that depicts the position of the dye labels (see above for the sequence of the siRNA). The distance between the two dyes is too high to show a significant amount of Förster Resonance Energy Transfer (FRET). Consequently FRET cannot be utilized for testing siRNA stability, however upon exciting the

dyes individually, a colocalization of the detected fluorescence signals of both dye labels indicates siRNA stability. The siRNA containing thin film is thus placed on a modified Laser Scanning Confocal Microscope (Zeiss LSM 410). High spatial resolution and detection efficiency were achieved with a high NA oil-immersion objective (Zeiss 40x/1.30 NA oil). The green fluorescent dye (ATTO532) was excited using a diode-pumped solid state laser (532 nm, Soliton, DLSOT-50, AlGaAs) and the fluorescence was detected using a dichroic filter (540 LP, AHF Analysentechnik, Tübingen, Germany) in combination with a fluorescence filter (675/250, Chroma Technology Corp, Bellows Falls, Vermont, USA). Fluorescence from ATTO647N was excited using a He-Ne gas laser (633 nm) and separated with the help of a dichroic mirror (Q 640LP, AHF) a notch filter (633 nm, Kaiser Optical Systems Inc., Ann Arbor, Michigan, USA) and an emission filter (HQ 720/150, AHF). The different dye labels were excited consecutively and the two images were overlaid. The fluorescence signal was detected on an APD (EG&G SPCM-AQ 141).

With this setup, the stability of siRNA inside the mesoporous Brij-56 templated film is tested compared to a reference sample (see Figure 4.22 b and c). A colocalization of a fluorescence signal in the green channel with a signal from the red channel indicates siRNA stability (under single molecule concentrations). However, this method only yields reliable information if the molecules do not diffuse in the time required to record both images. From previous measurements (data not shown), it is well-known that the observed molecules do not diffuse at low RH. The phenomenon of a reduced diffusivity at low RH was also described in Chapter 4.2.3. Consequently, all colocalization experiments discussed here were acquired at a RH below 10%, such that all molecules were immobile. Figure 4.22 b shows such an overlay image for siRNA inside the Brij-56 templated thin film. No colocalization of the red and the green fluorescence signals can be observed and thus the siRNA is not stable inside the mesoporous film. This shows that the siRNA is not double-stranded anymore. Whether the siRNA degrades further cannot be concluded from this measurement. The reference sample in Figure 4.22 c shows the same siRNA immobilized on Poly-L-Lysine. Colocalizing siRNA manifests itself through yellow spots created from an overlay of red and green fluorescence signals. A high degree of colocalization and thus intact siRNA can be found and the difference to Figure 4.22 b is clearly visible. This proves that the siRNA unfortunately degrades and the fluorescence signals observed in Figure 4.22 b must arise from dye containing fragments.

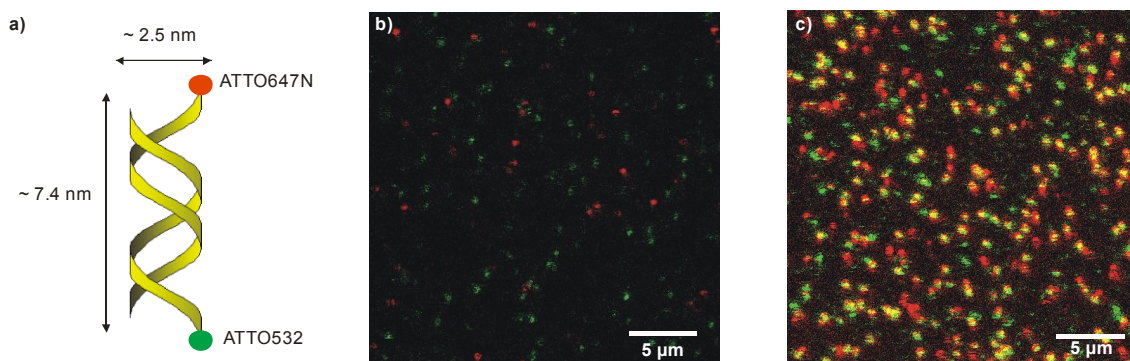


**Figure 4.22: Colocalization experiment for testing siRNA stability.** a+b) Overlay of the red and green fluorescence signal obtained after separate excitation with green (532 nm) and red (633 nm) laser wavelengths. a) siRNA inside the Brij-56 templated mesoporous silica film measured at a RH below 10%, where no siRNA dynamics is present. No colocalization of the signals can be observed. b) Reference sample: siRNA immobilized on Poly-L-Lysine. Intact siRNA gets visible through colocalization of the red and green fluorescence signals, thus yielding yellow spots. The numerous yellow signals indicate a high degree of siRNA stability.

In order to get more detailed insights into the process of siRNA fragmentation, movies of the diffusion of the fragments were acquired on the wide-field setup introduced in Chapter 4.2.2 for further data analysis. During these measurements, only the red fluorescent ATTO647N dye label attached to the siRNA was excited with a red He-Ne gas laser at 633 nm. According to the procedures described in Chapter 3.2.1.3, trajectories of the fragments can be obtained through SPT techniques (see Figure 4.23). The trajectory in Figure 4.23 a maps a fragment travelling throughout the porous network of the thin film thereby accessing different domains. Even more complex trajectories can be found, where the individual fragment shows very different modes of mobility (Figure 4.23 b). First, the fragment diffuses in a structured way throughout the porous channel network (red ellipse), then it suddenly diffuses randomly (green rectangle) and finally it gets trapped in the structure, for example at a defect or adsorption site, and is immobilized (yellow circle). During random diffusion the fragment moves either in unstructured defect regions of the mesoporous structure or on top of the film surface (see also the study of Kirstein *et al.*<sup>93</sup>).

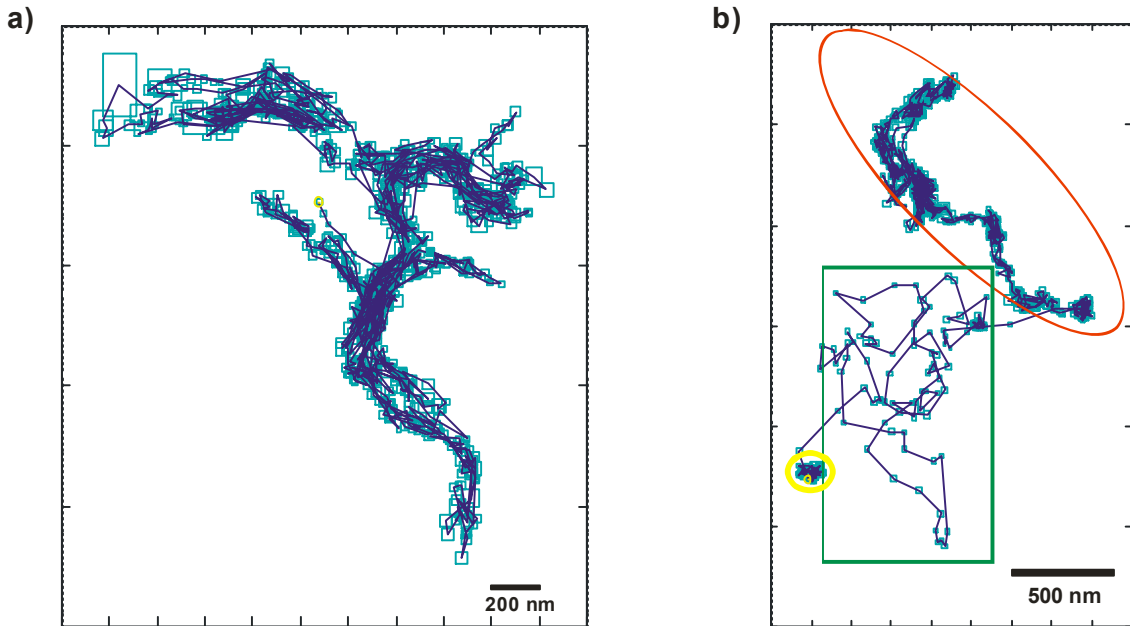


**Figure 4.23: Single molecule trajectories of fragments of siRNA.** a) The trajectory clearly maps the underlying porous network of the host structure. b) A more complicated trajectory showing: structured confined movement in the channel network (red ellipse), unstructured random diffusion in structural defects of the film or on top of the film surface (green rectangle) and immobile phase at the end (yellow circle).

The degree of siRNA degradation can be estimated with the help of the mean square displacement data extracted from the recorded movies (see Figure 4.24). Due to the above mentioned setup of the wide-field microscope, the trajectories displayed in Figure 4.23 do only display siRNA fragments containing an ATTO647N label. The MSD curves for these individual siRNA fragments were calculated and plotted *versus* time (green curves in Figure 4.24). In comparison, the diffusion dynamics of individual ATTO647N dye molecules embedded inside the same unfunctionalized Brij-56 templated films was measured and the corresponding MSDs were extracted accordingly (blue). If the siRNA degraded entirely only the remaining fluorescent label would be observed since the other species are non-fluorescent. In this case, the dynamics measured for the siRNA fragments should be identical to the dynamics measured for pure ATTO647N. However, the MSD plots of Figure 4.24 show that the ATTO647N molecules move faster compared to the siRNA fragments. This can be seen from the following mean diffusion coefficients that were calculated from the MSD curves assuming a 2D random walk:  $\langle D_{ATTO647N} \rangle = 1.5 * 10^3 \text{ nm}^2/\text{s}^2 \pm 8.1 * 10^2 \text{ nm}^2/\text{s}^2$  compared to  $\langle D_{siRNA \text{ fragm}} \rangle = 2.2 * 10^2 \text{ nm}^2/\text{s}^2 \pm 1.1 * 10^2 \text{ nm}^2/\text{s}^2$  for the siRNA fragments measured. The siRNA is thus

about one order of magnitude slower than the pure dye. This indicates that the siRNA does not degrade entirely.

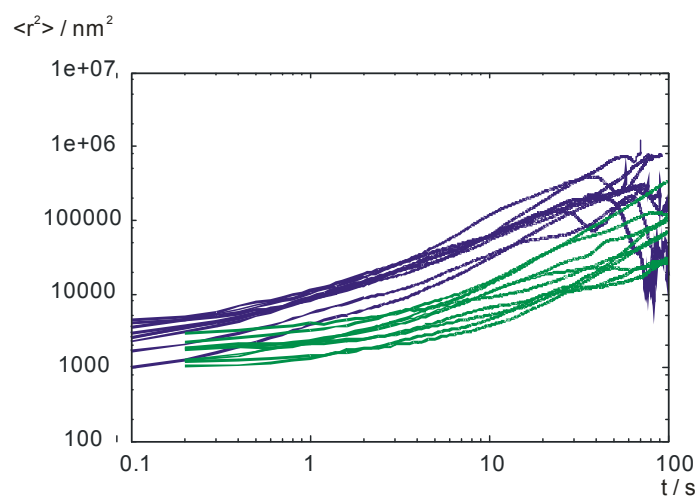


**Figure 4.24: Characterization of the diffusion dynamics.** Plot of the mean square displacement *versus* time. The MSDs of individual siRNA fragments (green) detected in the ATTO647N channel are plotted compared to the MSDs of individual ATTO647N dye molecules (blue).

Nevertheless, the siRNA does not tolerate the synthesis conditions of the thin films and the double-strand breaks. Consequently, thin template-filled films of mesoporous silica are not a suitable delivery structure for such fragile oligonucleotides. Therefore, new ways for the incorporation and the delivery of oligonucleotides needed to be found. Especially new loading strategies that circumvent the pH problem are necessary.

### 4.4.3 Observing oligonucleotide diffusion inside mesoporous silica delivery particles on a single molecule level

An alternative option of embedding oligonucleotides in mesoporous silica consists in a post-synthetic loading of the delivery system with the fragile biomolecules after removal of the surfactant. This strategy is tested on mesoporous SBA-15 silica particles, since spherically shaped objects are probably the morphology closest to a future application.

A 20 bp DNA sequence was loaded in aminopropyl- (8 mol %) / cyanopropyl- (2 mol %) functionalized SBA-15 particles in the following way. First, the surfactant P123 was removed

from the particles according to the protocols described in Chapter 4.4.1. Next, the SBA-15 powder was dissolved in a PBS buffer (pH = 7.4) and the dsDNA was added in single molecule concentration ( $\sim 10^{-10}$  -  $10^{-11}$  mol/L). The DNA double-strand is characterized by the following sequence: 5' GGA CGC CAG GGG GAA GCG AC TT ATTO647N 3'; 3' ATTO532 TT CCT GCG GTC CCC CTT CGC TG 5'. The dye labels (ATTO647N and ATTO532) are located on the opposite side (at the same end) of the double-strand. In order to test the stability of the dsDNA in the SBA-15 particles fluorescence movies of the RNA loaded particles were acquired on a wide-field setup based on an Eclipse TE200 (Nikon) epi-fluorescence microscope using a high numerical aperture oil-immersion objective (Nikon Plan Apo 100x, 1.40 NA, oil). The ATTO532 and ATTO647N fluorescent labels on the oligonucleotide double-strands were excited using a 532 nm diode pumped solid state laser (Cobolt samba TM Laser, cw, 100 mW LAB) and a 633 nm He-Ne gas laser with an intensity of  $0.14 \text{ kW cm}^{-2}$  for each laser. The samples were illuminated with both wavelengths at the same time. The red and green fluorescence of the fluorophores was separated using a dichroic mirror (dual line beamsplitter 532/633, AHF Analysentechnik, Tübingen, Germany). Fluorescence was detected with an EM-CCD camera in frame-transfer mode (Andor, iXon Dv897, 512 x 512 pixels). Incident laser light was blocked with bandpass filters: in the green channel: 650/250 (Chroma Technology Corp., Bellows Falls, Vermont, USA) and BrightLine HC 585/60 (AHF) and in the red channel: 730/140 (AHF). The double-strand was excited with green and red lasers at the same time and both detection channels were monitored in parallel. With this procedure, the stability of the dsDNA inside the SBA-15 particles can be checked on a single molecule level. Each time a signal colocalization of the red and the green detection channel can be observed a stable DNA double-strand is detected.

Figure 4.25 displays images from a movie acquired according to the above described methods. The images show individual DNA double-strands incorporated inside the aminopropyl- and cyanopropyl-functionalized mesoporous particle. Figure 4.25 a shows the fluorescence image detected in the channel mapping the red ATTO647N fluorescent dye, whereas Figure 4.25 b shows the channel mapping the green ATTO532 label. Due to the fact that the SBA-15 particles float inside the PBS buffer, the laser light has to pass media with different refractive indices. These non-matching refractive indices lead to a bad signal-to-noise ratio. The data presented in Figure 4.25 thus reach the limit of the wide-field microscope for single molecule detection. The yellow squares exemplarily highlight fluorescent signals present in both channels. For the sake of clarity only a few colocalizing signals are marked. The degree of colocalization for the

images of Figure 4.25 a and b reaches about 30%, which is mainly due to the bad signal quality. Nevertheless, stable dsDNA can be found inside the aminopropyl- and cyanopropyl-functionalized SBA-15 particles.

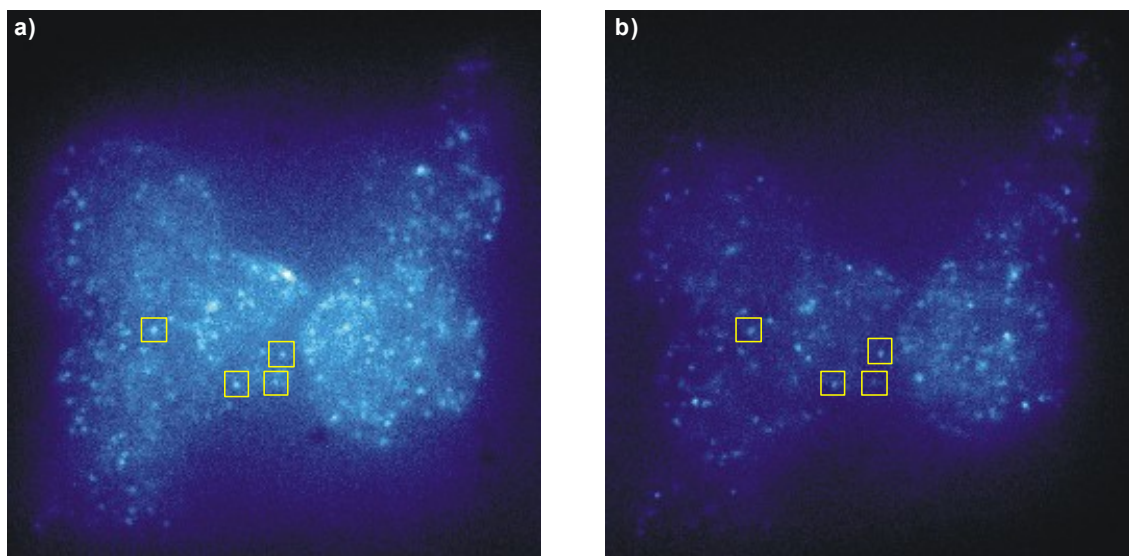


**Figure 4.25: Wide-field fluorescence images showing single 20 bp DNA double-strands inside mesoporous SBA-15 particles.** 20 bp dsDNA labelled with a green (ATTO532) and a red (ATTO647N) fluorescent dye on the opposite strands incorporated inside aminopropyl- (8 mol %) / cyanopropyl- (2 mol %) functionalized SBA-15 particles. The detected fluorescence signal of the red dye label is shown in a), whereas b) depicts the detected fluorescence signal of the green dye label. Both dyes were excited individually and a signal colocalization between a) and b) proves DNA stability. The yellow squares exemplarily highlight colocalizing signals and thus stable DNA double-strands. About 30% colocalization can be observed.

The diffusion of one of the colocalizing DNA double-strands of Figure 4.25 was evaluated according to the single particle tracking methods described in Chapter 3.2.1.3. The signals in each channel resulting from the ATTO647N and the ATTO532 label were tracked individually. Assuming a 2D random walk and fitting the signals to Eq. 3.3 yielded the following trajectories for the DNA double-strand (Figure 4.26). The trajectory of the red fluorescent ATTO647N label is displayed in red and the trajectory calculated from the green channel monitoring the ATTO532 dye is displayed in dark blue. The errors in determining the dye label position are shown in red and blue squares for the different channels. Even though not each point of both trajectories (red and dark blue) colocalizes both trajectories map a very similar motional behavior, which can only be explained by intact dsDNA. If the double-strand was broken, there would be no reason for both dye labels to move in such a concerted way. Consequently, the

single molecule measurements showed that the dsDNA in principle tolerates the loading procedure into the silica particle and remains stable after incorporation. The loading strategy after template removal thus proved successful and prevails over directly adding the oligonucleotide to the precursor solution like in Chapter 4.4.2. This results most likely from avoiding a direct contact of the fragile oligonucleotide with the acidic precursor solution. Under acidic conditions the purine bases of the DNA can be protonated. These protonated purine bases are good leaving groups such that the DNA can hydrolyse and thus degrade.

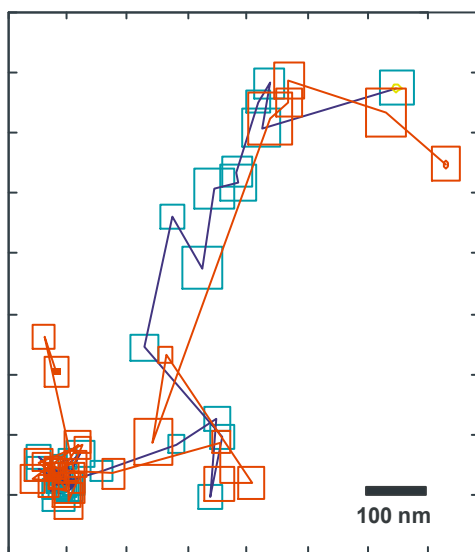


**Figure 4.26: Trajectories of the red and the green fluorescent dye label on the opposite strands of an DNA double strand diffusing inside a mesoporous SBA-15 particle.** The 20 bp dsDNA was incorporated inside aminopropyl- (8 mol %) and cyanopropyl- (2 mol %) functionalized SBA-15 particles and the trajectories were extracted from wide-field fluorescence movies. The trajectory of the red fluorescent dye (red) is superimposed on the trajectory of the green fluorescent label (dark blue). The squares in both trajectories indicate the positioning accuracy for each spot of the trajectory which is about 40 nm here. Even though not each point of both trajectories (red and dark blue) colocalizes both trajectories map a very similar motional behavior, which can only be explained by intact dsDNA.

The data of this chapter shows that single molecule experiments can also be used to gain valuable insights into oligonucleotide loaded mesoporous particles. In the previous studies, single molecule techniques were only applied to thin films of mesoporous silica. The SBA-15 particles float inside a buffered dsDNA solution and can readily be investigated optically. However, due to the non-matching refractive indices of the different media the laser light has to pass, the signal-to-noise ratio is significantly smaller compared to oligonucleotide loaded thin films. This still limits the amount of information that can be extracted from the

measurements. Yet, the measurements serve as a proof-of-principle demonstrating for the first time that individual oligonucleotides can be monitored in their diffusional behavior throughout a mesoporous drug-delivery particle on a single molecule level. The experiments thus pave the way for more detailed single molecule studies of these interesting samples.

#### 4.4.4 Loading SBA-15 mesoporous silica particles with siRNA

Since, we now know that oligonucleotides remain intact inside template extracted mesoporous silica particles, the loading behavior of differently functionalized SBA-15 silica particles with oligonucleotides shall be analyzed in more detail. To realize that siRNA was incorporated into the SBA-15 particles under ensemble concentrations ( $\sim 10^{-4} \text{ molL}^{-1}$ ). These ensemble measurements provide a better signal-to-noise ratio than the single molecule measurements of the previous chapter.

In order to get a first overview about the loading properties of the SBA-15 particles, four differently functionalized samples were synthesized (see Chapter 4.4.1): i) unfunctionalized, ii) cyanopropyl-functionalized (10 mol %), iii) aminopropyl- (8 mol %) and cyanopropyl- (2 mol %) functionalized and iv) aminopropyl- (5 mol %) and phenyl- (5 mol %) functionalized SBA-15. After surfactant removal, the SBA-15 powder was dissolved in a PBS buffer (pH = 7.4) and siRNA (20 bp) was added in ensemble concentration ( $\sim 10^{-4} \text{ molL}^{-1}$ ). After adding the siRNA to the buffered SBA-15 solution, the samples were incubated for 3 h, giving the siRNA sufficient time to access the particles. The following siRNA double-strand was used: 5' GGA CUC CAG UGG UAA UCU AC ATTO647N 3'; 3' CCU GAG GUC ACC AUU AGA UG ATTO532 5' (IBA GmbH, Göttingen, Germany). The double-strand is labelled with a green (ATTO532) and a red (ATTO647N) fluorescent dye at the 3' and 5' end of the opposite strands. In contrast to the previously used sequences, the dye pair is now located on the same side of the double-strand and can thus be used for checking siRNA stability through Förster-Resonance-Energy-Transfer (FRET): upon exciting the green dye, energy transfer will take place from the green (donor) to the red (acceptor) dye and fluorescence of the red dye can be monitored. However, FRET is very distance dependent and only works well between  $\sim 2 - 10 \text{ nm}$ . Consequently, a broken siRNA double-strand does not yield a FRET signal. Using FRET for monitoring siRNA stability

prevails over the colocalization method used in the previous chapters since the technique is far more sensitive and offers easy-to-access and reliable data.

The different samples were measured on a confocal microscope (Zeiss LSM510). All measurements with oligonucleotides and SBA-15 particles have been conducted in the following way: only the green fluorescent dye label was excited with a He-Ne-laser emitting at 543 nm through a high-NA objective (Zeiss Plan Neofluar, 40x/1.30 NA, oil-immersion). The fluorescence was filtered with the help of a beamsplitter (HFT, UV/488/543/633) in combination with a long-pass filter (LP 650) in order to detect the FRET fluorescence signal from the red fluorescent dye label. The FRET signal was detected on a photomultiplier. Consequently, this measurement setup allowed directly checking the siRNA stability.

Figure 4.27 shows fluorescence images of the four differently functionalized SBA-15 materials dissolved in the buffered siRNA solution. The several micrometers large mesoporous particles can be seen as spherically shaped objects. It is clearly visible that they tend to aggregate, independent of the attached functionality since always two or more spherical objects are attached to each other (see also Figure 4.21). The aggregation behaviour is mainly determined by the polarity of the solvent and the interactions of the particles with the solvent. Changing the solvent polarity can drastically alter the tendency to aggregate. In Figure 4.27 a aminopropyl- (5 mol %) / phenyl- (5 mol %) functionalized SBA-15 particles are shown. The siRNA fluorescence can be clearly detected inside the particle. Since the particle diameter exceeds the axial resolution of the microscope ( $\sim 900$  nm), the fluorescent circle shown in the Figure is a cut slicing through the spherical particle and all fluorescence detected thus stems from siRNA inside the mesoporous particle and not on its surface. Consequently, the particles detected are loaded successfully with siRNA. Effective loading of the particle can also be observed for an aminopropyl- (8 mol %) and cyanopropyl- (2 mol %) functionalized SBA-15 material (Figure 4.27 b), however in this case the relative amount of siRNA that gets loaded into the particle proves to be only about 75% of the amount of siRNA detected inside the aminopropyl- and phenyl- functionalized SBA-15 particles of Figure 4.27 a. This may result from the slightly larger pore size of the aminopropyl- and phenyl-containing particles compared to the aminopropyl- and cyanopropyl-containing particles (see Table 4.6). In contrast, cyanopropyl- (10 mol %) functionalized (Figure 4.27 c) and unfunctionalized (Figure 4.27 d) SBA-15 particles do not get loaded, even though the nitrogen sorption data of Table 4.6 clearly

proves that all four particle types are accessible and open to an exchange with the surrounding environment. This loading behavior cannot be explained by a simple pore-size effect. Table 4.6 shows that the pore sizes of the cyanopropyl-functionalized (Figure 4.27 c) and unfunctionalized (Figure 4.27 d) SBA-15 materials are even slightly larger than for the functionalizations that do allow siRNA incorporation. The observed behavior in Figure 4.27 c and d gets rather attributed to an unfavourable interaction of the surface of the particles with the negatively charged siRNA. All SBA-15 materials investigated possess hydroxyl groups on their surface that may be partially deprotonated. These (deprotonated) hydroxyl groups and the cyanopropyl groups seem to repel the siRNA because of their negative charge density. In contrast, the aminopropyl-functionality attached to the particles displayed in Figure 4.27 a and b seems to favour siRNA uptake, which may result from hydrogen bonding between the negatively charged siRNA and the amino groups that can be protonated. Taking these considerations into account the increased loading capacity of aminopropyl- and phenyl-containing silica particles of Figure 4.27 a compared to the aminopropyl- and cyanopropyl-containing particles of Figure 4.27 b could also result from the electrostatic repulsion between the negatively charged siRNA and the cyanopropyl-groups .

It would be interesting to study purely aminopropyl-functionalized SBA-15 particles. However, the corresponding synthesis solution does not yield a mesoporous powder but an undefined gelled structure. Only through adding co-functionalization such as cyanopropyl or phenyl to the precursor solution mesoporous SBA-15 particles can be obtained. Yet, this is not necessarily disadvantageous since for example the sterically demanding phenyl groups can further help to shield the siRNA from the surface hydroxyl groups.

The data of Figure 4.27 a and b do not only show successful loading of the particles. Additionally, due to the measurement procedure, namely the detection of the FRET signal, the data also prove that the siRNA observed in the particles is indeed intact. If the siRNA was unstable, the FRET signal would be no longer observed. Figure 4.28 shows with the help of a reference measurement where the siRNA was forced to degrade that this FRET signal is an excellent indicator for siRNA stability. In this measurement only the green fluorescent dye label was excited at 543 nm and both green and red fluorescent dye labels (ATTO647N and ATTO532) were detected simultaneously on the above introduced confocal microscopy setup by using a beamsplitter (HFT, UV/488/543/633) in combination with a long-pass filter LP 650

for the red channel and a long-pass filter LP 560 for the green channel. The red channel thus depicts the FRET signal due to energy transfer from the green to the red dye label. Figure 4.28 a shows the siRNA loaded particles in a PBS buffered solution at pH = 7. The siRNA excited in green clearly shows FRET, since the fluorescence of the red label can be detected. In accordance, the corresponding green channel depicting the fluorescence of the green dye label does not show any signal at that pH (Figure 4.28 b). If the same siRNA particle solution now gets prepared at pH = 1 through adding hydrochloric acid, the FRET signal in the red detection channel (Figure 4.28 c) vanishes and a signal of the green fluorescent label can be observed in the green detection channel (Figure 4.28 d). If the red ATTO647N fluorescent label would simply degrade due to the acidic pH, the green ATTO532 label should not start to fluoresce. The observed behaviour can only be due to degradation of the siRNA at pH = 1 (see discussion in Chapter 4.4.3). Since the siRNA is fragmented, the energy transfer cannot take place any longer and the green label starts to fluoresce. This proves that the FRET signal, such as in Figure 4.27, is a good criterion for siRNA stability.

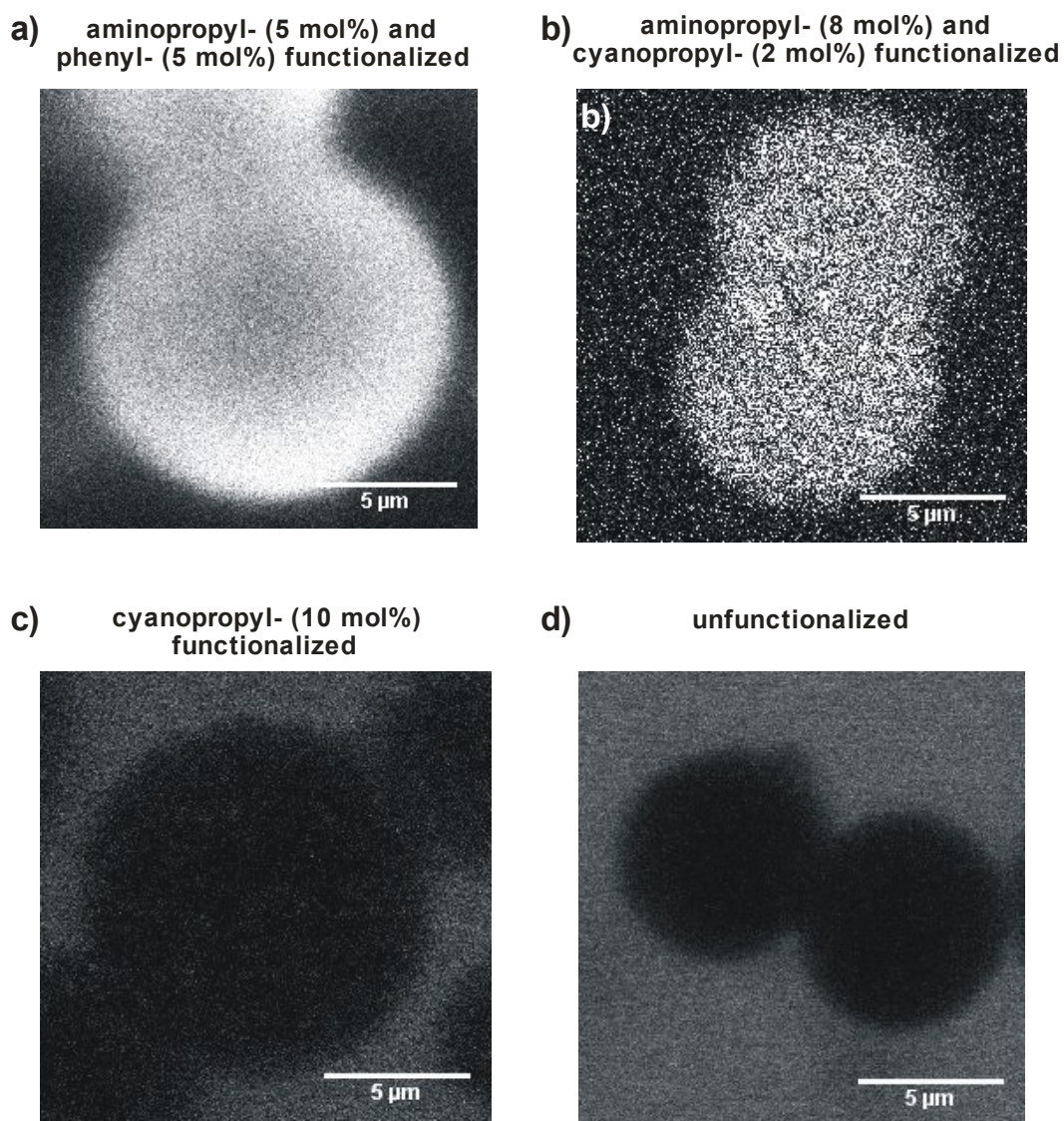


**Figure 4.27: Loading characteristics of functionalized mesoporous SBA-15 particles.** Four differently functionalized SBA-15 materials dissolved in a buffered siRNA solution: a) aminopropyl- (5 mol %) and phenyl- (5 mol %) functionalized, b) aminopropyl- (8 mol %) and cyanopropyl- (2 mol %) functionalized, c) cyanopropyl- (10 mol %) functionalized and d) unfunctionalized SBA-15. Whereas in (a + b) siRNA fluorescence can be detected inside the particles, the particles in (c + d) are unloaded, only weak fluorescence in the surrounding solution can be detected.

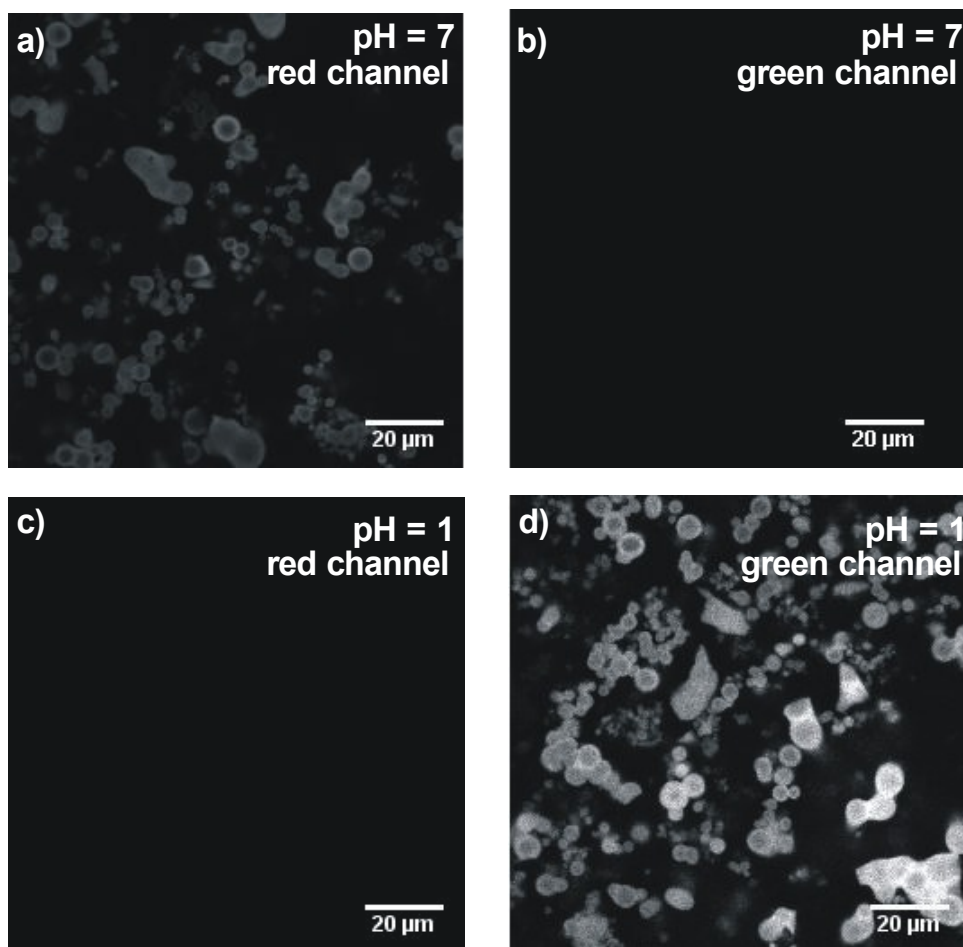


**Figure 4.28: Förster Resonance Energy Transfer as an indicator for oligonucleotide stability.** siRNA inside aminopropyl- (5 mol %) and phenyl- (5 mol %) functionalized SBA-15 particles. a) and c) display the channel of the red fluorescent ATTO647N label, b) and d) depict the channel of the green fluorescent ATTO532 label. a) and b) were measured at pH = 7, whereas c) and d) were measured at pH = 1. The FRET signal in the red channel gets lost by changing the pH from 7 to 1 indicating siRNA degradation. In contrast, the green labelling dye gets visible in d) after the termination of the energy transfer.

#### 4.4.5 Determining oligonucleotide mobility inside the delivery structure with FRAP

Since, we know now that aminopropyl-containing functionalities seem to favour siRNA uptake, oligonucleotide mobility inside these functionalized SBA-15 shall be characterized. To realize this, two different experiments have been conducted. i) The diffusion dynamics of the above mentioned 20 bp siRNA sequence was determined inside aminopropyl- (5 mol %) and phenyl-

(5 mol %) functionalized SBA-15 compared to aminopropyl- (8 mol %) and cyanopropyl- (2 mol %) functionalized SBA-15 particles. ii) The mobility of DNA double-strands of different length (20, 30, 60 and 90 bp) was determined inside the aminopropyl- and phenyl- functionalized SBA-15 particles. The following DNA double-strand sequences were used: 5' GGA CGC CAG GGG GAA GCG AC ATTO647N 3'; 3' CCT GCG GTC CCC CTT CGC TG ATTO532 5' for the 20bp DNA, 5' GGA CGC CAG GGG GAA GCG ACG GAC GCC AGG ATTO532 3'; 3' CCT GCG GTC CCC CTT CGC TGC CTG CGG TCC ATTO647N 5' for the 30 bp DNA, 5' GGA CGC CAG GGG GAA GCG ACG GAC GCC AGG CTG ATT TGA AGC TTA TGA CTT ATT GGA CCT ATTO532 3'; 3' CCT GCG GTC CCC CTT CGC CTC CTG CGG TCC GAC TAA ACT TCG AAT ACT GAA TAA CCT GGA ATTO647N 5' for the 60 bp DNA and 5' GGA CGC CAG GGG GAA GCG ACG GAC GCC AGG CTG ATT TGA AGC TTA TGA CTT ATT GGA CCT ATC TCT GAC ATA TTA TAC TAG GCT GTG TTT ATTO532 3'; 3' CCT GCG GTC CCC CTT CGC TGC CTG CGG TCC GAC TAA ACT TCG AAT ACT GAA TAA CCT GGA TAG AGA CTG TAT AAT ATG ATC CGA CAC AAA ATTO647N 5' for the 90 bp DNA (IBA GmbH, Göttingen, Germany). The sequences are chosen randomly. It was only checked that no large hairpins or bubbles are created that could additionally influence diffusion. Again, the attached dye pair allows for checking DNA stability through FRET. The measurements started 3 h after incubating the oligonucleotides inside the PBS buffered particle solution.

The oligonucleotide mobility was evaluated using the *Fluorescence Recovery after Photobleaching* (FRAP) technique introduced in Chapter 3.2.2, since this is an appropriate and widely used method to extract diffusion coefficients from fluorescent samples under ensemble concentration (see Chapter 3.2.2). The utilized confocal setup is identical to the setup introduced in the previous Chapter 4.4.4 with the following additional settings for the FRAP measurements: integration time per frame: 983.04 ms/frame; a new frame was recorded every 4 s; 10 scans before bleaching; circular bleaching region of 10 pixels in diameter. The quantitative evaluation of the recorded frame sequences and the data modeling was done by K. Schneider and A. Dobay in the group of H. Leonhardt (LMU Munich, Department of Biology, Munich Germany). The method of data evaluation in order to obtain fluorescence recovery curves is explained in Chapter 3.2.2.2.

Figure 4.29 displays the recovery curves obtained for the siRNA and the DNA sequences in the differently functionalized particles. For each sample at least 10 data sets (bleaching events) were acquired from several particles of the same sample. The loaded particles appear as

fluorescent circles (see Figure 4.27 a and b) and in order to get a statistically relevant overview the bleaching sites were chosen randomly inside the particle (in the particle center or closer to the edges of the particles). Figure 4.29 shows the mean fluorescence intensity recovery curve for each sample obtained through averaging the individual recovery curves obtained from each bleaching event. Figure 4.29 a shows that the recovery of the mean fluorescence intensity is significantly slower for siRNA inside aminopropyl- (5 mol %) and phenyl-(5 mol %) functionalized SBA-15 particles (black) than the recovery of siRNA fluorescence in aminopropyl- (8 mol %) and cyanopropyl- (2 mol %) functionalized particles (green). Even though the pore size was found to be smaller in cyanopropyl-containing particles compared to the phenyl containing particles (see Table 4.6) this can be rationalized since already the loading studies discussed in Figure 4.27 showed that an increased repulsive interaction must be present between the siRNA and the cyanopropyl-groups compared to the phenyl-groups. This increased repulsion leads to a faster recovery for cyanopropyl-containing SBA-15. Furthermore, a similar phenomenon was observed in Chapter 4.2.3, where the insertion of phenyl groups resulted in a deceleration of the diffusing species. It is important to note that the “error bars” displayed do not mirror the error in determining the mean fluorescence intensity, but originate from the inherent heterogeneity of the different mesoporous particles leading to a distribution of recovery dynamics. Similar heterogeneities were observed in Chapter 4.2.3. Additionally, Figure 4.29 b displays recovery curves for the 20 bp (red), 60 bp (blue) and 90 bp (black) DNA sequence diffusing inside aminopropyl- (5 mol %) and phenyl-(5 mol %) functionalized SBA-15 particles. It can clearly be seen that the recovery is significantly slower for increasing length of the DNA. In none of the cases the recovery is total. The mean fluorescence intensity before bleaching is normalized to unity and the postbleach mean fluorescence intensity does not reach unity again. This can result from immobile molecules present in the sample, since they can only get bleached but do not recover.<sup>189</sup> It is important to keep in mind that bleaching only means that the fluorophore gets irreversibly inactivated but this is not necessarily combined with a degradation of the DNA and hence the immobile DNA can still be present and block the adsorption sites inside the particle preventing new fluorescent DNA from diffusing in. In contrast bleached mobile DNA should be able to diffuse out of the particle. The data of Figure 4.29 b clearly show that the lack of recovery and thus the amount of immobile molecules increases significantly with increasing length of the DNA double-strand. This is not surprising since the long DNA can more easily get trapped inside the porous network.

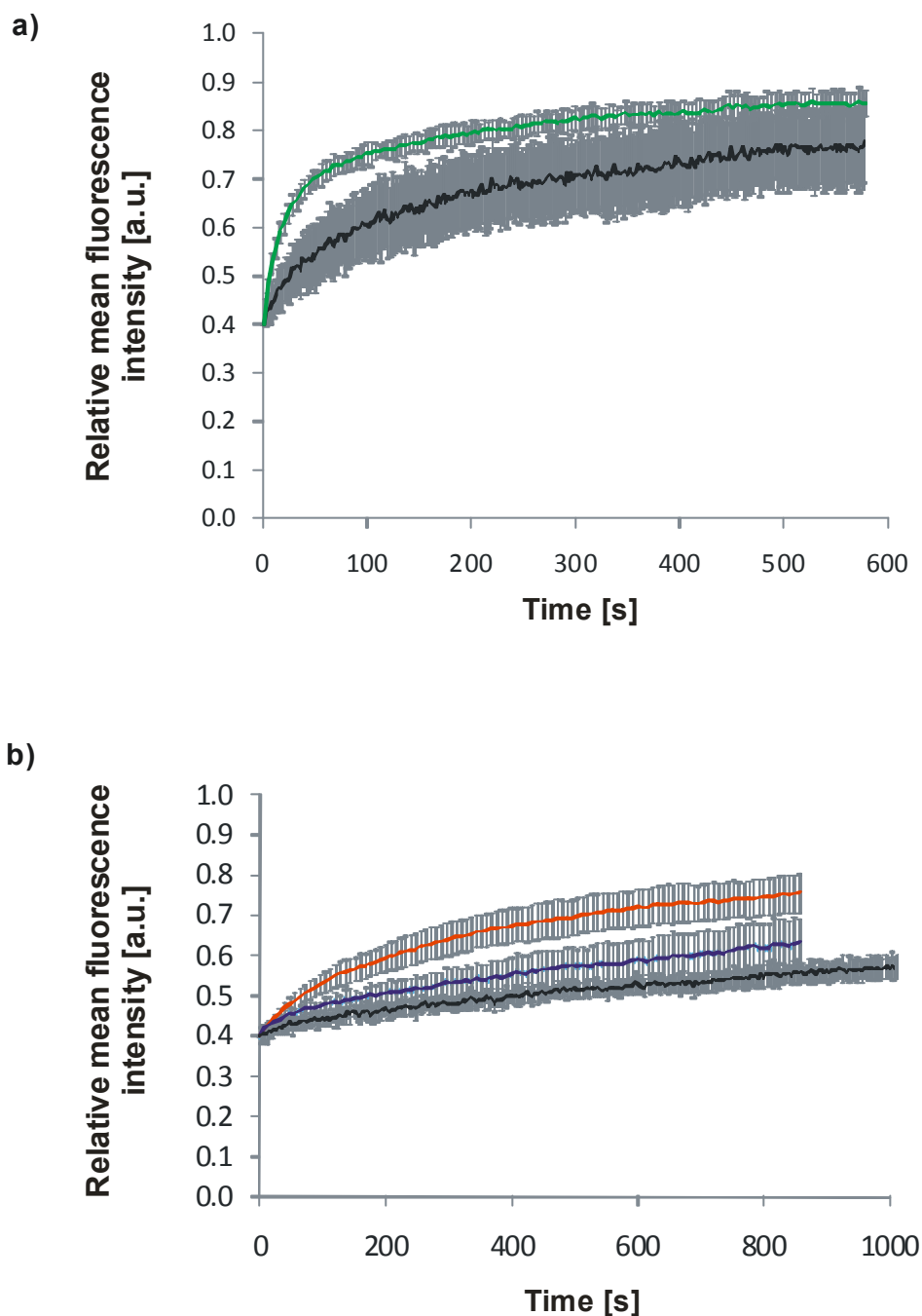


**Figure 4.29: FRAP recovery curves for the different oligonucleotides inside the functionalized SBA-15 particles.** a) The 20 bp siRNA sequence inside aminopropyl- (8 mol %) and cyanopropyl- (2 mol %) functionalized SBA-15 particles (green) and inside aminopropyl- (5 mol %) and phenyl-(5 mol %) functionalized SBA-15 particles (black). b) Aminopropyl- (5 mol %) and phenyl-(5 mol %) functionalized SBA-15 particles loaded with 20 bp DNA (red), 60 bp DNA (blue) and 90 bp DNA (black).

Next, the recovery curves are fitted to a diffusion model in order to extract diffusion coefficients and thereby quantify the mobility of the oligonucleotides inside the mesoporous particles (see Chapter 3.2.2.3). The model used is based on Eq. 3.23. However, this equation needed to be adapted assuming two diffusing populations. In this case the modeling function (Eq. 3.23) becomes

$$\begin{aligned}
 f(t) &= 1 - \phi + \phi \exp\left(\frac{-2\tau_{D_1}}{t}\right) \left[ I_0\left(\frac{2\tau_{D_1}}{t}\right) + I_1\left(\frac{2\tau_{D_1}}{t}\right) \right] \\
 &\quad + \theta \left( \phi \exp\left(\frac{-2\tau_{D_2}}{t}\right) \left[ I_0\left(\frac{2\tau_{D_2}}{t}\right) + I_1\left(\frac{2\tau_{D_2}}{t}\right) \right] \right. \\
 &\quad \left. - \phi \exp\left(\frac{-2\tau_{D_1}}{t}\right) \left[ I_0\left(\frac{2\tau_{D_1}}{t}\right) + I_1\left(\frac{2\tau_{D_1}}{t}\right) \right] \right) \\
 &= f_{D_1}(t) + \theta [f_{D_2}(t) - f_{D_1}(t)]
 \end{aligned} \tag{4.25}$$

with the two diffusion coefficients  $D_1$  and  $D_2$ . The superposition parameter  $\theta$  controls the relative contributions of the two populations.

Assuming two diffusing populations was necessary to adequately describe the data. Figure 4.30 demonstrates this on an exemplary recovery curve of siRNA diffusing inside an aminopropyl- and cyanopropyl-functionalized particle (black spots). The data was first fitted using a model according to Eq. 3.23 assuming only one diffusing population (blue line). This model does not allow to fit the data sufficiently. In contrast, a model according to Eq. 4.25 assuming two mobile populations (red line) fits the data much better. A further increase in the number of diffusion coefficients in the model does not significantly improve the quality of the fit. This data set is typical and consequently all FRAP data evaluation was done using the model of Eq. 4.25 with two diffusion coefficients.

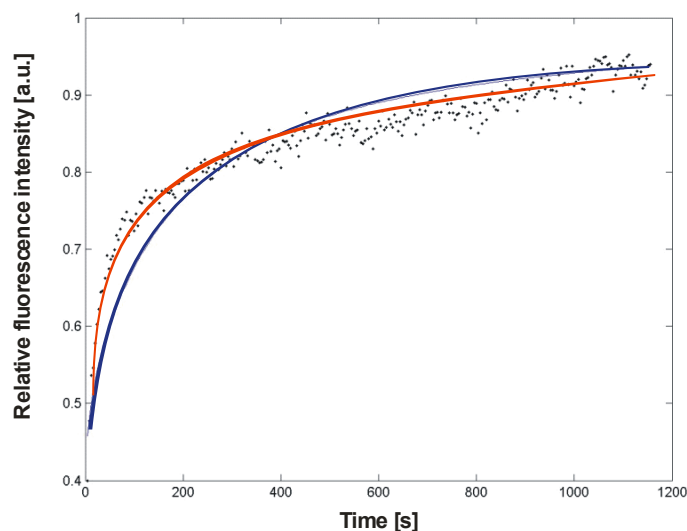


**Figure 4.30: Data modelling.** A typical fluorescence recovery curve (black spots) from siRNA inside an aminopropyl- (8 mol %) and cyanopropyl- (2 mol %) functionalized SBA-15 particle. The data is fitted to a model according to Eq. 3.23 assuming only one diffusing population (blue line) and a model according to Eq. 4.25 assuming two diffusing populations (red line). One can clearly see that the blue line does not fit the data adequately.

Modelling the data of Figure 4.29 according to Eq. 4.25 yields the two mean diffusion coefficients  $\langle D_{fast} \rangle$  and  $\langle D_{slow} \rangle$  for the mobile populations in each sample (see Figure 4.31). The mean diffusion coefficients obtained from siRNA inside aminopropyl- (8 mol %) and cyanopropyl- (2 mol %) functionalized SBA-15 particles (green) and inside aminopropyl- (5 mol %) and phenyl-(5 mol %) functionalized SBA-15 particles (black) are displayed in Figure 4.31 a, whereas the data for 20 bp DNA (red), 60 bp DNA (blue) and 90 bp DNA (black) diffusing inside aminopropyl- (5 mol %) and phenyl-(5 mol %) functionalized SBA-15 particles is displayed in Figure 4.31 b. The calculated values of  $\langle D_{fast} \rangle$  and  $\langle D_{slow} \rangle$  are listed in Table 4.7. The mean diffusion coefficient of the fast diffusing population  $\langle D_{fast} \rangle$  can be considered to display the diffusion of the oligonucleotide double-strand inside the mesoporous channels of the SBA-15 particles. The mean diffusion coefficients lie well in the range of diffusion coefficients known for diffusion dynamics inside a mesopore, which is in the range of hundreds to thousands  $\text{nm}^2/\text{s}$  (see for example Chapter 4.2.3 or the study of Kirstein et al.<sup>93</sup>). One can clearly see that the trends discussed in Figure 4.29 do get reflected in  $\langle D_{fast} \rangle$  (Figure 4.31 and Table 4.7). The siRNA is significantly slower in the phenyl-containing particles and the DNA dynamics gets reduced with increasing chain length.

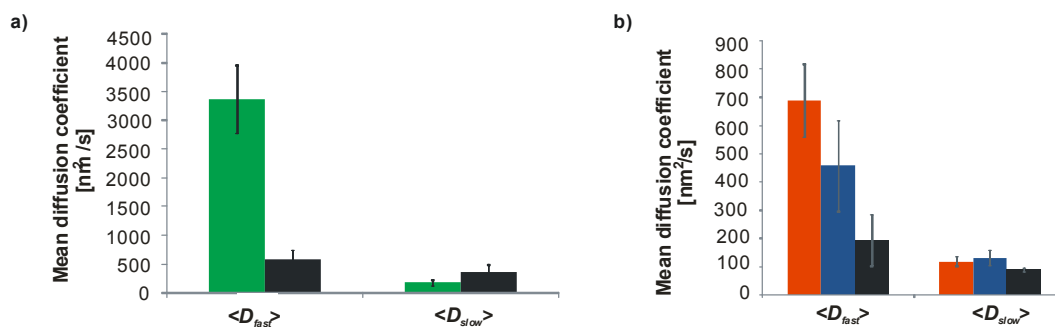


**Figure 4.31: Mean diffusion coefficients.** The two mean diffusion coefficients  $\langle D_{fast} \rangle$  and  $\langle D_{slow} \rangle$  for the mobile populations in each sample are displayed. a) siRNA inside aminopropyl- (8 mol %) and cyanopropyl- (2 mol %) functionalized SBA-15 particles (green) and inside aminopropyl- (5 mol %) and phenyl- (5 mol %) functionalized SBA-15 particles (black). b) Aminopropyl- (5 mol %) and phenyl- (5 mol %) functionalized SBA-15 particles loaded with 20 bp DNA (red), 60 bp DNA (blue) and 90 bp DNA (black).

Earlier in this chapter we discussed that assuming two mobile populations drastically increases the quality of the fit (Figure 4.30). Now, the question about the origins of this second slow diffusing population arises. Mathematically, this parameter is indeed relevant for fitting the data but what is its physical meaning and how does that slow population fit into our understanding of the diffusion processes inside the pore?

$\langle D_{slow} \rangle$  characterizes a second slow, yet not immobile, population. As mentioned above totally immobile molecules do not recover and cannot be seen in the dynamics of the recovery curve. Sprague *et al.* show that in the presence of binding sites a so-called effective diffusion coefficient can be observed.<sup>190</sup> This effective diffusion refers to a slowing down of the initially unhindered diffusion due to binding events. However, this would not necessarily explain a distinct second population. Interestingly,  $\langle D_{slow} \rangle$  does not show a clear trend for the different samples in contrast to  $\langle D_{fast} \rangle$ . So far, the origins of this phenomenon remain unclear. This question could be addressed in the future with further single molecule investigations, since they have proven to offer valuable insights into such mechanistic problems in the past.

**Table 4.7: Calculated mean diffusion coefficients for the fast and slow diffusing population.**

Oligonucleotide	aminopropyl and phenyl (5 + 5 mol %) [nm <sup>2</sup> /s]	aminopropyl and cyanopropyl (8 + 2 mol %) [nm <sup>2</sup> /s]
siRNA	$\langle D_{fast} \rangle = 5.7 * 10^2 \pm 1.7 * 10^2$	$\langle D_{fast} \rangle = 3.4 * 10^3 \pm 5.9 * 10^2$
	$\langle D_{slow} \rangle = 3.7 * 10^2 \pm 1.2 * 10^2$	$\langle D_{slow} \rangle = 1.8 * 10^2 \pm 4.9 * 10^1$
20 bp DNA	$\langle D_{fast} \rangle = 6.9 * 10^2 \pm 1.3 * 10^2$	---
	$\langle D_{slow} \rangle = 1.1 * 10^2 \pm 1.7 * 10^1$	---
60 bp DNA	$\langle D_{fast} \rangle = 4.6 * 10^2 \pm 1.6 * 10^2$	---
	$\langle D_{slow} \rangle = 1.3 * 10^2 \pm 2.6 * 10^1$	---
90 bp DNA	$\langle D_{fast} \rangle = 1.9 * 10^2 \pm 9.1 * 10^1$	---
	$\langle D_{slow} \rangle = 8.9 * 10^1 \pm 1.4 * 10^1$	---

In the course of these experiments also a 30 bp DNA sequence was investigated as mentioned above. However, the measured recovery curve did not at all fit into the displayed data of Figure 4.29 b and the extracted mean diffusion coefficient of the fast diffusing population was more than one order of magnitude higher than the values listed in Table 4.7. This obvious deviation from the rest of the experimental data could be attributed to an impurity present in the 30 bp DNA stock solution ordered. Figure 4.32 shows the data of a gel chromatographic analysis of the different DNA sequences used. Stock solutions of all utilized DNA sequences (20, 30, 60, and 90 bp) were tested with non-denaturing polyacrylamide-gel-electrophoresis (PAGE). For preparing the gel 5 mL of acrylamide (30%) were mixed with 1 mL of a Tris/Borate/EDTA (TBE) buffer (10x), 0.1 mL of an ammonium persulfate (APS) solution (10%), 0.004 mL of tetramethylethylenediamine (TEMED) and 5 mL of double-distilled water. Besides the DNA samples investigated here a 42 bp reference DNA was added. The electrophoresis was run at 120 V for about 1.5 h. PAGE analysis was done by K. Schneider in the group of H. Leonhardt (LMU Munich, Department of Biology, Munich, Germany). In Figure 4.32 a and b the DNA was excited at 532 nm. Fluorescence emission was detected at 555nm (Figure 4.32 a) and at 670nm (Figure 4.32 b). Consequently, Figure 4.32 b represents the FRET channel. This

explains, why in Figure 4.32 a the bands for the DNA sequences (except the reference) are only barely visible. This is due the high FRET efficiency and proves DNA stability. In comparison in the FRET channel (Figure 4.32 b) the DNA bands are much better detectable. The 20, 60 and 90 bp DNA bands behave as expected, *i.e.* the longer the double-strand the slower the diffusion in the gel. Yet the 30 bp DNA sequence shows unexpected bands (indicated by a red arrow) clearly visible in Figure 4.32 a and still weakly visible in Figure 4.32 b. This shows that a short fragment is present in the sample and according to Figure 4.32 a in a high amount. This impurity should not be contained in the sample and could interfere with the diffusion of the intact 30 bp DNA. Furthermore, the present impurity could have been directly detected with the LSCM setup, since for the FRAP measurements discussed above the confocal microscope was equipped with a LP 650 nm filter (see Chapter 4.4.4), which makes the microscope sensitive for wavelengths lower than the 670 nm detected with the gel analyzer in Figure 4.32 b. Additionally, the confocal microscope detection pathway is more sensitive than the fluorescence detection for the gel. This means that the high amount of short fragment present in the sample could indeed have interfered with the measurement, even though the impurity is only hardly visible in Figure 4.32 b. The presence of such a short fragment could explain why a diffusion coefficient for the 30 bp DNA was found lying one order of magnitude higher than the values for all other DNA sequences. Consequently, due to this apparent impurity the 30 bp data set was excluded from the above discussed results.

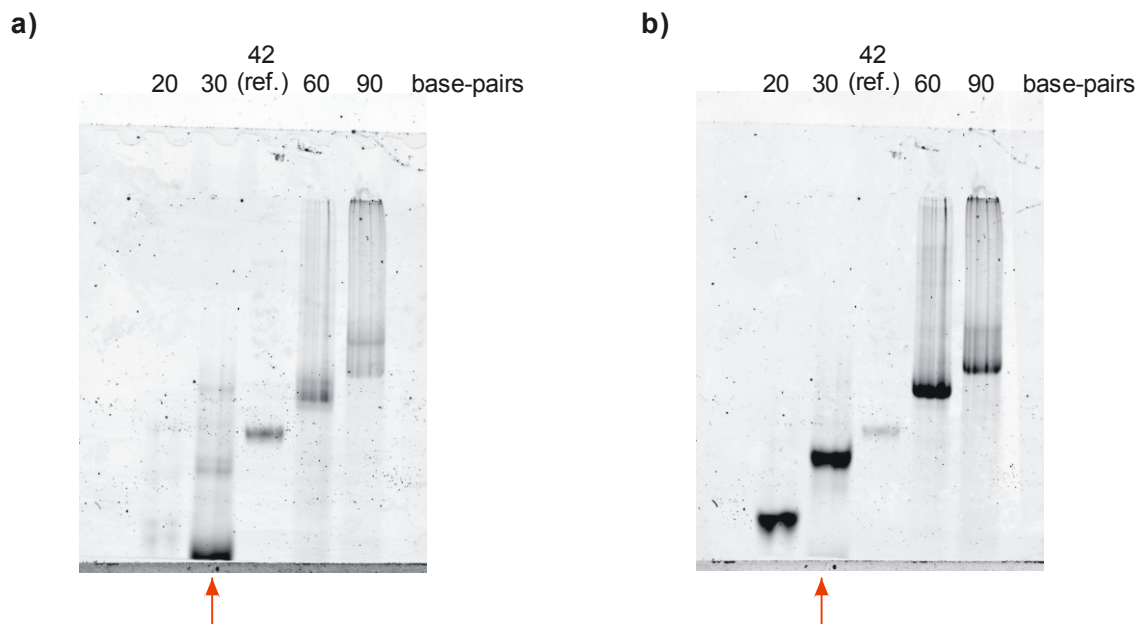


**Figure 4.32: Non-denaturing polyacrylamide-gel-electrophoresis.** The DNA samples were excited at 532 nm (a and b). Fluorescence emission was detected at a) 555 nm and b) 670nm.

b) thus maps the FRET signal. The red arrows indicates the unexpected bands in the 30 bp DNA sample.

### 4.4.6 Conclusion

This chapter was devoted to demonstrating that mesoporous silica can be utilized as drug-delivery system for oligonucleotides. In gene therapy and silencing, there is a constant need for novel smart delivery structures that efficiently transfer the therapeutic oligonucleotide to the target site. Due to its high versatility mesoporous silica can contribute to realizing novel strategies for the incorporation and delivery of this fragile class of biomolecules.

First, profiting from the knowledge acquired in the previous chapter, siRNA loading into thin surfactant templated mesoporous silica films was tested. Mesoporous silica in the form of thin films is not only a model system for other silica structures such as particles, but it could also be utilized in the form of a drug-loaded thin-film layer as an implant for directly covering tumor tissue or wounds after tumor resection. However, the guest molecule that shall be incorporated into such templated thin films needs to be added directly to the precursor solution. Unfortunately, the siRNA proved to be too fragile to withstand the conditions in the precursor solution and degraded into fragments. Consequently, a novel approach for the incorporation of siRNA into mesoporous silica was needed. In order to realize that aim, first, the template molecules were removed from the porous silica. Template removal was done by our collaborators in the group of T. Bein (LMU Munich, Dep. of Chemistry, Munich, Germany). The template can be removed through solvent extraction or calcination. In the study presented here, the solvent extraction method was chosen since this does not destroy covalently attached organic functional groups inside the pores, that would degrade during calcination. The template free mesoporous silica can then afterwards be loaded by simply immersing the host structure in a buffered siRNA solution. For this post-synthetic loading approach, mesoporous particles were utilized rather than thin films, since the particles might be easier to access by the biomolecules compared to thin films. The latter, especially after template removal, often suffer from an elliptical shrinkage of the pores that could hinder loading. Hence, mesoporous silica particles with a hexagonal porous network (SBA-15 type materials) were loaded with siRNA.

First, utilizing single molecule techniques, siRNA stability inside aminopropyl- and cyanopropyl-functionalized SBA-15 particles was proven. It could be demonstrated for the first time that SMM can be used for the investigation of the intricate host-guest interplay in such particle containing samples. Compared to the single molecule microscopy of thin films, particles floating inside a buffered solution are much more difficult to investigate since the signal-to-noise ratio is usually worse.

Further ensemble experiments proved that the loading characteristics of the SBA-15 particles critically depends on the surface functionalization. Unfunctionalized and cyanopropyl-functionalized SBA-15 could not be loaded with siRNA. This was attributed to an unfavourable interaction of the negatively charged siRNA with the negative charge density of these functional groups. However, through adjusting the surface polarity, by coating the channels with aminopropyl-groups, the particles get accessible for the siRNA and can efficiently be loaded. This might result from attractive interactions between the guest and the host due to hydrogen-bonding. The SBA-15 particles could further get loaded with DNA sequences, up to a double-stranded sequences of 90 bp in length. This is especially noteworthy, since the pores sizes of the mesoporous silica samples only range from about 7 – 8 nm. This demonstrates the achievement potential of these novel drug-delivery materials.

For all the utilized oligonucleotide sequences stability inside the drug carrier could be proven in the ensemble studies by Förster Resonance Energy Transfer experiments. All siRNA and DNA samples remain intact inside the delivery system. Furthermore, it was demonstrated that the diffusion dynamics of siRNA inside the template extracted particles can be tuned through adding functional groups. In the previous chapter, this was only demonstrated for template-filled structures. Moreover, the experiments showed that the diffusion dynamics of the DNA critically depends on their length and long DNA sequences show a higher tendency to get immobilized and trapped inside the porous network. Understanding the principles that govern oligonucleotide dynamics inside the drug-delivery system is of great importance for the generation of a so-called depot effect, which is a retarded release of the drug over a prolonged period of time.

The work of this chapter shows that mesoporous silica materials could enrich the currently available delivery strategies in gene therapy and RNA silencing and could thus in the future contribute to improving the available therapeutic options.



# 5 Fabricating mesoporous silica with large domains

In the previous chapters we have learnt that mesoporous silica is a very versatile material, since *e.g.* the pore sizes can be varied on a large scale ( $\sim 4 - 15$  nm in this work) and the surface properties can be fine-tuned by covalently linking a variety of organic functional groups.<sup>18, 19, 52, 144-147, 191</sup> However, there are two key parameters that could not be controlled efficiently so far: the domain growth and the absolute orientation of the channels in the porous material with respect to the substrate.

Usually, mesoporous materials do not show a uniform channel orientation over the entire macroscopic length of the sample, the channels are only aligned parallel to each other over short distances in so-called domains. The orientation of the individual domains is distributed statistically inside the material and their sizes can vary significantly ranging from nanometers to micrometers. However, the ability to control the orientation of the channels on the substrates and thereby create well-ordered domains would substantially increase the application potential of mesoporous silica since then, the materials can be designed in a tailor-made way according to the requirements of a given application. Realizing this has been a long-standing challenge, addressed *e.g.* by Yang *et al.* already in 1996.<sup>192</sup>

This chapter is divided into two sections highlighting different routes towards controlling the channel alignment and domain size in mesoporous silica.

The first section demonstrates how the relative humidity can be used to drastically increase the domain size inside Pluronic P123 templated thin films. The second section is devoted to

the fabrication of micrometer-sized domains of linearly oriented channels through guided growth by Micromoulding in Capillaries (MIMIC).<sup>59, 60</sup> This second study goes far beyond the scope of the first study since the experiments not only demonstrate how to generate large domains but also how to control the channel orientation over a macroscopic scale. This can be achieved through a so-called active patterning of mesoporous silica, *i.e.* a pattern transfer from a model, *e.g.* a stamp, onto the silica. This technique is of great interest for applications of mesoporous materials as *e.g.* optoelectronic devices,<sup>193</sup> oriented nanowires<sup>194</sup> and sensor/actuator arrays.<sup>195-197</sup>

## 5.1 Controlling domain size in P123 templated films through adjusting the relative humidity

Thin mesoporous silica films have been used extensively throughout this work. Their synthesis is well-known to be extremely sensitive on changes in the synthesis conditions.<sup>198</sup> Here, variations in the relative humidity during thin film condensation are used to create large domains in P123 templated films.

### 5.1.1 Introduction to the sample systems: preparation and characterization

Thin Pluronic P123 templated mesoporous silica films were synthesized again *via* an Evaporation Induced Self-Assembly (EISA) process through spin-coating a precursor solution. First 2.08 g (0.01 mol) tetraethyl orthosilicate (Aldrich) were mixed with 3 g of HCl (0.2 mol/L), 1.8 g of water and 7.9 g of ethanol and heated at 60 °C for 1 h to accomplish acid-catalysed hydrolysis and subsequent condensation of the silica precursor. This solution was mixed with a second solution containing 750 mg (0.013 mol) of Pluronic P123 (BASF) and 15.8 g of ethanol. Finally, a terrylene diimide dye derivative (N-(2,6-Diisopropylphenyl)-N'-(n-octyl)-terrylene-3,4:11,12-tetracarboxidiimide, AS-TDI)<sup>70</sup> kindly provided by the group of K. Müllen (MPI for

## 5.1 Controlling domain size in P123 templated films through adjusting the relative humidity

Polymer Research, Mainz, Germany) was added to the precursor solution at an ultralow concentration ( $10^{-10}$  –  $10^{-11}$  mol/L). The dye shows excellent photo-physics (high quantum yield and photostability) and is thus ideal for single molecule microscopy (see Figure 5.1 for the structure of the dye). 80  $\mu$ l of the dye containing precursor solution were then spin-coated onto a coverslip at 3000 rpm for 60 s. The relative humidity during spin-coating could be adjusted by mixing a dry stream of pressurized air with a humidified stream. The RH during the measurement could be adjusted likewise. The thin films were stored after synthesis for 3 h at a controlled RH prior to the measurement. Throughout the further experiments depicted in this chapter, the following relative humidities are differentiated: the spin-coating RH (scRH), the RH in which the samples were stored for the first 3 h after synthesis (stRH) and the measurement RH (mRH). Two sample types (d) and (w) synthesized under different humidity conditions are compared in this study: (d): scRH: 28%, stRH: 28%, mRH: 39% and (w): scRH: 57%, stRH: 57%, mRH: 39% indicating the “dry” and “wet” synthesis and storage conditions. For the sake of comparability the samples were measured at the same RH of 39%. The relative humidities listed here were measured with an accuracy of  $\pm 2\%$ .

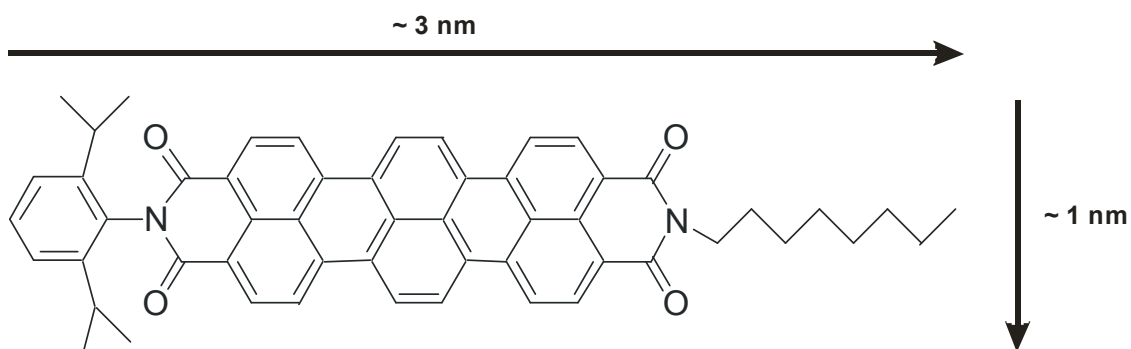


**Figure 5.1: Structure of AS-TDI, a terrylene diimide derivative.**<sup>70</sup> This dye is highly photostable and shows a good quantum. It is thus ideal for single molecule studies.

The thin films synthesized according to that protocol were characterized via 1D X-ray diffractometry (see Figure 5.2) by B. Platschek and M. Riederer (AK Prof. Bein, LMU München, Germany). Sample (d) (black) and (w) (blue) both exhibit 2D hexagonal order. From the  $2\theta$ -values the pore-to-pore distances  $a_0$  can be calculated yielding  $a_0(\text{d}) = 10.1 \text{ nm} \pm 0.2 \text{ nm}$  and  $a_0(\text{w}) = 10.3 \text{ nm} \pm 0.2 \text{ nm}$ . The pore-to-pore distance in both samples is thus equivalent. The additional signals in the X-ray diffractogram of sample (d) (black) are so-called Kiessig fringes that can be observed upon reflection of monochromatic X-rays from thin films.<sup>199</sup> They arise

from the interference of two reflected waves: one reflected from the surface of the thin P123 templated film, the second reflected from the mesoporous film-glass coverslip interface.<sup>200</sup> The Kiessig fringes only occur if the thin mesoporous film is very flat showing a homogeneous surface. They can be used to deduce film thickness. The appearance of those fringes does not at all indicate a poor quality of the thin film.

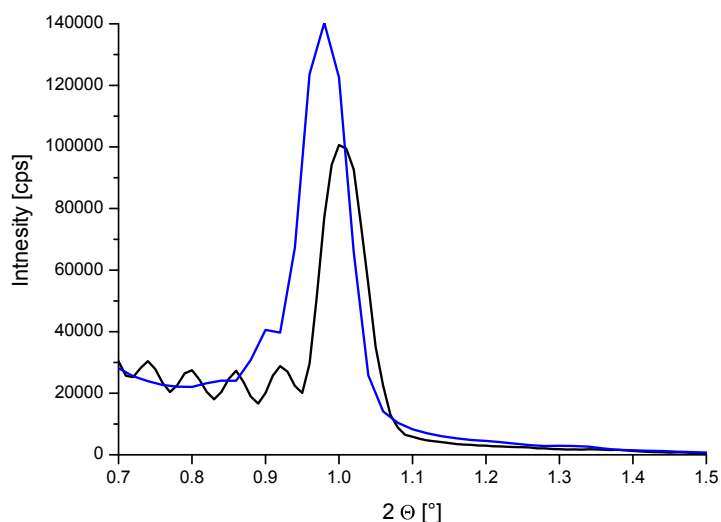


**Figure 5.2: 1D XRD diffractometry.** 1D X-ray diffractograms of the sample (d) (black) and the sample (w) (blue). (d): scRH: 28%, stRH: 28%, mRH: 39% and (w): scRH: 57%, stRH: 57%, mRH: 39%. Both samples exhibit 2d hexagonal order.

### 5.1.2 Relative humidity dependent domain formation observed through single molecule diffusion

Testing the domain size inside mesoporous silica films is not straightforward. Diffractometry techniques (XRD, GISAXS, etc.) suffer from the low sample volume of the thin films and do only yield averaged values for the region exposed to the rays. Transmission Electron Microscopy (TEM) can offer valuable insights into the structure of mesoporous silica, however scanning a larger sample area several micrometers in size requires the acquisition of numerous individual images which is very time-consuming. In contrast, the single molecule techniques applied earlier in this work proved very useful to gain information about mesoporous silica materials. In the previous chapter SMM was utilized primarily to extract dynamical information about the

guest molecules and drugs moving inside the porous network. In contrast, in this chapter SMM is used to reveal mainly structural information about the nature of the host material. In the past SMM was utilized repeatedly with great success to extract structural details of the host structure.<sup>91, 93-95</sup> The individual molecule is used as a beacon that sheds light onto the channel network. It is an extremely efficient probe for the characterization of its immediate environment. A molecule that is mobile or that can be mobilized can travel throughout the porous network and thereby cover micrometer long distances inside the film. Consequently, the molecule gathers an incredible amount of information along its walk. We simply need to find a way to access this information.

The thin films were investigated by wide-field microscopy on an Eclipse TE200 (Nikon) epifluorescence microscope with a high numerical aperture oil-immersion objective (Nikon Plan Apo 100\*, NA = 1.40). The molecules were excited at 633 nm with a He-Ne gas laser with an intensity of  $0.18 \text{ kWcm}^{-2}$  and their fluorescence was detected with a back-illuminated electron multiplying charge-coupled device (EM-CCD) camera in frame transfer mode (Andor iXon DV897,  $512 * 512$  pixels). Incident laser light was blocked by a dichroic mirror (640 nm cutoff, AHF) and a bandpass filter (730/140 AHF) (see Chapter 3.2.1.2).

With the above setup movies of the dye dynamics in the differently synthesized thin films, (d) and (w), were acquired with an integration time of 25 ms per frame and trajectories of the individual molecules were extracted (see Chapter 3.2.1.3 for details). Typical trajectories for both samples (d) and (w) are displayed in Figure 5.3. The difference is evident. In Figure 5.3 a the trajectory appears random and unstructured even though the molecules are inside the mesoporous structure since they could not be washed off. In case the molecules diffuse on the film surface, they can be easily removed by washing. In contrast, Figure 5.3 b shows a trajectory which is nicely structured. The molecule diffuses throughout the channel network and thereby accesses different domains.

In order to quantitatively compare the domain formation in both samples, methods to extract the domain size are necessary. Yet, this is not trivial at all, since no clear definition of the term 'domain' exists for these materials. Generally, a domain is usually referred to as a bundle of parallel aligned channels with the same orientation. Domain boundaries are then considered to be regions, where bundles of channels of very different orientation intersect one another.

These domain boundaries are often accompanied by dead-ends, where the intersecting channels are not connected. However, this definition is somewhat arbitrary since no clear parameters are described for a domain and a domain boundary. In order to be able to compare the samples (d) and (w) with respect to the domain size the following procedure was chosen within this work. 20 molecules were tracked from sample (d) and 50 molecules from samples (w). In the evaluated trajectories of sample (d) (see Figure 5.3 a) the domain size is so small that no individual domains could be recognized. Hence, the domain size must lie below the resolution limit, which is given by the positioning accuracy of the trajectory (about 35 nm for Figure 5.3 a, indicated by light blue squares). In contrast, the trajectories of sample (w) that show clearly visible domains (see Figure 5.3 b), were evaluated by manually measuring the areas the different domains cover. The evaluated domains in the trajectory of Figure 5.3 b are marked in red. Out of the 50 recorded trajectories of sample (w) 21 domains were measured, yielding 21 individual domain areas  $A_i$ . This directly yields a mean domain area  $\langle A \rangle$ , from which the mean domain size  $\langle d \rangle$  was calculated as the square root.  $\langle d \rangle$  was found to be  $300 \text{ nm} \pm 30 \text{ nm}$ . The apparent difference in domain size observed between Figure 5.3 a and b was created simply due to the different humidity conditions during thin film synthesis and storage in the first 3 h after synthesis.

The above utilized method proved very useful to determine domain sizes reproducibly. Nevertheless also this approach suffers from limitations. For example, molecules that access adjacent channels through openings in the pore walls instead of diffusing along one channel can yield a high domain size as well. However, nicely defined domains should show only a minimum number of defect openings between adjacent channels.

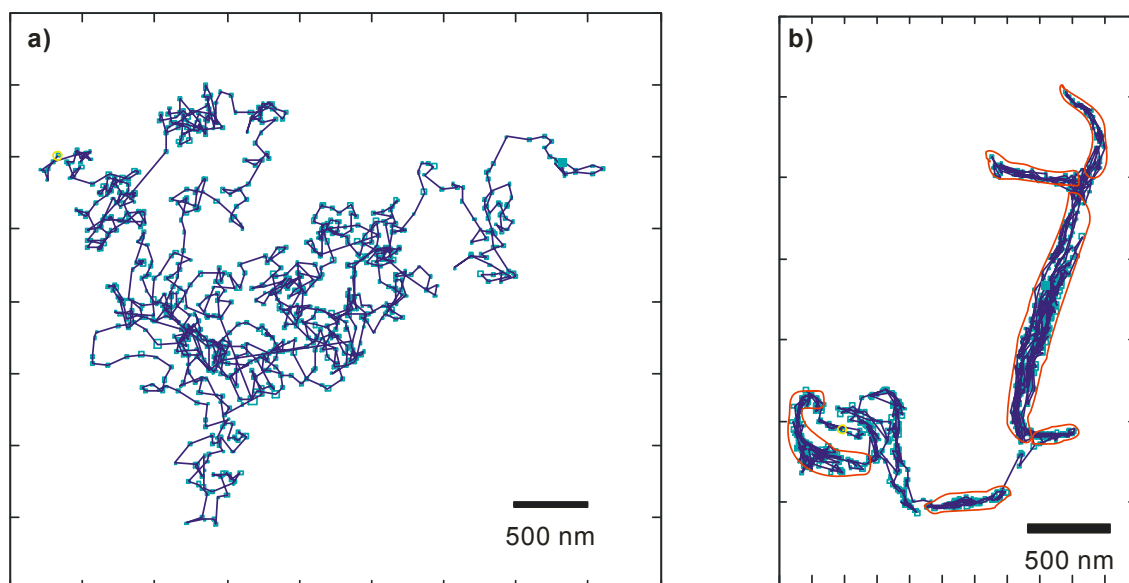


**Figure 5.3: Trajectories of single AS-TDI molecules inside P123 templated films synthesized under different humidity conditions.** a) (d): scRH: 28%, stRH: 28%, mRH: 39%. b) (w): scRH: 57%, stRH: 57%, mRH: 39%. Evaluated domains from this trajectory are marked in red.

Since sample (w) shows large domains this sample was investigated in greater detail in order to learn more about the nature of the domains. Figure 5.4 shows additional trajectories revealing further structural information. In Figure 5.4 a the molecule probes nicely structured domains. In contrast, Figure 5.4 b shows a molecule travelling first throughout structured regions in the film, then crossing an unstructured region and finally entering a structured region again. The unstructured part of the trajectory can result from a temporary movement of the molecule on the film surface or from a transit through an unstructured defect region inside the film. Figure 5.4 c shows a molecule also starting in structured domains, then diffusing in an unstructured manner and finally getting trapped at an adsorption site (e.g. a defect or a local confinement). These trajectories show that even under favourable humidity conditions the materials show additional adsorption and defect sites.

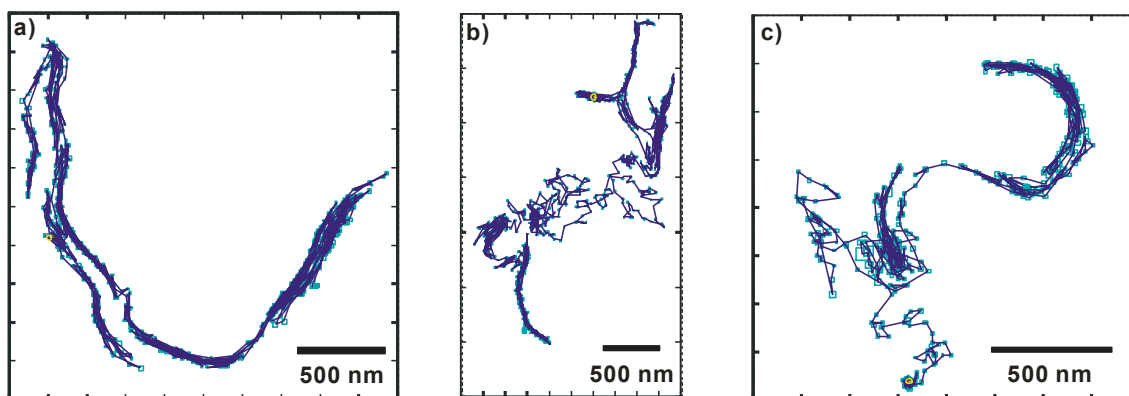


**Figure 5.4: Trajectories from sample (w) yielding further structural information.** Sample (w): scRH: 57%, stRH: 57%, mRH: 39%. Trajectories showing a) large nicely structured domains. b) a molecule first diffusing inside a nicely structured region of the film, then crossing an unstructured region or accessing the film surface and finally entering structured domains again. c) a molecule experiencing three different regions in a thin film: first probing structured domains, then switching to an unstructured region and finally getting trapped in a confinement or at a defect site.

From the trajectory data sets (20 molecules for sample (d) and 50 molecules for sample (w)) the mean square displacement curves for each individual molecule were extracted (Figure 5.5). The MSD curves of the molecules in sample (d) are depicted in blue whereas the data of sample (w) is displayed in red. For both samples the vast majority of molecules are mobile. Occasionally, an immobile molecule showing a flat MSD can be observed. This results from dye molecules getting trapped in small confinements or at defect sites. In order to quantify the dynamics of the mobile molecules the diffusion coefficient  $D$  was calculated for each individual molecule of the mobile population assuming a 2D random walk and fitting the MSD curve to Eq. 3.5. This yields the following mean diffusion coefficients  $\langle D_{dry} \rangle$  and  $\langle D_{wet} \rangle$  for the samples (d) and (w):  $\langle D_{dry} \rangle = 1.28 * 10^5 \text{ nm}^2/\text{s} \pm 4.16 * 10^4 \text{ nm}^2/\text{s}$  and  $\langle D_{wet} \rangle = 5.11 * 10^4 \text{ nm}^2/\text{s} \pm 2.43 * 10^4 \text{ nm}^2/\text{s}$ . It is important to note that the large standard deviation does not mirror the error in determining the mean diffusion coefficient but displays the inherent heterogeneity of the samples (see Chapter 4.2.3). For the sake of comparability the mean diffusion coefficients were determined only from trajectories showing purely mobile molecules. Rare cases of trajectories with partially trapped molecules, such as in Figure 5.4 c, were omitted. For example, the trajectory of Figure 5.4 c can be attributed to one of the two red MSD curves lying clearly below the majority of the population in Figure 5.5. The diffusion dynamics between structured and unstructured regions of a trajectory did not vary significantly.

Interestingly, the mean diffusion coefficient for sample (w) synthesized in wet conditions and showing structured diffusion is slightly lower compared to sample (d). According to the X-ray data the pore-to-pore distance in both samples is equivalent (about 10 nm). The difference in  $\langle D \rangle$  cannot be attributed to a different amount of water inside the pores since both samples were measured at the same mRH (after 10 min exposure to this mRH to give the samples time to equilibrate). If the higher humidity from the synthesis process would have remained inside the pores of sample (w), then a higher mean diffusion coefficient would be expected for this sample (in analogy to the experiments of Chapter 4.2.3). However, the opposite was observed. The slight difference in  $\langle D \rangle$  could be explained by the data evaluations. In order to compare the diffusion dynamics the MSDs from sample (d) and (w) were fitted with a 2D random walk according to Eq. 3.5. The trajectories of sample (d) (see Figure 5.3 a) can be fitted well by this model. In contrast, the trajectories of sample (w) (see for example Figure 5.3 b) show a dynamic that deviates from a random walk due to the confinement of the channels. Consequently, the utilized model yields for sample (w) a slightly lower mean diffusion coefficient.

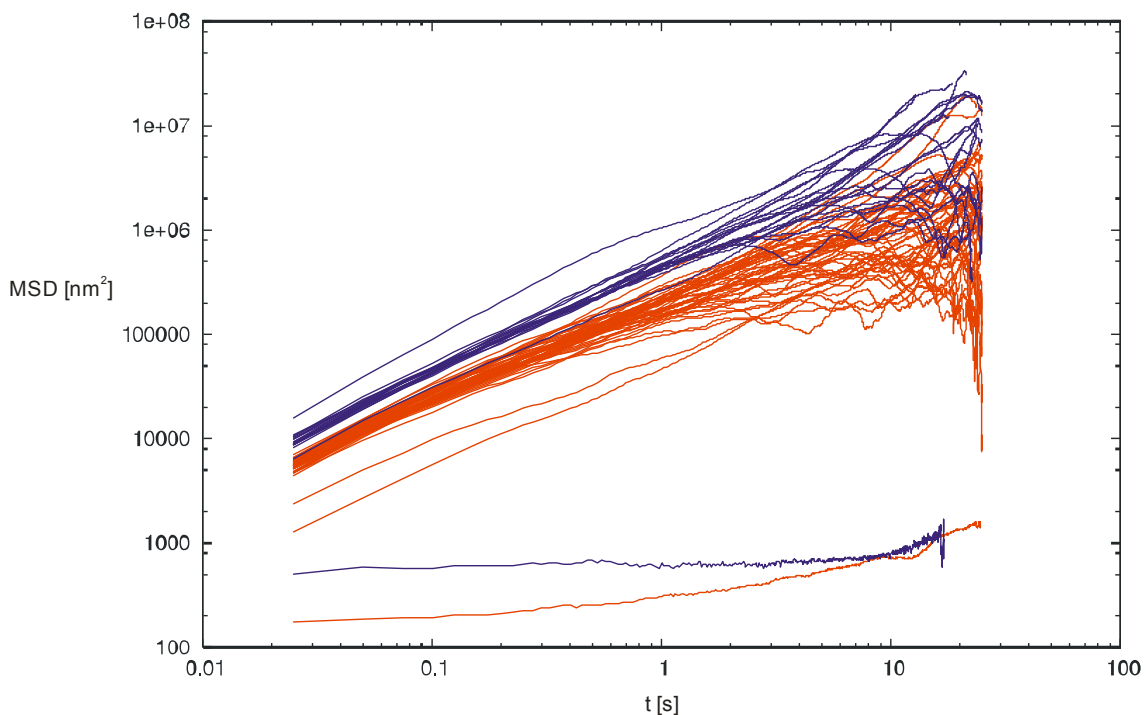


**Figure 5.5: Mean square displacement curves for the individual molecules measured in the samples (d) (blue) and (w) (red).** The MSD is plotted as a function of time. (d): scRH: 28%, stRH: 28%, mRH: 39%. (w): scRH: 57%, stRH: 57%, mRH: 39%.

The results discussed in this chapter are summarized in Table 5.8.

**Table 5.8: Relative humidity dependent domain formation.**

Sample	(d)	(w)
# evaluated molecules	20	50
domain size	< 35 nm	300 nm $\pm$ 30 nm
$\langle D \rangle$	$1.28 * 10^5 \text{ nm}^2/\text{s}$	$5.11 * 10^4 \text{ nm}^2/\text{s}$
$\sigma$	$4.16 * 10^4 \text{ nm}^2/\text{s}$	$2.43 * 10^4 \text{ nm}^2/\text{s}$

### 5.1.3 Conclusion

In summary, it could be shown that the domain size inside P123 templated thin films can be controlled through adjusting the relative humidity during the EISA process (spin-coating) and in the immediate time period after coating. Directly after evaporation induced self-assembly the thin films are still very sensitive and film condensation is ongoing, hence the relative humidity was kept constant for three hours after synthesis. Large domains about 300 nm in size could be synthesized through applying a relative humidity of 57%. In contrast, thin film synthesis under “unfavourable” humidity conditions (28% RH) results in domain sizes below the resolution limit of 35 nm due to the accuracy of molecular positioning. This demonstrates how sensitive the thin film synthesis reacts to changes in the surrounding environment. The above discussed insights could only be gained through highly sensitive single molecule techniques and would have been obscured to a large extent by other characterization techniques such as diffractometry. This study contributes to a profound understanding of the intricate mechanisms that govern domain growth and size inside silica materials. These insights are important since obtaining highly ordered mesoporous silica with only few defects is crucial for making these materials accessible for industrial applications.

## 5.2 Active patterning of channel alignment in mesoporous silica through Micromoulding in Capillaries

The next logical step in maximizing the application potential of mesoporous silica is an active patterning, *i.e.* a tailor-made design of the orientation of the channels inside porous silica materials. If a control over this parameter can be gained the materials will reach the ultimate level of versatility and they can be fabricated entirely according to the specific requirements of a given application. This would make them an even more powerful tool in the evolving field of nanotechnology.

In order to realize such an active patterning a technique called Micromoulding in Capillaries (MIMIC) is applied. MIMIC was introduced for mesoporous silica towards the end of the 1990s (for details see Chapter 2.2).<sup>59, 60</sup> In this thesis, MIMIC is used to synthesize macroscopically sized linearly oriented silica channel networks since these pore topologies are very interesting for future applications such as electrophoresis or catalysis. The work displayed in this chapter results from a close collaboration with the research group of T. Bein (LMU Munich, Department of Chemistry, Munich, Germany). In this chapter, first the detailed preparation and characterization procedures for actively patterned mesoporous silica structures are explained. The synthesis of the mesoporous samples as well as the entire characterization measurements depicted in Chapter 5.2.1 were done by B. Rühle in the group of T. Bein. They are displayed in this thesis since they are essential for understanding the experiments in the following second subsection, where single molecule measurements are used to gain insight into the channel orientation inside these materials.

The study presented here shows the first experiments with these novel fascinating materials. The experiments were conducted towards the end of the doctoral studies and they were planned to continue after this time. Consequently, this chapter only reports about the first experimental findings of this project but cannot yield a comprehensive model for all observed phenomena. Nevertheless, basic parameters will be determined to explain the key experimental observations.

### 5.2.1 Introduction to the sample systems: preparation and characterization

In order to fabricate mesoporous silica with actively patterned domains two “components” need to be brought together: a patterned stamp acting as structure-guiding form and the precursor solution for the mesoporous silica (see Figure 2.2 in Chapter 2.2).

The utilized patterned stamp consists of poly(dimethylsiloxane) (PDMS). In the confinements of the stamp pattern mesoporous silica can condensate and the resulting mesopore channel orientation is influenced by the form of the pattern. Stamps with different patterns were used throughout this study and will be introduced later.

For the synthesis of the mesoporous silica the following precursor solution recipe was used: 1.0 g tetraethyl orthosilicate (TEOS, 4.8 mmol) and 0.105 g of a 1 mol/L hydrochloric acid (0.105 mmol) were dissolved in 4.40 g ethanol (absolute, 95.5 mmol) and 0.7 g of water (39 mmol). This solution was stirred at 300 rpm in a closed pot for 1 h at 65 °C. Next, 0.475 g of the tri-block copolymer Pluronic F127 ( $\text{EO}_{106}\text{PO}_{70}\text{EO}_{106}$ , 35.4  $\mu\text{mol}$ ), the structure directing agent, were dissolved in 4.40 g of ethanol (absolute, 95.5 mmol). This template solution was stirred at 300 rpm for 1 h in a closed pot at ambient temperature. Then the template solution was added dropwise under stirring (400 rpm) to the TEOS containing solution. This mixture was stirred again for at least 2 h at ambient temperature before it can be used for synthesis of mesoporous silica. In order to incorporate fluorescent guest molecules into the channel network of the porous materials the fluorophores need to be added to this precursor solution.

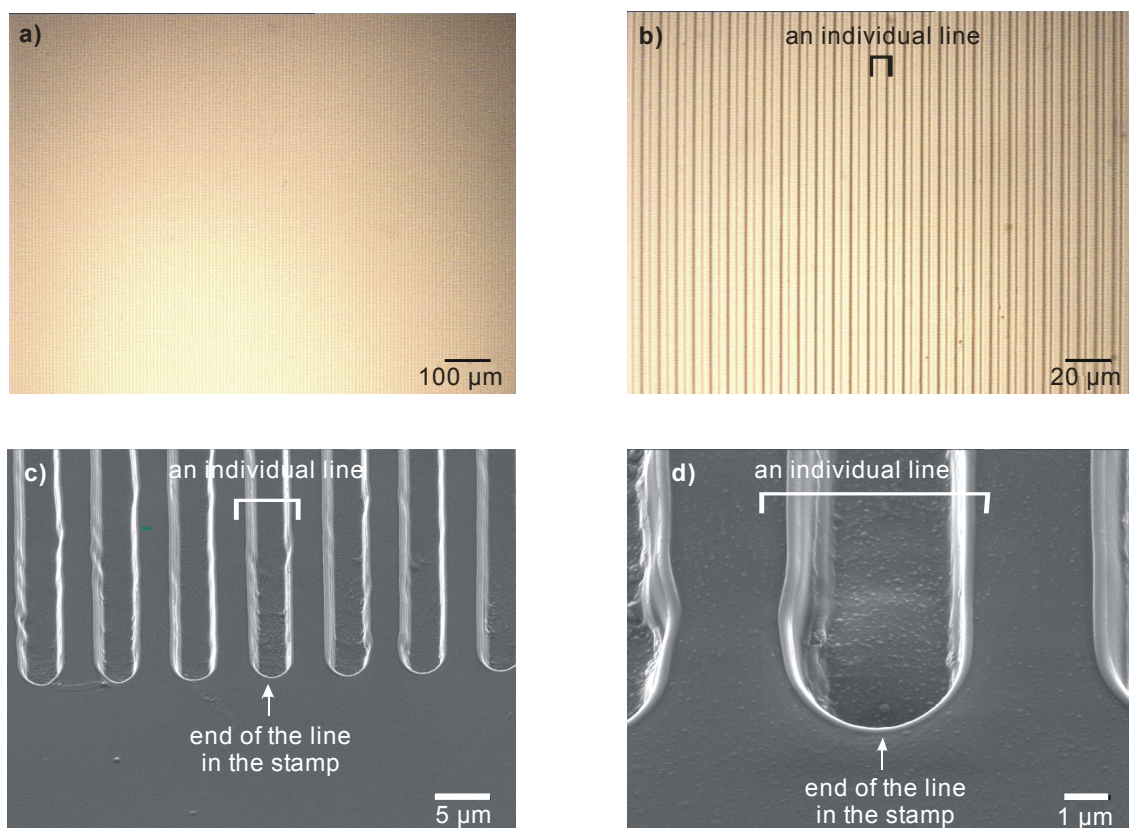
In the following paragraphs the stamps used in this study as well as the mesoporous silica fabricated through pattern transfer from the stamp will be characterized in detail. The samples were investigated using Light Microscopy (LM), Scanning Electron Microscopy (SEM), Atomic Force Microscopy (AFM) and 1D X-ray diffractometry (XRD) by B. Rühle in the group of T. Bein (LMU Munich, Department of Chemistry, Munich, Germany). LM images were acquired on a Olympus BH-2 Light Microscope, SEM micrographs were recorded on a JEOL JSM-6500F scanning electron microscope and AFM images were measured on a Nanoink NScriptor DPN

Writer Atomic Force Microscope. X-ray diffractograms were recorded using a Scintag XDS 2000 powder diffractometer in  $\theta/\theta$  Bragg-Brentano scattering geometry.

### 5.2.1.1 The PDMS stamps

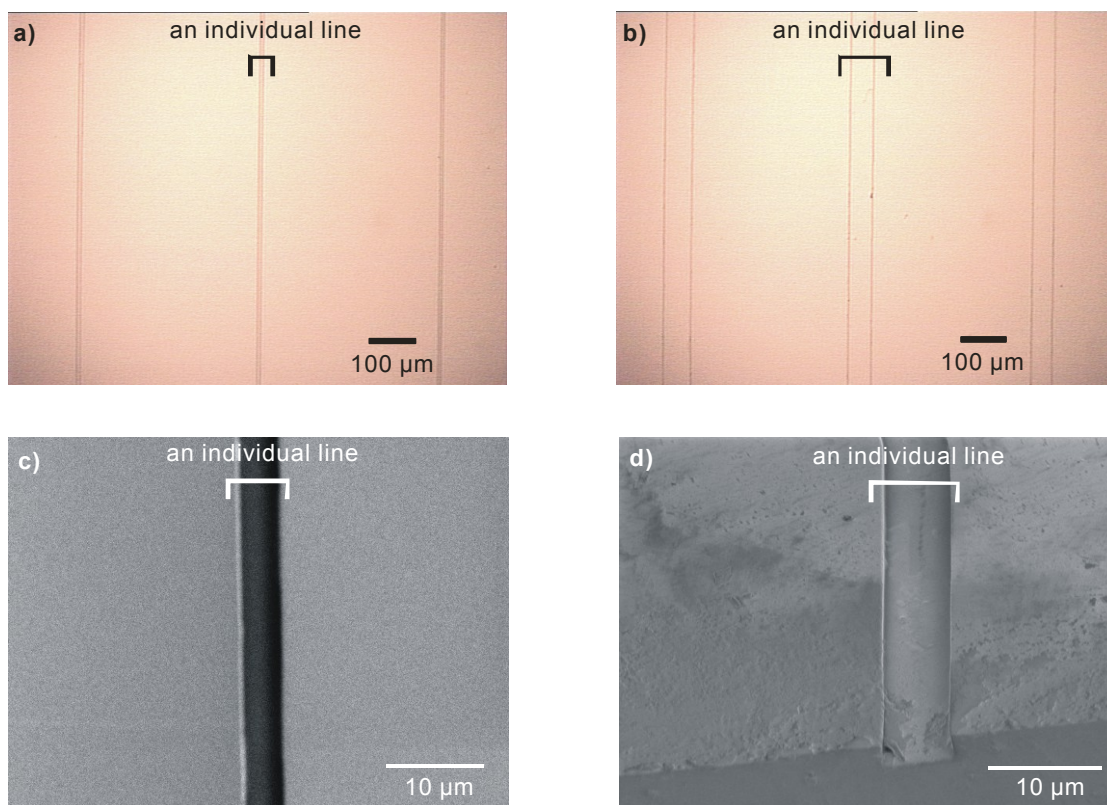
Two differently patterned PDMS stamps were used throughout this study: the so-called “UV-stamp I” and “UV-stamp II”. The denotation refers to the different manufacturing processes for creating the respective stamps.

Figure 5.6 shows LM and SEM images of the UV-stamp I. The stamp consists of PDMS and was created from a model (master) serving as a negative for the stamp. The pattern of the master was originally fabricated through UV-Lithography with the help of Y. Xiang in the group of G. Abstreiter (TU Munich, Walter Schottky Institute, Garching, Germany). Figure 5.6 a displays a Light Microscopy image of the PDMS stamp showing a large array of adjacent lines. The close-up in Figure 5.6 b shows the individual lines (marked with a black bracket) in more detail. An even more detailed view on the structure of the lines can be gained through Scanning Electron Microscopy (Figure 5.6 c). An individual line, marked in white is about 2  $\mu\text{m}$  deep ( $x$ , see Figure 5.8 for a schematic illustrating the stamp dimensions) and 4  $\mu\text{m}$  wide ( $y$ ). The spacing between adjacent lines is about 3  $\mu\text{m}$  ( $d$ ). Figure 5.6 d shows a close-up of the SEM image. The SEM images were taken close to the end of the stamp in order to show that the lines are closed at their ends. The relevance of this will be explained later.



**Figure 5.6: Light and Scanning Electron Microscopy images of the UV-stamp I (measured by B. Rühle<sup>201</sup>).** a) and b) show Light Microscopy images, whereas c) and d) show SEM images. An individual line is marked with a black bracket (c) and with a white bracket (c and d). The SEM images (c and d) were recorded close to the end of the stamp thus also displaying the end of the line, which is closed.

Finally, the UV-stamp II was characterized (Figure 5.7). The stamp consists of several individual hollow lines. Their width  $x$  ranges from 1.5  $\mu\text{m}$  up to several mm and increases gradually from line to line (see Figure 5.8). All lines of the stamp pattern are about 2  $\mu\text{m}$  deep ( $y$ ). Figure 5.7 a shows the narrow lines on one side of the stamp and Figure 5.7 b shows larger lines more in the center of the stamp. In both images an individual line is marked by a black bracket. The individual lines in the stamp are separated by about 200 – 400  $\mu\text{m}$  ( $d$ ). A SEM image of one of the lines from this UV-stamp II is given in Figure 5.7 c. In Figure 5.7 d the end of such a line at the lower end of the stamp is shown. One can clearly see that the line is open at the end in contrast to the lines in UV-stamp I (see Figure 5.6 d). This is typical for the UV-stamp II. The relevance of these openings will be explained later.



**Figure 5.7: Light and Scanning Electron Microscopy images of the UV-stamp II (measured by B. Rühle<sup>201</sup>).** a) and b) show Light Microscopy images, whereas c) and d) show SEM images. An individual hollow line is marked with a black bracket (a and b) and with a white bracket (d and e). d) This SEM image shows that the individual lines in the stamp are open at the end.

Figure 5.8 shows a schematic of the stamp thereby illustrating the stamp dimensions of UV-stamp I discussed in Figure 5.6 and UV-stamp II introduced in Figure 5.7. For the samples prepared with UV-stamp II the stamp and substrate polarity was modified. This will be discussed in Chapter 5.2.1.2.

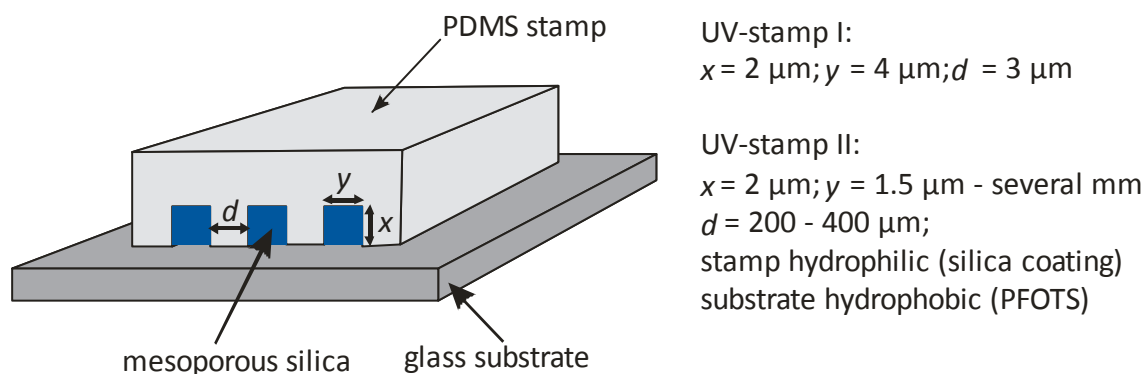


**Figure 5.8: Schematic view illustrating the stamp dimensions.** The dimensions of the lines in UV-stamp I and II are displayed. For the samples prepared with UV-stamp II the glass substrate was coated with a hydrophobic layer of *1H,1H,2H,2H*-perfluorooctyltrichlorosilane (PFOTS) and the stamp was prepared with a hydrophilic tetraethyl orthosilicate (TEOS) coating.

### 5.2.1.2 The mesoporous silica created through pattern transfer

After introducing the utilized stamps, now the mesoporous silica fabricated through pattern transfer via Micromoulding in Capillaries will be characterized. Details of the MIMIC technique were introduced in Chapter 2.2.

The mesoporous silica created with the help of UV-stamp I was characterized with Atomic Force and Scanning Electron Microscopy (Figure 5.9). The pattern transfer was achieved through pressing the stamp onto a droplet of the silica precursor solution (see Figure 2.2) and giving the solvents at least 24 h time to evaporate and the porous silica to condense. Figure 5.9 a shows an AFM image of two adjacent lines of mesoporous silica. They are each about  $1.9 \mu\text{m}$  in height. This shows that the precursor solution fills the pattern cavities nearly completely (compare to Figure 5.8). The SEM image in Figure 5.9 b shows a cross-section of several adjacent lines of mesoporous silica (an individual line is marked in white). In the close-up of Figure 5.9 c an individual line of silica can be seen. In the upper part an elliptically shaped bubble can be found, which is either an air bubble resulting from an incomplete filling of the

PDMS stamp during stamping. On the other hand this defect could have been created upon breaking the sample for recording the cross-section.

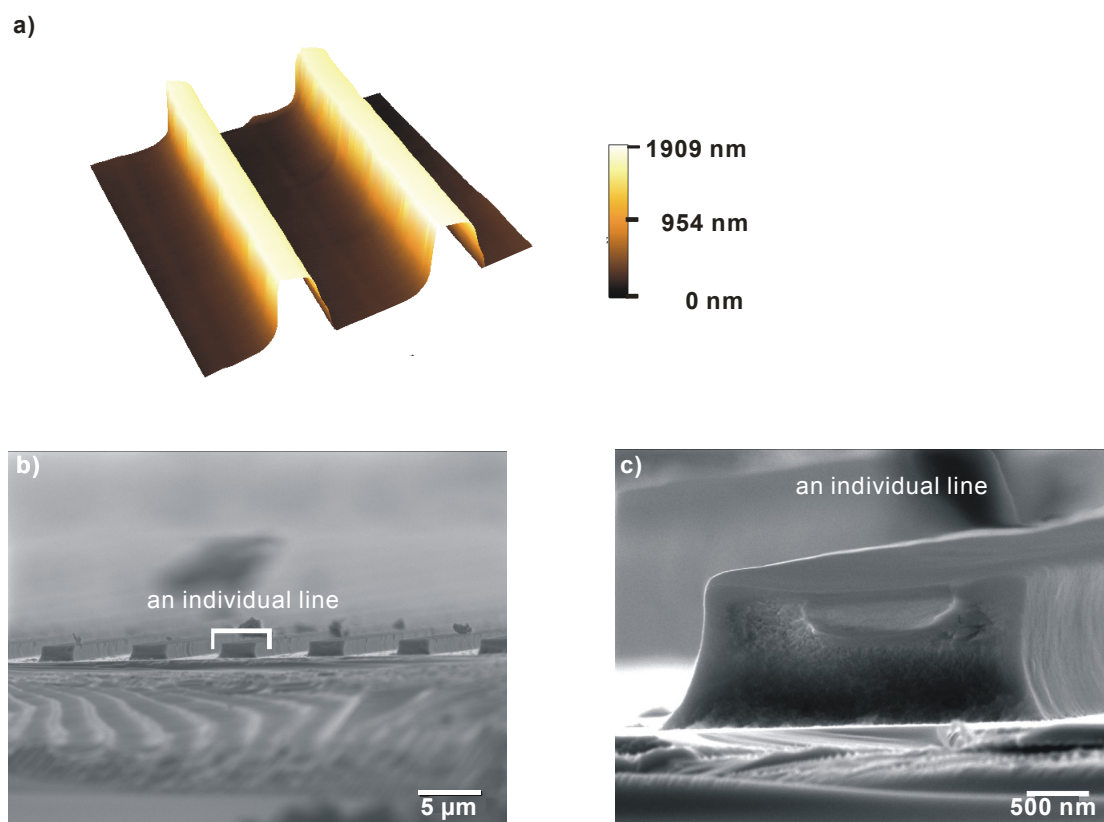


**Figure 5.9: Atomic Force and Scanning Electron Microscopy images of mesoporous silica fabricated through pattern transfer from the UV-stamp I (measured by B. Rühle<sup>201</sup>).** a) AFM image. The mesoporous silica formed is about 1.9 μm in height. SEM cross-sections showing b) a series of fabricated adjacent lines of mesoporous silica and c) an individual line of mesoporous silica formed.

Next, Figure 5.10 shows an AFM image from a line of mesoporous silica created through pattern transfer from the UV-stamp II. This pattern transfer was achieved by adding droplets of the precursor solution at both ends of the stamp such that the solution gets sucked into the stamp due to capillary forces (see Figure 2.2). The sample was then investigated only 24 h after preparation such that the solvents can evaporate and the mesoporous silica can condense. A combination of a hydrophilic stamp and a hydrophobic surface was chosen for the experiments for the following reasons. The precursor solution for the mesoporous silica consists of an ethanol/water mixture and is thus quite hydrophilic. In combination with a stamp that is hydrophobic the solution does not fill the stamp pattern efficiently since it does not get sucked in appropriately (data not shown). Furthermore, a hydrophobic glass substrate was chosen

since recent work<sup>202</sup> demonstrated that the polarity of the contact surfaces (from the silica to the stamp and from the silica to the glass cover slip) can influence the orientation of the silica channels. The UV-stamp II and the cover slip were prepared in the following way (see also Figure 5.8).

First, the PDMS stamp was put into an oxygen plasma for 90 s. After that the stamp was stored 3 h in a 3 mmol/L aqueous solution of tetraethyl orthosilicate which was acidified by adding 0.8  $\mu$ l of a 37% hydrochloric acid (fuming) per ml of water. This leads to a hydrophilization of the stamp since its surface gets covered with silicate.

Throughout the experiments it proved useful for the pattern transfer to coat the substrate, the glass cover slip, hydrophobic. This was realized by putting the cover slip into an oxygen plasma for 15 min. After that the cover slip was incubated for 3 h in an evacuated desiccator in which 100 mL of 1*H*,1*H*,2*H*,2*H*-perfluorooctyltrichlorosilane (PFOTS) were stored in a Petri dish in order to create a PFOTS atmosphere. This results in a hydrophobic layer of PFOTS on the cover slip.

In Figure 5.10 a it can be seen that the line of mesoporous material is not totally perfect. For example on the left side of the material, defects can be shown. This indicates that even for a favourable stamp-substrate-polarity an incomplete filling of the pattern with precursor solution occurs. However, only Figure 5.10 b shows the topology of the material in detail. This AFM data reveals that the pattern indeed does not get filled totally. The height of the pattern in the stamp is about 2  $\mu$ m. It is clearly evident that in the upper part of the structure close to the stamp the porous silica is distributed inhomogeneously. At the sides of the line, the materials reaches high up, whereas towards the center of the line the structure shows a U-shaped dip. This can result from a turbulent mixing during flushing the pores. Probably not all air inside the pattern can be released and this contributes to the observed incomplete filling with precursor solution. Even though the stamp pattern does not get completely filled in contrast to Figure 5.9, where the stamp was simply pressed onto the precursor solution, the method of filling the stamp through capillary forces can be useful since these capillary forces can influence the channel orientation. This influence will be discussed in detail in Chapter 5.2.2.

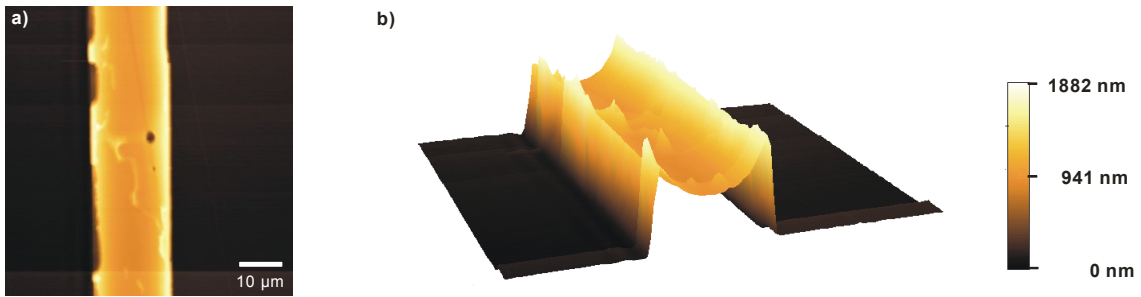


**Figure 5.10: AFM measurements of mesoporous silica created through pattern transfer from the UV-stamp II (measured by B. Rühle<sup>201</sup>).** a) Top view on the line of mesoporous silica. b) Side view showing the height of the line and its profile.

The structure of the mesoporous silica synthesized according to the above described methods can be tested through 1 D X-ray diffractometry. However, the amount of material provided by the synthesized MIMIC samples is too low for this characterization method such that XRD data can only be acquired from a model system: a dip-coated thin film was used (see **Figure 2.1** for details concerning dip-coating). Figure 5.11 shows a 1D X-ray diffractogram of such a F127 templated thin film. The data indicate that the precursor solution is capable of forming hexagonal porous structures. A  $2\theta$ -value of 0.72 was observed. This corresponds to a pore-to-pore distance of 14 nm.

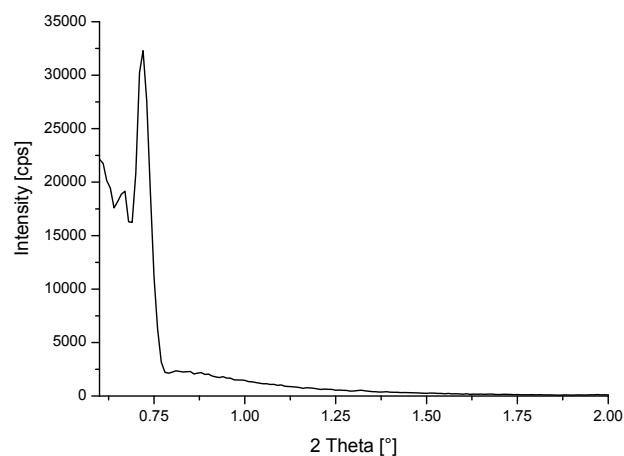


**Figure 5.11: X-ray diffractogram of a F127 templated mesoporous silica thin film (measured by B. Rühle<sup>201</sup>).** The utilized precursor solution is capable of forming hexagonal porous structures.

## 5.2.2 Characterizing channel alignment in actively patterned mesoporous silica with the help of single molecule microscopy

Above, different routes of synthesizing mesoporous silica through MIMIC in the confinements of PDMS stamps were introduced. However, with the characterization techniques used in the last chapter only the general morphology of the mesoporous silica was assessed. Now, efficient ways of testing the channel orientation inside the samples are needed, in order to test whether the pattern of the stamp influenced the channel orientation. Especially macroscopically sized linearly oriented channels are a desired morphology for mesoporous silica since many applications could profit from such tailor-made samples.

Diffraction based methods do not offer information about the channel orientation in the sample over macroscopic length scales (several cm) in an easy to access way. Moreover, they suffer from some critical limitations such as the small sample volume and they yield only averaged information about the irradiated areas. Solely by accurately mapping the motion of individual particles throughout their diffusion inside the materials an overview about the channel orientation inside the materials can be gained within a reasonable time. Single molecule approaches can thus contribute significantly to a better comprehension of this novel class of nanomaterials. Additionally, single molecule techniques are non-invasive and the samples do not require a special treatment prior to the measurement. Consequently, the sensitive domains cannot get altered due to the measurement conditions

Single molecule fluorescence images of the synthesized samples were recorded on an Eclipse TE200 (Nikon) epi-fluorescence microscope with a high numerical aperture oil-immersion objective (Nikon Plan Apo 100\*, NA = 1.40). AS-TDI (see Chapter 5.1.1 for details), a highly photostable fluorophore with excellent quantum yield, was incorporated into the materials in single molecule concentrations ( $10^{-10}$  –  $10^{-11}$  mol/L). The dye was kindly provided by the research group of K. Müllen (Max-Planck-Institute for Polymer Research, Mainz, Germany). The molecules were excited at 633 nm with a He-Ne gas laser with an intensity of  $0.23 \text{ kWcm}^{-2}$  and their fluorescence was detected with a back-illuminated electron multiplying charge-coupled device (EM-CCD) camera in frame transfer mode (Andor iXon DV897,  $512 * 512$  pixels).

Incident laser light was blocked by a dichroic mirror (640 nm cutoff, AHF) and a bandpass filter (730/140 AHF). For a schematic view on the setup see also Chapter 3.2.1.2.

### 5.2.2.1 Pattern transfer from UV-stamp I

First, a mesoporous silica sample fabricated through pattern transfer from an UV-stamp I (see Figure 5.6) was investigated. As mentioned previously the stamp pattern was transferred by pressing the stamp onto a droplet of the dye containing precursor solution and the samples were investigated only 24 h after preparation to allow sufficient time for solvent evaporation and silica condensation. For the single molecule measurements depicted in this chapter the stamp remained always on top of the mesoporous silica formed since stamp removal can damage and alter the silica structures. To characterize domain formation overlays of individual fluorescence images from recorded wide-field movies are displayed. Through overlaying the fluorescent signals of the dynamic single molecules the domain orientation gets clearly visible and a “fingerprint” of the channel orientation in the material can be recorded. This is a direct, simple and non-invasive way of assessing the channel orientation inside the samples. Figure 5.12 shows such an overlay image. The white bars indicate the orientation of a line in the pattern of the stamp. According to the stamp dimensions (see Figure 5.8) the line width  $y$  is 4  $\mu\text{m}$  and the lines are separated by a distance  $d$  of 3  $\mu\text{m}$ .

Interestingly, the diffusion of the individual AS-TDI molecules and thus the channel orientation of the porous silica are perpendicular to the pattern orientation throughout the entire recorded region. However, in order to increase the applicability of actively patterned silica, the fabrication of linearly oriented channels of high length is necessary. Yet, this can only be realized if the orientation of the channels can be aligned along the pattern. To realize that, the complicated mechanisms that govern the channel orientation need to be understood. The experiments in the following chapter will help to identify relevant parameters that determine the channel orientation. In order to systematically approach this difficult problem, UV-stamp II is better suited since its pattern, in contrast to UV-stamp I, is not uniform. The changes in the pattern of UV-stamp II allow to assess the influence of the pattern characteristics on the orientation of the channels.

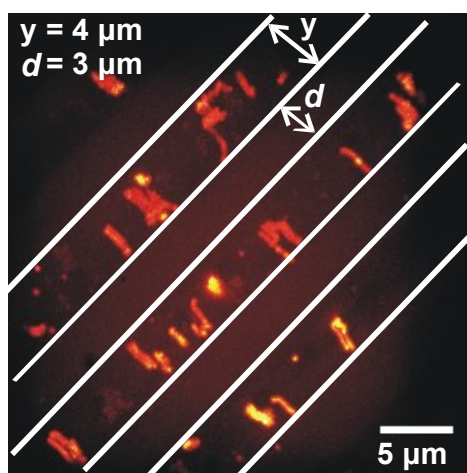


**Figure 5.12: Channel orientation inside mesoporous silica patterned by the UV-stamp I.** Overlay image of individual fluorescence images from a wide-field movie displaying AS-TDI diffusion inside the mesoporous silica. The dye motion reveals a “fingerprint” of the domain structure. The white bars indicate the orientation of a line in the pattern of the stamp. The line is  $4\ \mu\text{m}$  wide ( $y$ ) and the individual lines are separated by  $3\ \mu\text{m}$  ( $d$ ). The molecular diffusion reveals that the channels are aligned perpendicular to the pattern orientation.

### 5.2.2.2 Pattern transfer from UV-stamp II

The UV-stamp II was created with lines of different widths  $y$  ranging from  $1.5\ \mu\text{m}$  to several micrometers (see Figure 5.8) in order to assess the influence of the line width on the channel orientation. Furthermore, in contrast to the procedure described above for UV-stamp I, UV-stamp II was not pressed onto a droplet of the precursor solution but the solution was sucked into the stamp pattern by capillary forces (according to Figure 2.2 in Chapter Mesoporous Materials2.2). Consequently, the strength of the capillary force can be tested for their influence on the channel orientation.

Figure 5.13 displays results of mapping the channel structure in mesoporous silica fabricated through pattern transfer from the UV-stamp II. The mesoporous silica investigated in Figure 5.13 was measured in the same line of the pattern, yet at different distances from the ends of the stamp. Figure 5.13 a schematically depicts the different measurement positions. The data of Figure 5.13 b was acquired close to the end of the stamp whereas the data of Figure 5.13 c was measured close to the center of the stamp, but in both cases low in the material close to

the hydrophobic glass surface, since the data of Figure 5.10 indicate that the mesoporous structure formation is disturbed high up in the material column close to the stamp. The different measurement positions allow to assess the influence of the strength of the capillary flow on the channel alignment. Since the precursor solution droplets were placed at both ends of the stamp, the capillary flow is high for Figure 5.13 b and low for Figure 5.13 c since in the center of the stamp the flows from both sides mix. The line chosen from the stamp pattern shows a width  $y$  of about  $15\ \mu\text{m}$ . The line is indicated in Figure 5.13 b and c through white bars. In a region of high capillary flow (Figure 5.13 b) a high degree of alignment of the channels can be observed. Further, it is important to note that this measurement is the first proof of a successful alignment of the channels along the pattern lines in this study. This is an essential prerequisite for designing long macroscopically sized oriented channel structures since the stamps can basically be produced at any length. In contrast, Figure 5.13 c shows that close to the center of the stamp where the flow is slow and the both streams mix, the channel orientation gets changed. The orientation is less pronounced in the middle of the line and towards the outer edges of the line the channels get oriented again perpendicular to the line orientation. The loss of the channel alignment parallel to the pattern line for an increasing distance from the entrance to the stamp and thus for a decreasing strength of capillary flow is typical for all evaluated measurements, independent of the line width  $y$ . A high capillary flow seems to promote channel alignment along the pattern direction.

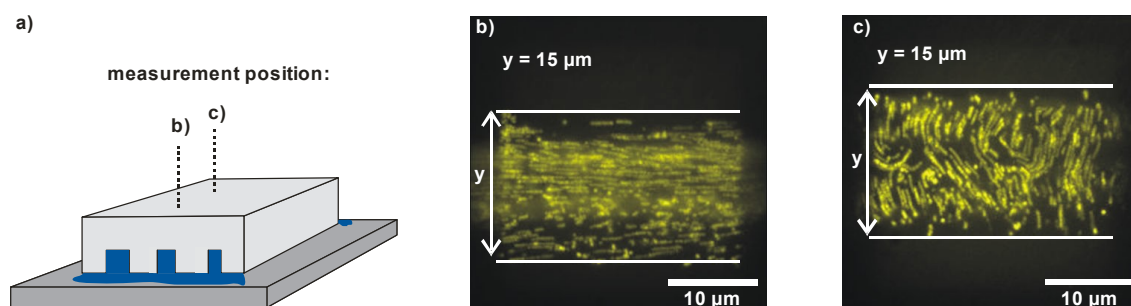


**Figure 5.13: Characterizing the influence of the capillary flow on the channel alignment of mesoporous silica formed *via* pattern transfer from the UV-stamp II.** a) Schematic indicating the different measurement positions of b) and c). The overlay images of b) and c) were measured in mesoporous silica of the same line width  $y$  of about  $15\ \mu\text{m}$  only at varying distances from the end of the stamp: b) close to the stamp end and c) close to the center of the stamp. Since the stamp was filled with the precursor solution through capillary flow b) and c) depict the influence of different strengths of the capillary flow. The white bars in b) and c) indicate the orientation of the line pattern in the stamp. The line selected from the stamp pattern shows a width  $y$  of about  $15\ \mu\text{m}$ .

Since the lines of the stamp pattern are about  $2\ \mu\text{m}$  deep ( $x$ , see Figure 5.8), with the wide-field microscope different height levels in the mesoporous silica can be observed. Figure 5.14 shows the results of such height depending measurements. In Figure 5.14 a schematic is shown depicting the different measurement positions for the data of Figure 5.14 b and c. The data was measured inside the mesoporous material in the same line of the stamp pattern, but at different height levels above the substrate: in the lower part of the material close to the glass substrate (b) and higher up in the material close to the hydrophilic stamp (c). The line selected from the stamp pattern shows a width  $y$  of about  $10\ \mu\text{m}$ . Figure 5.14 b shows a preferential alignment of the channels along the line of the pattern whereas in Figure 5.14 c the alignment changes. Especially near the outer edges of the line the channels are again aligned perpendicular to the orientation of the pattern. These results resemble the experimental findings of Figure 5.13. This is attributed to the following reasons. In the upper part of the silica material close to the stamp, the precursor solution gets more turbulently mixed and the mesoporous silica did not form properly according to the data of Figure 5.10. Furthermore, the glass substrate was prepared with a hydrophobic surface and the observed channel orientation is in good agreement with recent work revealing that channel alignment is indeed very dependent on the polarity of the contact surface.<sup>202</sup> It was shown that the channels align preferentially parallel to the pattern close to the hydrophobic glass substrate whereas the channels are oriented perpendicular to the pattern close to the hydrophilic stamp. However, if the stamp itself is prepared hydrophobic as well, the hydrophilic precursor solution does not efficiently get sucked into the stamp anymore because of the unfavourable surface polarity.

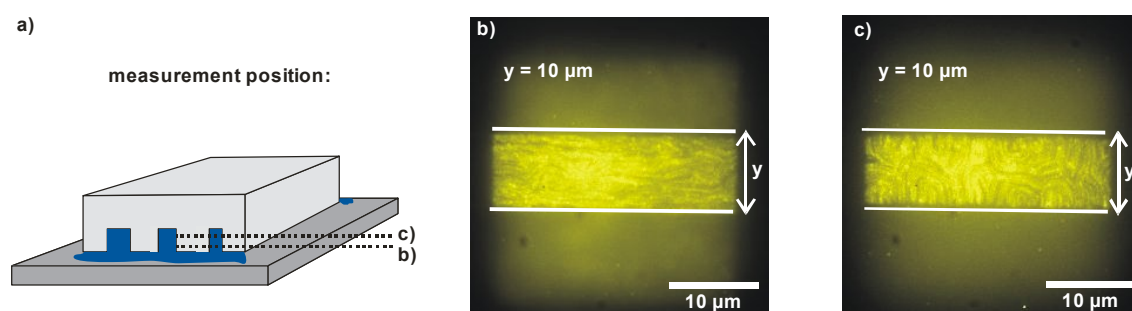


**Figure 5.14: Characterizing the channel alignment with varying height inside mesoporous silica material formed *via* pattern transfer from the UV-stamp II.** a) Schematic indicating the different measurement positions of b) and c). The overlay images of b) and c) were measured inside the mesoporous material in the same line of the stamp pattern, but at different height levels above the substrate: b) in the lower part close to the hydrophobic glass and c) higher in

the material close to the hydrophilic stamp. The white bars in b) and c) indicate the orientation of the line pattern in the stamp. The line selected from the stamp pattern shows a width  $y$  of about  $10\ \mu\text{m}$ .

If the capillary flow is a crucial parameter for the alignment of the mesoporous channels, then also a variation in the width  $y$  of the pattern line in the stamp should show an effect on that channel alignment. The wider the line, the weaker the capillary force will be. Figure 5.15 shows data of a measurement with variations in the line width  $y$ . A schematic displaying the different measurement positions is depicted in Figure 5.15 a). The overlay images were acquired in both cases in the lower part of the material close to the hydrophobic glass surface since we discussed in Figure 5.14 that the measurement height is also a critical parameter. Figure 5.15 b) shows a line of mesoporous silica created through pattern transfer from the UV-stamp II with a width  $y$  of about  $26\ \mu\text{m}$ , whereas the mesoporous silica shown in Figure 5.15 c) was fabricated in a line of about  $29\ \mu\text{m}$ . The loss in the alignment of the channels is clearly visible. Whereas the channels are well aligned in Figure 5.15 b), the channels in Figure 5.15 c) show domains of random orientation. Only at the edges of the line a slight preferential perpendicular direction can be assumed. This observation can be rationalized since the structure guiding contribution of the pattern gets reduced with increasing pattern width. This might result from an accompanying reduction in the strength of the capillary flow with increasing line width.

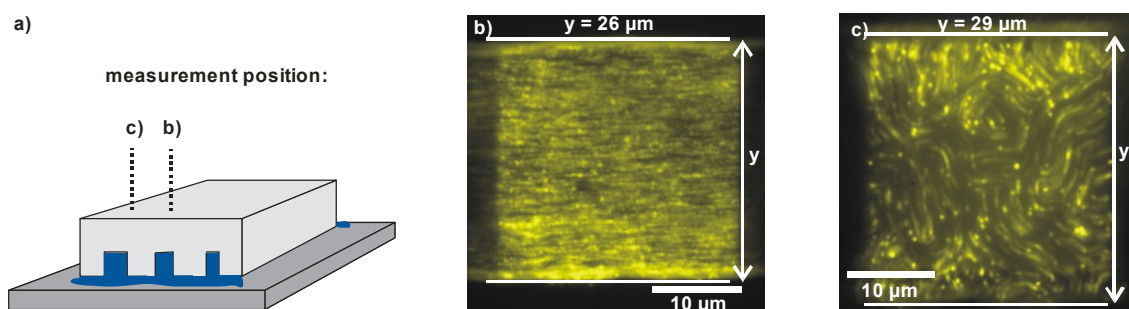


**Figure 5.15: Characterizing the influence of the line pattern width on the channel alignment of the mesoporous silica created through pattern transfer.** a) Schematic indicating the different measurement positions of b) and c). The overlay images of b) and c) were measured inside the mesoporous material in differently wide lines of the stamp pattern, but at the same height level low in the material close to the substrate. The line width  $y$  is b)  $26\ \mu\text{m}$  and c)  $29\ \mu\text{m}$ . The white bars in b) and c) indicate the orientation of the pattern line.

### 5.2.3 Conclusion

This chapter followed the aim of making mesoporous silica even more attractive for applications. The materials show a high degree of versatility, which makes them ideal structures for tailor-made applications. Many parameters such as the surface properties, morphologies, topologies, pore volume and diameter can be precisely controlled. However, the channel alignment could not be willingly determined and tuned to date. Yet for many applications, *e.g.* separation (electrophoresis), catalysis, waveguides and other material scientific as well as biomedical and lab-on-a-chip applications a precise control over the channel alignment and orientation could be highly desirable.

The single molecule measurements in combination with the characterization data of the stamps and the silica acquired by B. Rühle (group of T. Bein, LMU Munich, Department of Chemistry, Munich, Germany) demonstrated that the alignment of the channels and their orientation in mesoporous silica can be controlled through an active patterning process via the “Micromoulding in Capillaries”- technique. Not only the alignment of the channels with respect to each other but also the orientation of the channels with respect to the pattern and thus to an external coordinate system could be controlled. By applying the UV-stamp I linearly oriented channels several micrometers in length could be synthesized, yet only perpendicular to the orientation of the pattern. Through the selection of UV-stamp II as structure-guiding pattern the orientation of the channels in the silica could be partially arranged parallel to the pattern orientation.

The field of actively patterned nanomaterials is still only at a very beginning stage of its evolution. The displayed experiments prove that the synthesis of oriented mesoporous silica through MIMIC is a difficult process depending on many subtle parameters. The study depicted here was started towards the end of the doctoral studies and the described results are only a first report about this novel fascinating project. More detailed investigations need to follow to offer a complete and detailed understanding of the mechanistic processes governing channel alignment and orientation. Nevertheless, this study could identify some relevant parameters that influence the channel orientation inside a MIMIC pattern. The width  $y$  of the pattern lines, the surface interactions of the stamp, the substrate and the silica and the strength of the capillary flow during filling the stamp were discovered as key parameters for controlling the

channel orientation. The realized orientation of the channels along the pattern is an important step, since now, in principle, the absolute length of the porous silica channels is not limited and could be extended to centimeter scales. This is an essential prerequisite for applying those structures for example in electrophoresis or catalysis.



# 6 Summary and Outlook

## 6.1 Drug-delivery using mesoporous silica hosts

Within this work several important steps were made towards developing mesoporous silica as a novel class of efficient drug-delivery systems. First, it was shown that molecular dynamics can be fine-tuned inside the porous silica network through the covalent attachment of organic functional groups to the pore walls. These functionalizations form an organic carpet inside the pores that allows the precise control the interactions of the guest molecule with the host matrix. A highly photostable dye with good quantum efficiency was used in this study as a model for a drug molecule. Modifying the host-guest-interplay offered the possibility to tune the dye dynamics (within one order of magnitude in this study). The ability of controlling the drug dynamics is an essential prerequisite for generating a depot-effect, *i.e.* a retarded release of the drug from the delivery system over a prolonged period of time. Such a depot effect is one key feature for novel smart drug-delivery systems.

A second major contribution in this work dealt with mesoporous silica as drug-delivery system for the anti-cancer drug Doxorubicin hydrochloride. Especially in cancer chemotherapy, where the applied cytostatic drugs show a number of severe side-effects, patients could profit tremendously from novel smart delivery strategies. The results presented herein, demonstrate for the first time ever, how a clinically relevant cytostatic travels throughout and interacts with the delivery system on a single molecule level. It was shown that drug dynamics can be controlled and that the drug gets easily released from the host structure. The incorporation of the drug inside the delivery matrix does not affect its activity negatively, since the drug is still able to attack and kill malign cells efficiently after being released.

Finally, another important step consisted of incorporating fragile oligonucleotides such as short interfering RNA (siRNA) or short double-stranded DNA sequences into nanoporous silica particles. Gene therapy and gene silencing through RNA interference provide methods to selectively switch on and off certain genes and treat gene defects. Thus, they possess a high potential for revolutionizing medicine since novel therapies, especially for the vast number of hereditary diseases or cancer, could be developed. This field of biomedicine has evolved tremendously throughout the last two decades. However, for an efficient therapy the fragile oligonucleotides require smart delivery systems. Hence, in this work the dynamics of oligonucleotides inside mesoporous silica delivery systems of different morphologies was thoroughly investigated. Whereas the incorporation of siRNA into thin templated silica films *via* adding the biomolecules pre-synthetic directly to the precursor solution destroys the fragile biomolecules, a post-synthetic loading strategy proved successful. siRNA and dsDNA sequences up to 90 bp in length were loaded into hexagonal ordered (SBA-15) mesoporous silica particles. The template was removed *via* extraction prior to loading the oligonucleotides. It could be demonstrated that a wise modification of the channel surfaces seems to be necessary in order to allow oligonucleotide uptake by the particles. Only aminopropyl-containing functionalizations make the particles accessible for siRNA and dsDNA, whereas differently functionalized surfaces hinder the loading of the particles. This was attributed to a favourable oligonucleotide-aminopropyl-interaction *via e.g.* hydrogen bonding. Furthermore, oligonucleotide stability inside the carrier structure was proven exemplarily on a single molecule level as well as for all investigated oligonucleotides also on an ensemble level. Individual siRNA double-strands could be observed diffusing throughout the delivery system with unprecedented detail, demonstrating that single molecule techniques are capable of offering insight into these difficult samples. Additionally, it was proven through the Fluorescence Recovery after Photobleaching technique that organic functionalizations can be used even in template-free systems to control molecular dynamics. With this technique, the diffusion dynamics of siRNA and DNA double-strands up to 90 bp in length was investigated in detail, revealing immobile and mobile populations and clearly showing that the diffusion dynamics gets reduced significantly with increasing DNA double-strand length.

The three studies summarized above prove that mesoporous silica nanomaterials can provide solutions to current challenges in nanomedicine by offering a versatile platform for drug-delivery applications.

## 6.2 Creating large domains in mesoporous silica

The field of mesoporous silica materials emerged at the beginning of the 1990s and it has been evolving ever since. The materials show a high versatility which is the fundament of their huge achievement potential. Still nowadays, the materials can contribute smart solutions for long existing as well as new upcoming problems ranging from medicine to material science. For the important field of drug-delivery this was exemplarily shown in the first part of this work. However, there is a constant request for novel forms of mesoporous silica. The second part of this work was thus devoted to investigating and modifying two key material properties of mesoporous silica: the domain size and channel orientation inside the domain. Many parameters characterizing mesoporous silica, such as the pore volume and size and the surface properties, can be controlled to a large extent so far. However, fewer methods exist for tuning the domain size. Furthermore, controlling the mesoporous channel orientation over macroscopic scales is still a great challenge. Yet, gaining control over these parameters can be essential for enlarging the application potential of the materials.

In the second part of this work, first a method to maximize the domain size in P123 templated thin films was discussed. These films are well known to yield hexagonal ordered mesoporous structures, however their domain size can vary significantly. It was demonstrated that the relative humidity during the EISA process and in the first hours after film synthesis is a crucial parameter influencing the resulting domain sizes. Furthermore, it was shown that adjusting the relative humidity to about 50% – 60% yields micrometer sized well-structured domains. However, the resulting domains are oriented statistically and the orientation of the channels with respect to one another cannot be controlled.

Only, the “Micromoulding in Capillaries” (MIMIC) technology introduced later in this work allows to fabricate mesoporous silica with basically any required orientation of the channels. Through condensing the mesoporous silica inside the pattern of a PDMS stamp an efficient pattern transfer from the stamp to the mesoporous silica can be realized. The data presented in this work shows that the parameters governing the pattern transfer are manifold and subtle. Even though a thorough understanding of these processes is still missing, the experiments in this study offered first insights into the complicated nature of patterned silica materials. For a first approach, only linear patterns were used for fabricating mesoporous silica. The strength of the capillary flow with which the pattern lines were filled by the precursor solution and the width of the line seem to be relevant parameters determining the resulting mesoporous

channel orientation. It could be shown, that tuning these parameters allows to fabricate linearly oriented channels over macroscopic length scales. This can make the materials interesting for separation applications, *e.g.* as molecular sieves. Moreover, once long linearly oriented hexagonal mesoporous channel structures can be readily prepared, for example electrophoretic applications *e.g.* for the separation oligonucleotide molecules, come into perspective. Additionally, the materials could become very useful as novel waveguides and also lab-on-a-chip applications could profit from these mesoporous silica materials. This novel class of hybrid materials do thus show a high potential for various applications.

# 7 List of Abbreviations

<b>1D</b>	one dimension(al)
<b>2D</b>	two dimensions (dimensional)
<b>AAM</b>	Anodic alumina membrane, ano-disc
<b>AFM</b>	Atomic Force Microscopy/Microscope
<b>APD</b>	Avalanche photo-diode
<b>APS</b>	Ammonium persulfate
<b>BET</b>	Brunauer-Emmett-Teller
<b>bp</b>	base-pair(s)
<b>Brij 56</b>	Polyethylene glycol hexadecyl ether, $C_{16}H_{33}(OCH_2CH_2)_nOH$ , $n \sim 10$
<b>CMC</b>	Critical Micelle Concentration
<b>CTAB</b>	Cetyltrimethyl ammonium bromide
<b>DIP-TDI</b>	N,N'-Di(2,6-diisopropylphenyl)terrylene-3,4:11,12-tetracarboxydiimide
<b>dpss</b>	Diode pumped solid state (laser)
<b>ds</b>	Double-stranded
<b>EDTA</b>	Ethylenediaminetetraacetate
<b>EISA</b>	Evaporation Induced Self-Assembly
<b>(EM-)CCD</b>	(Electron multiplying) charge-coupled device

<b>F127</b>	Tri-block copolymer: poly(ethylene oxide) <sub>106</sub> -poly(propylene oxide) <sub>70</sub> -poly(ethylene oxide) <sub>106</sub> ; EO <sub>106</sub> PO <sub>70</sub> EO <sub>106</sub>
<b>FCS</b>	Fluorescence Correlation Spectroscopy
<b>FRAP</b>	Fluorescence Recovery after Photobleaching
<b>FRET</b>	Förster-Resonance-Energy-Transfer
<b>FWHM</b>	Full width at half maximum
<b>GISAXS</b>	Grazing-Incidence Small-Angle X-ray Scattering
<b>IC</b>	Internal Conversion
<b>ISC</b>	Intersystem Crossing
<b>IUPAC</b>	International Union of Pure and Applied Chemistry
<b>LM</b>	Light Microscopy
<b>LSCM</b>	Laser Scanning Confocal Microscopy <i>or</i> Microscope
<b>MIMIC</b>	Micromoulding in Capillaries
<b>miRNA</b>	microRNA
<b>mRH</b>	Measurement relative humidity
<b>mRNA</b>	messenger RNA
<b>MSD</b>	Mean square displacement
<b>NA</b>	Numerical Aperture
<b>P123</b>	Tri-block copolymer: poly(ethylene oxide) <sub>20</sub> -poly(propylene oxide) <sub>70</sub> -poly(ethylene oxide) <sub>20</sub> ; EO <sub>20</sub> PO <sub>70</sub> EO <sub>20</sub>
<b>PAGE</b>	Polyacrylamide-gel-electrophoresis
<b>PBS</b>	Phosphate buffered saline
<b>PDMS</b>	Poly(dimethylsiloxane)
<b>PFOTS</b>	1 <i>H</i> ,1 <i>H</i> ,2 <i>H</i> ,2 <i>H</i> -perfluorooctyltrichlorosilane
<b>QCM</b>	Quartz-crystal microbalance
<b>RH</b>	Relative humidity
<b>RNAi</b>	RNA interference

<b>ROI</b>	Region of interest
<b>rpm</b>	Rotations per minute
<b>SBA</b>	Santa Barbara Amorphous (type material)
<b>scrH</b>	Spin-coating relative humidity
<b>SEM</b>	Scanning Electron Microscopy
<b>siRNA</b>	Small interfering RNA
<b>SMM</b>	Single Molecule Microscopy
<b>SPT</b>	Single Particle Tracking
<b>ssNMR</b>	Solid-state Nuclear Magnetic Resonance
<b>STM</b>	Scanning Tunneling Microscope
<b>stRH</b>	Storage relative humidity
<b>TBE</b>	Tris/Borate/EDTA buffer
<b>TEM</b>	Transmission Electron Microscopy
<b>TEMED</b>	Tetramethylethylenediamine
<b>TEOS</b>	Tetraethyl orthosilicate
<b>TMB</b>	1,3,5-Trimethylbenzene
<b>XRD</b>	X-ray diffractogram/diffractometry



# 8 List of Publications and Contributions to Conferences

This chapter lists the publications that resulted of the work described in this thesis. Furthermore, all contributions to conferences are listed.

## 8.1 Publications

Parts of the results displayed in this thesis were published in the following journals:

- Chapter 4.2  
T. Lebold\*, L. A. Mühlstein\*, J. Blechinger, M. Riederer, H. Amenitsch, R. Köhn, K. Peneva, K. Müllen, J. Michaelis, C. Bräuchle, T. Bein: Tuning Single-Molecule Dynamics in Functionalized Mesoporous Silica, *Chem. Eur. J.*, **2009**, 15, 1661-1672.  
(T. L. and L. A. M. contributed equally to this work.)
- Chapter 4.3  
T. Lebold, C. Jung, J. Michaelis, C. Bräuchle: Nanostructured Silica Materials As Drug-Delivery Systems for Doxorubicin: Single Molecule and Cellular Studies, *Nano Letters*, **2009**, 9 (8), 2877-2883.

- Chapter 4.4  
manuscript in preparation

## 8.2 Contributions to Conferences

The works described in this thesis has been presented at numerous national and international conferences:

### Talks:

- 72<sup>nd</sup> Annual conference of the German Physical Society  
2008, Humboldt-Universität Berlin, Berlin, Germany.
- 20<sup>th</sup> German Zeolite Conference  
2008, Martin-Luther Universität Halle-Wittenberg, Halle, Germany.
- Summer School of the International Doctorate Program NanoBio Technology  
2008, Aiterbach am Chiemsee, Germany.
- 73<sup>rd</sup> Annual conference of the German Physical Society  
2009, Technische Universität Dresden, Dresden, Germany.
- 22<sup>nd</sup> German Zeolite Conference  
2010, Ludwig-Maximilians-Universität München, Munich, Germany.

### Poster contributions or equivalent:

- Workshop of the Center for NanoScience (Munich):  
“Emerging Nanosystems – From Quantum Manipulation to Nanobiomachnines”  
2006, Venice International University, Venice, Italy.
- Membership Meeting of the Elitenetwork Bavaria:  
“ENBcomeUnity2006 – Wissen schafft Verbindung”  
2006, Technische Universität München, Munich, Germany.
- 19<sup>th</sup> German Zeolite Conference  
2007, Universität Leipzig, Leipzig, Germany.
- 71<sup>st</sup> Annual conference of the German Physical Society  
2007, Universität Regensburg, Regensburg, Germany.

- Diffusion Fundamentals II – Basic Principles of Theory, Experiment and Application  
2007, Castle of L’Aquila, L’Aquila, Italy.
- 20<sup>th</sup> German Zeolite Conference  
2008, Martin-Luther Universität Halle-Wittenberg, Halle, Germany.
- Workshop of the Center for NanoScience (Munich):  
“Complex Nanosystems – Assembly, Control and Functionality”  
2008, Venice International University, Venice, Italy.
- 21<sup>st</sup> German Zeolite Conference  
2009, Christian-Albrechts-Universität zu Kiel, Kiel, Germany.
- NanoDay: Deutsches Museum München  
2009, Munich, Germany.
- 16<sup>th</sup> International Zeolite Conference:  
„Engineering of new micro- and meso-structured materials”  
2010, Hilton Sorrento Palace, Sorrento, Italy.



## 9 Bibliography

- [1] Y. Dzenis, Spinning continuous fibers for nanotechnology. *Science* **2004**, *304*, 1917.
- [2] D. Appell, Nanotechnology: Wired for success. *Nature* **2002**, *419*, 553.
- [3] R. Schlögl, S. B. Abd Hamid, Nanocatalysis: Mature science revisited or something really new? *Angewandte Chemie-International Edition* **2004**, *43*, 1628.
- [4] G. M. Whitesides, J. P. Mathias, C. T. Seto, Molecular Self-Assembly and Nanochemistry - a Chemical Strategy for the Synthesis of Nanostructures. *Science* **1991**, *254*, 1312.
- [5] G. M. Whitesides, Nanoscience, nanotechnology, and chemistry. *Small* **2005**, *1*, 172.
- [6] R. S. Friedman, M. C. McAlpine, D. S. Ricketts, D. Ham, C. M. Lieber, High-speed integrated nanowire circuits. *Nature* **2005**, *434*, 1085.
- [7] O. G. Schmidt, K. Eberl, Nanotechnology - Thin solid films roll up into nanotubes. *Nature* **2001**, *410*, 168.
- [8] P. Lalanne, J. P. Hugonin, Interaction between optical nano-objects at metallo-dielectric interfaces. *Nature Physics* **2006**, *2*, 551.
- [9] J. R. Heath, P. J. Kuekes, G. S. Snider, R. S. Williams, A defect-tolerant computer architecture: Opportunities for nanotechnology. *Science* **1998**, *280*, 1716.
- [10] Y. H. Gao, Y. Bando, Carbon nanothermometer containing gallium - Gallium's macroscopic properties are retained on a miniature scale in this nanodevice. *Nature* **2002**, *415*, 599.
- [11] P. Kohli, C. R. Martin, Smart nanotubes for biotechnology. *Current Pharmaceutical Biotechnology* **2005**, *6*, 35.
- [12] M. Ferrari, Cancer nanotechnology: Opportunities and challenges. *Nature Reviews Cancer* **2005**, *5*, 161.
- [13] O. Kayser, A. Lemke, N. Hernandez-Trejo, The impact of nanobiotechnology on the development of new drug delivery systems. *Current Pharmaceutical Biotechnology* **2005**, *6*, 3.
- [14] T. Kubik, K. Bogunia-Kubik, M. Sugisaka, Nanotechnology on duty in medical applications. *Current Pharmaceutical Biotechnology* **2005**, *6*, 17.
- [15] G. A. Silva, Introduction to nanotechnology and its applications to medicine. *Surgical Neurology* **2004**, *61*, 216.
- [16] J. Weiss, P. Takhistov, J. McClements, Functional materials in food nanotechnology. *Journal of Food Science* **2006**, *71*, R107.
- [17] P. Sanguansri, M. A. Augustin, Nanoscale materials development - a food industry perspective. *Trends in Food Science & Technology* **2006**, *17*, 547.
- [18] J. S. Beck, J. C. Vartuli, W. J. Roth, M. E. Leonowicz, C. T. Kresge, K. D. Schmitt, C. T. W. Chu, D. H. Olson, E. W. Sheppard, S. B. McCullen, J. B. Higgins, J. L. Schlenker, A New

- Family of Mesoporous Molecular-Sieves Prepared with Liquid-Crystal Templates. *Journal of the American Chemical Society* **1992**, *114*, 10834.
- [19] C. T. Kresge, M. E. Leonowicz, W. J. Roth, C. E. Vartuli, J. S. Beck, Ordered mesoporous molecular sieves synthesized by a liquid-crystal template mechanism. *Nature* **1992**, *359*, 710.
- [20] D. Y. Zhao, J. L. Feng, Q. S. Huo, N. Melosh, G. H. Fredrickson, B. F. Chmelka, G. D. Stucky, Triblock copolymer syntheses of mesoporous silica with periodic 50 to 300 angstrom pores. *Science* **1998**, *279*, 548.
- [21] D. Y. Zhao, Q. S. Huo, J. L. Feng, B. F. Chmelka, G. D. Stucky, Nonionic triblock and star diblock copolymer and oligomeric surfactant syntheses of highly ordered, hydrothermally stable, mesoporous silica structures. *Journal of the American Chemical Society* **1998**, *120*, 6024.
- [22] G. Binnig, H. Rohrer, C. Gerber, E. Weibel, Tunneling through a Controllable Vacuum Gap. *Applied Physics Letters* **1982**, *40*, 178.
- [23] G. Binnig, H. Rohrer, C. Gerber, E. Weibel, Surface Studies by Scanning Tunneling Microscopy. *Physical Review Letters* **1982**, *49*, 57.
- [24] G. Binnig, C. F. Quate, C. Gerber, Atomic Force Microscope. *Physical Review Letters* **1986**, *56*, 930.
- [25] W. E. Moerner, L. Kador, Optical-Detection and Spectroscopy of Single Molecules in a Solid. *Physical Review Letters* **1989**, *62*, 2535.
- [26] M. Orrit, J. Bernard, Single Pentacene Molecules Detected by Fluorescence Excitation in a *p*-Terphenyl Crystal. *Phys. Rev. Lett.* **1990**, *65*, 2716.
- [27] W. E. Moerner, M. Orrit, Illuminating Single Molecules in Condensed Matter. *Science* **1999**, *283*, 1670.
- [28] S. Nie, R. N. Zare, Optical Detection of Single Molecules. *Annu. Rev. Biophys. Struct.* **1997**, *26*, 567.
- [29] R. Langer, New Methods of Drug Delivery. *Science* **1990**, *249*, 1527.
- [30] A. Samad, Y. Sultana, M. Aqil, Liposomal Drug Delivery Systems: An Update Review. *Current Drug Delivery* **2007**, *4*, 297.
- [31] S. A. Agnihotri, N. N. Mallikarjuna, T. M. Aminabhavi, Recent advances on chitosan-based micro- and nanoparticles in drug delivery. *Journal of Controlled Release* **2004**, *100*, 5.
- [32] D. L. Mann, Targeted cancer therapeutics: the heartbreak of success. *Nature Medicine* **2006**, *12*, 881.
- [33] H. J. Guchelaar, C. H. H. Ten Napel, E. G. E. De Vries, N. H. Mulder, Clinical, Toxicological and Pharmaceutical Aspects of the Antineoplastic Drug Taxol: A Review. *Clinical Oncology* **1994**, *6*, 40.
- [34] A. Fire, S. Q. Xu, M. K. Montgomery, S. A. Kostas, S. E. Driver, C. C. Mello, Potent and specific genetic interference by double-stranded RNA in *Caenorhabditis elegans*. *Nature* **1998**, *391*, 806.
- [35] [http://nobelprize.org/nobel\\_prizes/medicine/laureates/2006/press.html](http://nobelprize.org/nobel_prizes/medicine/laureates/2006/press.html)
- [36] D. H. Everett, L. K. Koopal, *Manual of Symbols and Terminology for Physicochemical Quantities and Units - Appendix II: Definitions, Terminology and Symbols in Colloid and Surface Chemistry.*, International Union of Pure and Applied Chemistry (IUPAC), **1971**.
- [37] S. J. L. Billinge, E. J. McKimmy, M. Shatnawi, H. Kim, V. Petkov, D. Wermeille, T. J. Pinnavaia, Mercury Binding Sites in Thiol-Functionalized Mesostructured Silica. *Journal of the American Chemical Society* **2005**, *127*, 8492.
- [38] D. E. De Vos, M. Dams, B. F. Sels, P. A. Jacobs, Ordered mesoporous and microporous molecular sieves functionalized with transition metal complexes as catalysts for selective organic transformations. *Chemical Reviews* **2002**, *102*, 3615.

- [39] V. Rebbin, R. Schmidt, M. Fröba, Spherical Particles of Phenylene-Bridged Periodic Mesoporous Organosilica for High-Performance Liquid Chromatography. *Angewandte Chemie International Edition* **2006**, *45*, 5210.
- [40] N. Petkov, N. Stock, T. Bein, Gold Electroless Reduction in Nanosized Channels of Thiol-Modified SBA-15 Material. *Journal of Physical Chemistry B* **2005**, *109*, 10737.
- [41] B. Ye, M. L. Trudeau, D. M. Antonelli, Observation of a double maximum in the dependence of conductivity on oxidation state in potassium fulleride nanowires supported by a mesoporous niobium oxide host lattice. *Advanced Materials* **2001**, *13*, 561.
- [42] D. J. Cott, N. Petkov, M. A. Morris, B. Platschek, T. Bein, J. D. Holmes, Preparation of Oriented Mesoporous Carbon Nano-Filaments within the Pores of Anodic Alumina Membranes. *Journal of the American Chemical Society* **2006**, *128*, 3920.
- [43] C.-Y. Lai, B. G. Trewyn, D. M. Jeftinija, K. Jeftinija, S. Xu, S. Jeftinija, V. S. Y. Lin, A Mesoporous Silica Nanosphere-Based Carrier System with Chemically Removable CdS Nanoparticle Caps for Stimuli-Responsive Controlled Release of Neurotransmitters and Drug Molecules. *Journal of the American Chemical Society* **2003**, *125*, 4451.
- [44] I. Roy, T. Y. Ohulchanskyy, D. J. Bharali, H. E. Pudavar, R. A. Mistretta, N. Kaur, P. N. Prasad, Optical tracking of organically modified silica nanoparticles as DNA carriers: A nonviral, nanomedicine approach for gene delivery. *Proceedings of the National Academy of Sciences of the United States of America* **2005**, *102*, 279.
- [45] S. Giri, B. G. Trewyn, V. S. Y. Lin, Mesoporous silica nanomaterial-based biotechnological and biomedical delivery systems. *Nanomedicine* **2007**, *2*, 99.
- [46] S. Giri, B. G. Trewyn, M. P. Stellmaker, V. S. Y. Lin, Stimuli-Responsive Controlled-Release Delivery System Based on Mesoporous Silica Nanorods Capped with Magnetic Nanoparticles. *Angewandte Chemie International Edition* **2005**, *44*, 5038.
- [47] F. Torney, B. G. Trewyn, V. S. Y. Lin, K. Wang, Mesoporous silica nanoparticles deliver DNA and chemicals into plants. *Nature Nanotechnology* **2007**, *2*, 295.
- [48] J. Y. Ying, C. P. Mehnert, M. S. Wong, Synthese und Anwendungen von mit supramolekularen Templaten hergestellten mesoporösen Materialien. *Angew. Chem.* **1999**, *38*, 58.
- [49] G. Oye, J. Sjöblom, M. Stoecker, Synthesis, characterization and potential applications of new materials in the mesoporous range. *Advances in Colloid and Interface Science* **2001**, *89*, 439.
- [50] A. Monnier, F. Schuth, Q. Huo, D. Kumar, D. Margolese, R. S. Maxwell, G. D. Stucky, M. Krishnamurthy, P. Petroff, A. Firouzi, M. Janicke, B. F. Chmelka, Cooperative Formation of Inorganic-Organic Interfaces in the Synthesis of Silicate Mesostructures. *Science* **1993**, *261*, 1299.
- [51] Q. S. Huo, D. I. Margolese, U. Ciesla, P. Y. Feng, T. E. Gier, P. Sieger, R. Leon, P. M. Petroff, F. Schuth, G. D. Stucky, Generalized Synthesis of Periodic Surfactant Inorganic Composite-Materials. *Nature* **1994**, *368*, 317.
- [52] A. Firouzi, D. Kumar, L. M. Bull, T. Besier, P. Sieger, Q. Huo, S. A. Walker, J. A. Zasadzinski, C. Glinka, J. Nicol, D. Margolese, G. D. Stucky, B. F. Chmelka, Cooperative Organization of Inorganic-Surfactant and Biomimetic Assemblies. *Science* **1995**, *267*, 1138.
- [53] Q. S. Huo, R. Leon, P. M. Petroff, G. D. Stucky, Mesostructure Design with Gemini Surfactants - Supercage Formation in a 3-Dimensional Hexagonal Array. *Science* **1995**, *268*, 1324.
- [54] A. Firouzi, D. J. Schaefer, S. H. Tolbert, G. D. Stucky, B. F. Chmelka, Magnetic-Field-Induced Orientational Ordering of Alkaline Lyotropic Silicate-Surfactant Liquid Crystals. *J. Am. Chem. Soc.* **1997**, *119*, 9466.

- [55] P. C. A. Alberius, K. L. Frindell, R. C. Hayward, E. J. Kramer, G. D. Stucky, B. F. Chmelka, General predictive syntheses of cubic, hexagonal, and lamellar silica and titania mesostructured thin films. *Chemistry of Materials* **2002**, *14*, 3284.
- [56] S. Besson, T. Gacoin, C. Ricolleau, C. Jacquiod, J. P. Boilot, Phase diagram for mesoporous CTAB-silica films prepared under dynamic conditions. *Journal of Materials Chemistry* **2003**, *13*, 404.
- [57] F. Cagnol, D. Grosso, G. J. D. A. S. Soler-Illia, E. L. Crepaldi, F. Babonneau, H. Amenitsch, C. Sanchez, Humidity-controlled mesostructuration in CTAB-templated silica thin film processing. The existence of a modulable steady state. *Journal of Materials Chemistry* **2003**, *13*, 61.
- [58] V. Cauda, B. Onida, B. Platschek, L. Muhlstein, T. Bein, Large antibiotic molecule diffusion in confined mesoporous silica with controlled morphology. *Journal of Materials Chemistry* **2008**, *18*, 5888.
- [59] M. Trau, N. Yao, E. Kim, Y. Xia, G. M. Whitesides, I. A. Aksay, Microscopic patterning of orientated mesoscopic silica through guided growth. *Nature* **1997**, *390*, 674.
- [60] P. D. Yang, T. Deng, D. Y. Zhao, P. Y. Feng, D. Pine, B. F. Chmelka, G. M. Whitesides, G. D. Stucky, Hierarchically ordered oxides. *Science* **1998**, *282*, 2244.
- [61] E. Kim, Y. N. Xia, G. M. Whitesides, Polymer Microstructures Formed by Molding in Capillaries. *Nature* **1995**, *376*, 581.
- [62] P. Yang, G. Wirnsberger, H. C. Huang, S. R. Cordero, M. D. M. Gehee, B. Scott, T. Deng, G. M. Whitesides, B. F. Chmelka, S. K. Buratto, G. D. Stucky, Mirrorless Lasing from Mesostructured Waveguides Patterned by Soft Lithography. *Science* **2000**, *287*, 465.
- [63] G. Wirnsberger, P. D. Yang, H. C. Huang, B. Scott, T. Deng, G. M. Whitesides, B. F. Chmelka, G. D. Stucky, Patterned block-copolymer-silica mesostructures as host media for the laser dye rhodamine 6G. *Journal of Physical Chemistry B* **2001**, *105*, 6307.
- [64] B. J. Scott, G. Wirnsberger, G. D. Stucky, Mesoporous and mesostructured materials for optical applications. *Chemistry of Materials* **2001**, *13*, 3140.
- [65] A. Katiyar, S. Yadav, P. G. Smirniotis, N. G. Pinto, Synthesis of ordered large pore SBA-15 spherical particles for adsorption of biomolecules. *Journal of Chromatography A* **2006**, *1122*, 13.
- [66] S. Brunauer, P. H. Emmett, E. Teller, Adsorption of gases in multimolecular layers. *Journal of the American Chemical Society* **1938**, *60*, 309.
- [67] M. Mesa, L. Sierra, B. Lopez, A. Ramirez, J. L. Guth, Preparation of micron-sized spherical particles of mesoporous silica from a triblock copolymer surfactant, usable as a stationary phase for liquid chromatography. *Solid State Sciences* **2003**, *5*, 1303.
- [68] J. R. Lakowicz, *Principles of Fluorescence Spectroscopy*, 3rd ed., Springer Science+Business Media, LLC, New York, **2006**.
- [69] [https://www.atto-tec.com/attotecshop/product\\_info.php?info=p114\\_ATTO-647N.html&XTCsid=uhvo8hqbkhf48802lgg4r95tp0](https://www.atto-tec.com/attotecshop/product_info.php?info=p114_ATTO-647N.html&XTCsid=uhvo8hqbkhf48802lgg4r95tp0)
- [70] F. O. Holtrup, G. R. J. Muller, H. Quante, S. Defeyter, F. C. DeSchryver, K. Mullen, Terrylenimides: New NIR fluorescent dyes. *Chemistry-a European Journal* **1997**, *3*, 219.
- [71] F. Nolde, J. Q. Qu, C. Kohl, N. G. Pschirer, E. Reuther, K. Mullen, Synthesis and modification of terrylenediimides as high-performance fluorescent dyes. *Chemistry - A European Journal* **2005**, *11*, 3959.
- [72] C. Jung, B. K. Muller, D. C. Lamb, F. Nolde, K. Mullen, C. Bräuchle, A new photostable terrylene diimide dye for applications in single molecule studies and membrane labeling. *Journal of the American Chemical Society* **2006**, *128*, 5283.
- [73] A. Dubois, M. Canva, A. Brun, F. Chaput, J. P. Boilot, Photostability of dye molecules trapped in solid matrices. *Applied Optics* **1996**, *35*, 3193.

- [74] W. P. Ambrose, P. M. Goodwin, J. C. Martin, R. A. Keller, Single-Molecule Detection and Photochemistry on a Surface Using near-Field Optical-Excitation. *Physical Review Letters* **1994**, *72*, 160.
- [75] R. Zondervan, F. Kulzer, S. B. Orlinskii, M. Orrit, Photoblinking of rhodamine 6G in poly(vinyl alcohol): Radical dark state formed through the triplet. *Journal of Physical Chemistry A* **2003**, *107*, 6770.
- [76] p. Tamarat, A. Maali, B. Lounis, M. Orrit, Ten Years of Single-Molecule Spectroscopy. *J. Phys. Chem. A* **2000**, *104*, 1.
- [77] W. E. Moerner, A Dozen Years of Single-Molecule Spectroscopy in Physics, Chemistry and Biophysics. *J. Phys. Chem. B* **2002**, *106*, 910.
- [78] F. Kulzer, M. Orrit, Single-Molecule Optics. *Ann. Rev. Phys. Chem.* **2004**, *55*, 585.
- [79] S. Weiss, Fluorescence spectroscopy of single biomolecules. *Science* **1999**, *283*, 1676.
- [80] G. Seisenberger, M. U. Ried, T. Endreß, H. Büning, M. Hallek, C. Bräuchle, Real-Time Single-Molecule Imaging of the Infection Pathway of an Adeno-Associated Virus. *Science* **2001**, *294*, 1929.
- [81] A. Yildiz, J. N. Forkey, S. A. McKinney, T. Ha, Y. E. Goldman, P. R. Selvin, Myosin V walks hand-over-hand: Single fluorophore imaging with 1.5-nm localization. *Science* **2003**, *300*, 2061.
- [82] K. Shiroguchi, K. Kinosita, Myosin V walks by lever action and Brownian motion. *Science* **2007**, *316*, 1208.
- [83] K. Kitamura, M. Tokunaga, A. H. Iwane, T. Yanagida, A single myosin head moves along an actin filament with regular steps of 5.3 nanometres. *Nature* **1999**, *397*, 129.
- [84] K. Bacia, S. A. Kim, P. Schwille, Fluorescence cross-correlation spectroscopy in living cells. *Nature Methods* **2006**, *3*, 83.
- [85] S. Woermke, S. Mackowski, T. H. P. Brotsudarmo, C. Jung, A. Zumbusch, M. Ehrl, H. Scheer, E. Hofmann, R. G. Hiller, C. Brauchle, Monitoring fluorescence of individual chromophores in peridininchlorophyll-protein complex using single molecule spectroscopy. *Biochimica Et Biophysica Acta-Bioenergetics* **2007**, *1767*, 956.
- [86] F. Schindler, J. M. Lupton, J. Muller, J. Feldmann, U. Scherf, How single conjugated polymer molecules respond to electric fields. *Nature Materials* **2006**, *5*, 141.
- [87] C. A. Werley, W. E. Moerner, Single-molecule nanoprobe explore defects in spin-grown crystals. *Journal of Physical Chemistry B* **2006**, *110*, 18939.
- [88] K. S. McCain, D. C. Hanley, J. M. Harris, Single-Molecule Fluorescence Trajectories for Investigating Molecular Transport in Thin Silica Sol-Gel Films. *Anal. Chem.* **2003**, *75*, 4351.
- [89] D. A. VandenBout, W. T. Yip, D. H. Hu, D. K. Fu, T. M. Swager, P. F. Barbara, Discrete intensity jumps and intramolecular electronic energy transfer in the spectroscopy of single conjugated polymer molecules. *Science* **1997**, *277*, 1074.
- [90] C. Hellriegel, J. Kirstein, C. Bräuchle, Tracking of single molecules as a powerful method to characterize diffusivity of organic species in mesoporous materials. *New Journal of Physics* **2005**, *7*, 23.
- [91] C. Jung, C. Hellriegel, J. Michaelis, C. Bräuchle, Single-Molecule Traffic in Mesoporous Materials: Translational, Orientational, and Spectral Dynamics. *Advanced Materials* **2007**, *19*, 956.
- [92] C. Jung, C. Hellriegel, B. Platschek, D. Wöhrle, T. Bein, J. Michaelis, C. Bräuchle, Simultaneous measurement of orientational and spectral dynamics of single molecules in nanostructured host-guest materials. *Journal of the American Chemical Society* **2007**, *129*, 5570.

- [93] J. Kirstein, B. Platschek, C. Jung, R. Brown, T. Bein, C. Bräuchle, Exploration of nanostructured channel systems with single-molecule probes. *Nature Materials* **2007**, *6*, 303.
- [94] A. Zürner, J. Kirstein, M. Doblinger, C. Bräuchle, T. Bein, Visualizing single-molecule diffusion in mesoporous materials. *Nature* **2007**, *450*, 705.
- [95] C. Jung, J. Kirstein, B. Platschek, T. Bein, M. Budde, I. Frank, K. Müllen, J. Michaelis, C. Bräuchle, Diffusion of Oriented Single Molecules with Switchable Mobility in Networks of Long Unidimensional Nanochannels. *Journal of the American Chemical Society* **2008**, *130*, 1638.
- [96] <http://www.microscopyu.com/>
- [97] M. Lampton, B. Margon, S. Bowyer, Parameter-Estimation in X-Ray Astronomy. *Astrophysical Journal* **1976**, *208*, 177.
- [98] N. Bobroff, Position measurement with a resolution and noise-limited instrument. *Rev. Sci. Instrum.* **1986**, *57*, 1152.
- [99] A. Einstein, The motion of elements suspended in static liquids as claimed in the molecular kinetic theory of heat. *Annalen Der Physik* **1905**, *17*, 549.
- [100] H. C. Berg, *Random Walks in Biology*, New, expanded ed., Princeton University Press, **1993**.
- [101] J. Kirstein, Doctoral Thesis, Ludwig-Maximilians-University Munich **2007**.
- [102] C. M. Anderson, G. N. Georgiou, I. E. G. Morrison, G. V. W. Stevenson, R. J. Cherry, Tracking of Cell-Surface Receptors by Fluorescence Digital Imaging Microscopy Using a Charge-Coupled Device Camera - Low-Density-Lipoprotein and Influenza-Virus Receptor Mobility at 4-Degrees-C. *Journal of Cell Science* **1992**, *101*, 415.
- [103] G. J. Schütz, H. Schindler, T. Schmidt, Single-molecule microscopy on model membranes reveals anomalous diffusion. *Biophysical Journal* **1997**, *73*, 1073.
- [104] D. Axelrod, D. E. Koppel, J. Schlessinger, E. Elson, W. W. Webb, Mobility Measurement by Analysis of Fluorescence Photobleaching Recovery Kinetics. *Biophysical Journal* **1976**, *16*, 1055.
- [105] D. E. Koppel, D. Axelrod, J. Schlessinger, E. L. Elson, W. W. Webb, Dynamics of Fluorescence Marker Concentration as a Probe of Mobility. *Biophysical Journal* **1976**, *16*, 1315.
- [106] M. Edidin, *Fluorescence photobleaching and recovery, FPR, in the analysis of membrane structure and dynamics*, CRC Press, Boca Raton, **1994**.
- [107] P. A. Liebman, G. Entine, Lateral Diffusion of Visual Pigment in Photoreceptor Disk Membranes. *Science* **1974**, *185*, 457.
- [108] M. M. Poo, R. A. Cone, Lateral Diffusion of Rhodopsin in Photoreceptor Membrane. *Nature* **1974**, *247*, 438.
- [109] A. Ishihara, K. Jacobson, A Closer Look at How Membrane-Proteins Move. *Biophysical Journal* **1993**, *65*, 1754.
- [110] O. Seksek, J. Biwersi, A. S. Verkman, Translational diffusion of macromolecule-sized solutes in cytoplasm and nucleus. *Journal of Cell Biology* **1997**, *138*, 131.
- [111] F. Umenishi, J. M. Verbavatz, A. S. Verkman, cAMP regulated membrane diffusion of a green fluorescent protein-aquaporin 2 chimera. *Biophysical Journal* **2000**, *78*, 1024.
- [112] S. R. Chary, R. K. Jain, Direct Measurement of Interstitial Convection and Diffusion of Albumin in Normal and Neoplastic Tissues by Fluorescence Photobleaching. *Proceedings of the National Academy of Sciences of the United States of America* **1989**, *86*, 5385.
- [113] S. Ramanujan, A. Pluen, T. D. McKee, E. B. Brown, Y. Boucher, R. K. Jain, Diffusion and convection in collagen gels: Implications for transport in the tumor interstitium. *Biophysical Journal* **2002**, *83*, 1650.

- [114] T. K. L. Meyvis, S. C. De Smedt, P. Van Oostveldt, J. Demeester, Fluorescence recovery after photobleaching: A versatile tool for mobility and interaction measurements in pharmaceutical research. *Pharmaceutical Research* **1999**, *16*, 1153.
- [115] <http://rsb.info.nih.gov/ij/>
- [116] D. M. Soumpasis, Theoretical-Analysis of Fluorescence Photobleaching Recovery Experiments. *Biophysical Journal* **1983**, *41*, 95.
- [117] J. G. McNally, Quantitative FRAP in analysis of molecular binding dynamics in vivo. *Fluorescent Proteins, Second Edition* **2008**, *85*, 329.
- [118] V. P. Torchilin, Micellar nanocarriers: Pharmaceutical perspectives. *Pharmaceutical Research* **2007**, *24*, 1.
- [119] K. E. Uhrich, S. M. Cannizzaro, R. S. Langer, K. M. Shakesheff, Polymeric Systems for Controlled Drug Release. *Chem. Rev.* **1999**, *99*, 3181.
- [120] C. C. Muller-Goymann, Physicochemical characterization of colloidal drug delivery systems such as reverse micelles, vesicles, liquid crystals and nanoparticles for topical administration. *European Journal of Pharmaceutics and Biopharmaceutics* **2004**, *58*, 343.
- [121] R. Haag, Supramolecular drug-delivery systems based on polymeric core-shell architectures. *Angewandte Chemie-International Edition* **2004**, *43*, 278.
- [122] Y. Bae, S. Fukushima, A. Harada, K. Kataoka, Design of environment-sensitive supramolecular assemblies for intracellular drug delivery: Polymeric micelles that are responsive to intracellular pH change. *Angewandte Chemie-International Edition* **2003**, *42*, 4640.
- [123] K. S. Soppimath, T. M. Aminabhavi, A. R. Kulkarni, W. E. Rudzinski, Biodegradable polymeric nanoparticles as drug delivery devices. *Journal of Controlled Release* **2001**, *70*, 1.
- [124] A. Schlossbauer, J. Kecht, T. Bein, Biotin-Avidin as a Protease-Responsive Cap System for Controlled Guest Release from Colloidal Mesoporous Silica. *Angewandte Chemie International Edition* **2009**, *48*, 3092.
- [125] V. Cauda, C. Argyo, A. Schlossbauer, T. Bein, Controlling the delivery kinetics from colloidal mesoporous silica nanoparticles with pH-sensitive gates. *Journal of Materials Chemistry* **2010**, *20*, 4305.
- [126] A. Schlossbauer, S. Warncke, P. M. E. Gramlich, J. Kecht, A. Manetto, T. Carell, T. Bein, A programmable DNA-based molecular valve for colloidal mesoporous silica. *Angewandte Chemie International Edition* **2010**, accepted.
- [127] V. S. Y. Lin, Veni, vidi, vici and then ... vanished. *Nature Materials* **2009**, *8*, 252.
- [128] J. H. Park, L. Gu, G. von Maltzahn, E. Ruoslahti, S. N. Bhatia, M. J. Sailor, Biodegradable luminescent porous silicon nanoparticles for in vivo applications. *Nature Materials* **2009**, *8*, 331.
- [129] V. Cauda, A. Schlossbauer, T. Bein, Bio-degradation study of colloidal mesoporous silica nanoparticles: Effect of surface functionalization with organo-silanes and poly(ethylene glycol). *Microporous and Mesoporous Materials* **2010**, *132*, 60.
- [130] R. Kumar, I. Roy, T. Y. Ohulchanskyy, L. A. Vathy, E. J. Bergey, M. Sajjad, P. N. Prasad, In Vivo Biodistribution and Clearance Studies Using Multimodal Organically Modified Silica Nanoparticles. *Acs Nano* **2010**, *4*, 699.
- [131] A. J. Di Pasqua, K. K. Sharma, Y. L. Shi, B. B. Toms, W. Ouellette, J. C. Dabrowiak, T. Asefa, Cytotoxicity of mesoporous silica nanomaterials. *Journal of Inorganic Biochemistry* **2008**, *102*, 1416.
- [132] H. J. Eom, J. Choi, Oxidative stress of silica nanoparticles in human bronchial epithelial cell, Beas-2B. *Toxicology in Vitro* **2009**, *23*, 1326.

- [133] D. Napierska, L. C. J. Thomassen, V. Rabolli, D. Lison, L. Gonzalez, M. Kirsch-Volders, J. A. Martens, P. H. Hoet, Size-Dependent Cytotoxicity of Monodisperse Silica Nanoparticles in Human Endothelial Cells. *Small* **2009**, *5*, 846.
- [134] Y. S. Lin, C. L. Haynes, Impacts of Mesoporous Silica Nanoparticle Size, Pore Ordering, and Pore Integrity on Hemolytic Activity. *Journal of the American Chemical Society* **2010**, *132*, 4834.
- [135] A. Zürner, Rendered schematic animations and images of a mesoporous silica particle, **2009**.
- [136] H. Provendier, C. C. Santini, J. M. Basset, L. Carmona, Surface organometallic chemistry on oxides: The first well-defined selenium(IV) derivative grafted onto silica. *European Journal of Inorganic Chemistry* **2003**, 2139.
- [137] P. M. Visintin, R. G. Carbonell, C. K. Schauer, J. M. DeSimone, Chemical functionalization of silica and alumina particles for dispersion in carbon dioxide. *Langmuir* **2005**, *21*, 4816.
- [138] T. Maschmeyer, F. Rey, G. Sankar, J. M. Thomas, Heterogeneous Catalysts Obtained by Grafting Metallocene Complexes onto Mesoporous Silica. *Nature* **1995**, *378*, 159.
- [139] T. Yokoi, H. Yoshitake, T. Tatsumi, Synthesis of amino-functionalized MCM-41 via direct co-condensation and post-synthesis grafting methods using mono-, di- and tri-amino-organoalkoxysilanes. *Journal of Materials Chemistry* **2004**, *14*, 951.
- [140] K. Yamamoto, T. Tatsumi, Remarkable improvement in hydrothermal stability of MCM-41 by surface modification with Grignard reagents. *Chemistry Letters* **2000**, 624.
- [141] K. Yamamoto, T. Tatsumi, Organic functionalization of mesoporous molecular sieves with Grignard reagents. *Microporous and Mesoporous Materials* **2001**, *44(SISI)*, 459.
- [142] S. Angloher, T. Bein, Metalorganic modification of periodic mesoporous silica: aromatic nitrogen functionalities. *Journal of Materials Chemistry* **2006**, *16*, 3629.
- [143] S. Angloher, J. Kecht, T. Bein, Optimization of Reaction Conditions for the Metalorganic Modification of MCM-41. *Chemistry of Materials* **2007**, *19*, 3568.
- [144] C. E. Fowler, S. L. Burkett, S. Mann, Synthesis and characterization of ordered organo-silica-surfactant mesophases with functionalized MCM-41-type architecture. *Chem. Commun.* **1997**, 1769.
- [145] J. Aguado, J. M. Arsuaga, A. Arencibia, Adsorption of aqueous mercury(II) on propylthiol-functionalized mesoporous silica obtained by cocondensation. *Industrial & Engineering Chemistry Research* **2005**, *44*, 3665.
- [146] Q. H. Yang, J. Yang, J. Liu, Y. Li, C. Li, Synthesis and characterization of phosphonic acid functionalized organosilicas with bimodal nanostructure. *Chemistry of Materials* **2005**, *17*, 3019.
- [147] W. S. Han, Y. Kang, S. J. Lee, H. Lee, Y. Do, Y. A. Lee, J. H. Jung, Fabrication of color-tunable luminescent silica nanotubes loaded with functional dyes using a sol-gel cocondensation method. *Journal of Physical Chemistry B* **2005**, *109*, 20661.
- [148] M. Klotz, P.-A. Albouy, A. Ayrat, C. Menager, D. Grosso, A. Van der Lee, V. Cabuil, F. Babonneau, C. Guizard, The True Structure of Hexagonal Mesophase-Templated Silica Films As Revealed by x-ray Scattering: Effects of Thermal Treatments and of Nanoparticle Seeding. *Chemistry of Materials* **2000**, *12*, 1721.
- [149] M. Rauscher, T. Salditt, H. Spohn, Small-angle x-ray scattering under grazing incidence: The cross section in the distorted-wave Born approximation. *Physical Review B* **1995**, *52*, 16855.
- [150] M. P. Tate, V. N. Urade, J. D. Kowalski, T. C. Wei, B. D. Hamilton, B. W. Eggiman, H. W. Hillhouse, Simulation and interpretation of 2D diffraction patterns from self-assembled nanostructured films at arbitrary angles of incidence: From grazing incidence (above

- the critical angle) to transmission perpendicular to the substrate. *Journal of Physical Chemistry B* **2006**, *110*, 9882.
- [151] V. R. Karra, I. L. Moudrakovski, A. Sayari, Odd-even effect in the synthesis of mesoporous silicate molecular sieves in the presence of alkyl cetyl dimethyl ammonium bromide. *Journal of Porous Materials* **1996**, *3*, 77.
- [152] G. Sauerbrey, Verwendung Von Schwingquarzen Zur Wagung Dunner Schichten Und Zur Mikrowagung. *Zeitschrift für Physik* **1959**, *155*, 206.
- [153] A. Darga, J. Kecht, T. Bein, Probing the intrapore surface of phenyl-substituted nanoscale mesoporous silica-piezoelectric sorption measurements in thin films. *Langmuir* **2007**, *23*, 12915.
- [154] C. J. Brinker, G. W. Scherer, *Sol-Gel Science: The Physics and Chemistry of Sol-Gel Processing*, San Diego, **1990**.
- [155] Y. F. Lu, R. Ganguli, C. A. Drewien, M. T. Anderson, C. J. Brinker, W. L. Gong, Y. X. Guo, H. Soyez, B. Dunn, M. H. Huang, J. I. Zink, Continuous formation of supported cubic and hexagonal mesoporous films by sol gel dip-coating. *Nature* **1997**, *389*, 364.
- [156] D. Wagner, W. V. Kern, P. Kern, Liposomal Doxorubicin in Aids-Related Kaposi-Sarcoma - Long-Term Experiences. *Clinical Investigator* **1994**, *72*, 417.
- [157] Y. Collins, S. Lele, Long-term pegylated liposomal doxorubicin use in recurrent ovarian carcinoma. *Journal of the National Medical Association* **2005**, *97*, 1414.
- [158] J. O'Shaughnessy, Liposomal anthracyclines for breast cancer: Overview. *Oncologist* **2003**, *8*, 1.
- [159] J. A. MacKay, M. N. Chen, J. R. McDaniel, W. G. Liu, A. J. Simnick, A. Chilkoti, Self-assembling chimeric polypeptide-doxorubicin conjugate nanoparticles that abolish tumours after a single injection. *Nature Materials* **2009**, *8*, 993.
- [160] P. Horcajada, T. Chalati, C. Serre, B. Gillet, C. Sebrie, T. Baati, J. F. Eubank, D. Heurtaux, P. Clayette, C. Kreuz, J. S. Chang, Y. K. Hwang, V. Marsaud, P. N. Bories, L. Cynober, S. Gil, G. Ferey, P. Couvreur, R. Gref, Porous metal-organic-framework nanoscale carriers as a potential platform for drug delivery and imaging. *Nature Materials* **2010**, *9*, 172.
- [161] C. J. Brinker, Y. F. Lu, A. Sellinger, H. Y. Fan, Evaporation-induced self-assembly: Nanostructures made easy. *Advanced Materials* **1999**, *11*, 579.
- [162] *Please note: Doxorubicin may cause cancer. Especially during the spin-coating process harmful aerosols are generated. Working under especially equipped safety benches is mandatory. Respiratory protection and other equipment to avoid exposure are necessary.*
- [163] T. Lebold, L. A. Mühlstein, J. Blechinger, M. Riederer, H. Amenitsch, R. Köhn, K. Peneva, K. Müllen, J. Michaelis, C. Bräuchle, T. Bein, Tuning single-molecule dynamics in functionalized mesoporous silica. *Chemistry A European Journal* **2009**, *15*, 1661.
- [164] T. Schmidt, G. J. Schuetz, W. Baumgartner, H. J. Gruber, H. Schindler, Characterization of Photophysics and Mobility of Single Molecules in a Fluid Lipid Membrane. *J. Phys. Chem.* **1995**, *99*, 17662.
- [165] N. S. Angerman, C. L. Bell, T. A. Victor, S. S. Danyluk, Proton Magnetic-Resonance Study of Aggregation of Actinomycin-D in D<sub>2</sub>O. *Biochemistry* **1972**, *11*, 2402.
- [166] P. D'Arpa, L. F. Liu, Topoisomerase-Targeting Antitumor Drugs. *Biochimica Et Biophysica Acta* **1989**, *989*, 163.
- [167] M. A. Matzke, M. Primig, J. Trnovsky, A. J. M. Matzke, Reversible Methylation and Inactivation of Marker Genes in Sequentially Transformed Tobacco Plants. *Embo Journal* **1989**, *8*, 643.
- [168] M. Wassenegger, S. Heimes, L. Riedel, H. L. Sanger, Rna-Directed De-Novo Methylation of Genomic Sequences in Plants. *Cell* **1994**, *76*, 567.

- [169] Y. D. Park, I. Papp, E. A. Moscone, V. A. Iglesias, H. Vaucheret, A. J. M. Matzke, M. A. Matzke, Gene silencing mediated by promoter homology occurs at the level of transcription and results in meiotically heritable alterations in methylation and gene activity. *Plant Journal* **1996**, *9*, 183.
- [170] C. Napoli, C. Lemieux, R. Jorgensen, Introduction of a Chimeric Chalcone Synthase Gene into Petunia Results in Reversible Co-Suppression of Homologous Genes in Trans. *Plant Cell* **1990**, *2*, 279.
- [171] A. R. Vanderkrol, L. A. Mur, M. Beld, J. N. M. Mol, A. R. Stuitje, Flavonoid Genes in Petunia - Addition of a Limited Number of Gene Copies May Lead to a Suppression of Gene-Expression. *Plant Cell* **1990**, *2*, 291.
- [172] C. J. S. Smith, C. F. Watson, P. C. Morris, C. R. Bird, G. B. Seymour, J. E. Gray, C. Arnold, G. A. Tucker, W. Schuch, S. Harding, D. Grierson, Inheritance and Effect on Ripening of Antisense Polygalacturonase Genes in Transgenic Tomatoes. *Plant Molecular Biology* **1990**, *14*, 369.
- [173] J. M. Kooter, R. Vanblokkland, P. Delange, M. Stam, J. N. M. Mol, Posttranscriptional Transgene-Mediated Gene Silencing in Plants. *Journal of Cellular Biochemistry* **1994**, *115*.
- [174] C. E. Rocheleau, W. D. Downs, R. L. Lin, C. Wittmann, Y. X. Bei, Y. H. Cha, M. Ali, J. R. Priess, C. C. Mello, Wnt signaling and an APC-related gene specify endoderm in early *C. elegans* embryos. *Cell* **1997**, *90*, 707.
- [175] E. Bernstein, A. A. Caudy, S. M. Hammond, G. J. Hannon, Role for a bidentate ribonuclease in the initiation step of RNA interference. *Nature* **2001**, *409*, 363.
- [176] P. M. Waterhouse, H. W. Graham, M. B. Wang, Virus resistance and gene silencing in plants can be induced by simultaneous expression of sense and antisense RNA. *Proceedings of the National Academy of Sciences of the United States of America* **1998**, *95*, 13959.
- [177] A. J. Hamilton, D. C. Baulcombe, A species of small antisense RNA in posttranscriptional gene silencing in plants. *Science* **1999**, *286*, 950.
- [178] P. D. Zamore, T. Tuschl, P. A. Sharp, D. P. Bartel, RNAi: Double-stranded RNA directs the ATP-dependent cleavage of mRNA at 21 to 23 nucleotide intervals. *Cell* **2000**, *101*, 25.
- [179] S. M. Elbashir, J. Harborth, W. Lendeckel, A. Yalcin, K. Weber, T. Tuschl, Duplexes of 21-nucleotide RNAs mediate RNA interference in cultured mammalian cells. *Nature* **2001**, *411*, 494.
- [180] S. Parrish, J. Fleenor, S. Q. Xu, C. Mello, A. Fire, Functional anatomy of a dsRNA trigger: Differential requirement for the two trigger strands in RNA interference. *Molecular Cell* **2000**, *6*, 1077.
- [181] S. M. Hammond, E. Bernstein, D. Beach, G. J. Hannon, An RNA-directed nuclease mediates post-transcriptional gene silencing in *Drosophila* cells. *Nature* **2000**, *404*, 293.
- [182] C. Cogoni, G. Macino, Gene silencing in *Neurospora crassa* requires a protein homologous to RNA-dependent RNA polymerase. *Nature* **1999**, *399*, 166.
- [183] G. J. Hannon, RNA interference. *Nature* **2002**, *418*, 244.
- [184] C. C. Mello, D. Conte, Revealing the world of RNA interference. *Nature* **2004**, *431*, 338.
- [185] S. M. Hammond, Dicing and slicing - The core machinery of the RNA interference pathway. *Febs Letters* **2005**, *579*, 5822.
- [186] H. Mok, S. H. Lee, J. W. Park, T. G. Park, Multimeric small interfering ribonucleic acid for highly efficient sequence-specific gene silencing. *Nature Materials* **2010**, *9*, 272.
- [187] C. Hom, J. Lu, M. Liong, H. Luo, Z. Li, J. I. Zink, F. Tamanoi, Mesoporous Silica Nanoparticles Facilitate Delivery of siRNA to Shutdown Signaling Pathways in Mammalian Cells. *Small* **2010**, *6*, 1185.

- [188] A. Schlossbauer, D. Schaffert, J. Kecht, E. Wagner, T. Bein, Click chemistry for high-density biofunctionalization of mesoporous silica. *Journal of the American Chemical Society* **2008**, *130*, 12558.
- [189] E. A. J. Reits, J. J. Neefjes, From fixed to FRAP: measuring protein mobility and activity in living cells. *Nature Cell Biology* **2001**, *3*, E145.
- [190] B. L. Sprague, R. L. Pego, D. A. Stavreva, J. G. McNally, Analysis of binding reactions by fluorescence recovery after photobleaching. *Biophysical Journal* **2004**, *86*, 3473.
- [191] Q. S. Huo, D. I. Margolese, U. Ciesla, D. G. Demuth, P. Y. Feng, T. E. Gier, P. Sieger, A. Firouzi, B. F. Chmelka, F. Schuth, G. D. Stucky, Organization of Organic-Molecules with Inorganic Molecular-Species into Nanocomposite Biphasic Arrays. *Chemistry of Materials* **1994**, *6*, 1176.
- [192] H. Yang, A. Kuperman, N. Coombs, S. MamicheAfara, G. A. Ozin, Synthesis of oriented films of mesoporous silica on mica. *Nature* **1996**, *379*, 703.
- [193] J. H. Fendler, Self-assembled nanostructured materials. *Chemistry of Materials* **1996**, *8*, 1616.
- [194] W. Z. Li, S. S. Xie, L. X. Qian, B. H. Chang, B. S. Zou, W. Y. Zhou, R. A. Zhao, G. Wang, Large-scale synthesis of aligned carbon nanotubes. *Science* **1996**, *274*, 1701.
- [195] H. Sakai, R. Baba, K. Hashimoto, A. Fujishima, A. Heller, Local Detection of Photoelectrochemically Produced H<sub>2</sub>O<sub>2</sub> with a Wired Horseradish-Peroxidase Microsensor. *Journal of Physical Chemistry* **1995**, *99*, 11896.
- [196] E. Lindner, V. V. Cosofret, S. Ufer, R. P. Buck, R. P. Kusy, R. B. Ash, H. T. Nagle, Flexible (Kapton-Based) Microsensor Arrays of High-Stability for Cardiovascular Applications. *Journal of the Chemical Society-Faraday Transactions* **1993**, *89*, 361.
- [197] C. Ye, T. Tamagawa, P. Schiller, D. L. Polla, Pyroelectric PbTiO<sub>3</sub> Thin-Films for Microsensor Applications. *Sensors and Actuators a-Physical* **1992**, *35*, 77.
- [198] M. P. Tate, B. W. Eggiman, J. D. Kowalski, H. W. Hillhouse, Order and orientation control of mesoporous silica films on conducting gold substrates formed by dip-coating and self-assembly: A grazing angle of incidence small-angle X-ray scattering and field emission scanning electron microscopy study. *Langmuir* **2005**, *21*, 10112.
- [199] H. Kiessig, Interference of X-rays in thick layers. *Annalen Der Physik* **1931**, *10*, 769.
- [200] A. I. Alichanow, L. A. Arzimowic, Totalreflexion der Röntgenstrahlen an dünnen Schichten. *Zeitschrift für Physik* **1933**, *82*, 489.
- [201] B. Rühle, group of T. Bein, LMU Munich, Department of Chemistry, Butenandtstr. 11, Gerhard-Ertl-Building, 81377 Munich, **2010**.
- [202] H. Daiguji, N. Tatsumi, S. Kataoka, A. Endo, One-Dimensional Alignment of SBA-15 Films in Microtrenches. *Langmuir* **2009**, *25*, 11221.



# Acknowledgements

This work would not have been possible without the great support of many persons to whom I want to address my gratitude here:

First of all, I would like to cordially thank my supervisor, Professor Christoph Bräuchle, for giving me the opportunity to explore this interesting field of science that allowed me to expand my horizons due to its interdisciplinary character. Furthermore, I would like to thank him for the constant support, the advices and the great trust throughout the entire period of my PhD – and thanks for the nice conferences I was allowed to attend. :o)

Further, I want to thank my co-supervisor Professor Thomas Bein, whose expert knowledge about the complicated nature of mesoporous silica materials was of great value for elucidating this unknown universe.

In addition, I would like to thank Professor Jens Michaelis for the numerous fruitful discussions about the diverse projects depicted in this work and the encouraging suggestions for further interesting experiments. Many thanks go also to the collaborating group leaders I have been working with: Professor Heinrich Leonhardt, Professor Gerhard Winter and Professor Ernst Wagner.

Next, I would like to express my sincere gratitude to all collaborators and co-workers in the different groups that substantially supported this work through hard labor in the different labs around: Lea Mühlstein, Barbara Platschek, Andreas Zürner, Axel Schlossbauer, Tina Reuther and Bastian Rühle in the group of Thomas Bein. Katrin Schneider (great thanks for all the hard work), Akos Dobay and Lothar Schermelleh in the group of Heinrich Leonhardt. Stelijan Tinkov in the group of Gerhard Winter who showed me how to survive the experiments with Doxorubicin and staying fertile at the same time.

Many thanks to the entire Bräuchle/Lamb/Michaelis group for providing such a pleasant working atmosphere: especially Ioanna Andrecka, Anna Jasiak, Adam Muschielok, Peter Schwaderer, Stephan Wörmke, Melari Davies, Florian Feil, Karla de Bruin, my “golden girls” in the next office: Anna Sauer, Frauke König and Dorothee Schupp even though she’s not in the

next office. Barbara Treutlein and Julia Nagy, Nico and Iko, Matthias and Martin, Aurelie and Gregor, Michael and Peter S. as well as Viola ... and all the ones I forgot. I did not forget Robert, whom I want to thank sincerely for helping me in the lab and teaching me a lot of tricks in using word! I also do not want to forget all the Diploma and Master students as well as student assistants that worked with me: Julia Blechinger, Alexandra Schmidt and Johanna Schulten.

Many thanks also to Silke Steger and Monika Franke. Great thanks to Moritz Ehrl, the minister of finance in our group, who always made sure that some money arrives on my account. And thanks for the nice ÜDV and lunch time hours as well as for spending enlightenment about DIN 1338! Thanks also to the people from the fine mechanics and the electronics workshop.

Many thanks go to two special people from whom I was allowed to learn so much in the lab and with whom I could spend great time outside the lab! Johanna Kirstein and Christophe Jung, thanks for helping me so much during these years!!!

I further want to express my gratitude to my good friends outside the scientific universe that supported me a lot throughout the last years: especially I would like to thank Björn Bechtold, Alexander Weigel and Alexandra Lauer.

Finally, I would like to express my deep gratitude to the following persons:

Ein ganz besonderer Dank geht an meine Eltern Ingrid und Klaus-Peter Lebold, ohne die ich zuerst einmal nicht hier wäre :o) und ohne deren felsenfesten emotionalen Rückhalt in den letzten dreißig Jahren diese Arbeit nie entstanden wäre. Vielen Dank auch für das ganze Geld, also die finanzielle Unterstützung über all die Jahre. Ich weiß, wenn man ein Kind in die Welt setzt geht man gewisse – auch finanzielle – Verpflichtungen ein, aber dass es so lange dauert :o) This is why I would like to especially acknowledge financial and emotional support by people that never ever get acknowledged anywhere in the course of scientific publications and presentations, but should be acknowledged in the first: my parents.

There is one special person left on this planet that I did not thank so far: Sally Hall, my sweetheart, my pearl of the southern hemisphere and pride of Africa: I love you! Thank you so much for your great support, your understanding, your patience with all my flaws, your assistance and encouragement. Without all that, this work would not be the same and this world neither! Thanks for everything and even more.....

*Timo*

# Curriculum Vitae

## Persönliche Daten

---

**Name:** Timo Lebold  
**Geburtsdatum:** 15. Juni 1979  
**Geburtsort:** Miltenberg am Main  
**Staatsangehörigkeit:** deutsch  
**Familienstand:** ledig

## Ausbildung

---

**Sept. 1990 – Juli 1999:** Karl-Ernst Gymnasium Amorbach;  
Allgemeine Hochschulreife Juli 1999

**Sept. 1999 – Sept. 2000:** Blindeninstitutsstiftung Würzburg;  
Zivildienst

**Okt. 2000 – Okt. 2005:** Philipps-Universität Marburg;  
Studium der Chemie;  
Diplom-Vorprüfung: Okt. 2002; Diplom: Okt. 2005

**Okt. 2003 – März 2004:** University of Cambridge;  
Center for Atmospheric Science;  
SOKRATES Austauschstudium

**seit Februar 2006:** Ludwig-Maximilians-Universität München;  
Promotion;  
Wissenschaftlicher Angestellter am Lehrstuhl von Prof. Dr. C. Bräuchle

## Stipendien und Auszeichnungen

---

- Nov. 2009:** **Publication Award;**  
Center for Nanoscience (CeNS)
- seit Okt. 2006:** **Elitenetzwerk Bayern;**  
Mitglied im Internationalen Doktoranden-Kolleg Nano-Bio-Technologie (IDK-NBT)
- Okt. 2000 – Sept. 2002:** **Jubiläumstipendium des Fonds der Chemischen Industrie**
- Juni 1999:** **Buchpreis des Fonds der Chemischen Industrie;**  
Auszeichnung als bester Abiturient im Fach Chemie am Karl-Ernst Gymnasium Amorbach
- Feb. 1999:** **Chemie-Olympiade;**  
Teilnahme am bayerischen Landeseminar in Gendorf

## Praktika

---

- Aug. 2004:** **Jahr der Technik des Bundesministeriums für Bildung und Forschung;**  
Ausstellungsbetreuer auf dem Museumsschiff MS Technik
- Aug. 2003 – Sept. 2003:** **Jahr der Chemie des Bundesministeriums für Bildung und Forschung;**  
Ausstellungsbetreuer auf dem Museumsschiff MS Chemie
- Juli 2001 – Okt. 2001:** **Max-Planck-Institut für Polymerforschung Mainz;**  
Durchführung eines Forschungsprojektes